

**CONTINUOUS MANUFACTURING OF BETA-LACTAM
ANTIBIOTICS BY ENZYMATIC REACTIVE CRYSTALLIZATION**

A Dissertation
Presented to
The Academic Faculty

by

Matthew A. McDonald

In Partial Fulfillment
of the Requirements for the Degree
Doctor of Philosophy in the
School of Chemical & Biomolecular Engineering

Georgia Institute of Technology
December 2020

COPYRIGHT © 2020 BY MATTHEW A. MCDONALD

**CONTINUOUS MANUFACTURING OF BETA-LACTAM
ANTIBIOTICS BY ENZYMATIC REACTIVE CRYSTALLIZATION**

Approved by:

Dr. Andreas S. Bommarius, Advisor
School of Chemical & Biomolecular
Engineering
Georgia Institute of Technology

Dr. Blair K. Brettmann
School of Chemical & Biomolecular
Engineering
Georgia Institute of Technology

Dr. Martha A. Grover, Advisor
School of Chemical & Biomolecular
Engineering
Georgia Institute of Technology

Dr. Raquel L. Lieberman
School of Chemistry & Biochemistry
Georgia Institute of Technology

Dr. Ronald W. Rousseau, Advisor
School of Chemical & Biomolecular
Engineering
Georgia Institute of Technology

Date Approved: August 27, 2020

To those who have made me who I am today

To my parents, family, friends, coaches, colleagues, and teammates

ACKNOWLEDGEMENTS

First and foremost I would like to thank my advisors, and I have been lucky enough to have three of them. Dr. Andreas Bommarius has taught me how to be an independent researcher and has always had extraordinary confidence in my abilities as a scientist, sending me around the world to spread my findings; for that I will always be grateful. Dr. Martha Grover is the greatest critical thinker I have ever met; her comments have forced me to examine results and experimental hiccups from all angles, and have no doubt made me a better science communicator by a hundred-fold. And Dr. Ronald Rousseau, who shares so much of my curiosity for scientific phenomena (in reality I share *his* curiosity) and has supported me through some of the less-conventional periods of my doctoral studies, all while having an unbelievable eye for detail. I am certain my time at Georgia Tech would not have been successful without all three.

I would like to thank my many group members: Adam Caparco, Robbie Franklin, Thomas Kwok, Lukas Bromig, and all other members of the Bommarius Group, Stefani Kocavska, Tristan Kernick, Nils Persson, Youngjo Kim, Mike McBride, and all other members of the Grover Group, and finally Patrick Harris and Colton Lagerman, for joining me in this project. The undergraduates who I was lucky enough to mentor, Tunde Hambolu, Long Nguyen, Jonathan Bentata Benezry, and Grant Marshall, thank you for all your help.

The Atlanta Track Club has played a huge role in my time at Georgia Tech. My involvement with the team began when the captain of the Master's Team and School of Chemical and Biomolecular Engineering professor Victor Breedveld recruited me to Atlanta, and I am so thankful he personally reached out to me. My coaches, Amy and

Andrew Begley, have made me not just the best athlete I could be, but also a better, more responsible person. And most of all my teammates, thank you.

Most importantly I would like to thank my family and friends. My parents, for preparing me to be a successful graduate student and then letting me move so far away. My friends, for keeping me sane when need be and making this journey one of the greatest, most fun, experiences of my life.

TABLE OF CONTENTS

ACKNOWLEDGEMENTS	iv
LIST OF TABLES	ix
LIST OF FIGURES	xi
LIST OF SYMBOLS AND ABBREVIATIONS	xxi
SUMMARY	xxiv
CHAPTER 1. Introduction	1
1.1 Continuous manufacturing	2
1.2 Enzymatic beta-lactam synthesis	4
1.3 Reactive crystallization of amoxicillin and cephalexin	6
CHAPTER 2. Stability of Penicillin G Acylase	10
2.1 Introduction and motivation	10
2.2 Materials and methods	11
2.2.1 Chemicals	11
2.2.2 Enzyme Membrane Reactor	12
2.2.3 Non-isothermal continuous activity assay	13
2.2.4 Residual activity experiments	14
2.2.5 Reaction temperature dependence	14
2.3 Theory	15
2.4 Model fitting and parameter estimation	19
2.5 Results and discussion	20
2.5.1 Linear temperature scans	20
2.5.2 Simulated experiments	23
2.5.3 PGA deactivation model discrimination	26
2.5.4 PGA deactivation by batch assay	30
2.6 Conclusion	32
CHAPTER 3. Kinetics of PGA-catalyzed Synthesis of Ampicillin and Cephalexin	34
3.1 Introduction	34
3.2 Materials and methods	36
3.2.1 Materials	36
3.2.2 Determination of initial reaction rates	36
3.2.3 Determination of solubilities	38
3.2.4 Modelling	38
3.2.5 Reactive crystallization experiments	39
3.2.6 Process Characterization	39
3.3 Results and discussion	40
3.3.1 Solubility experiments	41

3.3.2	Initial rate experiments	42
3.3.3	Improved process model	46
3.3.4	Reactive crystallization experiments	49
3.4	Ampicillin summary	55
3.5	Other beta-lactams	56
CHAPTER 4. Kinetics of Cephalexin Crystallization with Co-solutes		58
4.1	Introduction	58
4.2	Materials and Methods	59
4.2.1	Nucleation and growth of crystals	59
4.2.2	Process analytical technology	60
4.2.3	Computational methods	64
4.3	Results and Discussion	67
4.3.1	Cephalexin monohydrate solubility	67
4.3.2	Primary nucleation kinetics	70
4.3.3	Secondary nucleation and mixing	74
4.3.4	Growth kinetics	83
4.3.5	Discussion of continuous manufacturing	86
4.4	Conclusion	87
CHAPTER 5. Ampicillin Crystal Growth Rates and Growth Rate Dispersion Measured by Image analysis		89
5.1	Introduction	89
5.2	Materials and Methods	91
5.3	Results	97
5.3.1	Growth rate dispersion at the population level	97
5.3.2	Growth rate dispersion at the individual level	99
5.4	Discussion	102
5.5	Conclusions	109
CHAPTER 6. Development of a Model for In Silico Design of an Optimal Process for Continuous Manufacturing of Beta-lactams		111
6.1	Introduction	111
6.2	Model Development	112
6.3	Methods	121
6.4	Results and Discussion	123
6.4.1	Attainable regions	123
6.4.2	Pareto-optimal fronts	129
6.4.3	Further improvements	137
6.5	Conclusion	139
CHAPTER 7. Implications of the Reactive Crystallizer Model: A Case Study on Product Purity		142
7.1	Introduction	142
7.2	Results and Discussion	144
7.2.1	Well-mixed enzymatic reactive crystallizer	144
7.2.2	Steady state multiplicity in reactive MSMPRs	148

7.2.3	Reactive crystallizers in series for robust purity	151
7.2.4	Evaluation of process robustness	157
7.3	Conclusions	160
7.4	Derivation of steady state uniqueness criterion in a reactive MSMR	162
CHAPTER 8. Process Analytical Technology for Continuous Manufacture of Beta-lactams		166
8.1	Introduction	166
8.2	Polarimetry	167
8.3	Attenuated total reflectance Fourier transform infrared spectroscopy	170
8.4	Focused Beam Reflectance Measurement	175
8.5	Particle Vision and Measurement	179
8.6	Other Process Analytical Technology	181
CHAPTER 9. The Pilot Plant: Progress Towards Operation of A Continuous Process for the Manufacture of Amoxicillin and Cephalexin		183
9.1	Introduction	183
9.2	Reaction and Crystallization	184
9.2.1	Mixed-suspension Mixed-product-removal Reactive Crystallizer	185
9.2.2	Plug Flow Reactive Crystallizer	190
9.3	Enzyme crystal separation	192
9.4	Filtration and washing	195
9.5	Control	198
9.6	Conclusion	199
CHAPTER 10. Future Directions and Past Reflections		202
REFERENCES		211
VITA		235

LIST OF TABLES

Table 2.1. Specific optical rotation of key species. Measured in 250 mM pH 7 sodium phosphate buffer at 20 °C. Measured at a wavelength of 589 nm along a path length of 10 cm. Under 20 mM the concentration dependence is linear.	14
Table 2.2. Reaction rate parameter values for equations 2.5 and 2.6, measured at 25 °C.17	17
Table 2.3. Values used in TEM-1 beta-lactamase simulated deactivation experiments. The value of ΔG^\ddagger is only dependent on the reaction, not the enzyme deactivation model, therefore the value for TEM-1 beta-lactamase was set to be the same as was measured for PGA for similarity of scale (actual value 54.2 kJ/mol).	24
Table 2.4. The number of parameters, P , residual sum of squares, RSS, and Akaike information criterion, AIC, for each model fit to the data generated from the saw-tooth temperature profile.	28
Table 2.5. Parameter values resulting from fitting Model 2 to the saw-tooth temperature profile given as 95% confidence intervals. ΔG_{deact} (kJ/mol) is given at 25 °C.	28
Table 2.6. Enzyme decay constants measured by batch residual rate experiments (Figure 2.9 middle and right).....	31
Table 2.7. Comparison of results from non-isothermal continuous assay with linear and saw-tooth temperature profiles analyzed with Model 1 and isothermal batch assay. Values are 95% confidence intervals.	32
Table 3.1. Summary of the optical rotation of the optically active species in ampicillin synthesis; 10 cm path-length at 589 nm. The specific rotation was measured at 298 K in 250 mM pH 7-phosphate buffer.	38
Table 3.2 Comparison of Assemblase® and the E. coli PGA used by Svedas <i>et al.</i> (pH 6.4 only) at 298 K. ⁷⁷ Assemblase with the other antibiotics studied in the course of this thesis are also reported with discussion at the end of the chapter.	45
Table 3.3. The maximum yield of ampicillin compared between the theoretical maximum, the control homogeneous experiment, and the reactive crystallization setup. The initial pH value is 6.75 and the reactants are equimolar.	53
Table 4.1. Parameter bounds used in constrained parameter fitting.	65
Table 4.2. Kinetic parameters for the crystallization of cephalixin monohydrate with 95% confidence interval. Confidence interval values marked “ns” indicate parameters that were not significantly different from a theoretically justified value, therefore they have been fixed at the theoretically predicted value	87
Table 5.1. Initial conditions for growth experiments.....	94
Table 6.1. Values of the rate and association constants shown in Figure 6.1 and equations 6.1-6.5. Notes: ^a Youshko <i>et al.</i> 2002 ⁶³ , ^b McDonald <i>et al.</i> 2017 ³² , ^c values calculated from published values of α , β_0 , and γ and invariants between mechanisms (e.g. ampicillin and amoxicillin have the same nucleophile, therefore they must have the same	

nucleophile association constant). Discussion of α , β_0 , and γ can be found in Chapter 3.	114
Table 6.2. Summary of the parameter values used to model the solubility of amoxicillin, ampicillin, cephalixin, their precursors, and their hydrolysis products. Notes: ^a Felix <i>et al.</i> 2016 ¹⁵⁷ , ^b Santana <i>et al.</i> 2010 ⁴⁵ , ^c Bezerra <i>et al.</i> 2013 ¹⁵⁶ , ^d McDonald <i>et al.</i> 2017 ³² , ^e This work.	117
Table 6.3. Summary of parameter values used to model the crystallization of amoxicillin and ampicillin. Notes: ^a Encarnación-Gómez <i>et al.</i> 2016 ⁴¹	117
Table 7.1. The parameter values used to model the crystallization of ampicillin and byproduct phenylglycine. ^{89, 170} Notes: ^a values for phenylalanine anhydrate used in place of phenylglycine, the crystallization kinetics of phenylglycine anhydrate have not been published but based on experiments during the course of this thesis they can be approximated satisfactorily with the similar molecule phenylalanine.....	143
Table 8.1. Evaluation of the simple linear model of optical rotation dependence on concentration. Specific rotation for a 10 cm cuvette at 20 °C at a wavelength of 589 nm, $\pm 95\%$ confidence interval.	170
Table 8.2. Summary of IR calibration models and validation for single species. *Data collected on ReactIR iC10 with 30 second scan time, all others collected on ReactIR 702L with 60 second scan time.....	172
Table 9.1. Summary of design conditions for reactor sizing, feed concentrations, and flow rates.	188
Table 9.2. Summary of expected performance of the basic pilot plant based on modeling and the values in Table 9.1.	188
Table 9.3. Summary of expected performance of the optimized pilot plant based on extensive modeling and the inputs from Table 9.1.	192

LIST OF FIGURES

<p>Figure 1.1. Overview of PGA catalyzed reactions and reactive crystallization. Top: synthesis reaction and crystallization of amoxicillin (horizontal arrows) with enzyme catalyzed primary and secondary hydrolysis reactions (vertical arrows). Bottom: synthesis and hydrolysis of cephalexin and reactant PGME with subsequent crystallization of cephalexin and phenylglycine.....</p>	5
<p>Figure 1.2. Graphical abstract depicting the results from each chapter as they build towards the CM process for beta-lactams, center.</p>	9
<p>Figure 2.1. Schematic of experimental setup. The reactor volume is the region to which the enzyme is confined by the ultrafiltration membrane. Mixing is maintained by a PTFE coated magnetic stir-bar and reactor temperature is manipulated by water bath 1 and monitored via an online thermocouple.</p>	13
<p>Figure 2.2. The three models explored in this study. N is the natively folded, active enzyme, U_j is an unfolded intermediate, and D is deactivated enzyme.</p>	18
<p>Figure 2.3. (A) The measured conversion versus time (dashed line) at three different temperature scan rates and Model 1 fits (solid lines) used to produce the data shown in (A) and (B). (B) The predicted ampicillin hydrolysis reaction rate as a function of time at the three temperature scan rates. (C) The fraction of active enzyme as a function of time at the three scan rates. Yellow: 10.92 K/h, red: 8.24 K/h, and blue: 5.42 K/h.</p>	21
<p>Figure 2.4. All three models are fit to the 5.42 K/h linear data. The solid yellow, blue, and red lines represent Model 1, Model 2, and Model 3, respectively. The dashed black line is the measured conversion, the green line is the observed temperature.</p>	22
<p>Figure 2.5. Model 1 fit to the 54.9 K/h linear temperature ramp conversion data.</p>	23
<p>Figure 2.6. Results of the simulated TEM-1 deactivation experiment.⁶² The reaction conditions are similar to those used for the non-isothermal continuous activity assay: the substrate is penicillin G and the product is penicilloic acid, the substrate feed concentration is 20 mM, the enzyme concentration is 5 μM, and the reactor residence time is 8 minutes. (A) Simulated TEM-1 (Model 3) non-isothermal continuous assay and fit with Model 1 and Model 2. (B) Simulated data based on TEM-1 (Model 3) and simulated data based on Model 1 and Model 2 fits at slower temperature scan rate. (C) Simulated data based on TEM-1 (Model 3) and simulated data based on Model 1 and Model 2 fits with saw-tooth temperature profile.</p>	25
<p>Figure 2.7 (A) The observed conversion of ampicillin and the fit of Model 1 (solid yellow), Model 2 (solid red), and Model 3 (solid blue) to the data (black dashed). (B) The fractions of active (solid) and deactivated (dashed) enzyme when the data in (A) are fit with Model 1. (C) The fractions of active (solid), reversibly unfolded (dotted), and deactivated (dashed) enzyme when the data in (A) are fit with Model 2. (D) The fractions of active (solid), 1st reversibly unfolded (dotted), 2nd reversibly unfolded (dash-dot), and deactivated (dashed) enzyme when the data in (A) are fit with Model 3. (E) The temperature as a function of time.....</p>	27

Figure 2.8. The melting temperature, T_m , and unfolding onset temperature, T_{onset} , of Assemblase PGA are shown as a function of pH value at two protein concentrations. The melting was measured by differential scanning fluorimetry (DSF). T_m is interpreted as the temperature where the DSF curve is at a maximum and T_{onset} is the temperature at which the DSF curve increases 5% above the baseline.	29
Figure 2.9. Results of batch deactivation assay of PGA. (Left) Ampicillin hydrolysis rate as a function of temperature. (Middle) Residual enzyme activity as a function of time and temperature. (Right) Model 1 deactivation constant as a function of temperature.	31
Figure 3.1 The overall reaction and crystallization scheme for the PGA-catalyzed synthesis of ampicillin, with crystallization of ampicillin and possible precipitation of phenylglycine. Synthesis is shown in blue, primary hydrolysis in yellow, secondary hydrolysis in orange, ampicillin trihydrate crystallization in green, and phenylglycine crystallization in red.	35
Figure 3.2. The solubility of 6-APA (■), ampicillin (◆), and phenylglycine (▲) as functions of pH value. Lines indicate modeled fit based on the Henderson-Hasselbalch equation with ionic strength correction. The solid ampicillin line represents ampicillin trihydrate while the dashed ampicillin line represents ampicillin sodium salt. PGME is not shown because it is highly soluble.	42
Figure 3.3. Synthesis (left) and hydrolysis (right) activity of Assemblase® as functions of pH at three different equimolar reactant concentrations. The activity is determined from the initial rate. Curves are to guide the eye.	43
Figure 3.4. The initial rate of ampicillin hydrolysis at different initial ampicillin concentrations and 6-APA concentrations.	44
Figure 3.5. The 6-APA dissociation constant at three different reactant concentrations (left) and the initial synthesis-to-hydrolysis ratio at three different reactant concentrations (right). The dissociation constant should not be concentration dependent, but it is confounded by the competing and binding of 6-APA to free enzyme and 6-APA to acyl-enzyme complex.	46
Figure 3.6. The pH profile of a typical reaction is illustrated in a system at equimolar initial concentrations of 160 mM to highlight the decrease in pH value with increasing conversion.	47
Figure 3.7. The improved kinetic scheme for DSM-Sinochem Assemblase®. Two pH-dependent equilibria have been added to the EAH form of PGA (top right). Abbreviations: E is free enzyme, EAH is acyl-enzyme complex, EAH_2^+ and EA^- are inactive forms of the acyl-enzyme complex, $\text{E}\cdot\text{PGME}$, $\text{E}\cdot\text{APA}$, $\text{EAH}\cdot\text{APA}$, and $\text{E}\cdot\text{Amp}$ are enzyme bound PGME, enzyme bound 6-APA, acyl-enzyme complex bound 6-APA, and enzyme bound ampicillin, respectively. PG is phenylglycine	49
Figure 3.8. The reaction course for the control reactor (left) and reactive crystallization scheme (right) at a pH value of 6.75. Error bars are one standard deviation, $n = 5$. Lines represent model predictions based on initial rate data. PGME concentration was not directly measured but can be determined via a mass balance. These profiles are representative of the concentration profiles obtained at all three initial pH values.	51

Figure 3.9. The selectivity of the reactive crystallization process is compared to the homogeneous reactor. The selectivity is defined as the total amount of ampicillin formed over the total amount of phenylglycine formed. The solid lines represent model predictions based on initial rate data. The error bars are one standard deviation.	52
Figure 3.10. Productivity of the reactive crystallization process is compared to the homogeneous reactor. The solid lines represent model predictions. The error bars represent one standard deviation.	54
Figure 3.11. The initial rate of cephalexin hydrolysis at different initial antibiotic concentrations and 7-ADCA concentrations.	57
Figure 4.1. (Left) Calibration of cephalexin solute concentration with ATR-FTIR. The difference in IR intensity between the 1369 cm^{-1} and 1305 cm^{-1} is correlated with the molar concentration. Points represent measurements and the shaded region shows the 95% prediction interval based on the linear best fit.	61
Figure 4.2. (Left) The number of crystals in suspension, as measured by extent of crystallization (bottom axis) and offline microscopy (top axis), was correlated with the number of chord counts observed online by FBRM. The FBRM counts were fit with a hyperbolic trend (solid curve) and initial linear trend (dashed line). Note the break in the axis for the final measured point. (Right) A 1/100 slurry dilution (in saturated solution) is shown. The area inside the red square has a volume of 6.25 nL and contains 51 crystals (counting those on the left and top borders but discounting those on the right and bottom borders). Using several images and randomly sampling different squares in the same image the total number density was determined to be 890 ± 89 billion crystals per liter for this sample. This image was sampled from the end of a batch of cephalexin with no co-solute and an initial supersaturation of 2.56.	62
Figure 4.3. An optical micrograph of product cephalexin crystals (left) and the result of processing that image (right). Counted crystals in green, discounted overlapping crystals in red, and discounted cutoff crystals in blue.	63
Figure 4.4. The number based CSD calculated from Figure 4.3. The CSD histogram was fit to a lognormal distribution (green solid curve), gamma distribution (pink dashed curve), and Weibull distribution (brown dotted curve).	67
Figure 4.5. Solubility of cephalexin, in moles of cephalexin per liter of solution, as a function of pH at $5.0\text{ }^{\circ}\text{C}$ (blue) and $25.0\text{ }^{\circ}\text{C}$ (red) with 95% confidence regions based on fitting the data to Equations 4.12 and 4.13.	69
Figure 4.6. PXRD patterns for cephalexin as received (blue), crystallized without a co-solute (red), with PGME co-solute (yellow), with 7-ADCA co-solute (green), and PXRD pattern of 7-ADCA (purple).	70
Figure 4.7. An example of pH trend (green dashed curve), saturation (blue dotted curve), and counts (red solid curve) during a typical batch cephalexin crystallization experiment. The inset shows FBRM nucleation detection in detail.	72
Figure 4.8. Experimental cumulative distribution functions of stochastic detection times, F, at three supersaturations: $S = 1.98$ (in red), $S = 2.27$ (in yellow), and $S = 2.56$ (in blue), were fit to Poisson distributions (curves) according to equation 4.1. The black points are	

experiments without a co-solute (squares $S = 1.98$, diamonds $S = 2.27$, and circles $S = 2.56$) and the red \times 's represent experiments with a co-solute ($S = 2.56$). The shaded regions are the 95% confidence regions based on the fit to equation 4.1.	73
Figure 4.9. Bootstrapping was used to determine the primary nucleation parameters. In this figure the parameters that gave the best fit to equation 4.2 (for data randomly generated by taking four samples from each of three data sets at different supersaturation values) are sorted and plotted for 200 bootstrap trials. The confidence interval lies between the 2.5 th and 97.5 th percentile.....	74
Figure 4.10. An optical micrograph of cephalexin monohydrate crystals formed in the presence of 7-ADCA co-solute (left) and a comparison of the number of nuclei created by primary nucleation and secondary nucleation based on fit parameters (right).	76
Figure 4.11. Three examples of anomalous FRBR readings suggesting that a dead zone had formed in front of the FBRM probe window at (from left to right) 140 minutes, 70 minutes, and 100 minutes. In all experiments, the counts followed an s-shape curve in time, eventually saturating when the snowstorm effect prevents the FBRM from detecting all crystals. In the experiments where a dead zone formed, the counts rapidly drop, suggesting crystals had stopped moving in front of the probe window.....	77
Figure 4.12. A mixing diagram for the crystallizer geometry used to determine cephalexin crystallization kinetics. Experiments marked with an open circle (\circ) were well mixed and were used to fit the kinetic model. Experiments marked with a cross (\times) showed poor mixing and experiments marked with a plus ($+$) showed significant foaming.	78
Figure 4.13. The stir rate (blue) was increased from 400 to 900 RPM for 5 minutes to generate a stable foam. The counts measured by FBRM (red) decreased during foam generation and did not return after the stir rate was dropped back to 400 RPM, indicating crystals had been permanently sequestered in the foam.	80
Figure 4.14. Left, the final CSD of cephalexin monohydrate without co-solute (blue), with 30 mM PGME co-solute (red), and 30 mM 7-ADCA co-solute (yellow). Right, the desupersaturation of cephalexin without co-solute (blue circle), with 30 mM PGME co-solute (red diamond), and 30 mM 7-ADCA co-solute (yellow square).	83
Figure 4.15. The critical supersaturation, S_{cr} , as a function of co-solute concentration. The lines are best fits of equation 4.20. The error bars are 95% confidence intervals.	84
Figure 4.16. HPLC analysis of purity of unwashed (light hue) and washed (dark hue) cephalexin monohydrate crystals formed in the presence of a co-solute at different concentrations. The 50 mM 7-ADCA point was excluded because 7-ADCA also crystallized giving a physical mixture of solid 7-ADCA and cephalexin monohydrate (consisting of roughly 30% 7-ADCA). Washing consisted of suspending 250 mg of product cephalexin in 5 mL of cold water ($<5^\circ\text{C}$) and stirring for 15 minutes under chilled conditions.	86
Figure 5.1. FE-SEM images of ampicillin trihydrate initial crystals. The scale bar is 30 μm in (a) and 2 μm in (b)-(f). Image (a) shows uniformity of initial crystals, (b) shows a fracture and splinter of an initial crystal, (c) and (d) show epitaxial growth and possibly twinning, (e) and (f) show ends of initial crystals. In (e) the end has several visible	

growth hillocks stemming from screw dislocations, in (f) two ends are shown, one
pristine pointed end with few growth steps, the other a clean break. 93

Figure 5.2. Microscope images of ampicillin trihydrate, colorized to enhance contrast.
The scale-bar is 100 μm : (a)-(f) images taken at 2, 20, 40, 60, 90, and 120 minutes,
respectively. 97

Figure 5.3. (a) The CSD of initial crystals (green circles) and fit to lognormal distribution
(solid green curve) and the CSD after 2 hours of growth (red squares) and fit to
lognormal distribution (dashed red curve) for experiments with an initial loading of 0.03
g, the bin widths are the same for both CSDs; (b) Cumulative distribution of growth rates
extracted from CSDs for experiments with an initial loading of 0.03 g (solid blue curve)
and a normal distribution with a mean of 0.84 and standard deviation of 0.43 $\mu\text{m}/\text{min}$
(dashed black curve) for reference. Note that the CSDs are lognormal while the growth
rate distribution is normal. 99

Figure 5.4. (a) The length (left axis, closed symbols) and width (right axis, open symbols)
of two individual crystals is plotted over time. Note the right axis scale is 5x the left axis
scale. Both crystals are fit to equation 5.1. (b) Left axis, histogram of R^2 values. Right
axis, mean growth rate for each bar in the R^2 histogram (with enough samples to compute
a meaningful mean and standard deviation, $n > 10$) with error bars of one standard
deviation. Note all bins for R^2 less than 0.8 have been grouped into a single red bin.... 100

Figure 5.5. A scatter plot of growth rates of individual crystals against the length of the
initial crystal for different initial loadings, with a linear correlation and 95% prediction
interval. Along the x-axis is the normalized number-based CSD histogram of the initial
crystal lengths, colored by loading. Along the y-axis is the normalized growth rate
distribution histogram of the initial crystals, colored by initial loading. 102

Figure 5.6. (a) Growth rate of individual crystals versus the initial loading of the
experiment in which the growth rate was measured, horizontal jitter is introduced to
illustrate the density of data points; (b) Growth rate of individual crystals versus the
critical time of the crystal. The solid lines are the linear best fits and the dashed curves
are the 95% prediction intervals 104

Figure 5.7. An image of growing crystals is divided into areas based on distance to
nearest growing crystal end. The areas are colored based on the volume represented by
the area and range from dark blue representing the smallest volume (0.1 nL) and yellow
representing the largest volume (2 nL). The areas are overlaid on the grayscale image
from which the data were generated. The white points are the crystal ends used in the
analysis, and the white curves connecting them illustrate how the crystal is represented in
the image analysis program GT Fiber. The red scale bar is 100 μm 106

Figure 5.8. The measured growth rate of the crystals in Figure 5.7 versus the calculated
growth rate of the same crystals based on the division of the image in Figure 5.7. 107

Figure 5.9. The CSD in an MSMPR producing ampicillin by PGA-catalyzed reactive
crystallization. The dashed curve represents the case with no GRD and the solid blue
curve shows the CSD when the growth rates follow a normal distribution as described in
Figure 5.3 (b). 109

Figure 6.1. The kinetic scheme for the mechanism of PGA. E is free PGA, S is acyl-donor (HOPGME or PGME), Nu is 6-APA or 7-ADCA, B is the byproduct (HOPG or phenylglycine), P is the antibiotic, EAH is the activated acyl-enzyme complex, EA and EAH₂ are dead-end complexes due to pH equilibria, ENu is PGA bound to 6-APA or 7-ADCA, ES is PGA bound to HOPGME or PGME, EANu is acyl-enzyme complex bound to 6-APA or 7-ADCA, and EP is PGA bound to antibiotic.³² 113

Figure 6.2. The solubility of amoxicillin (solid), ampicillin (dash), and cephalexin (dash-dot) (a), HOPG (solid) and phenylglycine (dash) (b), 6-APA (solid) and 7-ADCA (dash-dot) (c), and HOPGME as a function of pH with experimental data from Bezerra *et al.* 2013¹⁵⁵, Diender *et al.* 1998¹⁵⁶, Felix *et al.* 2016¹⁵⁷, Santana *et al.* 2010⁴⁵, Youshko *et al.* 2000⁷⁷, McDonald *et al.* 2017³², and Rudolph *et al.* 2001²², as well as this work. 116

Figure 6.3. Schematic representation of the system being modeled. The product classifier allows the residence time of the crystals to be independent of the solution and vary as a function of crystal size. The enzyme recycle is assumed to recycle a pure enzyme stream but does not affect the degradation of the enzyme. 118

Figure 6.4. The fractional error of several different solutions to the population balance to determine mean crystal length (L43) as a function of conversion. At higher conversion the error increases, however it is never more than 3%, even with the coarsest model (PBE 250) or the method of moments. In the legend, PBE indicates a complete solution of lines using the indicated number of bins to discretize the length domain. MOM indicates the method of moments..... 122

Figure 6.5. Demonstration of the geometric method for determination of the attainable region for the case of no crystallization, at pH 7 with 600 mM HOPGME and 400 mM 6-APA initially. The reaction vectors show the direction the system moves at each point in conversion space, the length of the arrow is proportional to the rate at which the system move in that direction (however the attainable region is agnostic of rate). Only 3% of the calculated reaction vectors are shown for readability. A line representing stoichiometric reaction of 6-APA and HOPGME is drawn to show how a perfectly selective enzyme would perform..... 125

Figure 6.6. The attainable region for production of amoxicillin with PGA (a) in a distinct reactor and separator scheme and (b) with a reactive crystallizer. The attainable region is expressed in terms of HOPGME conversion and a modified 6-APA conversion that better captures how much product can actually be recovered: 6-APA converted into amoxicillin trihydrate. The 800:400 mM, 600:400 mM, 400:400 mM and 200:400 mM HOPGME:6-APA feed concentration ratios are shown in blue, red, green, and yellow, respectively. The light-colored region represents the attainable region at pH 6.5 and the dark color represents pH 7. The dashed lines represent stoichiometric conversion of HOPGME and 6-APA to amoxicillin. 126

Figure 6.7. (a) the bounds of attainable mean crystal sizes for one, two, and three MSMPRs in series (● – 1 MSMPR, ▲ – 2 MSMPRs, ▼ – 3 MSMPRs). (b) the breakdown of the residence time of each MSMPR in a series of three MSMPRs (■ – 1st MSMPR, ◆ – 2nd MSMPR, ► – 3rd MSMPR) to reach the maximum mean crystal size. The feed concentrations are 800 mM HOPGME, 400 mM 6-APA, and steady state pH of 7.0..... 128

Figure 6.8. (a) the Levenspiel plot for amoxicillin production at 800:400 mM, 600:400 mM, 400:400 mM, 200:400 mM HOPGME:6-APA feed concentration ratios (blue, red, green, yellow, respectively) in a reactive crystallizer (solid curves) and a distinct reactor and separator (dashed curves). (b) Close-up of (a) for the 800:400 ratio; the dashed curve is the distinct reactor and separator, the dotted curve simulates a hypothetical variant of PGA without substrate inhibition by 6-APA, and dash-dot curve neither crystallizes nor has substrate inhibition, and the solid curve is reactive crystallization. 130

Figure 6.9. (a): Sizing a series of reactive MSMPRs, rectangles, and a plug flow reactive crystallizer, dash-outlined area under the curve, to achieve a desired conversion using the Levenspiel plots from Figure 6.8, in this case the 800:400 HOPGME:6-APA feed concentration ratio. (b) The Pareto-optimal front for productivity and conversion of 6-APA at 800:400 mM, 600:400 mM, 400:400 mM, 200:400 mM HOPGME:6-APA feed concentration ratios (blue, red, green, yellow, respectively) in a reactive crystallizer (solid lines) and a distinct reactor and separator (dashed lines). The data points are the result of solving the entire PBE for the 800:400 mM, pH 7.0 case. 132

Figure 6.10. (a) fractional yield as a function of conversion for reactive crystallizers (solid curves) and distinct reactor and separators (dashed curves) at four different feed concentration ratios: 800:400 mM, 600:400 mM, 400:400 mM, 200:400 mM HOPGME:6-APA (blue, red, green, yellow, respectively). (b) reactor geometry considerations based on fractional yield of HOPGME. Solid curves are reactive crystallization, dashed curves are distinct reaction and separation. 135

Figure 6.11. The Pareto-optimal surface for 6-APA conversion, productivity, and fractional yield for the reactive crystallization of amoxicillin. The blue region represents the attainable fractional yield as a function of productivity. The white curves represent constant conversion of 6-APA. 137

Figure 6.12. The CSD for a reactive MSMPR (red) and a reactive crystallizer with fines removal. 138

Figure 6.13. The effects of changing the enzyme concentration on the fractional yield (Φ), mean crystal size (\bar{L}_{43}), and productivity (P). The values of these attributes are shown relative to the value found with an enzyme concentration of 5 μM and a conversion of 70%. 1.0 μM , 2.5 μM , and 10 μM are shown in lavender, teal, and navy, respectively. 139

Figure 7.1. The attainable regions, in the PGME 6-APA conversion space, for ampicillin produced without *in situ* crystallization (a) and ampicillin produced by reactive crystallization (b). The blue, red, green, and yellow regions represent 800:400, 600:400, 400:400, and 200:400 mM PGME:6-APA initial/feed concentrations. The light-colored regions are at pH 6.5 and the dark colored regions are at pH 7.0. The dashed black lines represent stoichiometric conversion of PGME and 6-APA to ampicillin. The white-washed (lightest colored) regions on the right represent the regime in which phenylglycine and ampicillin crystallize simultaneously, jeopardizing product purity. 145

Figure 7.2. (a) the productivity of a reactive MSMPR (solid) and non-crystallizing well-mixed reactor (dashed) for different residence times and feed concentration ratios. (b) the conversion of 6-APA in a reactive MSMPR (solid) and non-crystallizing well-mixed

reactor (dashed) for different residence times and feed concentration ratios (blue 800:400, red 600:400, green 400:400, yellow 200:400 mM PGME:6-APA). The black dotted line represents the maximum conversion, as shown in Figure 7.1. 147

Figure 7.3. (a) The coexistence of two steady states over the range of residence times from 41.5 to 43 minutes, demonstrated by the hysteresis of the phenylglycine suspension density, M_T (top) and supersaturation, σ (bottom). The solid curves were generated by reaching steady state from a low suspension density initial state, and the dashed curves are from a high suspension density initial state. (b) A perturbation in the residence time of 5%, lasting 58 minutes and 60 minutes, leading the process to slowly decay back to the high-purity steady state and jump to the low-purity steady state, respectively. The noise at the second steady state in (b) stems from how the differential equation solver handles stiffness; solving for the steady state explicitly (by finding the roots of the equation) shows that the steady state is exactly 0.9856. 149

Figure 7.4. The operating curves in fractional yield versus conversion space for a plug-flow reactive crystallizer (top solid curve, \times) and a well-mixed reactive crystallizer (bottom solid curve, $+$) with feed concentration of 800 mM PGME and 400 mM 6-APA. The dashed curve represents a well-mixed reactor (no crystallization). The light shaded area is the region where reactive MSMPRs exhibit steady-state multiplicity and the dark shaded area is the region where primary nucleation results in impure ampicillin product regardless of reactor design. The labeled markers represent the residence time needed to reach the specified conversion and fractional yield in a plug flow (\times) and well-mixed reactive crystallizer ($+$). The blue, red, and yellow curves are plug-flow reactive crystallizer operating curves that are fed by reactive MSMPRS with residence times of 10, 25, and 35 minutes, respectively. 152

Figure 7.5. The solid curve shows the reaction rate with *in situ* crystallization while the dashed line shows the reaction rate without crystallization. The colored squares are the reactive MSMPRs operating at the specified conversion with size proportional to the MSMPR volume. The bolded solid line represents the range of conversion that occurs over the length of the PFRC, fed by each of the MSMPRs. 154

Figure 7.6. The productivity of the reactive MSMPR fed plug flow reactive crystallizer is shown by the degree of shading (lighter hues indicating greater productivity) in the well-mixed vessel (square) and the plug flow vessel (rectangle). The area of the square and rectangle are proportional to the volume of each vessel. The residence time of the reactive MSMPR is labeled in the square, the residence time of each plug flow reactive crystallizer is shown on the abscissa. The top, middle, and bottom reactors represent Designs 3, 2, and 1, the yellow, red, and blue operating curves in Figure 7.4. 156

Figure 7.7. The volume weighted CSD of ampicillin trihydrate resulting from the blue, red, and yellow operating lines in Figure 7.4. 157

Figure 7.8. (a) The purity of the effluent crystals from the different reactive crystallizer designs with a 10% decrease in phenylglycine solubility (darker shades) and 2 °C increase in temperature (light shades). (b) The productivity of the different reactive crystallizer configurations as well as a non-crystallizing well-mixed reactor at the same final 6-APA conversion of 90%. 159

Figure 7.9. The primary (blue) and secondary (red) nucleation rates of phenylglycine with a suspension density of 0.01 g/L.	163
Figure 7.10. The uniqueness criterion defined in equation (9) versus the residence time in a well-mixed reactive crystallizer with four different feed compositions (blue- 800:400 mM PGME:6-APA, red- 600:400 mM PGME:6-APA, green- 400:400 mM PGME:6-APA, and yellow- 200:400 mM PGME:6-APA). The points represent the residence time that gives the maximum productivity and are labeled with that productivity. Below the black dashed line is the region where steady state multiplicity can arise.	165
Figure 8.1. A polarimeter measures the optical rotation of a solution caused by chiral solutes by measuring the angle between two polarizers such that the maximum amount of light is allowed through.	169
Figure 8.2. The calibration curves for determination of the specific optical rotation of the species involved in ampicillin synthesis. The optical rotation was measured in water at 20 °C, at 589 nm, and in a 100 mm cuvette.	169
Figure 8.3. In ATR-FTIR evanescent waves are generated during the internal total reflection of the IR laser (red) in the ATR crystal (green). The evanescent waves only penetrate a few micrometers into the solution, such that hydrodynamics prevent crystals from being ‘seen’ by the laser.	171
Figure 8.4. The IR spectrum of cephalexin (left) and the linear calibration model used to convert the 1369 cm ⁻¹ peak height to concentration (right). Error bars represent standard deviation of n = 38 samples.	172
Figure 8.5. The FTIR signal from a continuous amoxicillin crystallization experiment with spectrum trace (red) and progression trace (black), highlighted in the insets to the right, showing an increasing signal as amoxicillin crystallizes over the probe window. At approximately 14000 seconds the probe was removed, cleaned, and reinserted into the crystallizer, resulting in the drop in peak height visible in the black progression trace.	175
Figure 8.6. The working principle of FBRM is illustrated. Large crystals are more likely to be ‘seen’ by the probe, but even large crystals can produce short chords, especially if they are high aspect ratio crystals like those of amoxicillin and cephalexin.	177
Figure 8.7. The snowstorm effect observed during the crystallization of cephalexin. Beginning with a small number of seed crystals (red), the initial population grows and breeds new crystals (yellow) until a maximum appears for chords 100 μm in length (green). Continued crystallization creates many fines, obscuring the large (~100 μm) chords and shifting the mode of the distribution down to ~25 μm (blue and purple). ...	177
Figure 8.8. Top left: Amoxicillin trihydrate. Top right: Cephalexin monohydrate. Bottom left: Phenylglycine. Bottom right: Cephalexin and phenylglycine, both produced curing a batch enzymatic reactive crystallization. Each image is 1.0 mm × 1.0 mm.	181
Figure 9.1. Basic pilot plant elements in blue/black, optimal design elements shown in green.	184
Figure 9.2. A diagram depicting how a multiplicity of steady states arise in an MSMPR-RC, based on the nucleation rate (solid curve) and crystal removal rate (dashed curve) dependence on suspension density. For a slow reaction (red curves) the removal rate is	

greater than the nucleation rate at all suspension densities; the reaction is not fast enough to sustain a crystal population, a condition known as wash out. For a medium speed reaction (yellow curves) two stable steady states exist, one with a stable crystal population (yellow square) and one with no crystal population. Systems to the left of the circle eventually converge to the wash out condition while systems to the right of the circle converge to the stable population. For the fast reaction (green curves) the behavior is the same as the medium speed reaction, except there is no wash out condition as the fast reaction generates enough supersaturation to sustain a population of primary nucleated crystals, hence the significant nucleation rate at low suspension density. This plot was created with the model from Chapter 7. 186

Figure 9.3. PVM images of amoxicillin (left) and cephalexin (right) spherulites. Both images are 1.0 mm². 190

Figure 9.4. Schematic of magnetic separation device. Green arrow, crystallizer effluent containing crystals and biocatalyst. Blue arrow, sweep solution. Purple arrow, permeate, to filtration units. Yellow arrow, retentate, recycled back to reactor. Magnetic particles accumulate above the bar magnet before being swept into the retentate stream. The scale of the device is <1 cm wide and <15 cm long. 193

Figure 9.5. Computational fluid dynamics analysis of a continuous magnetic particle separating device. The device, shown as seen from the top in (a), is a rectangular body with two inlets at one end and two outlets at the other. A magnet is placed parallel to the length of the separator body, pulling magnetic particles to that side. Two slices of the flow field are shown in (b), with velocity scale in (c). 194

Figure 9.6. The filtration rate of low (left) and high (right) aspect ratio (AR) cephalexin crystals, as measured by the time required to collect the solution in which the crystals were suspended. IN the case of the low AR crystals, complete filtration took less than two minutes, the sharp decrease in mass of collected solution is a result of deliquoring the filter cake. 196

Figure 9.7. Basic pilot plant as of July 2020, with schematic overlay. Prepared for first rounds of testing imminent. Ample space for expansion to the optimal pilot plant can be seen on the right side of the fume hood. The Chillers are color coded to their respective unit operation. PAT are shown in gray 200

Figure 10.1. PVM images of phenylglycine crystals adhered to bubbles. Left phenylglycine as received, middle pure phenylglycine during recrystallization, right phenylglycine crystallized during cephalexin synthesis (needle shaped crystals are cephalexin). All images are 1.0 mm². 204

Figure 10.2. Scheme depicting the reaction of ampicillin to cephalexin, and the possible conformation change induced by the acyl-donor. 206

LIST OF SYMBOLS AND ABBREVIATIONS

Subscripts

i	i^{th} moment of the size distribution
j	j^{th} component in solution (P, B, S, Nu)
k	k^{th} MSMPR in series of K MSMPRs
P	product (antibiotic)
B	byproduct (HOPG or phenylglycine)
S	acyl-donor substrate (HOPMGE or PGME)
Nu	β -lactam nucleophile (6-APA or 7-ADCA)
0	initial or total amount

Abbreviations

6-APA	6-aminopenicillanic acid, a β -lactam nucleophile
7-ADCA	7-desacetoxycephalosporanic acid, a β -lactam nucleophile
AIC	Akaike Information Criterion
API	Active pharmaceutical ingredient
ATR-FTIR	Attenuated total reflectance Fourier transformed infrared spectroscopy
CFR	Classified fines removal
CM	Continuous manufacturing
CLD	Chord length distribution
CPP	Critical process parameter
CQA	Critical quality attribute
CSD	Crystal size distribution
DSC	Differential scanning calorimetry
DSF	Differential scanning fluorimetry
EMR	Enzyme membrane reactor
FBRM	Focused beam reflectance measurement
HPG	4-hydroxyphenylglycine
HPGME	4-hydroxyphenylglycine methyl ester
HPLC	High performance liquid chromatography
MSMPR	Mixed suspension, mixed product removal crystallizer
PAT	Process analytical technology
PBE	Population balance equations
PBM	Population balance model

PFRC	Plug flow reactive crystallizer
PGA	Penicillin G acylase, enzyme
PGME	Phenylglycine methyl ester
PVM	Particle vision and measurement
PXRD	Powder x-ray diffraction
QbD	Quality by design
RSS	Residual sum of squares
SEM	Scanning electron microscopy

Latin characters

A	Filter area	m^2
B	total nucleation rate	$L^{-1} s^{-1}$
B_1	primary nucleation rate	$L^{-1} s^{-1}$
B_2	secondary nucleation rate	$L^{-1} s^{-1}$
B^o	surface energy constant	-
b	secondary nucleation rate power or temperature ramp intercept	-
c_j	concentration of species j	$mol L^{-1}$
c_j^*	saturation concentration of j	$mol L^{-1}$
$c_{p,j}^*$	saturation concentration of j at the isoelectric point	$mol L^{-1}$
D	diameter	m
$[E]$	free active enzyme concentration	$mol L^{-1}$
G	growth rate	$m s^{-1}$
ΔG	change in free energy	$kJ mol^{-1}$
ΔH	Enthalpy (of reaction, deactivation, unfolding)	$kJ mol^{-1}$
g	growth rate power	-
h	Planck's constant, 6.626×10^{-34}	$m^2 kg s^{-1}$
I	ionic strength	$mol L^{-1}$
k	Filter cake permeability	-
k_b	Boltzmann constant, 1.3806×10^{-23}	$m^2 kg s^{-2} K^{-1}$
k_{B1}	primary nucleation rate constant	$L^{-1} s^{-1}$
k_{B2}	secondary nucleation rate constant	$L^{-1} s^{-1}$
k_d	unfolded enzyme deactivation rate constant	$mol L^{-1} s^{-1}$
k_G	growth rate constant	$m s^{-1}$
K_U	equilibrium constant for enzyme unfolding	-
k_V	volumetric shape factor	-
L	crystal length	M
\bar{L}_{43}	volume weighted mean crystal size	M

M_T	slurry density	g L^{-1}
m	slurry density power or temperature ramp slope	-
n	number of points	-
$n(L,t)$	crystal size distribution	$\text{m}^{-1} \text{L}^{-1}$
n^o	boundary condition for zero sized particles	$\text{m}^{-1} \text{L}^{-1}$
N	rate of rotation	rad s^{-1}
$[N]$	Natively folded enzyme concentration	mol L^{-1}
P	Productivity	$\text{g L}^{-1} \text{hr}^{-1}$
Δp	Pressure drop across filter	Pa
$pK_{a,j}$	\log_{10} acid dissociation constant of species j	-
R	gas constant, 8.3145	$\text{J mol}^{-1} \text{K}^{-1}$
R_j	reaction rate of species j	$\text{mol L}^{-1} \text{s}^{-1}$
S	supersaturation ratio	-
ΔS	change in entropy	$\text{J mol}^{-1} \text{K}^{-1}$
t	Time	S
T	Temperature	K
T_m	Melting temperature	K
X	Conversion	-
z	charge of conjugate base	-

Greek characters

α	Svedas' alpha parameter	-
β	Svedas' beta parameter	mol L^{-1}
γ	Svedas' gamma parameter, or surface energy	-, J m^2
$\hat{\epsilon}_i$	residual of the i^{th} measurement	-
μ_i	i^{th} moment of the CSD	$\text{m}^i \text{L}^{-1}$
μ	solution viscosity	$\text{kg m}^{-1} \text{s}^{-1}$
ρ	density	kg L^{-1}
τ	residence time	min
$\tau_{i,s}$	residence time of the liquids, solids	min
$\hat{\sigma}$	mean squared error	-
Φ	fractional yield	-
Θ_{obs}	observed optical rotation	$^\circ$
ϑ_{comp}	specific optical rotation	$^\circ \text{mol}^{-1} \text{L}$
ω	rate of rotation	s^{-1}

SUMMARY

The enzymatic production of beta-lactam antibiotics can be simplified by integrating the synthesis and separation of the antibiotic within a single vessel. *In situ* crystallization during the synthesis of beta-lactam antibiotics improves yields by protecting the antibiotic, an intermediate in the enzyme catalyzed reaction pathway, from degradation by the enzyme. The design of a continuous synthesis, crystallization, and isolation (CSCI) process follows naturally because the reaction and crystallization kinetics are already coupled in the batch process. Rather than individually design and size several unit operations for use in series, a single unit that performs several operations at once was developed. The benefits of continuous reactive crystallization include simplified process control, improved environmental sustainability, and increased process performance. Enzyme catalysis decreases process mass intensity and increases reaction selectivity compared to chemical routes to beta-lactams. Use of process analytical technology (PAT) enables real time monitoring of critical process parameters (CPPs) to ensure production of pharmaceutical quality material. The kinetics of the enzyme reactions and antibiotic crystallization were determined in batch for ampicillin and cephalexin. A model of reactive crystallization was built and used to determine the optimal process configuration for continuous production of amoxicillin and cephalexin. Finally, implementation of the continuous process in the lab was begun. This process will enable more sustainable production of beta-lactam antibiotics with potential for on-demand production, especially important in light of recent drug shortages due to the 2020 SARS-CoV-2 pandemic.

CHAPTER 1. INTRODUCTION

Amoxicillin ranks as the most prevalent antibiotic, with cephalexin not far behind. Amoxicillin alone has a market of 4.4B USD and is the most prescribed antimicrobial in 60 out of 65 countries for which recent World Health Organization data are available.¹ Demand for beta-lactam medicines such as amoxicillin and cephalexin is also increasing rapidly, particularly in lower and middle income countries where demand has more than doubled since the year 2000.² Supply of these drugs is incredibly geographically concentrated; at the outset of the COVID-19 pandemic in February 2020, when China halted manufacturing, immediate worldwide shortages of amoxicillin and cephalexin followed.³ A scalable, lower-cost, on-demand manufacturing platform for these two antibiotics would directly address issues of increased demand and supply chain fragility. Ideally, such a platform would leverage recent technologies and design principles to minimize cost, environmental impact, contamination, waste, and more.

Enter Continuous Synthesis, Crystallization, and Isolation (CSCI) of beta-lactam antibiotics. The CSCI process developed in this thesis combines the agility of continuous manufacturing with the sustainability of biocatalytic antibiotic synthesis by a reactive crystallization mechanism. Continuous manufacturing (CM) can increase efficiency, improve product quality, decrease costs, and shrink environmental footprints associated with pharmaceutical manufacturing.⁴ Biocatalytic synthesis of beta-lactams is transitioning production of amoxicillin and cephalexin away from traditional chemical routes in favor of a greener alternative; however, the transition is not complete and legacy plants continue to produce large amounts of waste alongside antibiotics. Reactive crystallization couples

the driving force for product separation to that for product synthesis, improving efficiency and overcoming some limitations of the biocatalytic routes to amoxicillin and cephalexin.⁵

Furthermore, beta-lactam antibiotics are potent allergens, requiring strict containment for safe manufacturing. One study found that up to 0.5% of those exposed to penicillins became anaphylactic, requiring hospitalization to treat the severe allergic reaction.⁶ The FDA requires that penicillins, like amoxicillin, be produced in standalone facilities and recommends that similar precautions be taken for cephalosporins, like cephalexin.^{7, 8} Continuous manufacturing inherently reduces the risk of contamination as it avoids shared equipment and charging/discharging of batch vessels. Reactive crystallization further reduces this risk by combining two operations in one vessel. End-to-end CM has already been demonstrated as a containment strategy at the pilot plant scale in the production of highly potent anti-cancer drugs and could benefit beta-lactam manufacturing as well.⁹⁻¹¹

The remainder of the introduction will detail continuous manufacturing, synthesis of beta-lactams by the enzyme penicillin G acylase, and reactive crystallization of selected beta-lactams.

1.1 Continuous manufacturing

Presently, most pharmaceutical production relies on large batches being stockpiled and slowly dispensed, but this method cannot meet real-time demand; e.g. in response to a disease outbreak or supply disruption. Continuous manufacturing constantly feeds precursors to a unit operation and the unit constantly outputs products. End-to-end CM involves stringing multiple CM unit operations together, such that the products of one unit

operation serve as the precursors for the next one, with minimal holdup in between.¹² Continuous manufacturing is strongly encouraged by the US Food and Drug Administration for the reasons enumerated in the following paragraphs.¹³

Supply flexibility is built into CM. If the process is designed to be run without interruption, production can be scaled up or down by increasing or decreasing the throughput of the process.¹⁴ If startup and shutdown are not complex, a simpler way to adjust production according to demand is to change the length of time the process operates, all while operating at an optimized throughput. Batch manufacturing requires periods of storage interspersed between batches. Responding to a change in demand may require larger equipment or challenging recycling of supplies. Flexibility of supply makes continuous manufacturing especially attractive for markets with inconsistent demand, such as low to middle income countries.

A validated continuous process is more amenable to automated quality control.^{15, 16} Online monitoring, by process analytical technology (PAT), is simpler for CM than for batch as the process is ideally operated in a well-controlled state, often at a steady state. PAT only needs to confirm that the process is at the expected state, rather than check that the batch is following the expected trajectory.¹⁷ When it comes to process control, a stability analysis of the CM steady state can determine whether a perturbation, detected with PAT, will derail the process. In process control for batch manufacturing, it is necessary to know how a perturbation will propagate during the batch time course, a far more complicated analysis than a steady state stability analysis, to make meaningful corrections. Automated PAT reduces the likelihood of human errors. Finally, batches are

typically tested at the end of the batch, and should it fail to meet specifications the batch may be lost.¹³

Continuous manufacturing has the added bonus of improved tracking and tracing. As the entire process is monitored online, as soon as a quality defect is detected, the production line can be diverted, and the material possibly reprocessed, until the process returns to the quality steady state. In a batch process, a representative sample must be tested after each batch, and should it fail to meet quality specifications the entire batch is discarded, resulting in the loss of a much greater quantity of material. Additionally, in some discrete continuous processes, such as tableting, each and every tablet is tested by the online PAT, providing more robust quality than taking representative samples from a batch of material.^{18, 19}

1.2 Enzymatic beta-lactam synthesis

Synthesis of semisynthetic beta-lactams, such as amoxicillin and cephalexin, is typically catalyzed by the enzyme penicillin G acylase (PGA). A key obstacle to more efficient beta-lactam production is poor selectivity, as enzyme-catalyzed synthesis competes with enzyme-catalyzed primary and secondary hydrolysis (see Figure 1.1).²⁰ Amoxicillin is produced from the condensation of 6-aminopenicillanic acid (6-APA) with 4-hydroxy phenylglycine methyl ester (HPGME) and cephalexin is produced by the condensation of 7-aminodesacetoxycephalosporanic acid (7-ADCA) with phenylglycine methyl ester (PGME).²¹ While amoxicillin and cephalexin are the targets of the continuous manufacturing campaign, much of the work in this thesis is focused on ampicillin, produced by the condensation of 6-APA with PGME. Ampicillin is a particularly good model compound for a new process because phenylglycine, the byproduct of ampicillin

and PGME hydrolysis, is only sparingly soluble, rendering selectivity a greater challenge than with some other beta-lactams including cephalexin. The insolubility of phenylglycine elevates the problem of selectivity since excessive byproduct formation results in contaminated solid product. Solid product purity is a strict constraint throughout this thesis. The byproducts from amoxicillin hydrolysis, 4-hydroxy phenylglycine, is much more soluble, so lower selectivity interferes less with product purity.^{22, 23} The phenylglycine obstacle is not unique to ampicillin; it is shared with cephalexin, cefaclor, loracarbef, and others.

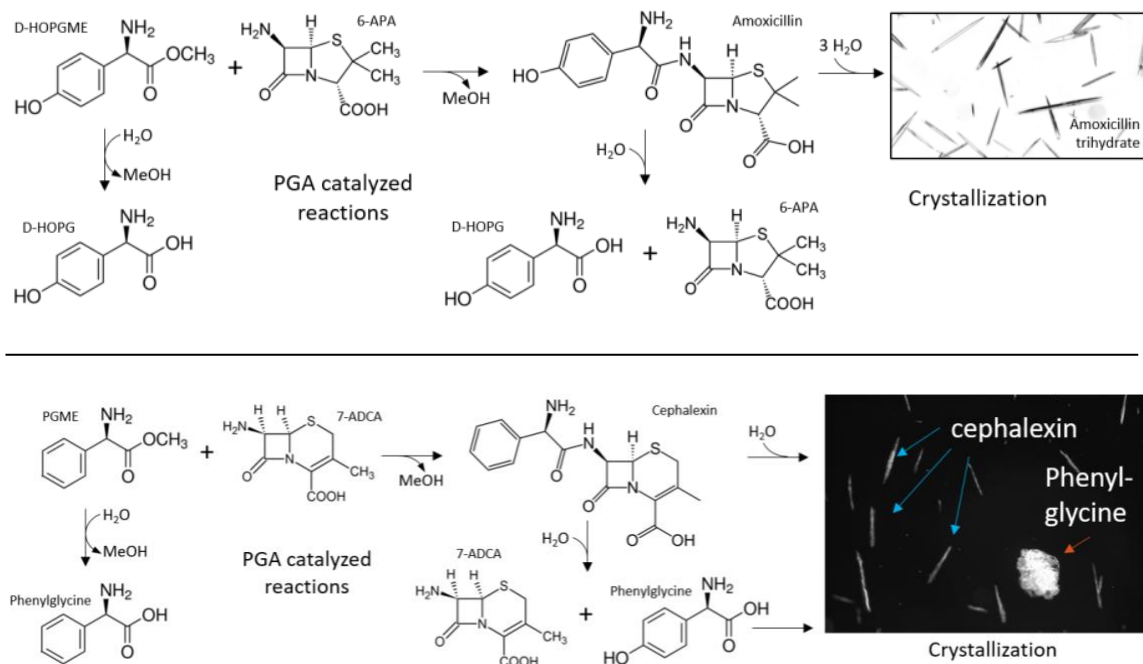


Figure 1.1. Overview of PGA catalyzed reactions and reactive crystallization. Top: synthesis reaction and crystallization of amoxicillin (horizontal arrows) with enzyme catalyzed primary and secondary hydrolysis reactions (vertical arrows). Bottom: synthesis and hydrolysis of cephalosporin and reactant PGME with subsequent crystallization of cephalosporin and phenylglycine

The first industrial use of PGA was to catalyze the hydrolysis of penicillin G, produced by fermentation, into phenylacetic acid and 6-APA, with 6-APA being the

starting point for other beta-lactams. PGA is found in the genome of over 40 microorganisms; recombinant *E. coli* PGA has always dominated production.²⁴ Early engineering of the enzyme focused on stability for reuse in 6-APA production. Being a heterodimeric enzyme, one focus was to covalently link the monomers to prevent dissociation and loss of activity,^{25, 26} or to mutate PGA to be produced as a monomer.²⁷ Immobilization has also been the subject of many studies, as it can covalently link the two monomers and improve reusability; Kallenberg *et al.* give a thorough review of PGA immobilization.²⁸ Other means of increasing stability include genome analysis of thermophiles,²⁹ use of ionic liquids,³⁰ and PEGylation.³¹

It was soon realized that PGA could catalyze the reverse reaction, but with a synthetic side chain rather than phenylacetic acid. Use of an activated side chain, such as the ester or amide of phenylglycine, enables approximately 50% yield of the semi-synthetic beta-lactam ampicillin, compared to nearly 100% yield for the less sustainable chemical route.³² ³³ Many researchers have developed methods to push the reaction towards synthesis and away from hydrolysis, such as using supersaturated 6-APA or 7-ADCA concentrations,³⁴ mutant PGA variants,³⁵ and fed-batch reactors.³⁶ Since the antibiotic is ultimately an intermediate in the enzyme-catalyzed reaction pathway, several different strategies have been used to isolate the antibiotic *in situ* and prevent subsequent hydrolysis, such as aqueous two phase extraction,³⁷ nanofiltration,³⁸ and complexation.³⁹ In this thesis a highly engineered PGA variant of unknown amino acid sequence, produced by DSM-Sinochem, Assemblase®, is used alongside reactive crystallization to isolate the antibiotic *in situ*.

1.3 Reactive crystallization of amoxicillin and cephalixin

Reactive crystallization, where a desired compound is driven to supersaturation by a chemical reaction, often enhances a reaction by pulling the equilibrium towards the products or isolating an intermediate from further reaction. Beta-lactams fall into the latter category. In the case of ampicillin, the equilibrium of secondary hydrolysis favors 6-APA and D-phenylglycine over ampicillin by about 100-fold while the equilibrium of the synthesis reaction was not determinable because no ampicillin was detected at equilibrium.⁴⁰ Work performed in this lab prior to this thesis has shown that simultaneous synthesis and crystallization of pure ampicillin is possible and feasible.⁴¹ This thesis has shown that the principles used for the reactive crystallization of ampicillin are also feasible for amoxicillin and cephalexin, with similar expected performance improvements.

Like all crystallization, reactive crystallization is governed by the concurrent phenomena of nucleation and growth.⁵ Nucleation is the appearance of new crystals while growth is the enlargement of existing crystals. Both phenomena are driven by supersaturation, which has many practical definitions that are all derived from the ratio of the chemical potential of the solute to its chemical potential at equilibrium.^{42, 43} Equilibrium is determined from the solute solubility, which may be a function of temperature, pH, solvent composition, and co-solute concentration.⁴⁴ One of the author's major undertakings during the course of this thesis was the preparation of a comprehensive review of reactive crystallization, with coauthors including three members of the doctoral advisory committee, and it is the best resource for more information on reactive.⁵ Relevant details of the beta-lactams studied, such as solubility and shape, follow, with specifics on kinetics, nucleation, growth, purity, and modeling in CHAPTER 4, CHAPTER 5, and CHAPTER 6.

The solubility of the antibiotics studied increases from amoxicillin to ampicillin to cephalexin. The solubility of each is also highly dependent on the pH value of the solution.⁴⁵ As PGA has a narrow range of operating temperatures the solubility of these antibiotics as a function of temperature was not studied. It was also observed that the solubility of these antibiotics may be affected by the presence of the reactants used in their synthesis. The solubility of the key byproduct of cephalexin (and ampicillin) synthesis is similar to that of cephalexin, creating the risk of a contaminated solid phase.

Both amoxicillin and cephalexin crystallize as needles, creating several challenges. First, needles can be difficult to handle, they do not filter quickly nor flow easily, making transfer of materials, even suspended in a slurry, a potential failure point.^{46, 47} Second, crystallization of needle-shaped particles can be difficult to monitor; common PAT often fail to capture a meaningful representation of the crystal size distribution because even low suspension density slurries can be quite dense optically.^{48, 49} Third, modeling crystallization of needle-shaped particles can be difficult because phenomena such as breakage and agglomeration are more common than for prismatic crystals.⁵⁰⁻⁵³ Adding controls to optimize particle size and shape during the process can be especially challenging as most crystallization control schemes have been developed around cooling crystallization and anti-solvent crystallization, not reactive crystallization, where several degrees of freedom may be lost in maintaining suitable reaction conditions.^{14, 54-56}

All of the nuances of beta-lactam antibiotics, continuous manufacturing, biocatalysis, and crystallization create a unique set of challenges and opportunities, to be explored in detail in the forthcoming chapters and future work beyond these pages.

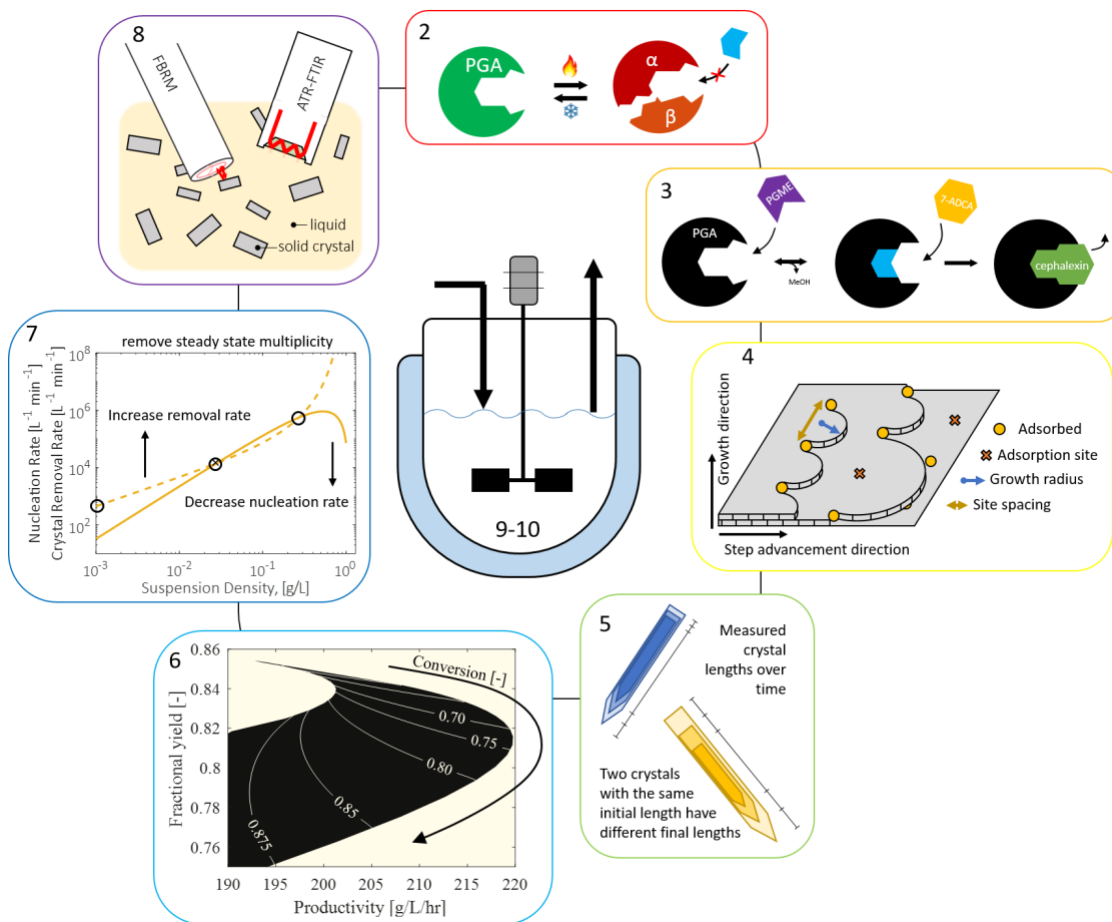


Figure 1.2. Graphical abstract depicting the results from each chapter as they build towards the CM process for beta-lactams, center.

CHAPTER 2. STABILITY OF PENICILLIN G ACYLASE¹

2.1 Introduction and motivation

The most important prerequisite for implementing a continuous manufacturing process is stability. If the catalyst to be used deactivates in less than a single residence time, such as in catalytic cracking during petroleum refining, much effort must be expended engineering a regeneration mechanism. If on the other hand the catalyst retains its activity for thousands of residence times the process may be run without regard to catalyst deactivation. Additionally, as process controllers may manipulate reactor or crystallizer temperature as a means of reaching the set point faster, the effect of temperature excursions on the catalyst should be known to limit unintentional deactivation. Like many chemical processes, the rate of an enzyme-catalyzed reaction typically increases with temperature; however, enzymes are less stable than non-biologic catalysts, permanently deactivating with mild temperature ($T > 60$ °C) and prolonged use. If deactivation of the enzyme is understood, a process can be designed that minimizes deactivation, rendering continuous operation feasible.^{26, 30, 31, 57, 58}

In this chapter, the deactivation of PGA is examined. Deactivation of PGA is probed by non-isothermal continuous activity measurement with a novel temperature profile, developed during the course of this thesis, as well as a conventional discrete residual activity assay.⁵⁹ The two activity measurement methods are compared and the

¹ Adapted from “Chemical Engineering Science, 187, McDonald, M.A.; Bromig, L.; Grover, M.A.; Rousseau, R.W.; Bommarius, A.S. Kinetic model discrimination of penicillin G acylase thermal deactivation by non-isothermal continuous activity assay, 79-86.” Copyright (2018), with permission from Elsevier.

ability of the non-isothermal assay to more effectively discriminate between models of deactivation is demonstrated. The free energy of deactivation ($\Delta G_{\text{deact}} = 98.70 \pm 0.05$ kJ/mol) and the heat of reversible unfolding ($\Delta H_1 = 236.1 \pm 0.9$ kJ/mol) of PGA are reported for the first time. The Akaike information criterion (AIC) is used to discriminate between proposed models fit to the non-isothermal assay.

2.2 Materials and methods

A new assay for model discrimination is presented. The activity of an enzyme confined in an enzyme membrane reactor (EMR) is continuously and indirectly measured as reaction conversion. The temperature of the EMR is varied, affecting both activity and enzyme deactivation rate. Different models can be fit to the activity measurements during the temperature scan to determine the kinetics and thermodynamics of enzyme deactivation. Typical experiments used to probe enzyme deactivation were used to validate the new assay. Experiments included residual activity assays (measuring the activity after incubating the enzyme at a set temperature for a set time) and reaction temperature dependence experiments (measuring the instantaneous reaction rate at elevated temperature before the enzyme has a chance to unfold).^{60, 61}

2.2.1 Chemicals

Ampicillin sodium salt was purchased from Fischer Scientific (Fair Lawn, NJ). 6-APA and D-phenylglycine were purchased from Alfa Aesar (Heysham, UK) and were used to construct polarimetry standard conversion curves. Optical rotation varies linearly with concentration and is additive between species. Specific optical rotations are summarized

in Table 2.1. Assemblase[®], a highly engineered variant of PGA, was obtained from DSM-Sinochem (Delft, Netherlands).

2.2.2 Enzyme Membrane Reactor

The reactor from EDS Maschinenbau GmbH (Linnich, Germany) consists of a jacketed stainless-steel vessel with a PTFE stir bar, a 10-kDa polyethersulfone membrane from EMD Millipore, and a working volume of 10.0 mL. The temperature of the reactor is controlled with a PolyTemp programmable water bath and measured with a thermocouple incorporated into the reactor body. Good mixing is maintained by constant stirring at 150 RPM, giving an impeller Reynolds number $Re = \frac{ND^2\rho}{\mu}$ ranging from 1.1×10^4 to 2.2×10^4 over the temperature range of interest (N is the number of rotations per second, D is the impeller diameter, ρ is the solution density, and μ is the solution viscosity). A Reynolds number above 1×10^4 implies turbulent flow and good mixing. The reactor feed consisted of 20 mmol/L ampicillin in 50 mmol/L sodium phosphate buffer at pH 7.0 stored at 5 °C. The ampicillin solution was fed to the reactor at a constant volumetric flow rate by an ISMATEC IPC (Munich, Germany) peristaltic pump. The flow rate was 1.0 mL/min for all experiments, giving a residence time of 10.0 minutes. The enzyme was added last at a concentration of 0.5 μ mol/L. Once the reactor reached steady state at 20.0 ± 0.1 °C, the temperature manipulation was begun. A schematic of the setup is shown in Figure 2.1.

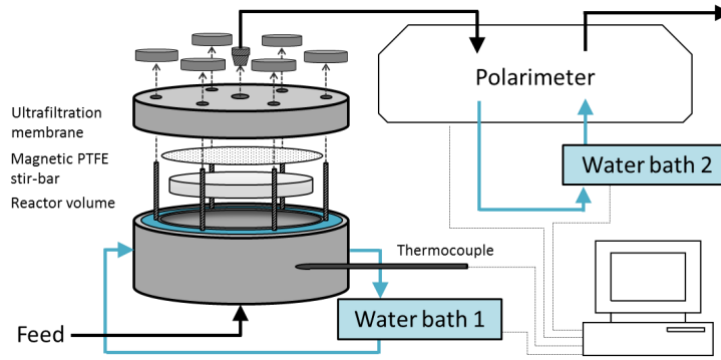


Figure 2.1. Schematic of experimental setup. The reactor volume is the region to which the enzyme is confined by the ultrafiltration membrane. Mixing is maintained by a PTFE coated magnetic stir-bar and reactor temperature is manipulated by water bath 1 and monitored via an online thermocouple.

2.2.3 Non-isothermal continuous activity assay

The concentration of ampicillin (and 6-APA and phenylglycine) was determined via polarimetry. The optical rotation was measured with a Rudolph Autopol IV polarimeter (Hackettstown, NJ, USA). The optical rotation, along with the measured reactor temperature, was exported in real time to a PC approximately once per second. The polarimeter flow cell has a volume of 1 mL and an optical path length of 100 mm and was maintained at 20.0 °C. All three species have distinct specific optical rotations ($\vartheta_{component}$, [degrees/mol/L]), rendering the concentration of ampicillin a function of observed optical rotation (Θ_{obs} , [degrees]) as well as feed ampicillin concentration (C_{A0}) and reaction stoichiometry. Stoichiometry is indicated in equation 2.5 where the subscripts A , B , and C refer to ampicillin, 6-APA, and D-phenylglycine, respectively.³² The observed rotation was converted to concentration by equation 2.1. $\vartheta_{component}$ values are summarized in Table 2.1.

$$C_A = \frac{\Theta_{obs} - C_{A0} (\vartheta_B + \vartheta_C)}{\vartheta_A - \vartheta_B - \vartheta_C} \quad (2.1)$$

Table 2.1. Specific optical rotation of key species. Measured in 250 mM pH 7 sodium phosphate buffer at 20 °C. Measured at a wavelength of 589 nm along a path length of 10 cm. Under 20 mM the concentration dependence is linear.

Species	Ampicillin	6-APA	D-phenylglycine
Measured specific optical rotation (°/mol/L)	96.9	61.6	-13.9

2.2.4 Residual activity experiments

Residual activity experiments were performed by incubating 1.0 mL of 5.0 $\mu\text{mol/L}$ PGA in 50 mmol/L sodium phosphate buffered at pH 7.0 at a constant elevated temperature for a fixed amount of time. The PGA solution was then added to 4.0 mL of 25.0 mmol/L ampicillin in 50 mmol/L sodium phosphate buffered at pH 7.0, giving a final concentration of 1.0 $\mu\text{mol/L}$ PGA and 20.0 mmol/L ampicillin. The solution was prepared in a single-sample polarimeter cell maintained at 20 °C. The optical rotation was measured for 3 minutes, during which the rotation decreased linearly. The residual activity was calculated as the rate of change in optical rotation divided by the rate of change in optical rotation for a sample that had not been incubated at elevated temperature. By this method, the time-temperature space was discretized, and individual measurements were taken in triplicate at each point.

2.2.5 Reaction temperature dependence

Concentrations of reactants and products were measured as a function of temperature by polarimetry. The single-sample cell, loaded with 5.0 mL of 20.0 mmol/L ampicillin solution in 50 mmol/L sodium phosphate buffered at pH 7.0, was allowed to equilibrate at the desired temperature. Once at the desired temperature, 25.0 μL of 200

$\mu\text{mol/L}$ PGA solution was added, giving a final PGA concentration of $1.0 \mu\text{mol/L}$. The rate was measured in the same manner as for the residual activity experiments.

2.3 Theory

Enzymes deactivate after long times or at (moderately) high temperatures or both. Typical stability assays require two sets of experiments, one examining time dependence and another probing temperature dependence. Manipulating EMR temperature (T) as a function of time (t) allows enzyme deactivation to be described as a function of only one variable (time or temperature).

$$T = f(t) \quad (2.2)$$

A simple model for the EMR is a well-stirred constant volume reactor, for which the non-steady-state concentration can be described by the equation

$$\frac{dC_A}{dt} = \frac{C_{A0} - C_A}{\tau} - r_A([N], C_A, T) \quad (2.3)$$

where C_A is the reactant concentration, C_{A0} is the feed reactant concentration, τ is the EMR residence time, and r_A is the reaction rate (for the system of interest) as a function of natively folded enzyme concentration, $[N]$, reactant concentration, C_A , and temperature, T .

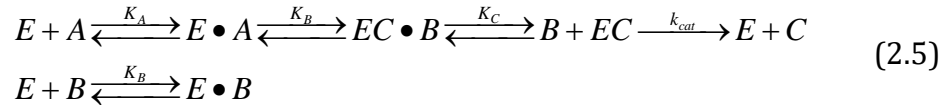
Previous non-isothermal EMR experiments have limited the rate of temperature change to about 1 Kelvin per reactor residence time. With this constraint the left hand side of equation 2.3 becomes negligible by the pseudo-steady-state-hypothesis.⁶² However, by directly solving the ordinary differential equation in equation 2.3, the pseudo-steady-state condition is not required and the rate of change of temperature is limited only by

practicalities such as experiment duration and heat transfer. Temperature profiles that maximize discrimination between deactivation models can be examined by considering transient concentrations.

For direct comparison between experiments of different feed concentrations (or substrates), conversion, X , can be used. Measuring the conversion allows determination of the concentration, through the relation below.

$$X = \frac{C_{A0} - C_A}{C_{A0}} \quad (2.4)$$

The reaction probed in this study was the hydrolysis of ampicillin to 6-aminopenicillanic acid (6-APA) and D-phenylglycine. The mechanism by which PGA catalyzes this reaction is complex but has been previously explained.^{63, 64} The kinetic scheme and resulting rate equation are shown in equations 2.5 and 2.6 respectively.



$$r_A = [N] \frac{k_{cat} K_C C_A}{K_A K_B C_B \left(1 + \frac{C_A}{K_A} \left(1 + \frac{1}{K_B} + \frac{K_C}{K_B C_B} \right) \right)} \quad (2.6)$$

E represents PGA, A is ampicillin, $E \bullet A$ is ampicillin bound PGA, EC is D-phenylglycyl-PGA complex, $EC \bullet B$ is 6-APA bound D-phenylglycyl-PGA complex, B is 6-APA, and C is D-phenylglycine. 6-APA may also bind to free PGA, forming $E \bullet B$ and causing product inhibition. In equation 2.6 $[N]$ represents the concentration of natively folded (active)

enzyme, $K_{A,B,C}$ are equilibrium constants, and C_B is the product (6-APA) concentration. Values of the equilibrium constants are summarized in Table 2.2.³²

Table 2.2. Reaction rate parameter values for equations 2.5 and 2.6, measured at 25 °C.

Reaction rate parameter values	
K_A (mol/L)	0.095
K_B (unit less)	1.083
K_C (mol/L)	0.080

The Eyring-Polanyi equation, which describes the variance of reaction rate with temperature through transition state theory, is only applied to k_{cat} . k_{cat} represents the rate-limiting hydrolysis step, therefore the equilibrium constants' dependence on temperature is assumed to be negligible compared to that for k_{cat} .

The Eyring-Polanyi equation is given by

$$k_{cat} = \frac{k_B T}{h} \exp\left(\frac{-\Delta G^\ddagger}{RT}\right) \quad (2.7)$$

where k_B is the Boltzmann constant, h is Planck's constant, R is the gas constant, and ΔG^\ddagger is the free energy barrier of the hydrolysis reaction.

Several models of deactivation are found to describe the change in concentration of native enzyme, $[N]$, for various enzymes. These models include the two-state first-order irreversible model, the three-state Lumry-Eyring model, and the four-state molten-globule model.⁶⁵⁻⁶⁷ These are referred to as Model 1, 2, and 3, respectively, and are represented in Figure 2.2. Other models of enzyme deactivation exist, some are based on mechanism and

others are empirical; Models 1, 2, and 3 were chosen to demonstrate the non-isothermal continuous activity assay. Model 1 represents the simplest case where an enzyme decays irreversibly and with no detectable intermediates. Model 2 adds an unfolded intermediate to account for the time required for the enzyme to unfold and the observation that most enzymes exposed to high heat for a short period do not lose as much activity as Model 1 predicts.⁶⁸ Model 3 builds on Model 2 by introducing a second unfolded intermediate to explain the observation of multiple distinct transitions in differential scanning calorimetry (DSC).^{67, 69}

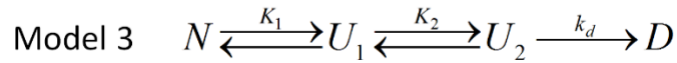
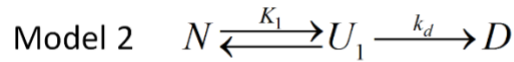


Figure 2.2. The three models explored in this study. N is the natively folded, active enzyme, U_j is an unfolded intermediate, and D is deactivated enzyme.

In all models, *N* represents natively folded enzyme, *U_j* represents the *j*th reversibly unfolded and inactive intermediate, and *D* represents permanently deactivated enzyme. The deactivation rate constants (*k_d*) are presumed to follow the Eyring-Polanyi equation where the free energy of deactivation $\Delta G_{deact} = \Delta H_{deact} - T \Delta S_{deact}$, so that

$$k_d = \frac{k_B T}{h} \exp\left(\frac{-\Delta H_{deact}}{RT}\right) \exp\left(\frac{\Delta S_{deact}}{R}\right) \quad (2.8)$$

The deactivation equilibrium constants (*K_j*) are assumed to follow van't Hoff equilibria

$$K_j = \exp\left(\frac{\Delta H_j}{R} \left(\frac{1}{T_{m,j}} - \frac{1}{T}\right)\right) \quad (2.9)$$

where ΔH_j is the change of enthalpy between enzyme conformations $j-1$ and j (i.e. between N and U_1 or between U_1 and U_2) and is assumed to be constant. $T_{m,j}$ is the temperature at which K_j is equal to unity.

The fraction of native enzyme depends on the current distribution of enzyme states; therefore, the relation between $[N]$ and time (or temperature) is formulated as an initial value problem that can be numerically integrated. Equation 2.10 gives the expression for Model 1, 2, and 3 when $n = 0, 1,$ and $2,$ respectively:

$$\frac{d[N]}{dt} = -[N] \frac{k_d \prod_{j=1}^n K_j - \frac{d}{dT} \left(\sum_{i=1}^n \prod_{j=1}^i K_j \right) \frac{dT}{dt}}{1 + \sum_{i=1}^n \prod_{j=1}^i K_j} \quad (2.10)$$

Equation 2.10, being independent of reactant concentration (C_A), is solved first and then substituted into equation 2.3 to find the reactant concentration exiting the reactor as a function of time (or temperature). With the definitions of K_j and k_d (eqns. 2.8 and 2.9) the model can be fit to experimental concentration data. The addition of more enzyme states in Model 2 and Model 3 increases the number of parameters compared to Model 1. More parameters enable these models to over fit data that would more appropriately be fit by a simpler model. Care must be taken to ensure that the selected model of deactivation is the best representation of the underlying mechanism of deactivation.

2.4 Model fitting and parameter estimation

All modeling was done in MATLAB. Model parameters were fit by iterative least squares with the MATLAB function *nlinfit*. 95% confidence intervals were generated using the MATLAB function *nlparci*. The differential equation solvers *ode45* and *ode15s* were used to integrate equation 2.3 and 2.10, respectively (equation 9 becomes stiff under certain parameter values).

The Akaike Information Criterion (AIC) was used to assist model selection. AIC is an estimator of model quality; however, AIC does not test the absolute quality of a model in the same sense that null hypothesis testing does. When comparing models, the model with the lowest AIC value (regardless of sign) is the best quality. When using least squares estimation with normally distributed errors, the AIC may be calculated by

$$\text{AIC} = n \log(\hat{\sigma}^2) + 2P \quad (2.11)$$

where n is the number of independent measurements, $\hat{\sigma}^2 = \frac{\sum(\hat{\varepsilon}_i)^2}{n}$, $\hat{\varepsilon}_i$ are the estimated residuals from the fitted model, and P is the number of parameters.^{70, 71} AIC provides an easily computed and easily interpreted evaluation of tradeoff between goodness of fit (captured by the logarithm term) and model complexity (captured by the $2P$ term).

2.5 Results and discussion

2.5.1 Linear temperature scans

The simplest temperature profile is a linear increase, as defined in equation 2.12. The results of three linear temperature scans are shown in Figure 2.3.

$$T(t) = mt + b \quad (2.12)$$

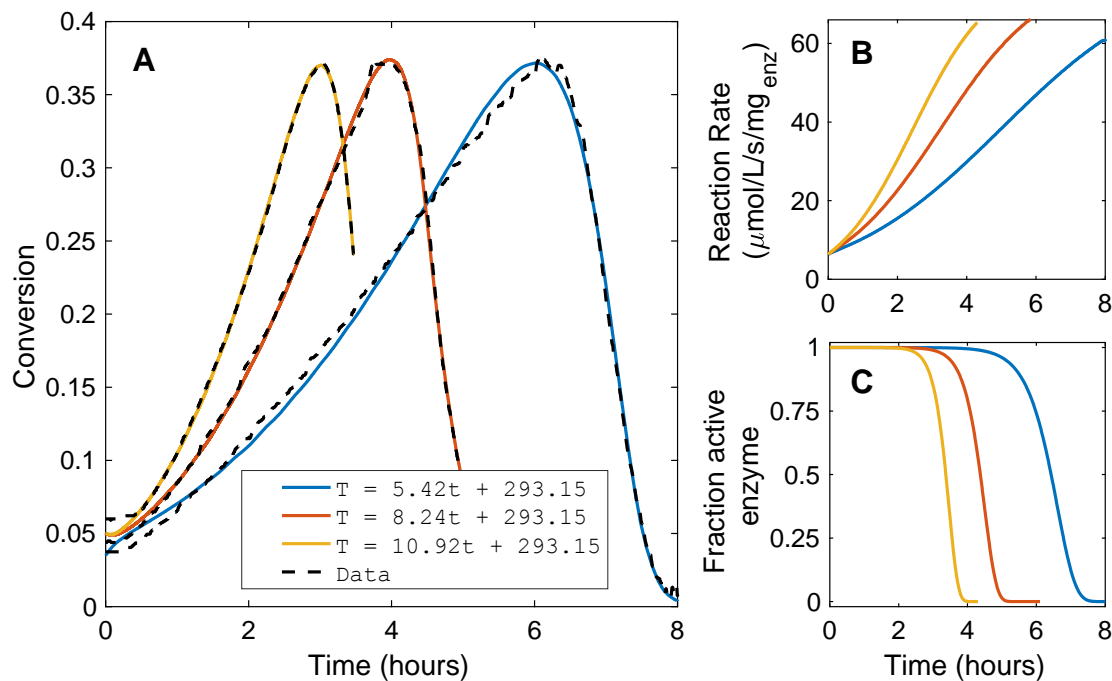


Figure 2.3. (A) The measured conversion versus time (dashed line) at three different temperature scan rates and Model 1 fits (solid lines) used to produce the data shown in (A) and (B). (B) The predicted ampicillin hydrolysis reaction rate as a function of time at the three temperature scan rates. (C) The fraction of active enzyme as a function of time at the three scan rates. Yellow: 10.92 K/h, red: 8.24 K/h, and blue: 5.42 K/h.

Figure 2.3.A shows conversion versus time for a linear increase in temperature with three different rates, $m = 5.42$ K/h (blue), $m = 8.24$ K/h (red), and $m = 10.92$ K/h (yellow) and $b = 293.2$ K for all three. The data show an increase in enzyme activity with increasing temperature followed by a steep decline as the enzyme rapidly unfolds beyond approximately 54 °C, corresponding to a conversion of 0.37 (at 3 hours, 4 hours, and 6 hours for the yellow, red, and blue lines, respectively). Figure 2.3.B shows the hypothetical reaction rate without enzyme deactivation. As the temperature increases the conversion increases leading to product inhibition. Product inhibition causes the reaction rate temperature dependence, shown in Figure 2.3.B, to deviate from an exponential increase, as would be expected from the Eyring-Polanyi equation. The fraction of active enzyme,

shown in Figure 2.3.C, combined with the reaction rate from Figure 2.3.B, leads to the observed conversion versus time shown in Figure 2.3.A. Model 1 is used to fit the three scan rates. In each case Model 1 sufficiently describes observed conversion, but Figure 2.4 shows how all three models can fit the data.

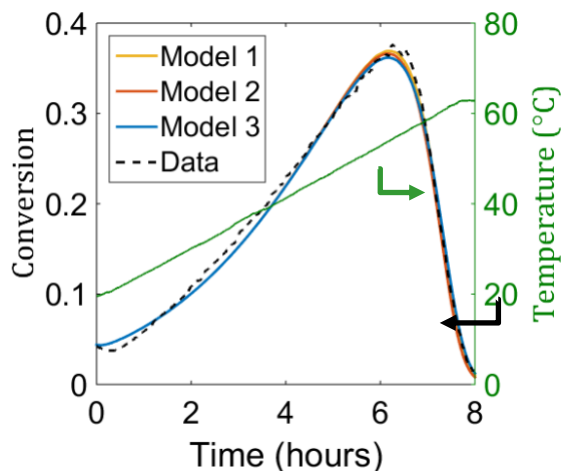


Figure 2.4. All three models are fit to the 5.42 K/h linear data. The solid yellow, blue, and red lines represent Model 1, Model 2, and Model 3, respectively. The dashed black line is the measured conversion, the green line is the observed temperature.

Models 2 and 3, in addition to Model 1, also describe the results observed when the temperature profile follows equation 2.12. Figure 2.4 shows the $m = 5.42$ K/h (blue) data set from Figure 2.3.A fit by all three models. Based on AIC values ($AIC_1 = 10.3$, $AIC_2 = 10.7$, and $AIC_3 = 37.9$), Model 1 is the best candidate for the process that generated the data. However, the AIC values of Model 1 and 2 are similar and it has previously been shown that most enzyme deactivation cannot be adequately described by Model 1.^{72, 73} To confirm that Model 1 is representative of the true deactivation process, additional experiments are needed that attempt to falsify Model 1 based on the underlying mechanistic differences between Models 1, 2, and 3. A single linear temperature profile for the non-

isothermal continuous activity assay is not sufficient to discriminate between the three models.

Changing the linear scan rate should differentiate semi-reversible mechanisms (Models 2 and 3) and irreversible mechanisms (Model 1), but in practice this is not the case. From equation 2.10, Models 2 and 3 are dependent on the scan rate (dT/dt) while Model 1 is independent of the scan rate. Equation 2.10 suggests that faster scan rates should give larger maximum conversions, however, Figure 2.3 shows that Model 1 fits the data at three different scan rates and there is no appreciable difference in maximum conversion. The parameters from fitting the data in Figure 2.3 also predicted the observed conversion when the scan rate was increased by an order of magnitude ($m = 54.9$ K/h); see Figure 2.5. Faster scan rates are hard to achieve employing a water bath and slower scan rates become impractically slow.

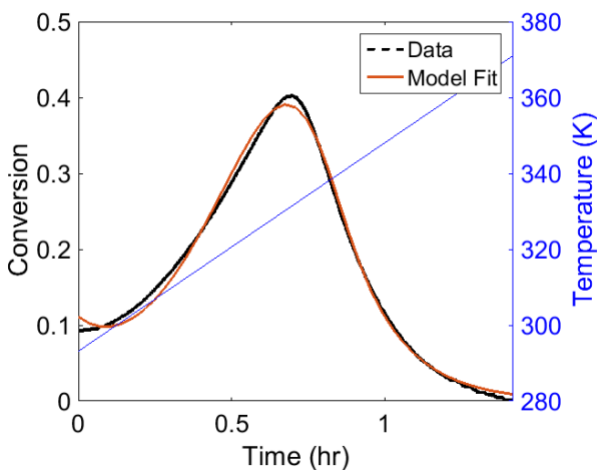


Figure 2.5. Model 1 fit to the 54.9 K/h linear temperature ramp conversion data.

2.5.2 Simulated experiments

To maximize differences between the models, experiments with TEM-1 β -lactamase, previously shown to follow Model 3, were simulated and the simulated data were refit with Models 1 and 2. The values of the parameters used in the simulation are given in Table 2.3.⁶² Noise, corresponding to a maximum 3% random error in the measured variable (approximately 0.05° optical rotation), was added to the simulated data before fitting the models. The simulation temperature profile was then changed, and new data were generated from the simulated model (Model 3) as well as from the fit models (Models 1 and 2). A temperature profile was then generated that would increase the experimentally observable difference between the models.

Table 2.3. Values used in TEM-1 beta-lactamase simulated deactivation experiments. The value of ΔG^\ddagger is only dependent on the reaction, not the enzyme deactivation model, therefore the value for TEM-1 beta-lactamase was set to be the same as was measured for PGA for similarity of scale (actual value 54.2 kJ/mol).

ΔG^\ddagger (kJ/mol)	ΔH_1 (kJ/mol)	$T_{m,1}$ (K)	ΔH_2 (kJ/mol)	$T_{m,2}$ (K)	ΔG_{deact} (kJ/mol)
67.4	74.9	309.2	699.7	324.7	100.6

The novel temperature profile is motivated by differential scanning calorimetry (DSC), a popular method to observe protein unfolding. DSC can be used to observe conformational changes upon heating and cooling to test models of denaturation. Similar temperature increases and decreases can be implemented with the continuous activity assay. However, DSC detects all conformational changes that alter the protein heat capacity, whereas the continuous activity assay only observes changes in activity. The specificity for activity is especially useful when probing enzymes because, as Rodriguez-Larrea *et al.* showed, enzymes may refold into non-functional conformations that produce

DSC thermograms indistinguishable from the functional conformation.⁷⁴ It is possible that many enzymes that are believed to have functional reversibility also refold to an inactive form.

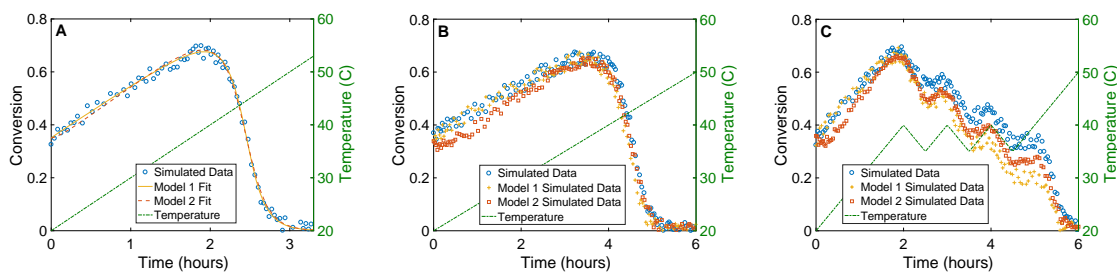


Figure 2.6. Results of the simulated TEM-1 deactivation experiment.⁶² The reaction conditions are similar to those used for the non-isothermal continuous activity assay: the substrate is penicillin G and the product is penicilloic acid, the substrate feed concentration is 20 mM, the enzyme concentration is 5 μ M, and the reactor residence time is 8 minutes. (A) Simulated TEM-1 (Model 3) non-isothermal continuous assay and fit with Model 1 and Model 2. (B) Simulated data based on TEM-1 (Model 3) and simulated data based on Model 1 and Model 2 fits at slower temperature scan rate. (C) Simulated data based on TEM-1 (Model 3) and simulated data based on Model 1 and Model 2 fits with saw-tooth temperature profile.

The temperature profile is most effective when it probes the main differences between models, namely functional reversibility. Figure 2.6 illustrates the process described above for a saw-tooth temperature profile. The saw-toothed profile in this example was designed to deactivate approximately equal amounts of enzyme with each temperature oscillation. Figure 2.6.A shows a simulated TEM-1 beta-lactamase experiment with a linear scan rate of 10 K/h and the corresponding Model 1 and Model 2 fits. Figure 2.6.B shows three simulated TEM-1 beta-lactamase experiments with a linear scan rate of 5 K/h. One experiment was generated with the true model (Model 3) from (A) and two other experiments were generated from the results of the fits with Models 1 and 2 from (A). With a 3% random error it is nearly impossible to differentiate the three sets of data, confirming that practical changes to a linear scan rate do not provide observable changes

in the conversion profile. Figure 2.6.C is the same as (B) but with a saw-tooth temperature profile (at 10 K/h) that makes clear the differences between the models even with 3% measurement error. While Models 1 and 2 can approximate data produced by Model 3 with a linear temperature profile, the saw-tooth profile effectively differentiates Models 1 and 2 from the true model (Model 3) by the third temperature oscillation.

The same simulation procedure used for TEM-1 beta-lactamase was used on lysozyme, an enzyme whose deactivation was previously shown to follow Model 2.⁶⁹ The simulation showed that a saw-tooth temperature profile considerably differentiates Model 2 from Model 1.

2.5.3 *PGA deactivation model discrimination*

The temperature profile from the simulated experiment in Figure 2.6.C was implemented for PGA and shows Model 2 best describes PGA deactivation. Figure 2.7.A shows the observed ampicillin conversion along with the fit for each Model. Figure 2.7.B-D shows the distribution of enzyme in each state (native, unfolded, deactivated) obtained when each model is fit to the data in panel A. The irreversibility of Model 1 manifests in the overshoot when fitting the peaks in conversion; the lack of unfolded intermediate results in harder transitions between heating and cooling (deactivating and stabilizing conditions). Model 2 is better able to fit the data by using the unfolded intermediate as a buffer to soften the transition from heating to cooling; the maxima in unfolded population align with the peaks in the temperature in Figure 2.7.C. The unfolded intermediates in Model 3 also give a better fit than Model 1, however, as shown in Figure 2.7.D, the relative proportion of enzyme in the first unfolded state is nearly zero at all times, indicating only

one unfolded state is important. A second solution to fitting the data with Model 3 results in the population of the first unfolded state being substantial and the population in the second unfolded state being nearly zero, however the goodness of fit was equal to that shown in Figure 2.7. This is interpreted to mean only one intermediate is important, which is the mechanism captured by Model 2.

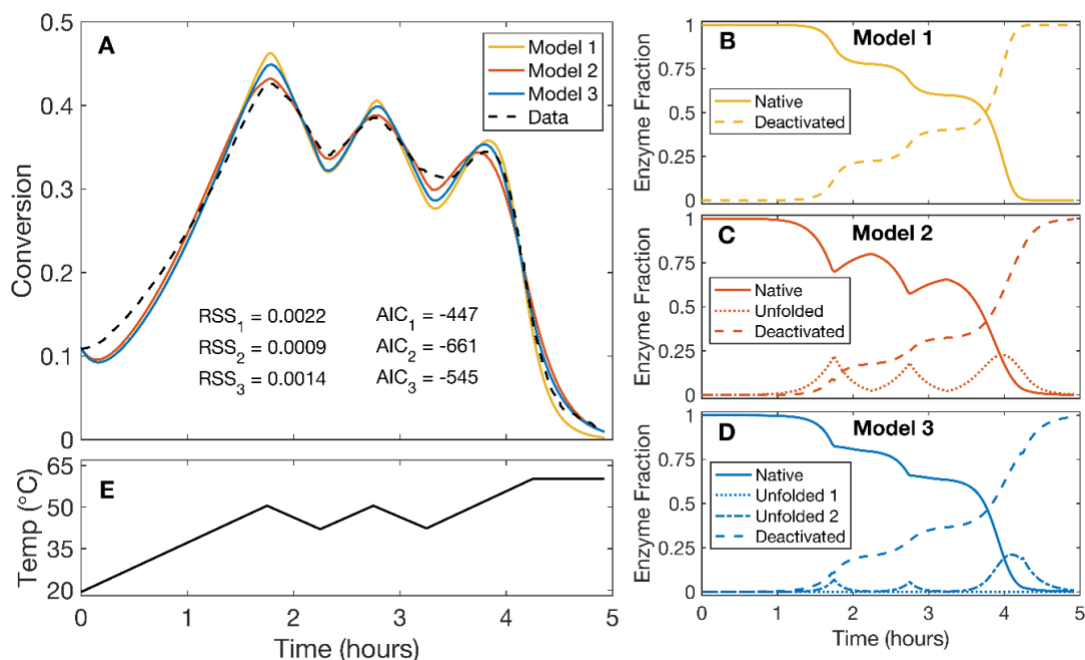


Figure 2.7 (A) The observed conversion of ampicillin and the fit of Model 1 (solid yellow), Model 2 (solid red), and Model 3 (solid blue) to the data (black dashed). (B) The fractions of active (solid) and deactivated (dashed) enzyme when the data in (A) are fit with Model 1. (C) The fractions of active (solid), reversibly unfolded (dotted), and deactivated (dashed) enzyme when the data in (A) are fit with Model 2. (D) The fractions of active (solid), 1st reversibly unfolded (dotted), 2nd reversibly unfolded (dash-dot), and deactivated (dashed) enzyme when the data in (A) are fit with Model 3. (E) The temperature as a function of time.

The residual sum of squares (RSS) and AIC values, shown in Table 2.4, support Model 2 as best representing the underlying deactivation process. The parameters from fitting the saw-tooth profile are given in Table 2.5. The melting temperature of PGA measured by differential scanning fluorimetry (DSF) is 332 ± 4.9 K, which is consistent

with the fit value of $T_{m,1}$ of 328.4 ± 0.1 K. Only one transition was observed with DSF, which also supports Model 2 over Model 3. Figure 2.8 shows the onset of melting and melting temperature as measured by DSF for PGA at two different concentrations and six pH values. No variation was found with concentration, indicating that aggregation is not a primary driver of deactivation. DSF also suggests that PGA is more stable in slightly acidic solution compared to neutral conditions, however other factors, such as solubility and PGA activity, have greater influence on choice of operating pH for the continuous process, and so the non-isothermal continuous activity measurement was only conducted at pH 7.

Table 2.4. The number of parameters, P , residual sum of squares, RSS, and Akaike information criterion, AIC, for each model fit to the data generated from the saw-tooth temperature profile.

Model	P	RSS	AIC
Model 1	3	0.0022	-447
Model 2	4	0.0009	-661
Model 3	6	0.0014	-545

Table 2.5. Parameter values resulting from fitting Model 2 to the saw-tooth temperature profile given as 95% confidence intervals. ΔG_{deact} (kJ/mol) is given at 25 °C.

	Model 1	Model 2	Model 3
ΔG^\ddagger (kJ/mol)	67.40 ± 0.02	67.38 ± 0.01	67.41 ± 0.02
ΔG_{deact} (kJ/mol)	121.2 ± 2.4	98.70 ± 0.05	100.17 ± 0.04
ΔH_1 (kJ/mol)		236.1 ± 0.9	219.8 ± 0.04
$T_{m,1}$ (K)		328.4 ± 0.1	362.9 ± 0.1
ΔH_2 (kJ/mol)			203.85 ± 0.18
$T_{m,2}$ (K)			298.1 ± 0.1

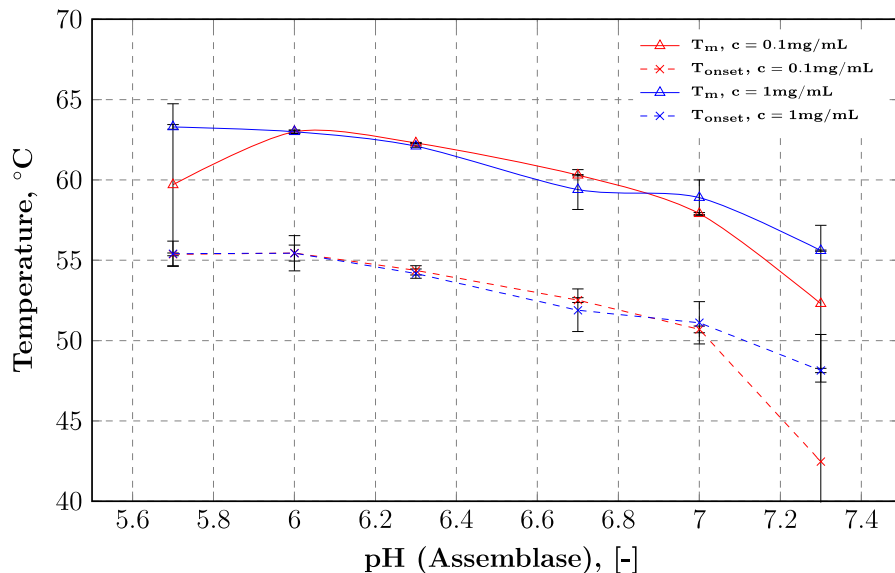


Figure 2.8. The melting temperature, T_m , and unfolding onset temperature, T_{onset} , of Assemblase PGA are shown as a function of pH value at two protein concentrations. The melting was measured by differential scanning fluorimetry (DSF). T_m is interpreted as the temperature where the DSF curve is at a maximum and T_{onset} is the temperature at which the DSF curve increases 5% above the baseline.

From the simulations in Figure 2.7.C, it is clear that PGA deactivation is not strongly reversible, as indicated by the low fraction of PGA in the reversibly unfolded state (U_I), which reaches a maximum of about 20%. The low reversibility may be because PGA is a heterodimer formed from a single precursor sequence. Proteins activated by proteolytic processing often unfold irreversibly because the mature amino acid sequence does not encode the same folding as the precursor sequence.⁷⁵ PGA likely refolds up to the point when the two monomers dissociate, at which point proper refolding is less likely. Grinberg *et al.* employed DSC to deduce that the α subunit of PGA unfolds reversibly while the β subunit aggregates upon dissociation of the heterodimer.⁷⁶ While aggregation was not observed in this study, their results are consistent with the observed limited reversibility found for PGA. Their results, combined with the results of this study, may suggest the structure of the α subunit is less critical than that of the β subunit, on which the active site

serine residues. This limited reversibility still informs process design of beta-lactam synthesis by PGA because the catalyst has some resilience to temperature fluctuations in the reactor, which could enable operation closer to stability limits.

2.5.4 *PGA deactivation by batch assay*

In addition to the continuous non-isothermal activity measurements, the residual activity was also assayed by the conventional batch isothermal method for PGA. Both the reaction rate and the fraction of active enzyme as a function of temperature are needed for comparison to the non-isothermal assay. The results of these experiments are shown in Figure 2.9. The reaction rate is presented as an Eyring-Polanyi plot in Figure 2.9 (left), the residual enzyme activity at six different temperatures is shown with exponential decay fits (equivalent batch-wise to Model 1) to the data in Figure 2.9 (middle), and the decay constants are plotted in Eyring-Polanyi linearized space in Figure 2.9 (right). The decay constants are also listed in Table 2.6. Enthalpy and entropy can be determined from Eyring plots. The free energy of the reaction determined by this method agrees well with that found by fitting the non-isothermal experiments and is relatively constant over the temperature range of interest (indicated by the small entropy of reaction). A comparison between these methods is summarized in Table 2.7.

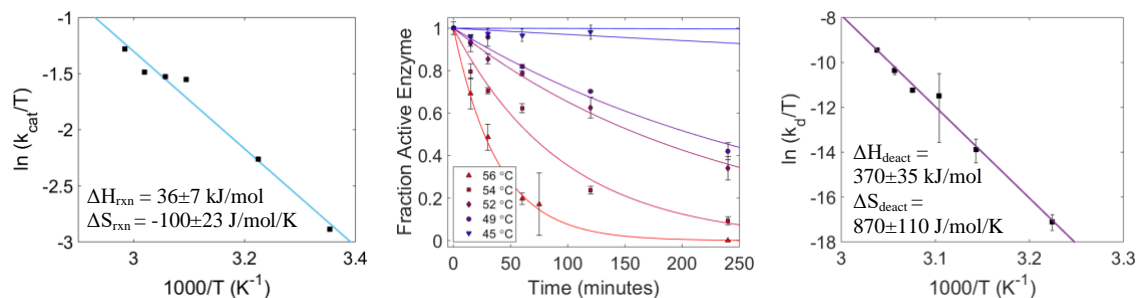


Figure 2.9. Results of batch deactivation assay of PGA. (Left) Ampicillin hydrolysis rate as a function of temperature. (Middle) Residual enzyme activity as a function of time and temperature. (Right) Model 1 deactivation constant as a function of temperature.

Table 2.6. Enzyme decay constants measured by batch residual rate experiments (Figure 2.9 middle and right)

Temperature (K)	Decay Constant (standard deviation) [s ⁻¹]
310	1.15×10^{-5} (0.2×10^{-6})
318	0.00030 (0.00008)
322	0.00329 (0.00212)
325	0.00426 (0.00016)
327	0.01039 (0.00094)
329	0.02570 (0.00113)

As the batch method relies on discrete measurements it does not provide the same resolution as the continuous method, therefore, model discrimination is much more difficult. It does, however, provide estimates of the enthalpy and entropy of deactivation for Model 1. The confidence intervals from the isothermal batch assay are much wider than those from the non-isothermal continuous assay, for both the linear and saw-tooth temperature scans (shown in Table 2.7); however, the results are consistent with those from the Model 1 fits. The disagreement between the values determined from the linear and saw-tooth temperature profiles is expected because it was previously shown that Model 1 does not represent the data-generating process. However, the congruence of the isothermal batch

results with both continuous results gives additional validation of the continuous non-isothermal activity assay; when an incorrect model (Model 1) is fit to both data sets the same result is produced by the continuous and batch methods.

Table 2.7. Comparison of results from non-isothermal continuous assay with linear and saw-tooth temperature profiles analyzed with Model 1 and isothermal batch assay. Values are 95% confidence intervals.

	Linear temperature scan	Saw-tooth temperature scan	Isothermal batch
ΔG^\ddagger (kJ/mol)	68.9 ± 0.1	67.40 ± 0.02	67 ± 14
ΔH_{deact} (kJ/mol)	355 ± 2	350.7 ± 0.6	370 ± 35
ΔS_{deact} (J/mol/K)	771 ± 5	770 ± 2	870 ± 110

2.6 Conclusion

Determination of the mechanism of enzyme deactivation is not always possible with a linear temperature scan when the enzyme activity is observed continuously. The theoretical framework for the continuous non-isothermal assay has been expanded to enable a larger range of experiments for better differentiation of deactivation models. The technique is explored in depth for three models and experimental data from PGA is examined with each model. However, the assay is generalizable to any deactivation model. The results indicate model discrimination is most effective with temperature profiles that include heating and cooling. Compared to batch-wise enzyme activity measurement, the non-isothermal continuous assay provides more data faster to enable discrimination with single experiments.

PGA and TEM-1 beta-lactamase were examined in real and simulated experiments, respectively. Linear temperature scans suggested that PGA deactivates according to Model

1. However, in a simulated linear scan experiment, TEM-1 beta-lactamase, which is known to deactivate according to Model 3,⁶² could be better fit by Models 1 and 2. Novel temperature profiles were simulated for TEM-1 beta-lactamase and designed to maximize the experimentally observable difference between the models. A saw-tooth profile proved to be the simplest sufficient profile, demonstrating that TEM-1 beta-lactamase deactivation is indeed captured best with Model 3. Next, PGA deactivation was probed with the saw-tooth temperature profile, which showed that PGA deactivation is slightly reversible. Batch-wise experiments, commonly used to probe enzyme activity during thermal deactivation, were not able to discriminate between any of the models but are consistent with the results from the non-isothermal continuous assay. Applying the saw-tooth temperature profile in combination with the Akaike information criterion for model discrimination not only pointed to Model 2 as the best fit for PGA deactivation but yielded activation and deactivation Gibbs Free enthalpies, enthalpies, and entropies with unprecedented precision.

CHAPTER 3. KINETICS OF PGA-CATALYZED SYNTHESIS OF AMPCILLIN AND CEPHALEXIN²

3.1 Introduction

To design the physical pilot plant for a CM reactive crystallization process for beta-lactams one needs to know that rates at which the reaction proceeds under different process conditions. The kinetics of PGA synthesis (and hydrolysis) of beta-lactams has been published by many,^{63, 77-83} including those in our lab.^{41, 84} This thesis builds on the work of the aforementioned citations to examine reactive crystallization and CM; this chapter specifically improves on those previously cited by expanding the mechanistic understanding of PGA catalyzed beta-lactam production to include pH-specific behavior and substrate inhibition, two formerly unreported facets of PGA catalysis.

The primary obstacle to more highly efficient β -lactam production by PGA is poor selectivity, as kinetically controlled synthesis competes with both primary and secondary hydrolysis (Figure 3.1). Ampicillin, produced by the condensation of 6-aminopenicillanic acid (6-APA) with D-phenylglycine methyl ester (PGME) and the subject of this chapter, is a particularly good model compound for this process. Phenylglycine, the byproduct of ampicillin (and cephalixin) secondary hydrolysis, is only sparingly soluble, rendering selectivity a greater challenge than with amoxicillin. Ampicillin is also less soluble and more easily available than cephalixin (and its precursor 7-ADCA) and is therefore favored

² Adapted from “Chemical Engineering Science, 165, [McDonald, M.A.](#); Bommaris, A.S.; Rousseau, R.W. Enzymatic reactive crystallization for improving ampicillin synthesis, 81-88.” Copyright (2017), with permission from Elsevier.

for reactive crystallization experiments over cephalexin. The insolubility of phenylglycine elevates the problem of selectivity since excessive byproduct formation results in contaminated solid product.

Selectivity is affected by both the rate of PGME hydrolysis and ampicillin hydrolysis. The ratio of rates of synthesis and hydrolysis (V_S/V_H) is used to characterize the differential selectivity; it is a property of the enzyme at the specified conditions and is therefore denoted S_{enz} . The value of this ratio at zero conversion (the initial ratio, $[V_S/V_H]_0$), often also denoted as the synthesis-to-hydrolysis ratio (S/H), captures the enzyme specificity for ampicillin synthesis over primary hydrolysis, and has been the subject of several studies regarding enzyme and reaction engineering.^{64, 85-87} The ratio of total ampicillin and phenylglycine produced up to a specified time—the integral selectivity ($S_{process}$), which is the quantity that captures the behavior of real reactors—depends on both primary and secondary hydrolysis, and has seen far less investigation because of the challenges posed by secondary hydrolysis.

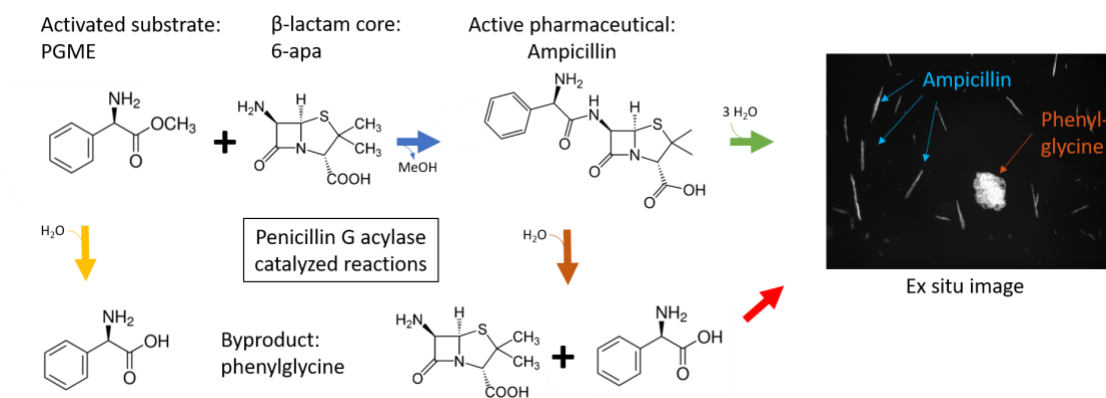


Figure 3.1 The overall reaction and crystallization scheme for the PGA-catalyzed synthesis of ampicillin, with crystallization of ampicillin and possible precipitation of phenylglycine. Synthesis is shown in blue, primary hydrolysis in yellow, secondary hydrolysis in orange, ampicillin trihydrate crystallization in green, and phenylglycine crystallization in red.

Reactive crystallization, where a desired compound is driven into supersaturation by a chemical reaction, is typically used to push the reaction equilibrium to the right (i.e. towards a desired product). However, Figure 3.1 shows that ampicillin is not the equilibrium product but rather is an intermediate; the equilibrium of secondary hydrolysis favors 6-APA and D-phenylglycine over ampicillin by about 100-fold while the equilibrium of the synthesis reaction was not determinable because no ampicillin was detected at equilibrium.⁴⁰ In the present work we develop a crystallization-based process that isolates the intermediate and therefore increases the integral selectivity without the enzyme engineering required to affect the differential selectivity. Our own previous work has shown that simultaneous synthesis and crystallization of pure ampicillin is possible.⁴¹ In the following sections we demonstrate that the crystallization of ampicillin is advantageous and can be optimized for selectivity and productivity.

3.2 Materials and methods

3.2.1 Materials

PGME was from Sigma-Aldrich (St. Louis, MO). Phenylglycine, ampicillin sodium salt, and anhydrous ampicillin powder were from Alfa Aesar (Willard Hill, MA). 6-APA and ampicillin trihydrate were from TCI America (Portland, OR). DSM-Sinochem (Delft, The Netherlands) kindly supplied the enzyme Assemblase®, with a protein concentration of 17 mg/mL and a specific activity for ampicillin hydrolysis of 1600 U/mg protein at pH 7.8 and 25 °C. All materials were used as received.

3.2.2 Determination of initial reaction rates

The reaction of 6-APA and PGME was performed in an Anton-Paar MCP 500 polarimeter thermostated at 298 K. The contents were constantly mixed via circulation through the flow-cell by a peristaltic pump. The working volume was 5.0 mL. Samples of 50.0 μL were periodically withdrawn for analysis by high-performance liquid chromatography (HPLC). The concentration of reactants varied from 5.0 mM to 80 mM. The concentration of enzyme was 1.25 μM and was added after the temperature in the cell had equilibrated. The pH value was maintained at the desired level by 100 mM phosphate buffer. The pH value was measured before and after the reaction and changed by less than a tenth of a pH-unit between the start and end of the reaction.

The rates of both primary and secondary hydrolysis were measured individually by polarimetry. PGME, 6-APA, ampicillin, and phenylglycine are all optically active, and specific rotations as determined in this study are summarized in Table 3.1. By measuring change in optical rotation with time, combined with knowledge of the reaction stoichiometry, the rate of either PGME hydrolysis or ampicillin hydrolysis could be determined in real time.

The rate of ampicillin synthesis was measured by a Shimadzu Prominence HPLC with a 4.6 x 100 mm Phenomenex C18 reverse-phase column. The eluent consisted of 30:70 v/v acetonitrile and water with 0.69 g/L SDS and 0.69 g/L NaH_2PO_4 . The flowrate was 0.75 mL/min. The initial synthesis to hydrolysis ratio was determined by comparing accumulation of ampicillin and phenylglycine directly.

Table 3.1. Summary of the optical rotation of the optically active species in ampicillin synthesis; 10 cm path-length at 589 nm. The specific rotation was measured at 298 K in 250 mM pH 7-phosphate buffer.

Species	D-PGME	6-APA	Ampicillin	D-phenylglycine
Specific Optical Rotation (°/mol/L)	-23.6	61.6	96.9	-13.9

3.2.3 Determination of solubilities

The solubility of each species as a function of pH was determined with the saturation approach.⁴⁵ The pH value of a saturated suspension was adjusted by titration with 2 M HCl or NaOH while the temperature was held steady at 298 K and the vessel was stirred constantly. After equilibrium was reached (as indicated by unchanging pH value, typically over 1 hour) samples were withdrawn through a 0.45- μ m filter and diluted, either 1:200 for analysis by HPLC or 1:10 for examination by polarimetry. The results of HPLC and polarimetry vary by less than 5% and the average of the two values was used for the purposes of modeling the system.

3.2.4 Modelling

The reaction kinetics were determined experimentally and modelled in MATLAB. The crystallization kinetics have previously been determined and were also modelled in MATLAB.^{88, 89} The pH value was calculated via a charge balance and species balance.⁹⁰ Since the reaction kinetics were found to be rate-limiting, the system was regarded as consisting of two time scales, with the transition between the two scales determined by thermodynamics rather than kinetics for computational simplicity. The pairing of these two kinetic processes along with separation into different scales and pH changes necessitated

construction of a purpose-built semi-implicit Euler integrator to determine concentration trajectories.

3.2.5 Reactive crystallization experiments

To seed the reactive crystallizer, 14.1 mg/mL of ampicillin trihydrate were added to a solution of PGME and 6-APA in equimolar amounts. The solubility of ampicillin trihydrate is less than 14.1 mg/mL (see Figure 3.2, equivalent to 35 mM dissolved ampicillin), which means that, at equilibrium and before the reaction is started, the resulting mixture is a suspension of dissolved and solid phase ampicillin (5-15% seed crystals, depending on pH value). To simulate the homogeneous (non-crystallizing) process, 13.0 mg/mL of ampicillin sodium salt (equivalent to 35 mM dissolved ampicillin) was added to the reaction solution. The solubility of ampicillin sodium salt is greater than 13.0 mg/mL, resulting in complete dissolution of the ampicillin and a solution slightly supersaturated with respect to ampicillin trihydrate (see Figure 3.2, solid versus dashed ampicillin curves). The solutions were titrated to the same initial pH value with 2 M NaOH. The reaction was initiated by the addition of the enzyme. At the highest reactant concentrations crystal formation through primary nucleation was sometimes observed in the homogeneous experiments; in such cases, these data were not used to compare the process with and without crystallization. The reactive crystallization experiments were conducted at constant stirring in a 298 K water bath. Aliquots of 50.0 μ L were periodically withdrawn for analysis by HPLC using the same HPLC procedure described above.

3.2.6 Process Characterization

Previous studies of enzymatic ampicillin synthesis define process metrics, such as selectivity or conversion, in many different ways. We have chosen to define *process selectivity* as the total ampicillin produced divided by the total phenylglycine produced (see equation 3.1) while *enzymatic selectivity* is defined as the instantaneous synthesis to hydrolysis ratio (see equation 3.2).

$$S_{\text{process}} = \frac{[\text{Amp}]}{[\text{PG}]} \quad (3.1)$$

$$S_{\text{enz}} = \frac{V_{\text{syn}}}{V_{\text{hydro}}} \quad (3.2)$$

We define *conversion* with respect to PGME since 6-APA is both consumed by synthesis and produced by secondary hydrolysis.

$$X_{\text{PGME}} = \frac{[\text{PG}] + [\text{Amp}]}{[\text{PGME}]_{\text{init}}} = \frac{[\text{PGME}]_{\text{init}} - [\text{PGME}]}{[\text{PGME}]_{\text{init}}} \quad (3.3)$$

The *yield* is defined with respect to 6-APA because it captures aspects of synthesis, primary hydrolysis, and secondary hydrolysis.

$$Y = \frac{[\text{Amp}]}{[\text{6APA}]_{\text{init}}} \quad (3.4)$$

The *productivity* is the amount of ampicillin produced per amount of enzyme per time to phenylglycine saturation.

$$P = \frac{[\text{Amp}]}{\tau [\text{Enz}]_0} \quad (3.5)$$

3.3 Results and discussion

3.3.1 Solubility experiments

The reaction scheme (Figure 3.1) shows sequestering the ampicillin in a solid phase can compete with secondary hydrolysis. Since the solid phase must be relatively pure in ampicillin to avoid subsequent purification steps, the solubilities of species other than ampicillin should not be exceeded. The measured solubilities of the relevant compounds are shown in Figure 3.2. The low solubility of ampicillin trihydrate relative to 6-APA and PGME points toward implementation of a practical reactive crystallization process; nevertheless, the low phenylglycine solubility significantly limits the operating range that results in high-purity ampicillin. Figure 3.2 shows that at pH values up to 7 the solubility of ampicillin and phenylglycine are very similar, however, in slightly basic conditions (pH 7-8), ampicillin is significantly more soluble than phenylglycine, rendering operation in basic conditions unfavorable because of the large amount of product that will remain in solution. The decrease in solubility of ampicillin above pH values of 8 (dashed line) is the result of crystallization of ampicillin sodium salt as opposed to ampicillin trihydrate. We aim to only produce ampicillin trihydrate and therefore will not operate above a pH value of 8.

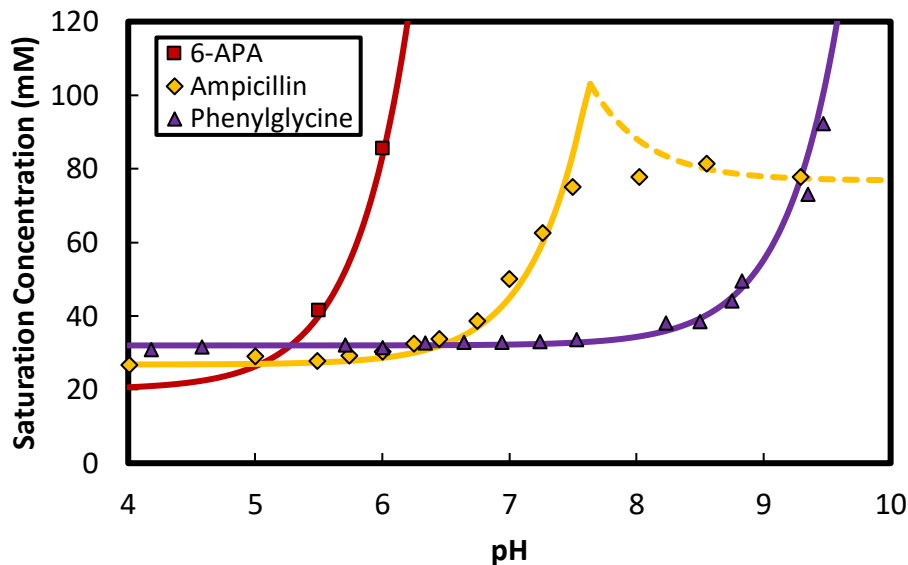


Figure 3.2. The solubility of 6-APA (■), ampicillin (◆), and phenylglycine (▲) as functions of pH value. Lines indicate modeled fit based on the Henderson-Hasselbalch equation with ionic strength correction. The solid ampicillin line represents ampicillin trihydrate while the dashed ampicillin line represents ampicillin sodium salt. PGME is not shown because it is highly soluble.

3.3.2 Initial rate experiments

The change in solubility with pH value has been previously documented,^{22, 45, 91} but the enzyme activity as a function of pH value is poorly characterized. Previous studies of the effect of pH value on ampicillin synthesis have reported trends, sometimes conflicting, regarding specific reaction rates and yields.^{87, 92, 93} In the present work, the pH dependence of enzyme activity towards primary hydrolysis and synthesis was found to be very similar. Figure 3.3 shows that in three equimolar mixtures of 6-APA and PGME, each at a different concentration, the maximum activity of the enzyme occurred at around pH 8 for both synthesis and primary hydrolysis. From this result it was determined that two significant protonation/deprotonation equilibria exist and likely affect a common intermediate through which the synthesis and primary hydrolysis reactions proceed. The lower pKa was

observed at a pH value of 7.1 and the higher pKa was observed at a pH value of 8.5. Figure 3.3 also shows that synthesis of ampicillin increases with higher reactant concentrations, but hydrolysis activity decreases as the reactant concentrations are raised. The decrease in hydrolysis suggests competition between 6-APA and water; increasing the amount of 6-APA decreases the relative frequency at which hydrolysis can occur.

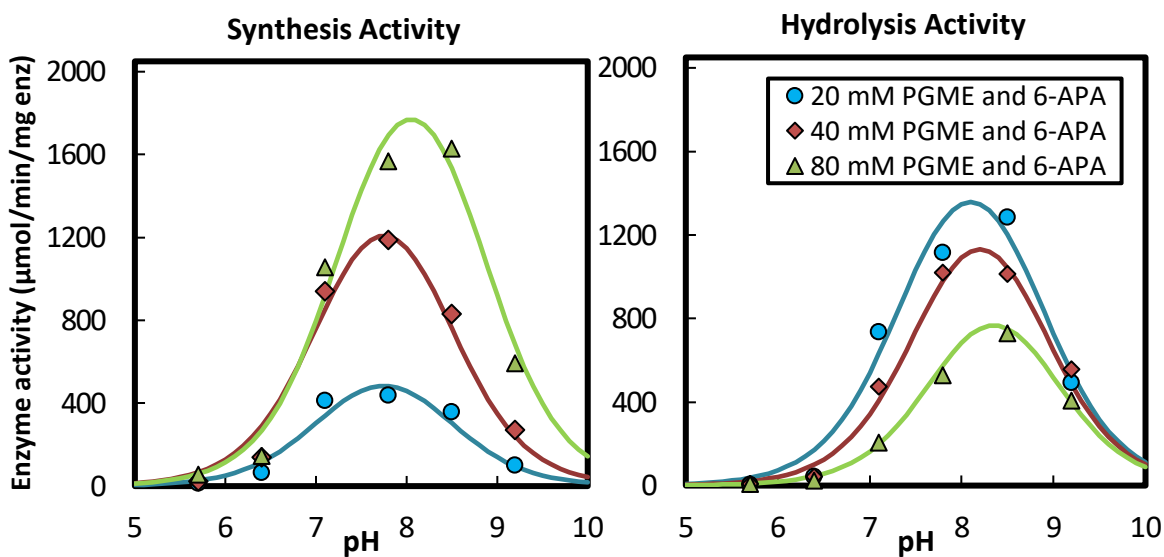


Figure 3.3. Synthesis (left) and hydrolysis (right) activity of Assemblase® as functions of pH at three different equimolar reactant concentrations. The activity is determined from the initial rate. Curves are to guide the eye.

From the initial-rate experiments, the PGA used in this study (commercially available Assemblase® from DSM-Sinochem) was characterized in the framework established by Svedas *et al.* for α -chymotrypsin and later applied to PGA (and other serine and cysteine proteases).⁶³ The proposed mechanism involves the binding of an acyl-donor (PGME) to the enzyme and subsequent formation of a covalent adduct between the acyl-donor and the active site serine of PGA. This adduct, the acyl-enzyme complex, is likely the intermediate step affected by the acidity/basicity of the solution. The adduct is highly

susceptible to a nucleophilic attack either by a desired nucleophile or water. Once formed, the acyl-enzyme complex binds a nucleophile (6-APA in the case of ampicillin) which then reacts with the acyl-enzyme complex and breaks the covalent bond to the critical serine residue. The nucleophilic attack produces enzyme-bound ampicillin, which is then released to solution, or, if water attacks the acyl-enzyme complex, phenylglycine. Binding of 6-APA does not prevent hydrolysis, but it significantly reduces it, as can be seen in Figure 3.4 below.

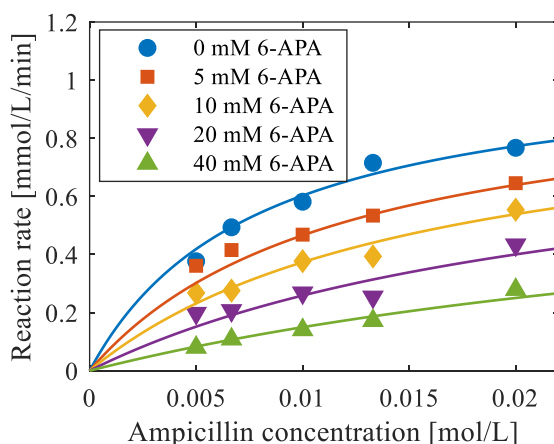


Figure 3.4. The initial rate of ampicillin hydrolysis at different initial ampicillin concentrations and 6-APA concentrations.

Svedas *et al.* used three parameters to evaluate enzymes that fit this mechanism, α , β_0 , and γ where α describes the enzyme specificity for the acyl-donor over the desired product (PGME over ampicillin), β_0 describes the reactivity of the nucleophile (6-APA) in the hypothetical situation of near-zero nucleophile concentration, and γ describes the fraction of acyl-enzyme complex hydrolyzed after binding the nucleophile.⁶³ These three parameters are composites of parameters derived from the rate constants and equilibrium constants in the kinetic scheme described by Svedas *et al.*⁶³ In fitting our initial rate

experiments, only β_0 was found to be a function of pH value. Of α , β_0 , and γ , only β_0 depends on the binding of 6-APA, which Figure 3.5a shows is a function of pH value. The parameter values we determined for Assemblase® and those Svedas *et al.* determined for PGA from *E. coli* are summarized in Table 3.2.⁷⁷ Our enzyme has better affinity for PGME over ampicillin (captured by α ; high α values desirable), which will slow secondary hydrolysis compared to primary hydrolysis and synthesis, it more strongly binds 6-APA at comparable pH values (captured by β_0 , high β_0 values desirable), which will decrease rates of primary hydrolysis, and it is slightly less likely to hydrolyze the acyl-enzyme complex once 6-APA binds (captured by γ , low γ values desirable), which will slow hydrolysis.

Table 3.2 Comparison of Assemblase® and the *E. coli* PGA used by Svedas *et al.* (pH 6.4 only) at 298 K.⁷⁷ Assemblase with the other antibiotics studied in the course of this thesis are also reported with discussion at the end of the chapter.

Enzyme	Antibiotic	α [-]	β_0 [M ⁻¹]							γ [-]
			pH:	5.7	6.4	7.1	7.8	8.5	9.2	
Assemblase	ampicillin	3.9	160	120	62	38	27	18	0.038	
<i>E. coli</i> PGA	ampicillin	2.3	60						0.056	
Assemblase	amoxicillin	4.6	210	140	94	63	41	27	0.122	
Assemblase	cephalexin	8.9	370	240	160	110	71	47	0.020	

Additionally, Figure 3.5b shows that the initial synthesis-to-hydrolysis ratio also depends on pH value, with slightly acidic conditions favoring synthesis. Higher concentrations of reactants in equimolar amounts also resulted in higher initial synthesis-to-hydrolysis ratios $[V_s/V_h]_0$. However, a more basic pH value does not hamper the secondary hydrolysis of ampicillin, indicating the nucleophilic attack by 6-APA on the acyl-enzyme complex is not pH-dependent. These results reaffirm the trend in Figure 3.5a,

that the binding of 6-APA to the acyl-enzyme complex (but not the nucleophilic attack itself) is pH-dependent, with more basic conditions discouraging binding of 6-APA. The selectivity of the initial reaction is therefore improved in slightly acidic conditions, however, since synthesis and secondary hydrolysis both scale similarly with pH value, the issue of integral selectivity goes unaddressed by pH modulation.

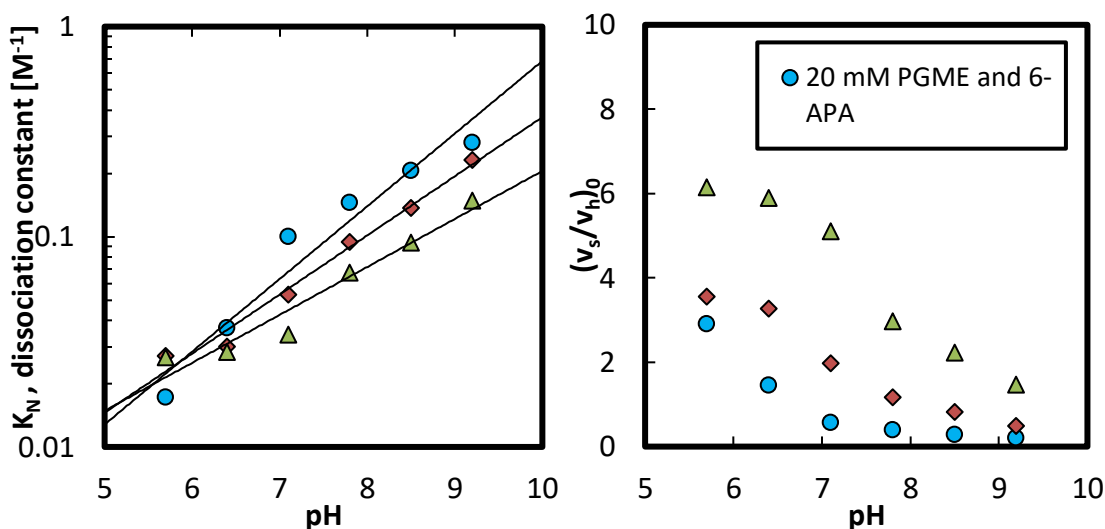


Figure 3.5. The 6-APA dissociation constant at three different reactant concentrations (left) and the initial synthesis-to-hydrolysis ratio at three different reactant concentrations (right). The dissociation constant should not be concentration dependent, but it is confounded by the competing and binding of 6-APA to free enzyme and 6-APA to acyl-enzyme complex.

3.3.3 Improved process model

As expected from the stoichiometry (formation of an acid, phenylglycine, from an ester, PGME), the pH value of the reactor dropped during the course of the reaction. Because the activity of the enzyme decreases as the pH value decreases in the range of pH 7.8 to 5.7, the pH value of the three different initial conditions decreased by different amounts, with the highest initial pH decreasing the most. This drop in pH value appears to be beneficial to the process: as the reactants are consumed the selectivity of the enzyme

increases. A representative pH profile is shown in Figure 3.6. Here, the reactant concentrations were increased to 160 mM and the reaction time was extended to better illustrate the pH change behavior. The initial increase in pH value corresponds to the consumption of 6-APA, an acid, but is quickly overtaken by the production of phenylglycine. The small disturbance at approximately 180 minutes is the result of crystallization of ampicillin (this system was initially unseeded) and the sudden depletion of ampicillin supersaturation slightly increased the pH value. This behavior was predicted by the model but is only found at concentrations high enough to spur primary nucleation; we mainly worked below these concentrations to avoid issues with 6-APA solubility.

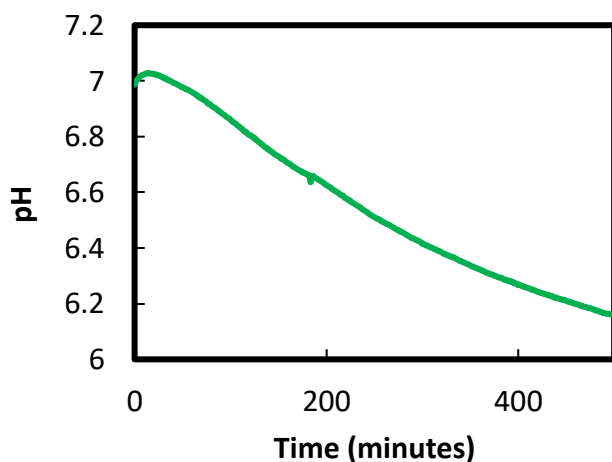


Figure 3.6. The pH profile of a typical reaction is illustrated in a system at equimolar initial concentrations of 160 mM to highlight the decrease in pH value with increasing conversion.

The strong influence of pH on synthesis and hydrolysis reaction rates has not been quantified nor modelled in previous work. The strength of the Svedas *et al.* model lies in its ability to describe the selectivity of the system accurately using only three fitted parameters, α , β_0 , and γ , as defined above.⁹⁴ Integrating this model to determine concentrations as a function of time, which is necessary for predicting crystallization, requires fitting eight parameters: K_S , K_P , K_N , k_2 , k_3 , k_4 , k_{-4} , and k_5 . The significance of each parameter can be seen in Figure 3.7. This model, which is currently the most adept at

describing this system based on known mechanism and first principles (as opposed to bypassing mechanistic arguments with computational methods such as neural networks),⁸³ ⁹⁵ requires refitting the kinetic parameters for every pH value. Since the reaction causes a change in pH (unless sufficiently buffered), the Svedas *et al.* model is only applicable to pH-stated systems. Operating at constant pH, however, may not provide the best yield and results in the additional formation of salts that need to be discarded.⁸⁷

We have found that two protonation/deprotonation reaction equilibria are necessary to describe the enzyme activity towards synthesis, primary, and secondary hydrolysis and that 6-APA binding (and therefore β_0) is a strong function of pH value. In Figure 3.7 we show the reformulated model. We introduced acidic and basic reactions between the acyl-enzyme complex (EAH) and protonated and deprotonated forms of the acyl-enzyme complex (EAH₂⁺ and EA⁻). The reaction cannot move forward from the protonated and deprotonated forms. While there may exist several additional pH-dependent protonation and deprotonation reactions, these two were sufficient to describe the experimental system. The relationship between the 6-APA dissociation constant (K_N) and pH value could be approximated as exponential in slightly acidic conditions that solubility already dictates we operate in. The model therefore defined β_0 as a function of pH in accordance with the exponential estimate.

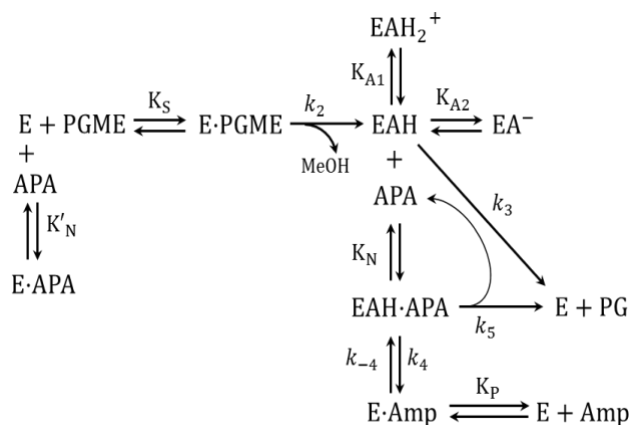


Figure 3.7. The improved kinetic scheme for DSM-Sinochem Assemblase®. Two pH-dependent equilibria have been added to the EAH form of PGA (top right). Abbreviations: E is free enzyme, EAH is acyl-enzyme complex, EAH_2^+ and EA^- are inactive forms of the acyl-enzyme complex, $\text{E}\cdot\text{PGME}$, $\text{E}\cdot\text{APA}$, $\text{EAH}\cdot\text{APA}$, and $\text{E}\cdot\text{Amp}$ are enzyme bound PGME, enzyme bound 6-APA, acyl-enzyme complex bound 6-APA, and enzyme bound ampicillin, respectively. PG is

Additionally, secondary hydrolysis by the enzyme was competitively inhibited by 6-APA (see Figure 3.4), motivating the addition of another equilibrium between free enzyme and 6-APA bound acyl-enzyme complex (not to be confused with the desired binding of 6-APA and acyl-enzyme complex). This addition has been proposed previously but lack of data and a small perceived influence had led to its elimination by previous authors in favor of a computationally simpler model.⁸⁰

Ampicillin crystallization kinetics from previous studies indicate that crystallization is significantly faster than the reactions when the enzyme is sufficiently dilute.^{88, 89} With the assumption that ampicillin crystallization is much faster than ampicillin synthesis, our model partitions the system into a solution phase and solid phase and assumes that significant supersaturation is never generated. This assumption negates the occurrence of primary nucleation; Encarnación-Gómez *et al.* showed that large supersaturation is needed for primary nucleation, especially in the presence of 6-APA.⁴¹ However, when seed crystals are present, as in our study, they can grow and participate in secondary nucleation.

3.3.4 Reactive crystallization experiments

Ampicillin was synthesized at 298 K and three different initial pH values: 6.00, 6.35, and 6.75. Experiments were initiated with equimolar amounts of PGME and 6-APA. The concentration of each reactant for all experiments was chosen to be 85 mM, the saturation concentration of 6-APA at pH 6. The initial concentration of ampicillin was chosen to be 35 mM to simulate an initial conversion of 30% (from an initial concentration of 120 mM). At this conversion solid ampicillin is present and thus the need for crystal seeding is avoided. The initial addition of ampicillin is justified because at low conversions the ampicillin has not yet reached saturation and therefore, in a batch process, both the reactive crystallizer and homogeneous reactor follow the same dynamics. In the reactive crystallizer, solid ampicillin represents approximately 13%, 7%, and 2% of the initial ampicillin present at pH 6.00, pH 6.35, and pH 6.75, respectively. These correspond to initial supersaturations ($S = C/C^*$) of 1.15, 1.07, and 1.02 in the homogeneous reactor.

Figure 3.8 shows the course of ampicillin production for the control reactor and reactive crystallizer. The data begin at 25 minutes because the results of the first 25 minutes are simulated by the initial ampicillin addition. The reactive crystallizer shows higher final concentration of ampicillin and lower final concentration of phenylglycine. Figure 3.8 also demonstrates the robustness of our model; the solid curves represent predictions based on integrating initial rate data and they match the observed concentrations remarkably well. The increased conversion (see equation 3.3) of reactive crystallization can be seen in the steeper PGME consumption curve at longer times. The enhanced process selectivity of reactive crystallization can also be seen in the relative final ampicillin and phenylglycine concentrations.

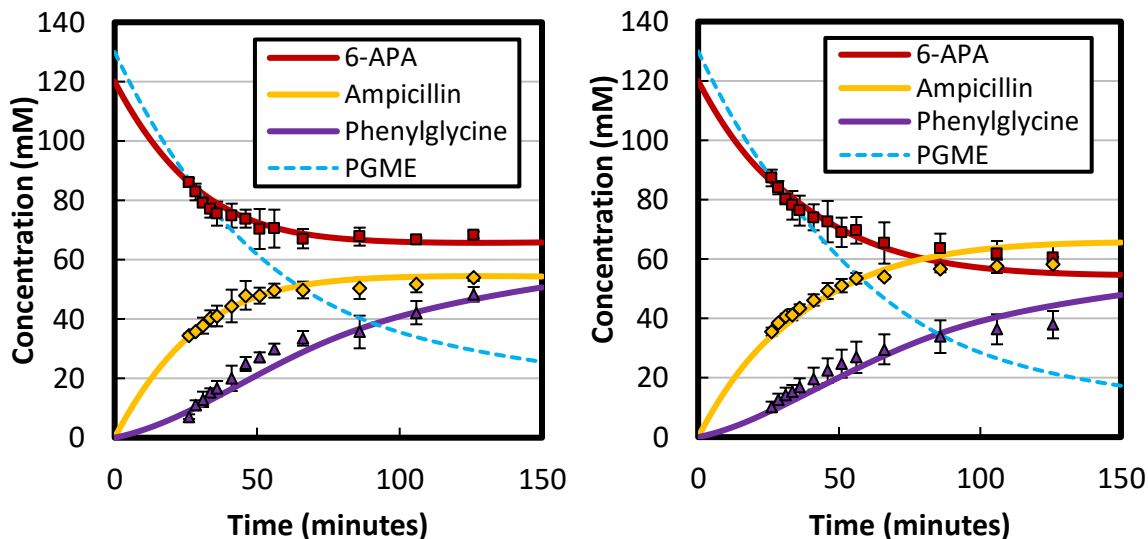


Figure 3.8. The reaction course for the control reactor (left) and reactive crystallization scheme (right) at a pH value of 6.75. Error bars are one standard deviation, $n = 5$. Lines represent model predictions based on initial rate data. PGME concentration was not directly measured but can be determined via a mass balance. These profiles are representative of the concentration profiles obtained at all three initial pH values.

The overall process selectivity is increased by reactive crystallization. Figure 3.9 shows how the process selectivity is increased by nearly 50% at all three initial pH values tested. Additionally, the solid lines, again representing the model predictions based on initial rate data, predict the increase in selectivity relatively well. The increase in selectivity in the reactive crystallizer over the homogeneous reactor is due to the reduction in secondary hydrolysis—which both degrades ampicillin and forms phenylglycine—by crystallization. These data support our hypothesis that crystallization can be used to isolate the reactive intermediate in the enzymatic reaction pathway. The increasing selectivity with decreasing pH value matches what is expected from the increased enzymatic selectivity, which is enhanced by slightly acidic conditions, a consequence of the acidity dependence of enzyme-6-APA binding.

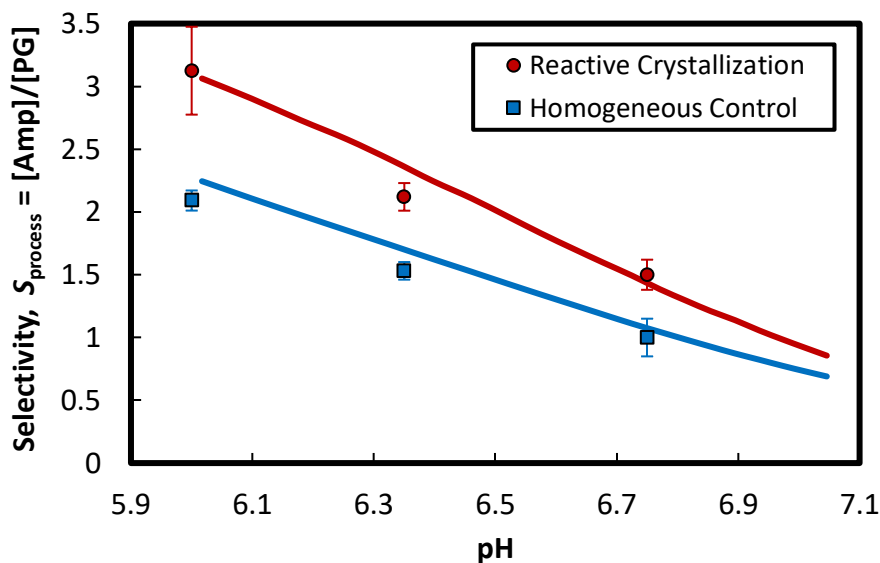


Figure 3.9. The selectivity of the reactive crystallization process is compared to the homogeneous reactor. The selectivity is defined as the total amount of ampicillin formed over the total amount of phenylglycine formed. The solid lines represent model predictions based on initial rate data. The error bars are one standard deviation.

The yield (see equation 3.4) is maximized (Y_{\max}) when the ampicillin concentration is highest which occurs when the rates of synthesis and secondary hydrolysis are equal. It would not be desirable to operate the process to reach Y_{\max} because of diminishing returns of ampicillin with respect to the amount of phenylglycine being produced. However, Y_{\max} is still a valuable means to evaluate the process, especially because there exists a theoretical maximum determinable using the parameters α , β_0 , and γ previously discussed. Gololobov *et al.* derived the following expression for Y_{\max} and determined it was valid for papain (a cysteine protease with a similar mechanism to PGA) when the initial amount of acyl-donor was greater than or equal to the initial amount of nucleophile (n_0 in equations 3.6 and 3.7).⁹⁶

$$Y_{\max} = \frac{\beta n_0}{\alpha} \left(\frac{\alpha}{1 + \beta n_0} \right)^{\left[1 - \frac{\alpha}{1 + \beta n_0} \right]^{-1}} \quad (3.6)$$

$$\beta = \left(\frac{1}{\beta_0} + \gamma n_0 \right)^{-1} \quad (3.7)$$

Applying the relation above to our system yielded good agreement between the homogeneous control experiments and the theoretical maximum (the center two columns in Table 3.3). Reactive crystallization broke the theoretical maximum, increasing the maximum yield by nearly 10% at lower 6-APA concentrations and more than 20% at the higher 6-APA concentration (both with initial pH value of 6.75). The increase over the theoretical maximum is caused by the decreased rate of secondary hydrolysis.

Table 3.3. The maximum yield of ampicillin compared between the theoretical maximum, the control homogeneous experiment, and the reactive crystallization setup. The initial pH value is 6.75 and the reactants are equimolar.

Conditions	Y_{\max} theoretical (eqn. 6)	Y_{\max} control experiment	Y_{\max} reactive crystallization
$n_0 = 120$ mM	0.449	0.451	0.486
$n_0 = 240$ mM	0.540	0.500	0.665

Aside from the limits of reactant solubility at lower pH value, operating below neutral conditions seems to be highly favorable. However, there is a tradeoff with productivity as the pH value decreases. The activity of the enzyme, towards both synthesis and hydrolysis, decreases considerably below pH value 5.5. Figure 3.10 shows that the productivity has a maximum around pH value 6.5. This is the consequence of not tolerating phenylglycine supersaturation to guarantee product purity. We have defined the characteristic time for the productivity as the time until phenylglycine reaches saturation. Therefore, the optimal productivity balances the lower enzyme activity at low pH value with the lower selectivity at high pH value. As the plots in Figure 3.10 reveals, the model

appears to underpredict the productivity of the homogeneous system. One possible explanation is that the model in fact underpredicts the productivity (τ) of both systems, but only appears to underpredict the homogeneous system because in measuring the concentration of the reactive crystallization system a well-mixed, representative sample must be withdrawn for HPLC, and it is possible that crystals have settled despite mixing with a magnetic stir-bar. The data appear to follow the same trend as the model; however, the large error bars prevent us from confirming this finding. We can conclude that reactive crystallization slightly boosts the productivity at these reaction conditions.

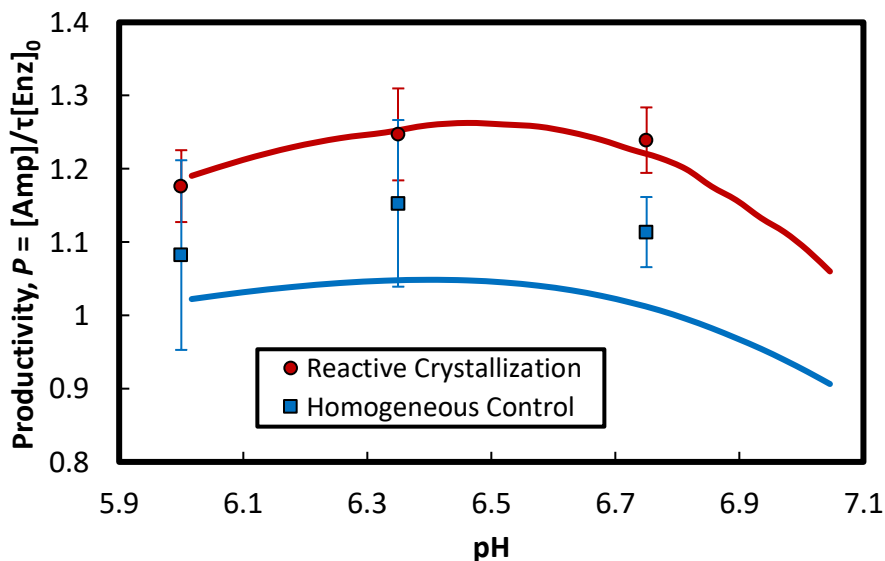


Figure 3.10. Productivity of the reactive crystallization process is compared to the homogeneous reactor. The solid lines represent model predictions. The error bars represent one standard deviation.

We have already shown that increasing reactant concentration can increase the synthesis to hydrolysis ratio. However, there is also evidence that increasing the reactant concentrations will increase the benefit of reactive crystallization since increasing the concentrations speeds-up the reaction but leaves solubility unchanged. This results in the same amount of ampicillin being subject to secondary hydrolysis regardless of initial

conditions. The effect of this can already be seen in Y_{\max} . The benefit of increasing concentration of PGME and/or 6-APA is expected to be seen in both selectivity and productivity as well.

3.4 Ampicillin summary

Reactive crystallization can be employed to increase the selectivity of ampicillin. The increased selectivity for ampicillin results from the decreased secondary hydrolysis of ampicillin because the enzyme cannot degrade the solid ampicillin. Different enzymes also have different propensities for synthesis versus hydrolysis; Assemblase® from DSM-Sinochem, compared to previous studies of PGA from *E. coli*, has greater PGME/Ampicillin affinity by approximately 70%, stronger nucleophile binding by 100%, and lower acyl-enzyme bound 6-APA hydrolysis by 60%. Using Assemblase® for both reactive crystallization and homogeneous reaction, the selectivity is increased by approximately 50% in the reactive crystallization scheme over the conventional liquid-phase-only reactor. The yield with reactive crystallization is also improved by more than 20% over the theoretical maximum that does not consider isolating the product from secondary hydrolysis. The productivity is also higher with reactive crystallization, although only by 10-20% at our reaction conditions. The selectivity is highest at initial pH value 6.0, the lowest pH value tested, however, the productivity peaks around initial pH value 6.5. The pH sensitive model, regressed only with initial rate data, is capable of accurately predicting concentration profiles for non-pH-stat batch reactions at any degree of conversion. By separating the reaction into a solid and dissolved phase the model also accurately predicts the behavior of reactive crystallization of ampicillin, including the increase in selectivity. The pH value is shown to influence the activity of the enzyme as

well as the binding of the β -lactam 6-APA to the acyl-enzyme complex. Our model predicts and the experiments confirm that reactive crystallization presents a more efficient means than reaction in liquid-phase-only to produce ampicillin and possibly other β -lactams.

3.5 Other beta-lactams

So far, this chapter has focused on elucidating the mechanisms of PGA and the interplay of the enzyme-catalyzed reaction with the sequestration of ampicillin in the solid phase. Parameters to model the reaction were determined for the ampicillin system. Later the same parameters were determined for cephalexin by the same techniques, and for amoxicillin by analyzing published data with this new model. Figure 3.11 shows the inhibition of cephalexin hydrolysis by 7-ADCA, in the same fashion as Figure 3.4 showed ampicillin hydrolysis inhibited by 6-APA. Comparing the two figures shows that this variant of PGA has a stronger affinity for 7-ADCA than 6-APA, as the reaction is arrested more by 7-ADCA than 6-APA. Using the same techniques as described for ampicillin the α , β_0 , and γ grouped parameters were determined for cephalexin and are reported alongside those for ampicillin in Table 3.2.

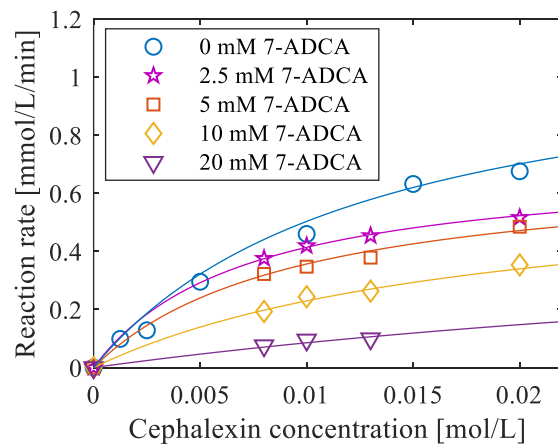


Figure 3.11. The initial rate of cephalixin hydrolysis at different initial antibiotic concentrations and 7-ADCA concentrations.

For amoxicillin, sufficient published synthesis data exist for Assemblase® to determine parameter values. It helps that amoxicillin and ampicillin use the same nucleophile, 6-APA, and therefore have considerable overlap in their respective parameter values. These values will be used in later chapters for the design and evaluation of a CM process.

CHAPTER 4. KINETICS OF CEPHALEXIN CRYSTALLIZATION WITH CO-SOLUTES³

4.1 Introduction

Scale-up of end-to-end CM in the pharmaceutical industry requires detailed knowledge of the mechanism and kinetics of each phenomenon in the process. Crystallization has been used to purify the active pharmaceutical ingredient (API) in most published end-to-end CM studies.^{9, 12, 21, 97, 98} So far, published end-to-end CM crystallization studies have been at the lab scale, where space-time yield is a low priority. Sustainable production of large-scale APIs such as amoxicillin and cephalexin requires optimization of space-time yield while maintaining product attributes such as crystal size and shape, which necessitates comprehensive understanding of crystallization kinetics. Cephalexin crystallization kinetics were determined before amoxicillin, as cephalexin enzymatic reactive crystallization is especially challenging due to the potential for phenylglycine precipitation. Amoxicillin on the other hand does not have to be as exactly optimized, as 4-hydroxy phenylglycine is unlikely to contaminate the product, and therefore estimates of the crystallization kinetics, based on similar molecules, should be sufficient for the CM pilot plant.^{89, 99} While there are few data on cephalexin crystallization in the literature, studies published on similar β -lactams, such as ampicillin,

³ Adapted with permission from “[McDonald, M.A.](#); Marshall, G.D.; Bommarius, A.S.; Grover, M.A.; Rousseau, R.W. Crystallization Kinetics of Cephalexin Monohydrate in the Presence of Cephalexin Precursors. *Crystal Growth & Design* **2019**, *19*, 5065-5074.” Copyright 2019 American Chemical Society.

have focused on kinetics in pure systems that do not reflect the purification needed in real crystallization processes.^{88, 89}

Crystallization kinetics depend on the presence of other species as well as the process conditions.¹⁰⁰⁻¹⁰² To address this issue, in this study cephalexin monohydrate is crystallized in the presence of two other species found in the enzymatic synthesis of cephalexin: the reactants 7-aminodesacetoxycephalosporanic acid (7-ADCA) and D-phenylglycine methyl ester (PGME).^{21, 32, 63} Based on the chemistry of cephalexin, 7-ADCA, and PGME, this research provides insights into the mechanism of crystallization and the incorporation of impurities. The mechanistic understanding of crystal growth inhibition could simplify the evaluation of other co-solutes on the crystallization of cephalexin or other β -lactam antibiotics. Online process analytical technologies (PAT) are employed to monitor and help determine crystallization kinetics.^{89, 103, 104} Use of extensive PAT in a batch experiment can simplify the translation of PAT tools to a continuous process.^{105, 106} Additionally, the impact of mixing intensity is explored to inform decisions on how a continuous operation could be implemented.

4.2 Materials and Methods

4.2.1 Nucleation and growth of crystals

Experiments began with 75 mL of deionized water in a Mettler-Toledo OptiMax 1001 workstation with a 250-mL capacity vessel (inner diameter 62 mm, liquid height approximately 45 mm) controlled to 25.0 °C. A 40-mm diameter, 9.0 mm high, 4-blade stainless-steel impeller with blades inclined at 45° was suspended 8 mm above the reactor bottom. A temperature probe, pH meter, Mettler-Toledo G400 focused beam reflectance

measurement (FBRM) probe, and Mettler-Toledo ReactIR iC10 attenuated total reflectance Fourier transform infrared (ATR-FTIR) probe, created significant baffles in the reactor and recorded their respective measurements. The stir rate was varied from 200 to 800 rpm, resulting in Reynolds numbers, Re , ranging from 5,000 to 21,000. Background spectra of water were collected for 10 minutes, then the non-crystallizing co-solutes, either 7-ADCA (TCI America, Portland OR) or PGME (Sigma-Aldrich, St. Louis MO), were added at the desired concentration and dissolved, and a second background was collected for 10 minutes. Cephalexin monohydrate (TCI America, Portland OR) was dissolved in known increments, to create a new ATR-FTIR concentration calibration curve at the start of each experiment. The solubility of cephalexin, a zwitterion, depends on pH; sodium hydroxide (Sigma-Aldrich, St. Louis MO) was used to adjust the pH to 7.6 ± 0.2 to dissolve the cephalexin. Complete dissolution was verified online with FBRM. Supersaturation was generated by adjusting the pH by dosing 2 M hydrochloric acid (Ricca Chemical, Arlington TX) at a rate of 0.3 pH units per minute with a Mettler-Toledo SP-50 Dosing Unit. Crystallization occurred under isothermal and constant volume conditions (primary nucleation occurred after addition of acid) and was observed for 2-6 hours, depending on the primary nucleation induction time (which is stochastic).

4.2.2 *Process analytical technology*

Infrared spectroscopy data were used to measure the concentration of cephalexin present in solution during the experiment. The difference in peak height between 1369 cm^{-1} and 1305 cm^{-1} (see supplemental Figure S1 for cephalexin IR spectrum) was found to correlate linearly with the dissolved cephalexin concentration, as shown in Figure 4.1. This

concentration measurement was independent of the PGME and 7-ADCA concentration after applying a baseline correction to remove the co-solute spectrum.

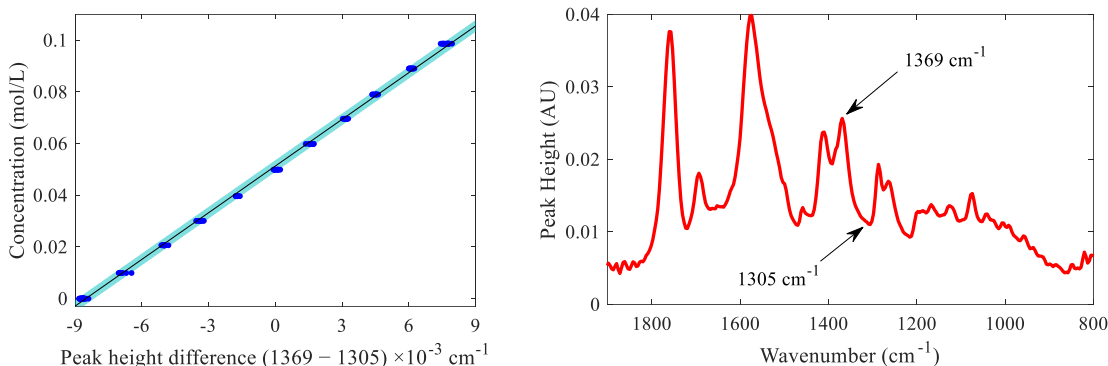


Figure 4.1. (Left) Calibration of cephalixin solute concentration with ATR-FTIR. The difference in IR intensity between the 1369 cm⁻¹ and 1305 cm⁻¹ is correlated with the molar concentration. Points represent measurements and the shaded region shows the 95% prediction interval based on the linear best fit.

FBRM data were used to measure crystal chord counts per second (‘counts’) and crystal chord length distributions (CLDs). In contrast to the robust concentration measurements, see Figure 4.1, previous studies have found counts and CLDs to be qualitative, which makes them useful for detecting nucleation and observing trends in suspension density but ill-suited to determining a true crystal size distribution (CSD).^{107, 108} To determine the efficacy of FBRM for this system, a simulated crystallization experiment was used to map crystal counts to the number density of crystals in suspension.^{109, 110} The details of the simulated crystallization are as follows; a suspension of crystals produced by the method previously described was incrementally added to a saturated solution of cephalixin and the resulting increase in FBRM counts was observed. The counts and suspension density do not linearly correlate, the counts saturate as the suspension density increases (see Figure 4.2, left). This observation has previously been termed the snowstorm effect where a flurry of small particles obscures the FBRM from

accurately sampling the crystal population. The rapid onset of the snowstorm effect at low weight fraction of solids was likely due to the needle-like morphology and small average size of the cephalexin crystals. A linear approximation of the count-suspension density relationship could be made below approximately 40,000 counts (2 g/L, approximately 10% of the final suspension density), where each count per second corresponded to approximately 1.5 ± 0.2 million crystals per liter. The FBRM was only used qualitatively because increases in crystallization extent did not result in significant increases in counts. The number density of crystals in suspension was estimated by image analysis with a hemocytometer counting chamber, Figure 4.2, right.

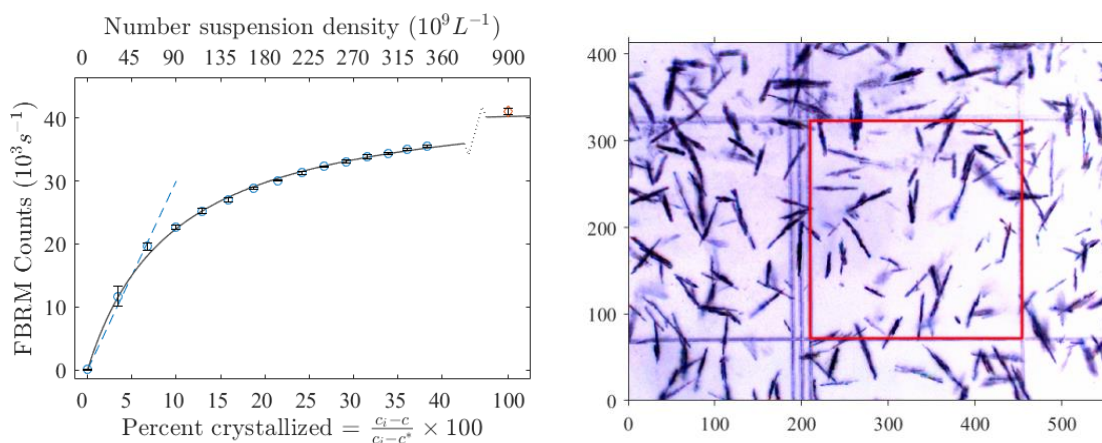


Figure 4.2. (Left) The number of crystals in suspension, as measured by extent of crystallization (bottom axis) and offline microscopy (top axis), was correlated with the number of chord counts observed online by FBRM. The FBRM counts were fit with a hyperbolic trend (solid curve) and initial linear trend (dashed line). Note the break in the axis for the final measured point. **(Right)** A 1/100 slurry dilution (in saturated solution) is shown. The area inside the red square has a volume of 6.25 nL and contains 51 crystals (counting those on the left and top borders but discounting those on the right and bottom borders). Using several images and randomly sampling different squares in the same image the total number density was determined to be 890 ± 89 billion crystals per liter for this sample. This image was sampled from the end of a batch of cephalexin with no co-solute and an initial supersaturation of 2.56.

The solids were best characterized by offline microscopy, using image analysis to directly measure a CSD. At the end of each experiment, samples of the suspension were

diluted in saturated cephalexin solution at the same pH and temperature and several microscope images were collected, giving the dimensions of thousands of individual crystals. A counting chamber with demarcated volumes was used to estimate the number suspension density, see Figure 4.2 for details. Image processing for CSD construction was conducted in MATLAB; Figure 4.3 shows an optical micrograph (left) and processed image (right). Objects with an aspect ratio greater than 3.5 (shown in green) were counted as single crystals and used to construct a number based CSD. Objects with an aspect ratio less than 3.5 (red) were assumed to be overlapping or clumped crystals and were therefore excluded from the CSD; individual crystals with an aspect ratio less than 3.5 may exist but must have formed by breaking of a larger crystal, a phenomenon not considered in this study. Objects on the border of the frame (blue) were discounted because their true size is unknown.

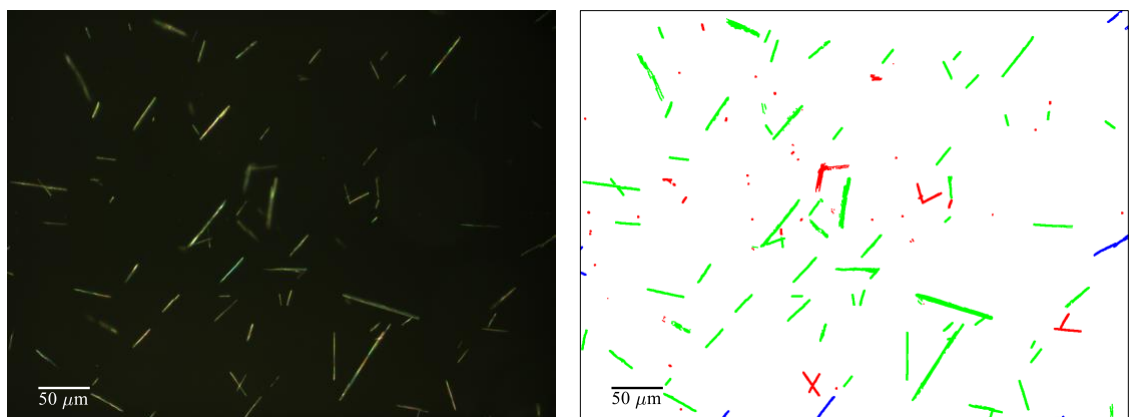


Figure 4.3. An optical micrograph of product cephalexin crystals (left) and the result of processing that image (right). Counted crystals in green, discounted overlapping crystals in red, and discounted cutoff crystals in blue.

High performance liquid chromatography (HPLC) was used to analyze samples offline. A gradient of 10 mM pH 7 sodium phosphate buffer and acetonitrile, starting at

100:0 buffer: acetonitrile and linearly decreasing to 40:60 buffer: acetonitrile over 10 minutes baseline separated 7-ADCA, cephalexin, and PGME in a 150 mm C18 reverse phase column.

4.2.3 Computational methods

The rate of primary nucleation was determined independent of secondary nucleation and growth. Being a stochastic process, primary nucleation was assumed to follow a Poisson distribution¹¹¹, where the rate of primary nucleation, J , was determined from the induction time distribution, F (equation 4.1). Here F is the cumulative fraction of experiments where primary nucleation occurred, V is the system volume, t is the induction time (time at which a crystal is detected), and t_G is the time required for a crystal nucleus to grow to a detectable size.¹¹²

$$F = 1 - \exp[-JV(t - t_G)] \quad (4.1)$$

The primary nucleation rate, J , depends on the supersaturation, $S = c/c^*$, according to equation 4.2, with a rate constant, k_J . The B_o term is related to the energy required to create the surface of a crystal nucleus.⁸⁸

$$J = k_J S \exp\left(\frac{-B_o}{\ln^2 S}\right) \quad (4.2)$$

After the induction time had elapsed the concentration was fit to a one-dimensional population balance model (PBM), shown in Equation 4.3, where n is the crystal population as a function of length, L , and time, t . The PBM was solved with the method of moments defined in equations 4.4 and 4.5, where μ_i is the i^{th} moment of the population, n .²¹ Crystal growth (G , equation 4.6) was assumed to be independent of size and unaffected by growth-rate dispersion. Dependence of growth rate on supersaturation was assumed to follow a

power law where the exponent, g , was constrained to be between 1 and 2, in accordance with the crystal growth theory of Burton, Frank and Cabrera.¹¹³ Secondary nucleation (B , equation 4.7) was modeled as a power law with respect to the growth rate, suspension density (M_T), and specific power input divided by kinematic viscosity (ε/ν); b , m , and p are the exponents on the growth, suspension density, and power input terms, respectively. A solute balance constructed within the method of moments framework and defined by equation 4.8 was used to couple cephalixin solute concentration and crystal growth.

$$\frac{\partial(n(L,t)V(t))}{\partial t} + \frac{\partial(n(L,t)G(t)V(t))}{\partial L} = (J(t) + B(t))V(t) \quad (4.3)$$

$$\frac{d\mu_0(t)}{dt} = (J(t) + B(t))V(t) \quad (4.4)$$

$$\frac{d\mu_i(t)}{dt} = i\mu_{i-1}(t)G(t) \quad (4.5)$$

$$G = k_G (S - 1)^g \quad (4.6)$$

$$B = k_B G^b M_T^m (\varepsilon/\nu)^p \quad (4.7)$$

$$\frac{dc}{dt} = -3\rho k_v G \mu_2 \quad (4.8)$$

The kinetic parameters were constrained to give physically meaningful values, summarized in Table 4.1.

Table 4.1. Parameter bounds used in constrained parameter fitting.

Parameter	Symbol	Lower bound	Upper bound
Growth rate pre-exponential	k_G	0	∞
Growth rate exponent	g	1	2
Secondary nucleation pre-exponential	k_B	0	∞
Secondary nucleation exponent	b	0	1
Suspension density exponent	m	0	2
Mixing power exponent	p	0	2

At the end of the crystallization, samples of the product crystals were taken and analyzed under a microscope. The number based CSD measured via image analysis was approximated by a lognormal probability distribution function, fit with the MATLAB function *lognfit*,

$$f(x) = \frac{1}{x\sigma\sqrt{2\pi}} \exp\left[\frac{-(\ln x - \bar{m})^2}{2\sigma^2}\right] \quad (4.9)$$

with parameters \bar{m} and σ .

Figure 4.4 shows the CSD calculated from the image in Figure 4.3. The gamma distribution¹¹⁴ and Weibull distribution¹¹⁵ were also investigated, however, the lognormal distribution provided the best fit (the residual sum of squares, RSS, was smallest for the lognormal, the values computed for the data in Figure 4.4 were $RSS_{lognormal} = 6.6$, $RSS_{gamma} = 18.9$, $RSS_{Weibull} = 53.2$). For determination of kinetic parameters, data from dozens of images were combined to produce a more robust CSD. The moments of the CSD were approximated from the lognormal distribution by the following equation.

$$\ln\left(\frac{\mu_i}{\mu_0}\right) = \bar{m}i + \frac{1}{2}\sigma^2i^2 \quad \forall i = 0, 1, \dots, N_\mu \quad (4.10)$$

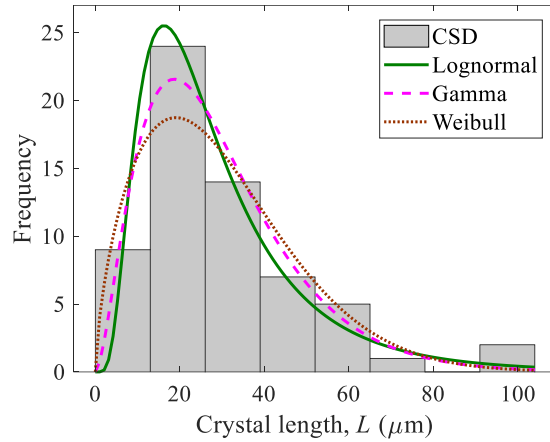


Figure 4.4. The number based CSD calculated from Figure 4.3. The CSD histogram was fit to a lognormal distribution (green solid curve), gamma distribution (pink dashed curve), and Weibull distribution (brown dotted curve).

The RSS was computed with Equation 4.11 where N_μ is the number of moments and N_y is the number of concentration measurements. The moments of the CSD, μ_i , were calculated from the lognormal fit of the CSD, and were compared to the moments fit with equations 4.4 and 4.5, $\hat{\mu}_i$. The measured concentration, y_j , was compared to the fit concentration \hat{y}_j . The logarithm rectified the difference in scale between moments and concentration.¹¹⁶ Fitting the CSD moments simultaneously with the concentration information, by minimizing RSS with the MATLAB function *fmincon*, proved to be more effective than using the FBRM counts in determining kinetic parameters.¹⁰⁷

$$\text{RSS} = \log \left[\sum_{i=0}^{N_m} (m_i - \hat{m}_i)^2 \right] + \log \left[\sum_{j=1}^{N_y} (y_j - \hat{y}_j)^2 \right] \quad (4.11)$$

4.3 Results and Discussion

4.3.1 Cephalexin monohydrate solubility

Solubility as a function of pH must be determined to develop a model of the nucleation and growth kinetics and the effects of additional solutes on crystallization. Figure 4.5 presents data showing the solubility, defined in this study as moles of cephalixin per liter of solution, over the pH range for which cephalixin is anionic and zwitterionic. Since enzymatic cephalixin synthesis is adversely affected by a low pH, solubility at more acidic pH conditions was not examined; nevertheless, the solubility is expected to increase as the solute takes on a positive charge. The solubility is a minimum at the isoelectric point, pI , and increases with increasing pH in proportion with the amount of anionic cephalixin, according to equation 4.12.⁹¹ The minimum solubility does not depend strongly on temperature, but the pK_a is a function of temperature leading to a solubility-temperature relationship captured empirically by equation 4.13.¹¹⁷

$$c^* = c_{pI}^* \left(1 + \frac{10^{-pK_a}}{10^{-pH}} \right) \quad (4.12)$$

$$pK_a = 14.6 - 1703/T - 0.018T \quad (4.13)$$

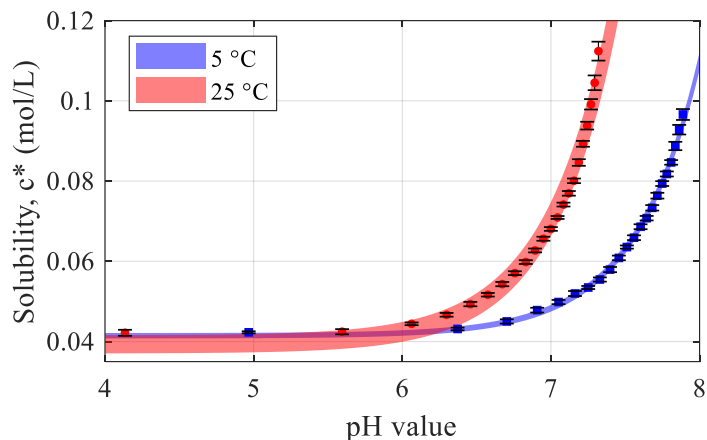


Figure 4.5. Solubility of cephalixin, in moles of cephalixin per liter of solution, as a function of pH at 5.0 °C (blue) and 25.0 °C (red) with 95% confidence regions based on fitting the data to Equations 4.12 and 4.13.

The solubilities in Figure 4.5 were obtained by crystallizing cephalixin as described in the methods, and then adding base to increase the pH and dissolve the product crystals. Once equilibrated (indicated by stable FBRM counts, temperature, and pH), the concentration was measured with ATR-FTIR. Dissolving the cephalixin as received by adding base in a controlled fashion produced an ATR-FTIR concentration curve that appeared to show solubility decreasing as the pH increased; however, decreasing FBRM counts showed that the crystals were in fact dissolving. As shown in Figure 4.6, powder x-ray diffraction (PXRD) confirmed that both the cephalixin as received and as crystallized are the same crystal form. The hydrophobic nature of the crystals, and their resulting tendency to collect at air-water interfaces, could explain the discrepancy between ATR-FTIR and FBRM data. The cephalixin as received initially adhered to the dry ATR-FTIR probe window, giving anomalous concentration measurements, while cephalixin crystallized in-situ did not adhere to or nucleate on the submerged probe.

Interestingly, 7-ADCA did nucleate on the ATR-FTIR probe window, which placed an upper bound on the 7-ADCA co-solute concentration. The solubility of 7-ADCA is also a function of pH and, at 50 mM and above, it crystallized concurrently with cephalexin. PXRD showed that crystals produced with 50 mM 7-ADCA had the same pattern as cephalexin but with two additional broad peaks at 6° and 13° corresponding to crystalline 7-ADCA. The peaks in the pattern did not shift, which suggested that the cephalexin did not contain a stoichiometric amount of 7-ADCA (i.e. formed a different crystal phase) but may have contained trace 7-ADCA impurities. The breadth of two 7-ADCA peaks could indicate the solid 7-ADCA phase has poor crystallinity or is present in small quantities. The simplest interpretation of these data is a physical mixture of two distinct solid phases; the desired cephalexin monohydrate and 7-ADCA. The solubility of PGME is at least two orders of magnitude greater than cephalexin or 7-ADCA and therefore it did not appear in the solids analyzed by PXRD.

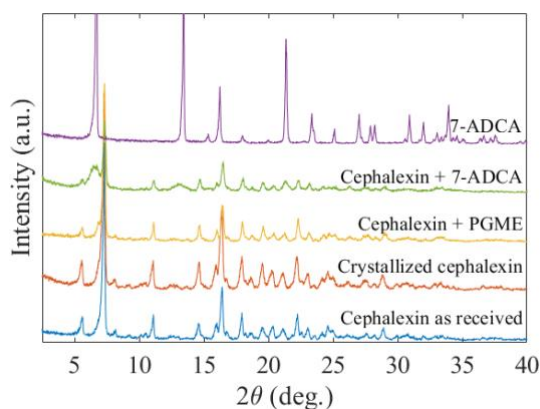


Figure 4.6. PXRD patterns for cephalexin as received (blue), crystallized without a co-solute (red), with PGME co-solute (yellow), with 7-ADCA co-solute (green), and PXRD pattern of 7-ADCA (purple).

4.3.2 Primary nucleation kinetics

Figure 4.7 shows the course of a typical experiment, which was comprised of three stages: the preparation stage (before time zero), the primary nucleation stage (from zero to the time at which crystals were detected by the FBRM), and the growth and secondary nucleation stage (after the detection time). During the preparation stage the solution was undersaturated and the FBRM confirmed a clear solution. The zero time point, $t = 0$, was the time at which the solution becomes saturated by the addition of acid. The primary nucleation phase began at $t = 0$ and continued until an inflection in the FBRM counts, shown in the inset in Figure 4.7, indicated that nucleation had occurred. Prior to nucleation, the FBRM counts were steady around zero; after nucleation detection, counts rapidly increased, followed after several minutes by a significant drop in supersaturation (as measured by ATR-FTIR). Shortly after nucleation detection, the counts saturated and useful information about crystallization could only be monitored in real time by ATR-FTIR.

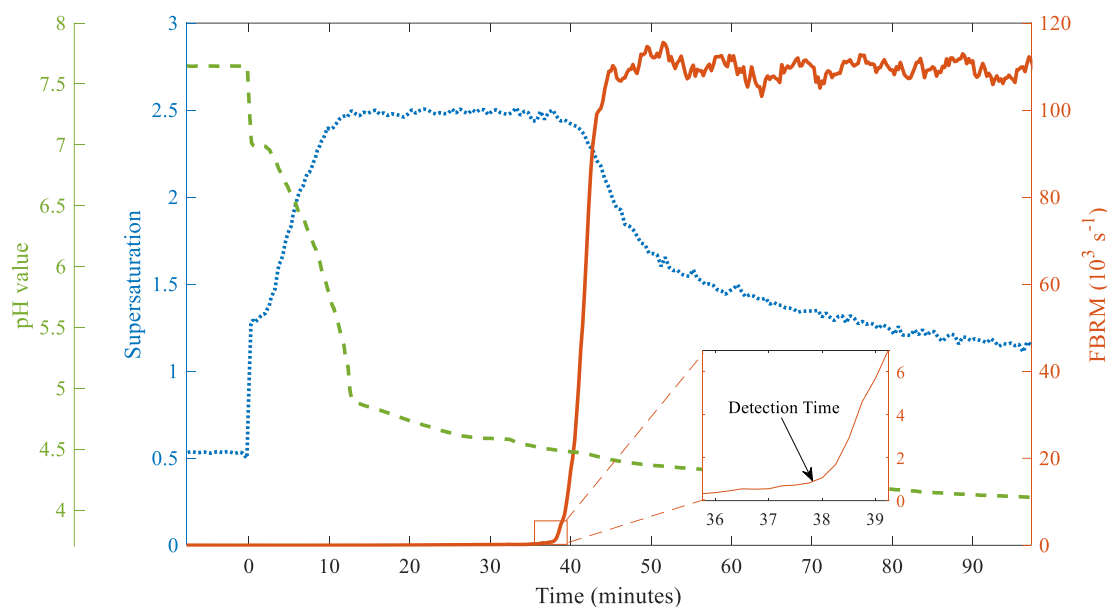


Figure 4.7. An example of pH trend (green dashed curve), saturation (blue dotted curve), and counts (red solid curve) during a typical batch cephalixin crystallization experiment. The inset shows FBRM nucleation detection in detail.

The primary nucleation detection time was independently measured 47 times, divided into three sets of experiments with different supersaturation: $S = 1.98$ ($n_{exp} = 13$), $S = 2.27$ ($n_{exp} = 11$), and $S = 2.56$ ($n_{exp} = 23$) where $S = c/c^*$.¹¹⁸ All primary nucleation experiments were conducted at 25 °C. Crystallization of cephalixin in the presence of 7-ADCA and PGME was conducted at a cephalixin supersaturation of $S = 2.56$, leading to a larger set for $S = 2.56$. The detection times at each supersaturation were sorted to create a cumulative distribution function and were fit to a Poisson distribution, from which the nucleation rate, J , at that value of S could be determined using equation 4.1. The time for a nucleus to grow to a detectable size, t_G , was fit simultaneously with J . Figure 4.8 shows the detection times for cephalixin crystallization without a co-solute (●) and cephalixin crystallization with 7-ADCA and PGME co-solutes (×). The fit to the Poisson distribution did not include experiments with co-solutes present. However, a Kolmogorov-Smirnov test

failed to reject the null hypothesis that the detection time distributions with and without the co-solute experiments sampled different underlying phenomena at the 95% confidence level. This finding, made visual by the fact that the detection times with co-solute were well interspersed within the pure cephalixin detection times in Figure 4.8, led to the conclusion that the co-solutes did not impact primary nucleation.

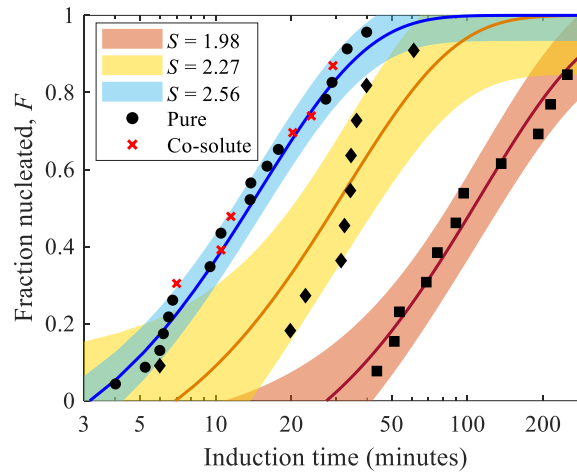


Figure 4.8. Experimental cumulative distribution functions of stochastic detection times, F , at three supersaturations: $S = 1.98$ (in red), $S = 2.27$ (in yellow), and $S = 2.56$ (in blue), were fit to Poisson distributions (curves) according to equation 4.1. The black points are experiments without a co-solute (squares $S = 1.98$, diamonds $S = 2.27$, and circles $S = 2.56$) and the red \times 's represent experiments with a co-solute ($S = 2.56$). The shaded regions are the 95% confidence regions based on the fit to equation 4.1.

The nucleation rates from Figure 4.8 were used to determine the primary nucleation prefactor (k_f) and exponential (B_o) by fitting the rates to equation 4.2. The exponential factor (B_o) is related to the energy required to create the new particle surface (γ) and the molecular volume of cephalixin (v) by equation 4.14.⁸⁸

$$B_o = \frac{16\pi v^2 \gamma^3}{3(kT)^3} \quad (4.14)$$

The molecular volume is $v = 4.32 \times 10^{-28} \text{ m}^3$, computed from the density (1.403 g/cm^3)¹¹⁹ and molecular weight (365.4 g/mol) of cephalexin monohydrate. The value of the energy required to create new surface area (determined from the value of B_o) can lend insight into growth and inhibition mechanisms (see below). Bootstrapping was used to construct confidence intervals from the small experimental sample set ($n_{exp} = 38$, with three different values of S); four experiments were randomly sampled at each supersaturation, and equation 4.2 was refit 200 times. Based on this analysis, the value of k_J (with 95% confidence interval) is 2.54 (1.39 9.00) and the value of B_o is 1.79 (1.28 2.88). The confidence intervals are asymmetric because the data are not normally distributed, instead the confidence interval was bound by the 2.5th and 97.5th percentiles (corresponding to $\alpha = 0.05$) of the bootstrap values of k_J and B_o , see Figure 4.9.¹²⁰ Based on this analysis, a cephalexin monohydrate nucleus has surface energy of $\gamma = 3.41$ (3.05 4.00) mJ/m² which indicates heterogeneous primary nucleation (i.e. on the crystallizer surface).¹²¹

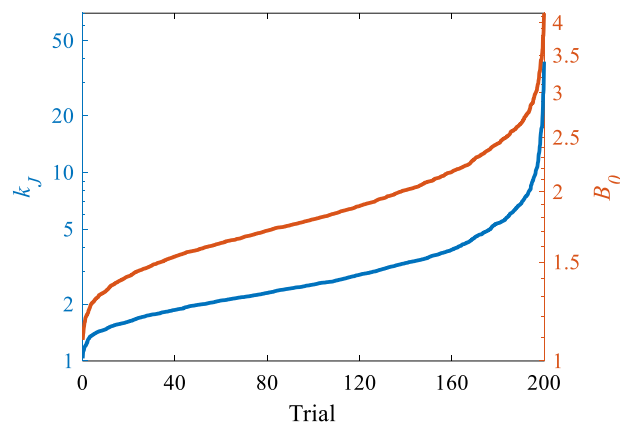


Figure 4.9. Bootstrapping was used to determine the primary nucleation parameters. In this figure the parameters that gave the best fit to equation 4.2 (for data randomly generated by taking four samples from each of three data sets at different supersaturation values) are sorted and plotted for 200 bootstrap trials. The confidence interval lies between the 2.5th and 97.5th percentile.

4.3.3 Secondary nucleation and mixing

Secondary nucleation, unlike primary nucleation, is assumed to be a deterministic phenomenon that can be empirically modeled with the power law in equation 4.7. The suspension density is related to the third moment of the crystal size distribution by equation 4.15, with crystal density ρ_c and crystal volume shape factor k_v , or can be calculated with a material balance for a batch crystallization, with molecular weight $M_w = 365.4$ g/mol, to avoid the need to determine a value for the shape factor.

$$M_T = \rho_c k_v \mu_3 = M_w (c_0 - c) \quad (4.15)$$

The specific power input, the (ε/v) term in equation 4.7, can be estimated from the Power Number (N_p), the slurry density (ρ_s), impeller rotational velocity (ω), diameter (D), and crystallizer volume (V), by equation 4.16.

$$\varepsilon = \frac{N_p \rho_s \omega^3 D^5}{V} \quad (4.16)$$

The Power Number for a 45° pitched four-bladed impeller in this reactor geometry and range of rotational velocities is 1.74.¹²² The values of m and p , the exponents on the suspension density term and specific power input term in equation 4.7, respectively, are related to the source of secondary nuclei: $m = 1$ implies secondary nucleation is predominately the result of crystal-impeller collisions or fluid shearing while $m = 2$ implies crystal-crystal collisions are most important. When $m = 1$, a value of $p = 1$ indicates crystal-impeller collisions contribute most to secondary nucleation while $p = 2$ indicates inertial eddies shear nuclei from existing crystals.¹²³ The stir rate was to be varied to determine the principal mechanism by which cephalixin secondary nuclei are bred, informing scale-up and adaptation to different reactor geometries, as well as strategies to manipulate the CSD. However, as will be discussed later, unique properties of cephalixin monohydrate

prevented investigation of a wide enough range of stir rates to determine the mechanism of crystal breeding.

Figure 4.10 is an optical photomicrograph of cephalexin monohydrate crystallized with 7-ADCA as a co-solute. It shows a population of cephalexin monohydrate crystals, all of which have a needle-like aspect ratio, but three have exceedingly high aspect ratios. A reasonable explanation for their size is they were formed from primary nucleation and, therefore, had significantly more time at an elevated supersaturation than those formed later in the process. Another hypothesis is that crystal breakage may play a role in reducing the population of large crystals; it is rational to assume that needle-like crystals are prone to breakage and that exceedingly long crystals should break more readily.⁵² This image, along with the fit values for the primary and secondary nucleation rates aligned with previous findings that secondary nucleation breeds several orders of magnitude more crystals than primary nucleation (Figure 4.10 right).¹⁰⁷

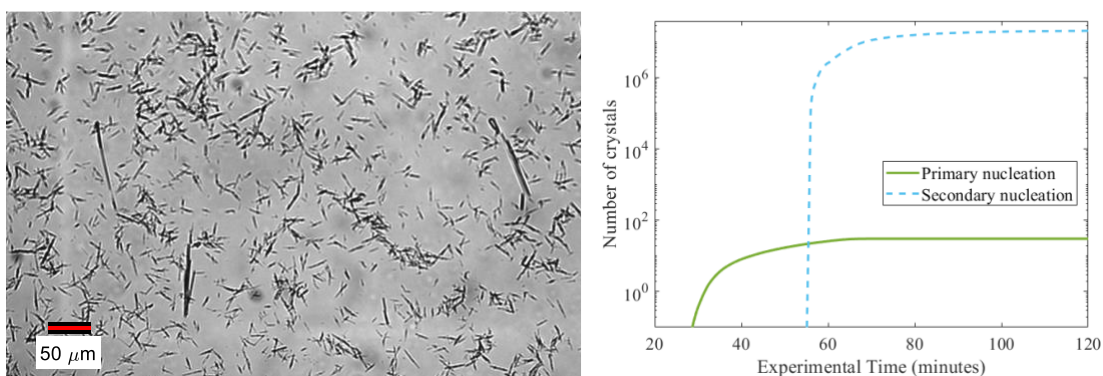


Figure 4.10. An optical micrograph of cephalexin monohydrate crystals formed in the presence of 7-ADCA co-solute (left) and a comparison of the number of nuclei created by primary nucleation and secondary nucleation based on fit parameters (right).

In the present work, secondary nucleation kinetics could be accurately determined only over a narrow range of stirrer speeds. At low rpm, crystals formed on probe surfaces

and then grew into the less turbulent regions surrounding the probe/baffle, creating a dead (poorly mixed) zone. The zone spread until only the region in immediate contact with the impeller was being mixed. The dead zones were detected by anomalous FBRM readings (see Figure 4.11) and were confirmed visually and with a tracer experiment that showed reduced volume. At high stir rates, the crystallizer also exhibited poor mixing due to the formation of stable foam on top of the slurry. These two phenomena limited the range of stir rates where crystallization kinetics could be precisely observed to the yellow region in Figure 4.12.

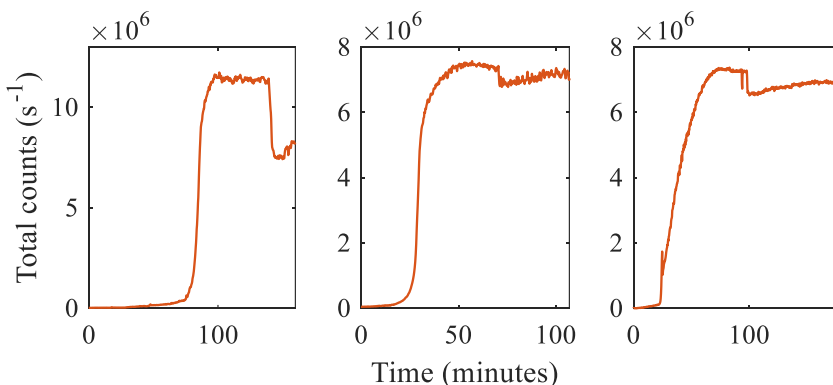


Figure 4.11. Three examples of anomalous FBRM readings suggesting that a dead zone had formed in front of the FBRM probe window at (from left to right) 140 minutes, 70 minutes, and 100 minutes. In all experiments, the counts followed an s-shape curve in time, eventually saturating when the snowstorm effect prevents the FBRM from detecting all crystals. In the experiments where a dead

zone formed, the counts rapidly drop, suggesting crystals had stopped moving in front of the probe window.

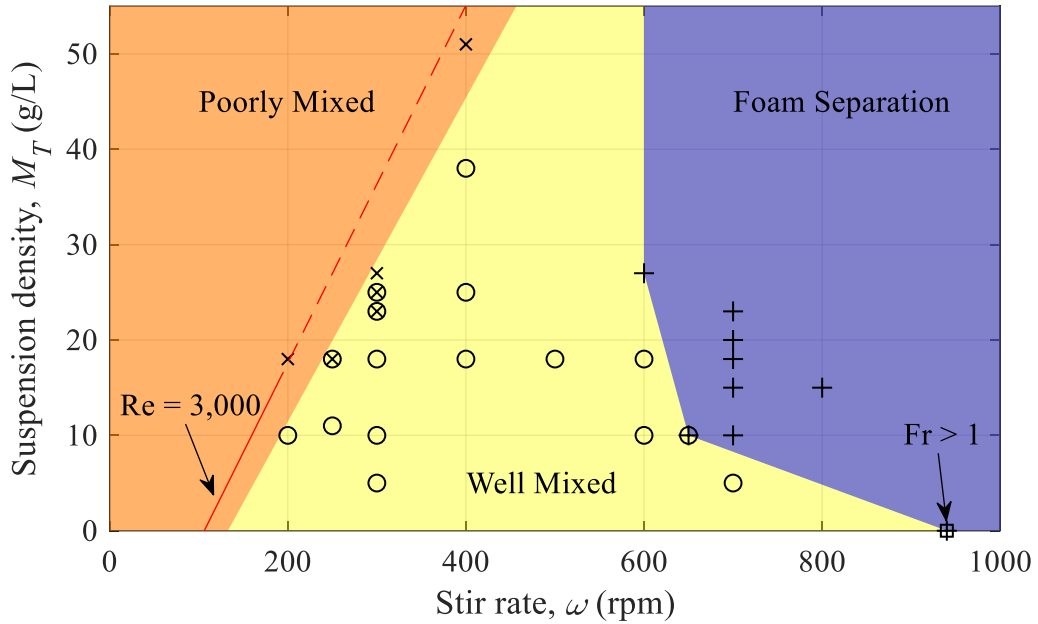


Figure 4.12. A mixing diagram for the crystallizer geometry used to determine cephalixin crystallization kinetics. Experiments marked with an open circle (○) were well mixed and were used to fit the kinetic model. Experiments marked with a cross (×) showed poor mixing and experiments marked with a plus (+) showed significant foaming.

In Figure 4.12, the boundary between the poorly mixed (orange) and well mixed (yellow) regions was linearly regressed with the cross (×) points; the boundary compares favorably with the theoretical boundary based on transition to turbulent flow as determined by the measured (solid red line) and extrapolated (dashed red line) Reynolds Number, Re , defined in equation 4.17.

$$Re = \frac{\omega D^2}{\nu} \quad (4.17)$$

At suspension densities as low as 1.5%, crystallization in a quiescent vessel led to a “sherbet-like” slurry that would not flow under force of gravity. Similar non-flowability

is observed in the non-mixed regions in low-rpm experiments. The non-flowability can be explained through the lens of yield stress; below a critical mixing intensity the slurry behaves as a solid, however above a certain stress the material yields and flows as a slurry. Formation of dead zones is a function of both rpm and solids concentration. Dead zones, where the stress due to mixing is below the yield stress, may be expected when the Reynolds number indicates predominately laminar flow ($Re < 3,000$);¹²⁴ however, the red line in Figure 4.12 shows the observed sherbet behavior occurred at Reynolds numbers greater than 3,000. The density used in equation 4.17 was calculated with the known solids fraction, using a measured liquid density of 1.005 g/mL for a saturated solution at pH 4.5 and a solid density of 1.403 g/mL. The viscosity was measured with a capillary viscometer, which was not practical for solids fraction greater than 1%. Measuring the viscosity of suspensions is difficult; the measured viscosity is an estimate useful for qualitative interpretation of the mixing results. A linear relation between solids fraction and viscosity was measured (kinematic viscosity, $\nu = 43M_r + 94$, measured in St and g/L) and used to construct the solid portion of the red line in Figure 4.12 and then extrapolated to higher solids fractions (dashed red line). Dead zones were accompanied by a decrease in the observed rate of desupersaturation, and experiments showing poor mixing behavior were excluded from the parameter fitting routine.

The boundary of the foaming (blue) region is the convex hull of the experiments that generated foam, with the zero suspension density point being determined with the Froude number, Fr. The foam generated at high stirrer speeds consisted of air bubbles and entrained mother liquor stabilized by the needle-shaped crystals. Engineered needle-shaped particles have been used to stabilize surfactant foams,¹²⁵ and the presence of the

crystals in the cephalixin system is critical to the foam stability. Foaming was only observed once crystallization began, and foam accumulated and did not collapse when mixing ceased; FBRM results showed a reduction in counts of nearly 30% which qualitatively indicated a significant amount of solids was sequestered in the foam, see Figure 4.13. The Froude number indicates formation of aerating surface vortices when Fr is of order unity; in Figure 4.12, $Fr = 1$ is indicated at $\omega = 930$, however the real transition is less well-defined than the abrupt change at $\omega = 930$. Fr, defined in equation 4.18 (where g_r is the acceleration due to gravity), predicted significant aeration at greater than 900 rpm, however Figure 4.12 shows significant foaming occurred at stir rates as low as 650 rpm (blue region). Foam forming experiments were also excluded in the parameter fitting routine, leaving a narrow window in which to operate (yellow region in Figure 4.12).

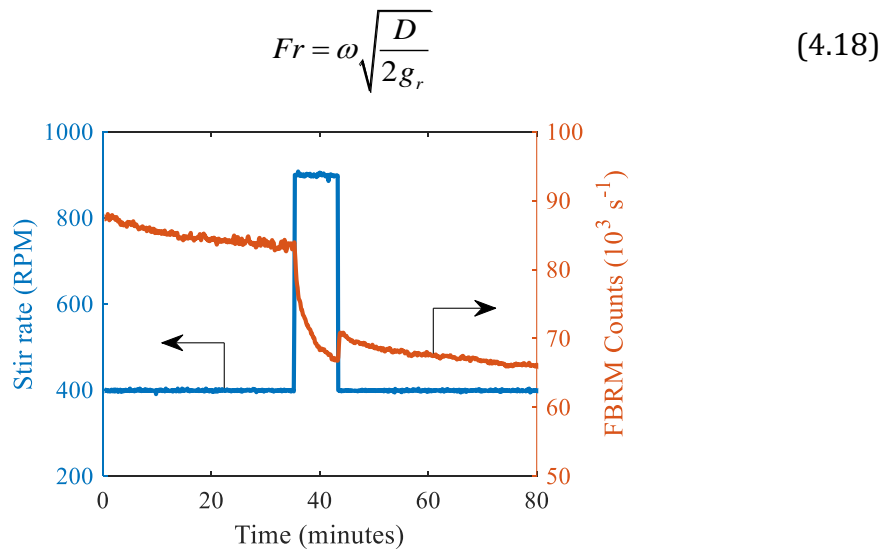


Figure 4.13. The stir rate (blue) was increased from 400 to 900 RPM for 5 minutes to generate a stable foam. The counts measured by FBRM (red) decreased during foam generation and did not

return after the stir rate was dropped back to 400 RPM, indicating crystals had been permanently sequestered in the foam.

Equation 4.7 assumes a power law relationship between stirring energy input ε and secondary nucleation rate, B , hence the need to examine a range of stirring rpm. Within the narrow range of well-mixed ω there was no obvious correlation between ε (as calculated with equation 4.16) and B . Therefore, the stir power input exponent, p , was set to zero to avoid overfitting the limited data. All further experiments were conducted at 400 rpm for consistency.

With $p = 0$ and no co-solute present, the secondary nucleation rate and growth rate were simultaneously fit (see the next section for discussion of growth rate). The secondary nucleation prefactor, k_B , had a value $2.98 \times 10^5 \text{ min}^{-1} \text{ L}^{-1}$ (95% C.I: 1.01×10^5 4.95×10^5). The secondary nucleation exponent, b , had a fit value of 0.99, which was not statistically different from $b = 1$. Since there is a theoretical justification for b to be unity,¹²³ b was set to 1 and a confidence interval was not calculated. The suspension density exponent, m , was found to be 0.46 (0.30 0.62). A value of $m < 1$ suggests secondary nuclei form from crystal-impeller collisions, but not all crystals breed nuclei upon impeller impact; perhaps only crystals of a certain size breed secondary nuclei in such events.

Since secondary nucleation is defined in terms of the growth rate (see equation 4.7), the effect of co-solutes on secondary nucleation was mathematically captured by the effect of co-solutes on growth rate, which are discussed in the next section. That the growth rate equation completely captured the co-solute dependence may indicate that secondary nucleation occurs by attrition of larger crystals,¹²⁶ however these data are too sparse to exclude other, less pronounced, effects of co-solutes on secondary nucleation, e.g. surface

nucleation.¹²⁷ In any case, the functional dependence of secondary nucleation and growth on supersaturation is empirical and appears to be the same.

In Figure 4.14 (left), the CSD is shown for pure cephalixin, with PGME (30 mM) as co-solute, and with 7-ADCA (30 mM) as co-solute. A Kolmogorov-Smirnov test (which is agnostic to the underlying distribution) failed to reject the null hypothesis that the measured CSD for pure cephalixin and measured CSD for PGME co-solute sampled different underlying distributions at the 95% confidence level. However, as is apparent from the yellow bars at long crystal lengths in Figure 4.14 (left), a Kolmogorov-Smirnov test rejected the null hypothesis (at the 95% confidence level) that the pure CSD and 7-ADCA co-solute CSD came from the same distribution. This result was repeated in several data sets. When fitting the experiments with 7-ADCA co-solute, the value of m (the suspension density exponent in equation 4.7) was consistently at the high end of the confidence interval determined for pure cephalixin monohydrate (0.30–0.62). Simulated experiments *in silico* showed that larger values of m result in wider spread CSDs. It is possible that the presence of 7-ADCA increased the sensitivity of secondary nucleation to the suspension density (i.e. increased m), however, there was no statistically significant difference between the values of m determined from fitting pure experiments and co-solute containing experiments. Therefore, it was concluded that co-solutes did not have a substantial impact on the kinetics of secondary nucleation (beyond the proportionality between B and G established in equation 4.7), especially when compared to the impact of co-solutes on the kinetics of crystal growth.

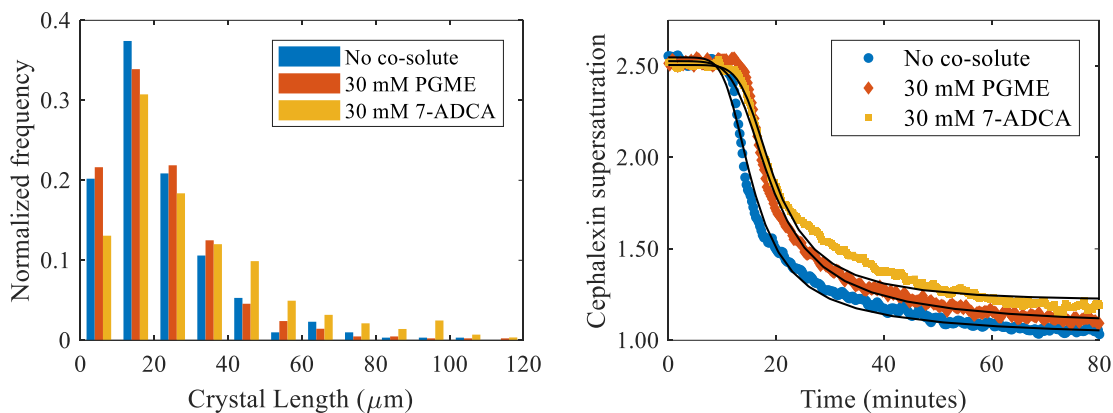


Figure 4.14. Left, the final CSD of cephalixin monohydrate without co-solute (blue), with 30 mM PGME co-solute (red), and 30 mM 7-ADCA co-solute (yellow). Right, the desupersaturation of cephalixin without co-solute (blue circle), with 30 mM PGME co-solute (red diamond), and 30 mM 7-ADCA co-solute (yellow square).

4.3.4 Growth kinetics

The different co-solutes had different impacts on crystal growth. Having determined that the co-solute impact on nucleation was negligible compared to the impact on growth (these two phenomena were determined simultaneously while fitting crystallization experiments with the PBM), the decrease in desupersaturation rate observed in the presence of co-solutes, particularly 7-ADCA, was the result of growth inhibition by the co-solutes. Two models of growth inhibition were considered, a competitive model based on co-solute and solute competing for surface adsorption sites,^{128, 129} and a step-pinning model based on adsorbed co-solutes impeding advancing growth steps.¹³⁰ Both models captured the decreased rate of desupersaturation, however only the step-pinning model accounts for the observed incomplete desupersaturation seen in the presence of co-solutes. In Figure 4.14 (right) the cephalixin supersaturation stopped decreasing at long times in the presence of PGME (red diamonds) or 7-ADCA (yellow squares), a behavior captured by the step pinning model of growth.

$$G = \begin{cases} k_G (S - S_{cr})(S - 1)^{g-1} & S > S_{cr} \\ 0 & S \leq S_{cr} \end{cases} \quad (4.19)$$

In the step-pinning mechanism of crystal growth inhibition, a modified growth rate, defined in equation 4.19, is used when the supersaturation is above a critical supersaturation, S_{cr} , and zero growth rate is used when the supersaturation is below S_{cr} . The critical supersaturation prevents the solution from completely desupersaturating. Figure 4.15 shows how the critical supersaturation increased as the concentration of each co-solute increased.

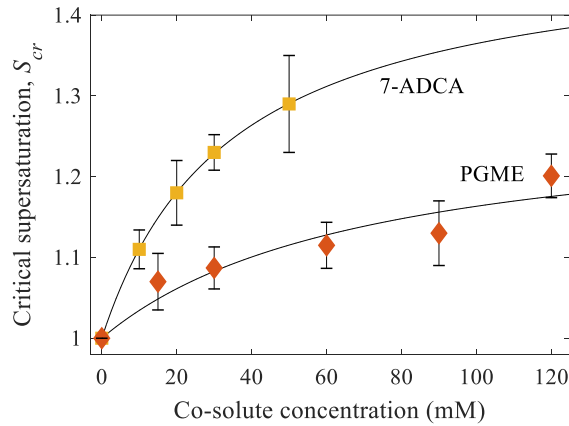


Figure 4.15. The critical supersaturation, S_{cr} , as a function of co-solute concentration. The lines are best fits of equation 4.20. The error bars are 95% confidence intervals.

The Langmuir adsorption isotherm was used to fit the dependence of the critical supersaturation on co-solute concentration because the step-pinning mechanism is based on co-solutes adsorbing onto the growing surface. The critical supersaturation depends on the energy required to create new cephalixin monohydrate surface, γ , the area of the growth unit, a , the average spacing between adsorption sites, l , the Langmuir equilibrium coefficient, K , and the concentration of co-solute, c_{cs} according to equation 4.20. Using the value of γ calculated from primary nucleation and the fit of S_{cr} in Figure 4.15, the ratio a/l

evaluated to approximately 1 (fit value of 1.15) for 7-ADCA and 0.5 (fit value of 0.61) for PGME, suggesting that 7-ADCA adsorption sites and cephalexin monohydrate growth units are equally spaced but PGME adsorption sites are spaced over every two growth units. 7-ADCA, containing both an acid and an amine group may be able to form hydrogen bonds with the cephalexin monohydrate crystal in two locations, while PGME, containing only an amine group, may only form a hydrogen bond with the growing crystal in one location. However this interpretation is not definite as there is substantial uncertainty surrounding the values of a/l , especially for PGME where the fit to equation 4.20 is poor (see Figure 4.15). PGME and 7-ADCA may also preferentially adsorb onto different crystal faces.

$$S_{cr} = \frac{\gamma a K c_{cs}}{k T l (1 + K c_{cs})} + 1 \quad (4.20)$$

The needle-like morphology causes a small crystal surface area (the faces on the ends) to account for the majority of desupersaturation. At high supersaturation, the strong adsorption of 7-ADCA onto the fast-growing faces suggests the possibility that 7-ADCA would be incorporated into the cephalexin monohydrate crystal; PGME on the other hand would not be expected to incorporate into the crystal to the same extent. PXRD did not show any peak shifts in the pattern for cephalexin crystallized with the 7-ADCA co-solute, indicating the 7-ADCA and cephalexin are not crystallizing together (as a co-crystal) in a distinct crystal lattice. HPLC analysis, shown in Figure 4.16, demonstrated that crystals produced with 7-ADCA co-solute contained 7-ADCA in proportion with the amount of initial 7-ADCA, even after washing with cold water. However, the amount of 7-ADCA was always less than 0.2% by weight of the final product after washing, indicating washed

crystals were of pharmaceutical quality. PGME was not detected in washed crystals produced with PGME co-solute.

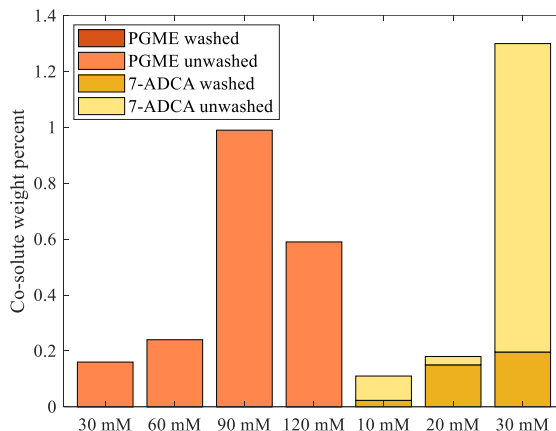


Figure 4.16. HPLC analysis of purity of unwashed (light hue) and washed (dark hue) cephalixin monohydrate crystals formed in the presence of a co-solute at different concentrations. The 50 mM 7-ADCA point was excluded because 7-ADCA also crystallized giving a physical mixture of solid 7-ADCA and cephalixin monohydrate (consisting of roughly 30% 7-ADCA). Washing consisted of suspending 250 mg of product cephalixin in 5 mL of cold water (<5 °C) and stirring for 15 minutes under chilled conditions.

4.3.5 Discussion of continuous manufacturing

All aspects of the design of an end-to-end CM process for cephalixin need to consider the crystallization kinetics of cephalixin monohydrate. The rate of primary nucleation is slow, even at considerable supersaturation, therefore the process should rely on secondary nucleation, either by recycling product crystals or using a well-mixed crystallizer. Secondary nucleation did not depend on the mixing intensity within the range of mixing intensities that were feasible for the studied crystallizer geometry. However, the stir rate was important because cephalixin monohydrate suspensions have a propensity to form poorly mixed “sherberts” with insufficient agitation and difficult-to-handle foams with excess agitation.

In the enzymatic synthesis of cephalexin, one of the parameters than can be used to optimize the process is the reactant concentration ratio of PGME and 7-ADCA.²¹ This work suggests that, from the viewpoint of crystallization, it is best to run the reaction lean in 7-ADCA. Complete consumption of 7-ADCA in the reaction will lead to lower crystal growth inhibition, rendering more of the cephalexin recoverable (by crystallization) in a shorter time. A 7-ADCA lean process is further supported by the finding that 7-ADCA is more likely than PGME to incorporate into the cephalexin monohydrate crystal, albeit at part per thousand concentrations, and that 7-ADCA is more valuable than PGME.

4.4 Conclusion

The crystallization kinetics of cephalexin monohydrate are reported for the first time in an aqueous environment, summarized in Table 4.2, and the effect of co-solutes that would be found in the enzymatic synthesis of cephalexin were investigated. The solubility was determined over a range of pH values (4 to 8) and at two temperatures (5.0 °C and 25.0 °C), crystallization kinetics were explored only at 25.0 °C. Primary nucleation of cephalexin monohydrate occurred slowly, even at high supersaturation ($S > 2$), and was not impacted by the presence of PGME or 7-ADCA co-solutes. The secondary nucleation of cephalexin birthed many more crystals than primary nucleation (see Figure 4.10) and depended on the growth rate and suspension density, but did not appear to depend on the mixing power in the regime accessible in this crystallizer geometry. At low mixing intensity the needle-shaped crystals were prone to forming dead zones while at high mixing intensities the needle-shaped crystals stabilized the formation of difficult-to-handle foam.

Table 4.2. Kinetic parameters for the crystallization of cephalexin monohydrate with 95% confidence interval. Confidence interval values marked “ns” indicate parameters that were not significantly

different from a theoretically justified value, therefore they have been fixed at the theoretically predicted value

Parameter name	symbol [units]	Value	Lower bound	Upper bound
Primary nucleation prefactor	k_J [$\text{min}^{-1} \text{L}^{-1}$]	2.54	1.39	9.00
Primary nucleation exponential	B_o	1.79	1.28	2.88
Secondary nucleation prefactor	k_B [$\text{min}^{-1} \text{L}^{-1}$]	2.98×10^5	1.01×10^5	4.95×10^5
Secondary nucleation exponent	b	1.0	ns	ns
Suspension density exponent	m	0.46	0.30	0.62
Mixing power exponent	p	0	ns	ns
Growth prefactor	k_G [$\mu\text{m min}^{-1}$]	6.52	5.16	7.43
growth exponent	g	2.0	ns	ns

The crystal growth rate was inhibited by both co-solutes, though 7-ADCA was a more potent inhibitor. 7-ADCA inhibited cephalexin crystal growth by adsorbing onto the growing faces and impeding the advancement of growth steps. These results in aggregate all suggest that an end-to-end CM process for cephalexin would be most efficient in a 7-ADCA-lean configuration.

CHAPTER 5. AMPICILLIN CRYSTAL GROWTH RATES AND GROWTH RATE DISPERSION MEASURED BY IMAGE ANALYSIS⁴

5.1 Introduction

In the previous chapter the crystallization kinetics of cephalexin monohydrate were determined in conditions that simulated the expected conditions in the CM reactive crystallization process. Supersaturation of cephalexin was generated by manipulating the pH value of the solution, whereas in the CM process supersaturation will be generated by the PGA-catalyzed synthesis reaction. In this chapter, using ampicillin as a model compound, the crystal growth kinetics were examined when supersaturation was generated by the PGA reaction. The results from the previous chapter informed analysis of the data gathered for this study.

The experimental techniques used in this chapter also differ significantly from those used in the previous chapter. Here, individual crystals are observed growing, whereas in the study on cephalexin, crystal growth was inferred from measured changes in solution composition. One of the benefits of observing each crystal growing individually is the large amount of data collected enables examination of the distribution of crystal growth rates, referred to as growth rate dispersion (GRD). Previously only the mean growth rate was calculable. It should be noted that the original motivation for the experiments in this chapter

⁴ Adapted from “[McDonald, M.A.](#); [Bommarius, A.S.](#); [Grover, M.A.](#); [Rousseau, R.W.](#) Direct Observation of Growth Rate Dispersion in the Enzymatic Reactive Crystallization of Ampicillin. *Processes* **2019**, *7*, 390.”

was to estimate the specific surface area of a sample of crystals, however, the observed GRD made that difficult. The implications of GRD for a continuous process are significant, with the potential to create a product size distribution skewed heavily towards large crystals.

Growth rate dispersion is a deviation from McCabe's ΔL law which states that "geometrically similar crystals of the same material suspended in the same solution grow at the same rate".¹³¹ Past research has yielded a number of distinct mechanisms that can lead to or explain GRD.¹³² One explanation is size dependent growth (SDG), whereby larger crystals grow faster. SDG has been proven to be a manifestation of GRD. The crystals with the faster growth rates grow to become larger, as opposed to the notion that crystals that are larger now grow faster.¹³³ Another model states that crystals undergo random fluctuations (RF) in growth rate but all have the same time-average growth rate.¹³⁴ The constant crystal growth model states that nuclei are created with an intrinsic growth effectiveness based on surface features.¹³⁵ Still other models contend that different rates of attrition of different sized crystals¹³⁶ and different crystal faces explains GRD,¹³⁷ surface charge distributions can cause GRD,¹³⁸ or the presence of additives or adsorbing species can enhance or inhibit growth, leading to growth oscillations and GRD.¹³⁹ In this study it is shown that GRD observed in ampicillin trihydrate is most easily explained by the constant crystal growth model and that surface morphology and crystal imperfections (such as dislocations) are likely the cause, although the influence of additives, in this case the ampicillin precursors 6-aminopenicillanic acid (6-APA) and D-phenylglycine methyl ester (PGME), may have an important influence.

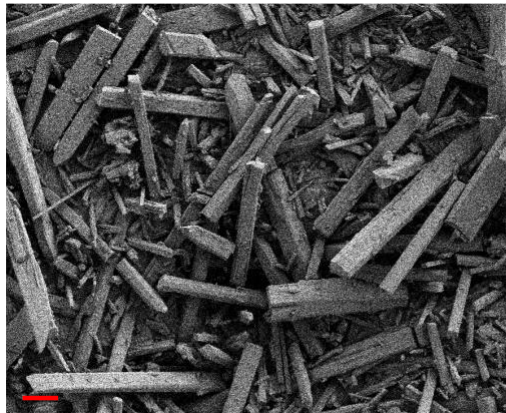
In this study, the growth rates of individual ampicillin trihydrate crystals were measured by optical microscopy as ampicillin was generated by the PGA-catalyzed condensation of 6-APA and PGME. The PGA-catalyzed generation of supersaturation enabled precise control over the supersaturation of ampicillin.⁴¹ The catalyst and reactants were homogenous and the reactants were initially present, eliminating mass transfer effects and inhomogeneity that complicate the analysis of reactive crystallizations and anti-solvent crystallizations involving the volumetric addition of different species.^{140, 141} The entire experiment was isothermal, eliminating the heat transfer and subsequent inhomogeneity that complicate analysis of cooling crystallization.^{111, 142} The control over supersaturation also obviated the need for complex flow apparatuses used to maintain a supersaturation set point in other single crystal growth experiments.^{135, 143} One recent study used simulation to look at GRD with these simplified conditions (homogeneous, isothermal, non-nucleating batch);¹⁴⁴ here a unique experimental system enables probing GRD experimentally with these simplifications. Rather than reconstruct the growth rate distribution from crystal size distributions (CSDs), which requires assumptions about the form of the distribution,^{145, 146} the growth rate distribution in the present work is observed directly, enabling simple determination of the mechanism of GRD. Up to ~100 crystals can be analyzed in a single small-volume experiment (<20 microliters) requiring only a microscope and camera.

5.2 Materials and Methods

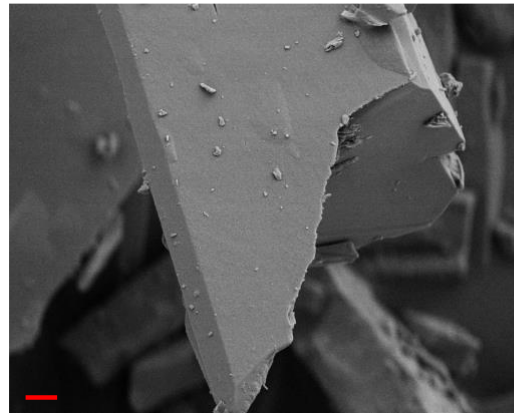
Seed crystals were prepared as follows. Ampicillin trihydrate crystals were formed at room temperature by dissolving ampicillin sodium salt (>99%, Fischer Scientific, Geel, Belgium) and neutralized by adding concentrated hydrochloric acid. All seed crystals were grown in the same batch, which was unseeded. Crystals were sieved and the 212- to 300-

μm fraction was used as seed crystals. Breakage occurred during sieving and most of the seed crystals were smaller than $212 \mu\text{m}$, demonstrating the difficulty in sieving needle shaped crystals (their small cross section allows them to slip through the sieve despite having a long characteristic size). Seeding sometimes connotes addition of a small amount of crystals to breed a large population of crystals via secondary nucleation; since nucleation is suppressed in this study, the seed crystals are from here on referred to as initial crystals.

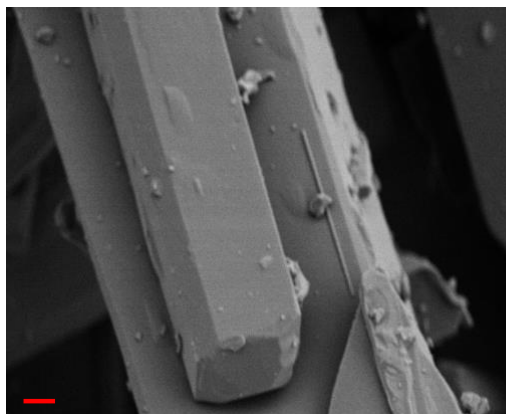
Field emission scanning electron micrographs of the initial crystals (Figure 5.1) were obtained using a Zeiss Ultra-60 FE-SEM with an accelerating voltage of 3 kV using the high vacuum mode at room temperature. Samples were gold-sputtered for 30 seconds using a Hummer 6 Gold Sputterer to give an approximate thickness of 5 nm.



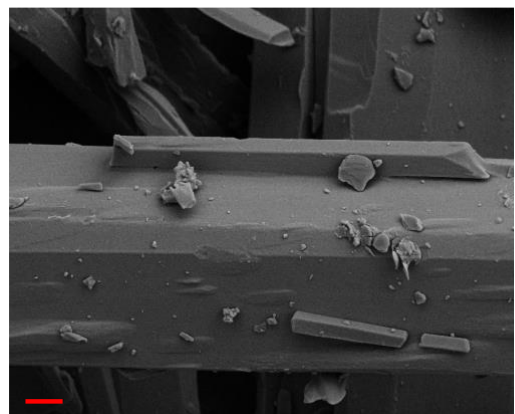
(a)



(b)



(c)



(d)

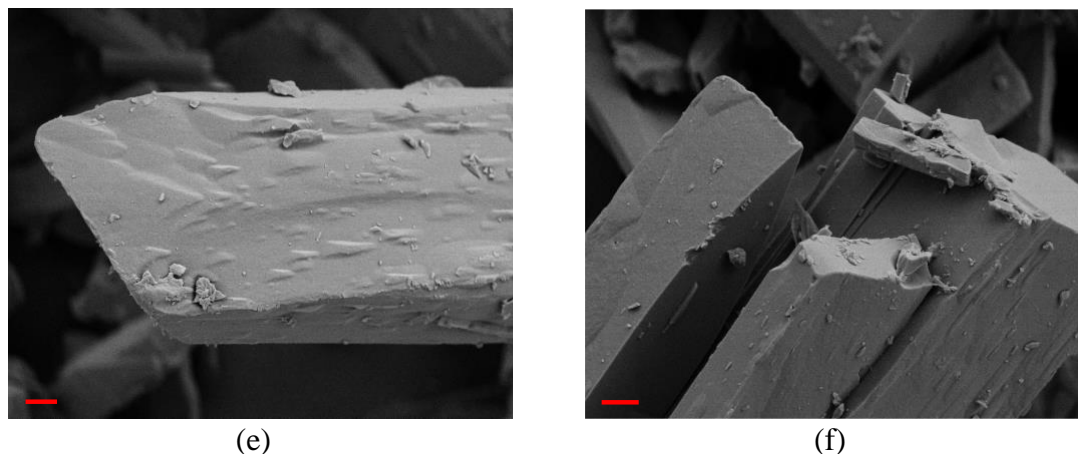


Figure 5.1. FE-SEM images of ampicillin trihydrate initial crystals. The scale bar is 30 μm in (a) and 2 μm in (b)-(f). Image (a) shows uniformity of initial crystals, (b) shows a fracture and splinter of an initial crystal, (c) and (d) show epitaxial growth and possibly twinning, (e) and (f) show ends of initial crystals. In (e) the end has several visible growth hillocks stemming from screw dislocations, in (f) two ends are shown, one pristine pointed end with few growth steps, the other a clean break.

Growth experiments were prepared as follows: 0.111 grams of 6-aminopenicillanic acid (6-APA, >98% purity, TCI America, Portland, OR, 200 mmol/L) was suspended in 1766 μL of DI water. To dissolve the 6-APA, 634 μL of 1.0 M sodium hydroxide (>98%, Sigma Aldrich, St. Louis, MO, 250 mmol/L) was added to the 6-APA suspension. To the now clear 6-APA solution, 0.103 grams of phenylglycine methyl ester hydrochloride (PGME, >95%, Sigma Aldrich, St. Louis, MO, 200 mmol/L) was added. The PGME•HCl dissolved immediately. To this solution, 0.01 to 0.05 grams of ampicillin trihydrate initial crystals were added, and the suspension was then incubated at 25.0 $^{\circ}\text{C}$ for 15 minutes with agitation to allow the ampicillin to partially dissolve and saturate. The addition of these crystals saturates the solution *and* provides initial crystals for observation of growth, at 0.01 g 57% of this initial charge dissolves, at 0.05 g only 11% of the initial charge dissolves. The suspension was divided into three aliquots of 665 μL allowing three repeats of each experiment. To a single aliquot, 35.0 μL of PGA stock solution (10.0 mg/mL, Assemblase®, DSM-SinoChem, Delft, Netherlands) was added. Once the PGA was added,

the suspension was mixed with a magnetic stir-bar, 15.0 μL of suspension was rapidly pipetted with a wide-bore pipette tip (to avoid classifying particles by size) onto a glass microscope slide, the droplet was covered with a glass cover slip, the cover slip was sealed with silicon oil, and the microscope began recording images; the entire process from addition of PGA to beginning of data collection took approximately one minute. Images were collected with a temperature-controlled microscope, set at 25.0 $^{\circ}\text{C}$, at a rate of one frame every two minutes, totaling two hours. The initial conditions for each experiment, based on this procedure, are listed in Table 5.1.

Table 5.1. Initial conditions for growth experiments.

Experimental variable	Value
Volume (of one aliquot)	700 μL
6-APA concentration	200 mmol/L
PGME concentration	200 mmol/L
Ampicillin concentration	18 mmol/L
PGA concentration	5.0 $\mu\text{mol/L}$
Ampicillin trihydrate initial loading	0.01 – 0.05 g
pH value	6.50
Temperature	25.0 $^{\circ}\text{C}$

A Leica DM LM microscope with a temperature-controlled stage was used with incident lighting and 200x total magnification (20x Leica PL Fluotar objective lens and 10x eyepiece magnification). A CoolSNAP-Pro CF camera with 36-bit color imaging was attached to the TV port; the field of view was 1040-by-1392 pixels, corresponding to 1100-by-1480 microns. Images were collected with Image-Pro Plus and exported to MATLAB for analysis.

The images collected were analyzed with GT Fiber.^{147, 148} GT Fiber is a program designed to measure the lengths of fibers in images and has the advantage that it can distinguish when two fibers (or crystals) overlap or cross, an issue which has rendered image analysis of other needle-like crystals difficult.^{48, 51} As there was no convection during the experiment, individual crystals did not move substantially between frames and could be tracked over the course of the entire experiment. With the initial frame, individual crystals to be tracked were selected, by hand, and their length and width calculated with GT Fiber. Figure 5.2 (a) shows the initial frame from a single experiment; every additional frame was fit with GT Fiber, using the previous frame to identify the crystals of interest. Figure 5.2 (b-f) shows the same experiment over 2 hours of growth. The lengths and widths of each individual crystal over time were extracted, from which growth rates could be determined. While the length calculation is robust, the width measurement is more uncertain; the crystals are transparent (only their edges are visible, see Figure 5.2) so there is no obvious edge along which to measure the width. In total, 1,003 ampicillin trihydrate crystals were observed by this method. Occasionally, two crystals would grow end to end (confusing the image analysis) or out of the image frame (resulting in unobservable growth); these crystals were removed from the dataset, giving a working set of 887 crystals.

To make inferences about the properties of the entire population of crystals, as well as the properties of ampicillin trihydrate itself, from this sample of 887 crystals required the use of several different statistical tools. A discussion of those tools is included here to enable the reader to quickly understand the coming results. The *Lilliefors statistical test* tests the null hypothesis that the data are sampled from a normally distributed population without specifying the mean or variance of the population. The test statistic is the maximum

distance between the sample cumulative distribution and the cumulative normal distribution with mean equal to the sample mean and variance equal to the sample variance. Tables of critical values have been computed by Monte Carlo methods and are widely available.¹⁴⁹ The *coefficient of determination*, R^2 , is a measure of the amount of variance explained by the model. R^2 will be close to unity when there is little noise (compared to signal) and the model has high predictive power; when there is significant noise (compared to signal) R^2 will be close to zero regardless of the model. The *root mean squared error*, RMSE, measures the differences between estimated values and observed values, making it more robust against noise compared to R^2 . However, RMSE is scale dependent, and therefore is not used to compare an estimator's predictions on different sets of observed values; rather it should be used to compare different estimator's performance on a single set of observed values. A *t*-test can be used to assess if the means of two sets of data are significantly different, given that the means come from a normally distributed population. *Spearman's rho*, ρ_S , is a rank correlation coefficient that assesses whether or not a monotonic (i.e. one-to-one) functional relationship exists between two variables. When ρ_S is zero there is no monotonic relationship between the variables and when ρ_S is unity there is a perfect monotonic relationship; a *t*-test can be used to determine if ρ_S is significantly different from zero, thus assessing the significance of the correlation between two variables. Finally, the results are reported as *95% confidence intervals*, meaning that if the study was repeated multiple times on different sample crystals, 95% of the calculated confidence intervals would cover the true value. Higher confidence levels will give larger confidence interval widths, 95% confidence is common and was therefore chosen to be the level used in this study.

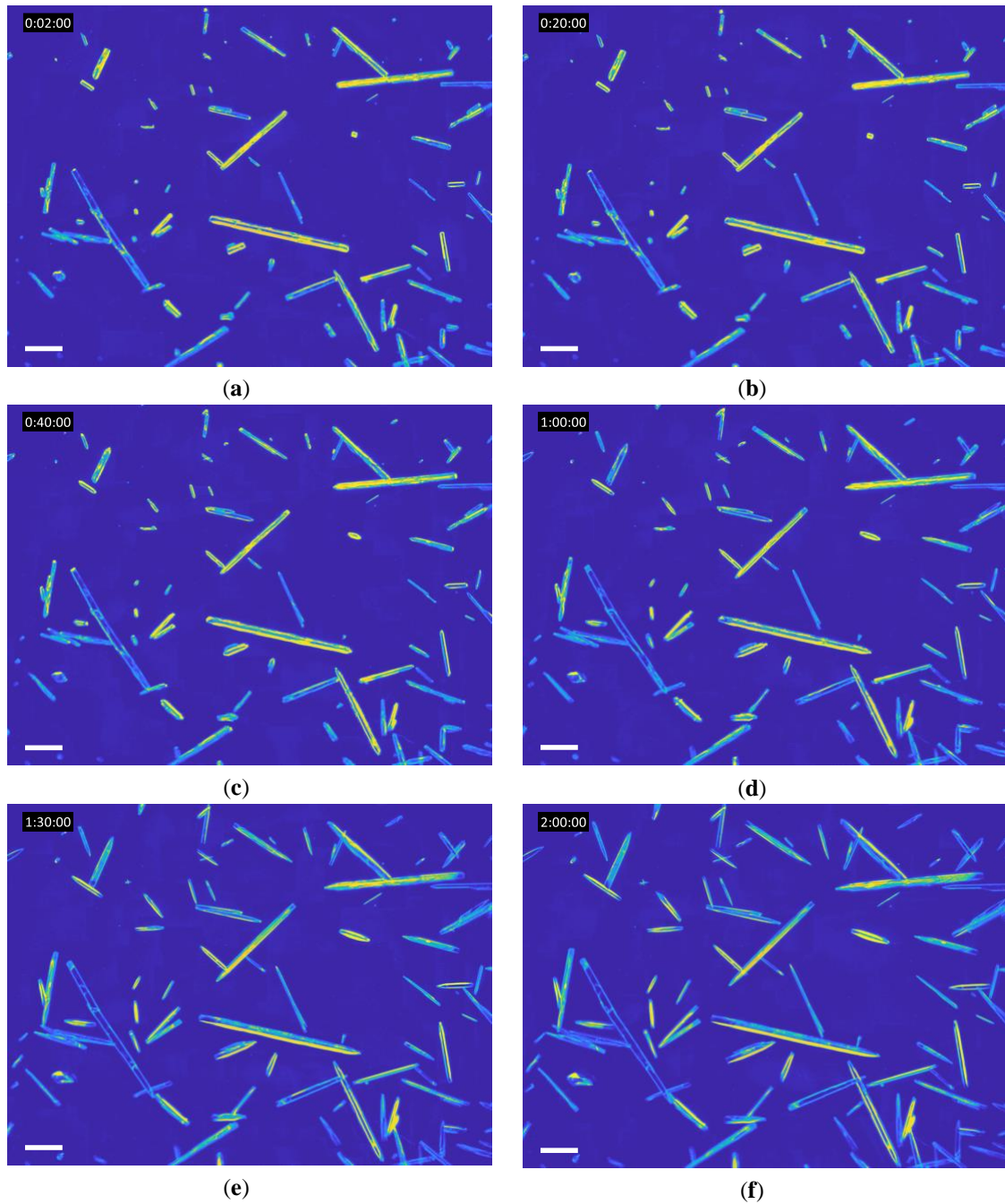
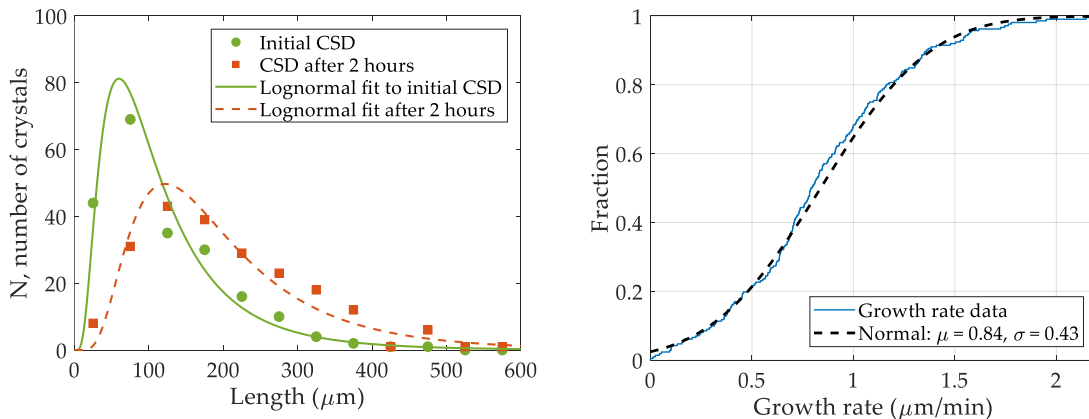


Figure 5.2. Microscope images of ampicillin trihydrate, colored to enhance contrast. The scale-bar is 100 μm : (a)-(f) images taken at 2, 20, 40, 60, 90, and 120 minutes, respectively.

5.3 Results

5.3.1 Growth rate dispersion at the population level

Previous studies on growth rate dispersion have predominately focused on changes in the crystal size distribution that could not be explained by nucleation or growth. The evolution of the CSD was examined in this study as well to enable simple comparison to past studies. Figure 5.3 (a) shows how the CSD widened over the course of 2 hours, in this case for the experiments with an initial loading of 0.03 grams. Lognormal fits to the initial and 2-hour CSD are included. A Lilliefors statistical test, which tests for normality without prior knowledge of the mean or standard deviation, failed to reject the null hypothesis that the log-transformed CSDs came from a normally distributed population at the 99% confidence level. Figure 5.3 (b) shows the cumulative distribution of growth rates from the same loading (0.03 grams, the combined results from 10 repetitions of the same experiment) and a normal distribution for reference. Here, a Lilliefors statistical test failed to reject the null hypothesis that the growth rate distribution came from a normally distributed population at the 99% confidence level. This is consistent with the central limit theorem which suggests the growth rates should be distributed normally, given that the growth rate is the combination of many distinct processes (such as bulk diffusion, surface diffusion, and solute attachment), each of which may be randomly, but not necessarily normally, distributed.



(a)

(b)

Figure 5.3. (a) The CSD of initial crystals (green circles) and fit to lognormal distribution (solid green curve) and the CSD after 2 hours of growth (red squares) and fit to lognormal distribution (dashed red curve) for experiments with an initial loading of 0.03 g, the bin widths are the same for both CSDs; (b) Cumulative distribution of growth rates extracted from CSDs for experiments with an initial loading of 0.03 g (solid blue curve) and a normal distribution with a mean of 0.84 and standard deviation of 0.43 $\mu\text{m}/\text{min}$ (dashed black curve) for reference. Note that the CSDs are lognormal while the growth rate distribution is normal.

5.3.2 Growth rate dispersion at the individual level

The growth of a single crystal was described by the piecewise equation below, where t_{cr} is the time required for a critical supersaturation to be generated, L_{init} is the length of the initial crystal, and G is the growth rate after reaching the critical supersaturation.

$$L = \begin{cases} L_{init} & 0 < t \leq t_{cr} \\ L_{init} + G(t - t_{cr}) & t > t_{cr} \end{cases} \quad (5.1)$$

Figure 5.4 (a) shows the result of fitting two crystals, both from the same experiment under the same conditions, to equation 5.1. At the same time, the widths of the crystals, also shown in Figure 5.4 (a), follow no obvious trend; the challenge of measuring the width is illustrated by ‘Crystal 2’ apparently widening and then thinning between 50 and 110 minutes. For ‘Crystal 2,’ the aberrant widening appears to be the result of a change in the optical properties of the crystal surface. Initially the surface is rough and opaque, the surface smoothens and becomes transparent during growth, but surface healing is not uniform in time or space. Here, the transient optical behavior led to an apparent increase in crystal width which then appeared to thin as the optical properties became more uniform across the crystal.

Equation 5.1 fits the data remarkably well; Figure 5.4 (b) shows an analysis of the goodness of fit for the entire data set in the form of a histogram of coefficient of

determination values (R^2). Of the crystals examined (i.e. did not grow end-to-end or out of frame), 84% have fits with $R^2 > 0.95$ (the five rightmost bins), but there is a significant population with low R^2 , indicated by the leftmost, red bin in Figure 5.4 (b). On the right-hand axis of Figure 5.4 (b) the mean and one standard deviation of the growth rates for all the crystals in that R^2 bin are shown, the slow mean growth rate for the poorly fit crystals explains why the R^2 is small. R^2 measures the amount of variance explained by the model; when the growth rate is zero none of the variance in length can be explained by growth, rather signal noise dominates, and $R^2 = 0$. Other measures of goodness of fit, such as root-mean-square error (RMSE), are not skewed by low growth rate, but RMSE is not scale invariant and will indicate a worse fit for a large crystal than a small crystal with the same R^2 .

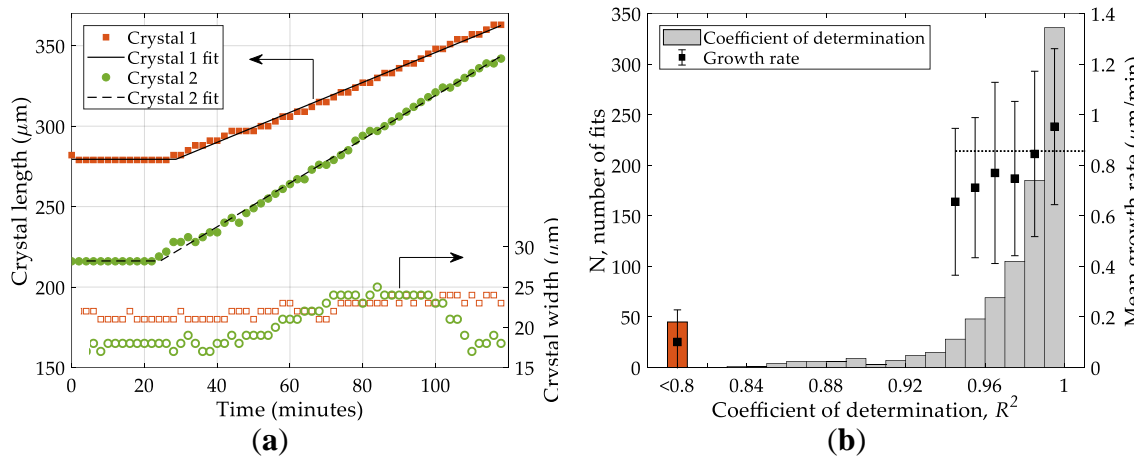


Figure 5.4. (a) The length (left axis, closed symbols) and width (right axis, open symbols) of two individual crystals is plotted over time. Note the right axis scale is 5x the left axis scale. Both crystals are fit to equation 5.1. (b) Left axis, histogram of R^2 values. Right axis, mean growth rate for each bar in the R^2 histogram (with enough samples to compute a meaningful mean and standard deviation, $n > 10$) with error bars of one standard deviation. Note all bins for R^2 less than 0.8 have been grouped into a single red bin

Upon close inspection of Figure 5.4 (a) the model does not capture the transition from no growth to growth with perfect accuracy. In many crystals, an initial burst of growth

occurs when the ends of the initial crystals (which have been blunted by breakage during solids handling) grow into facets (the equilibrium shape); Figure 5.2 shows blunt-ended crystals initially, and pointed growing crystals later. The accelerated initial growth can be seen in Figure 5.4 (a), particularly for ‘Crystal 2’, which also shows that the initially smaller crystal grows faster. However, this trend is not found when all crystals are viewed in aggregate. The growth rate does not increase with time as might be expected in a system with size-dependent growth (SDG) or randomly fluctuate as would be expected with random fluctuations (RF).

In considering all crystals, the growth rate shows a large amount of variation. Figure 5.5 shows the growth rate of crystals versus the initial length for five different initial loadings, and a linear regression has an $R^2 = 0.07$, indicating the initial length explains very little of the observed variation in growth rate. The slope of the linear correlation between L_{init} and G is positive, with a 95% confidence interval of 0.9×10^{-3} to 1.4×10^{-3} , demonstrating that longer initial crystals do in fact grow faster, as is expected with the size dependent and constant crystal growth models. Breakage of the initial crystals can explain the weakness of the correlation between L_{init} and G , but it does not account for the large scatter of growth rates. Rather, in the constant crystal growth model the dispersion of growth rates is attributed to intrinsic properties of individual crystals, not any easily measured quality like length.

The normalized empirical histogram of the growth rates is shown next to the y-axis and the normalized empirical histogram of the initial lengths is shown beneath the x-axis and. The distributions are divided between five initial loadings; it can be seen that the highest loading (shown in purple) has the largest population of small crystals initially and

lowest average growth rate while the smallest loading (shown in red) has a wider distribution of crystal lengths initially and the fastest average growth rate.

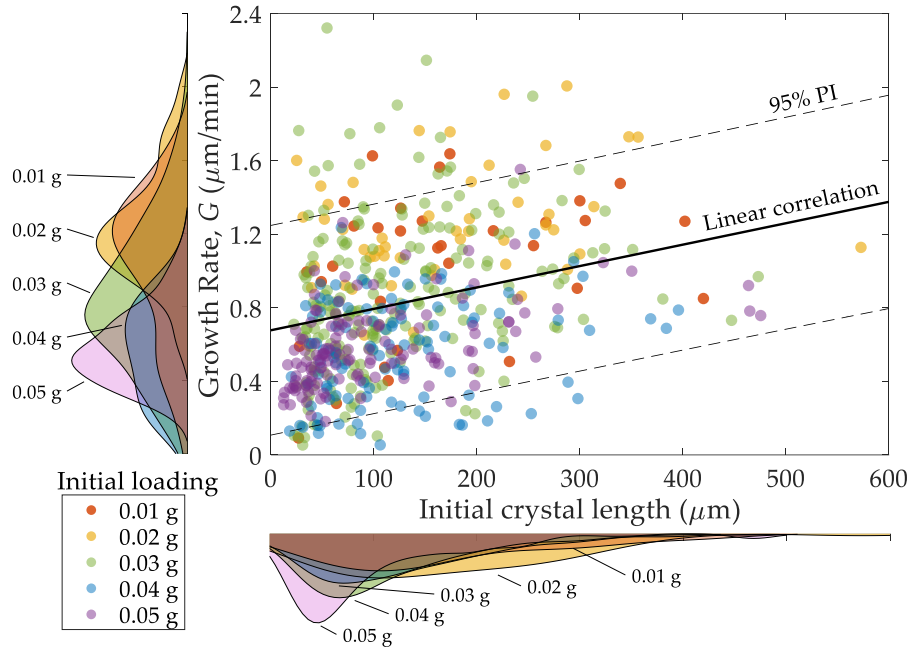


Figure 5.5. A scatter plot of growth rates of individual crystals against the length of the initial crystal for different initial loadings, with a linear correlation and 95% prediction interval. Along the x-axis is the normalized number-based CSD histogram of the initial crystal lengths, colored by loading. Along the y-axis is the normalized growth rate distribution histogram of the initial crystals, colored by initial loading.

5.4 Discussion

Over the course of 2 hours, the mean crystal width increased from 18.9 μm to 21.5 μm. This change in width corresponds to an increase of approximately two pixels. All measurements are discretized by the camera making it impossible to measure accurate width trends for individual crystals, but for the population the two-pixel change in width is significant at the 99% confidence level. Since the width change is so small it is assumed most of the growth occurs at the ends of the needles. Equation 5.2 characterizes the rate of

accumulation of dissolved ampicillin c as solute is generated by the reaction R and consumed by the ends of the crystals.

$$\frac{dc}{dt} = R - \rho AG \quad (5.2)$$

where ρ is the density of the crystal, A is cross-sectional area of the crystal, and G is growth rate of the crystal.

Shortly after the critical time, t_{cr} , the linear increase in length over time suggests that the concentration reaches a pseudo steady state such that the left-hand side of equation 5.2 goes to zero. Since the reaction rate is constant across experiments, the product of area and growth rate must be constant. At higher loadings there is more area, therefore, one expects to observe a decrease in growth rate. The relationship between area and initial loading is not obvious. At a loading of 0.01 g, 57% of the initial crystal mass dissolved during the initial dissolution step to form a saturated solution (see Methods). Many small crystals may have dissolved entirely, leaving mostly large crystals, evidenced by the broader distribution of initial sizes in Figure 5.5. At a loading of 0.05 g, only 11% of the initial crystal mass dissolved. Less dissolution of each crystal was required to saturate the solution; many of the small crystals that would have entirely dissolved in the 0.01 g loading were observable in the growth phase of the 0.05 g loading experiments.

Figure 5.6 (a) shows that the growth rate is negatively correlated with the initial loading, but that initial loading is a poor predictor for growth rate given the large scatter in the data and the low $R^2 = 0.10$. The 95% prediction interval given by the dashed curves are correspondingly wide to capture the variance in the growth rate. It is also possible that the

simple hyperbolic relationship, $G = a/(x+b)$, may not be appropriate for the aforementioned reasons.

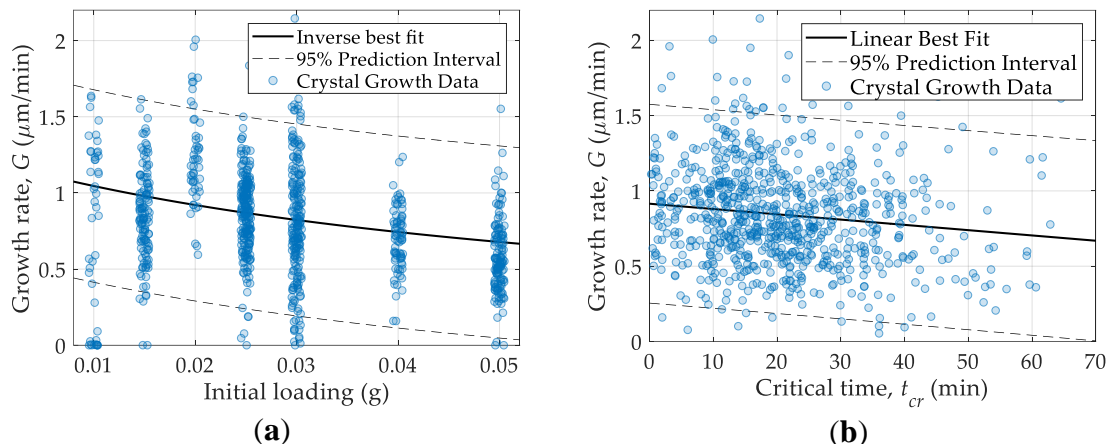


Figure 5.6. (a) Growth rate of individual crystals versus the initial loading of the experiment in which the growth rate was measured, horizontal jitter is introduced to illustrate the density of data points; (b) Growth rate of individual crystals versus the critical time of the crystal. The solid lines are the linear best fits and the dashed curves are the 95% prediction intervals

There also exists a weak but statistically significant (at the 95% confidence level) correlation between critical time and growth rate. Longer critical times are correlated with slower growth rates, independent of initial loading, as can be seen in Figure 5.6 (b) where the 95% confidence interval on the slope is -8.1×10^{-3} to -5.9×10^{-3} . There is evidence that the presence of other species, in this case the reactants 6-APA and PGME, can inhibit the growth of ampicillin crystals,^{150, 151} which may lead to lack of growth below a critical supersaturation. The lack of growth is postulated to arise from the other species adsorbing to the edge of growth steps and preventing the step from advancing; halting the layer-by-layer growth mechanism.⁹⁹⁻¹⁰¹ The advance of edges along the length of the crystal is visible on some crystals in the videos provided with the Supplemental Material, although to be visible at this magnification they must be groups or bunches of growth steps.

Again, the scatter in the data is large, $R^2 = 0.15$, making critical time only weakly predictive of growth rate, however both are affected by similar surface phenomena. An underlying property of the crystal surface could be affecting both growth rate and critical time but by different mechanisms, resulting in the observed correlation and providing evidence that the distribution of growth rates results from a distribution of crystal properties (the spacing of the adsorbed species on the edge of advancing growth steps determines the critical supersaturation required to overcome the impinging adsorbed molecule).¹⁰⁰ The distance between adsorbed molecules on the edge should follow a geometric distribution (assuming each adsorption site is identical), as the length and number of edges increases the probability of gaps between adsorbed molecules large enough to support growth also increases, even with the same fractional coverage of sites. Therefore, in this experimental procedure, crystals with longer growth step edges are expected to have shorter critical times and higher growth rates. Different numbers and arrangements of dislocations in the crystal can lead to different lengths of growth step edges as well as different growth rates.^{113, 135}

Finally, given that the system is not mixed, it must be considered whether the distribution of growth rates could be attributed to the slight differences in local supersaturation due to the random scattering of crystals. For this analysis, it is still assumed that growth occurs predominately at the ends of the crystals (as is seen in Figure 5.4), such that only the ends of the crystals act as a sink for ampicillin generated in the bulk. It is also assumed that there is no bulk flow and that the height dimension is insignificant (sampled volumes measure $1290 \times 967 \times 43$ microns L \times W \times H). With these assumptions, the images can be divided into areas such that each area contains a single growing crystal end

that is the only sink for dissolved ampicillin in that area. Figure 5.7 shows how one such image was divided.

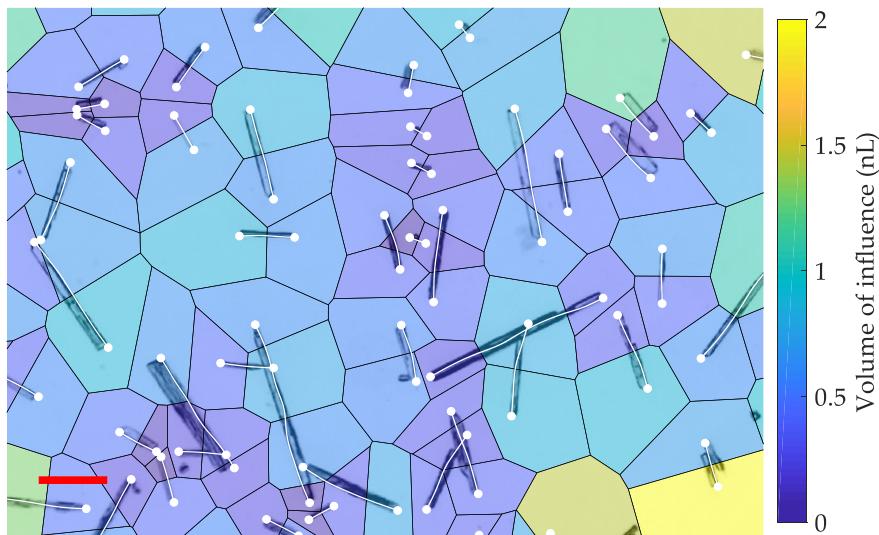


Figure 5.7. An image of growing crystals is divided into areas based on distance to nearest growing crystal end. The areas are colored based on the volume represented by the area and range from dark blue representing the smallest volume (0.1 nL) and yellow representing the largest volume (2 nL). The areas are overlaid on the grayscale image from which the data were generated. The white points are the crystal ends used in the analysis, and the white curves connecting them illustrate how the crystal is represented in the image analysis program GT Fiber. The red scale bar is 100 μm .

Since the reaction rate is the same throughout the bulk and if GRD is the result of the random placement of crystals only, the growth rate of each crystal should be correlated with the area over which that crystal serves as the dissolved ampicillin sink (controlled for the growing area of the sink). Instead, no correlation was found between the area of influence and the growth rate; Figure 5.8 shows the expected growth rate (calculated from the known rate of ampicillin generation based on the PGA kinetics and the areas of influence) versus the measured growth rate for the experiment shown in Figure 5.7. The calculation under-predicts the growth rate, likely because the width is overestimated during the image analysis. It is visually obvious that the data are not correlated, with a 95%

confidence interval on the slope ranging from -0.50 to 0.99, indicating no linear relationship (Spearman's rho indicates no one-to-one relationship, linear or otherwise). No correlation was found when the same analysis was applied to other experiments not shown in Figure 5.7. To describe the growth rate of an individual crystal requires knowledge of the collective system properties (i.e. supersaturation, temperature, etc.) *and* intrinsic crystal properties (dislocation frequency, surface features). While many correlations exist and can partly be explained by system properties, the large scatter in the data are in line with the constant crystal growth model where GRD is explained in terms of intrinsic crystal properties.

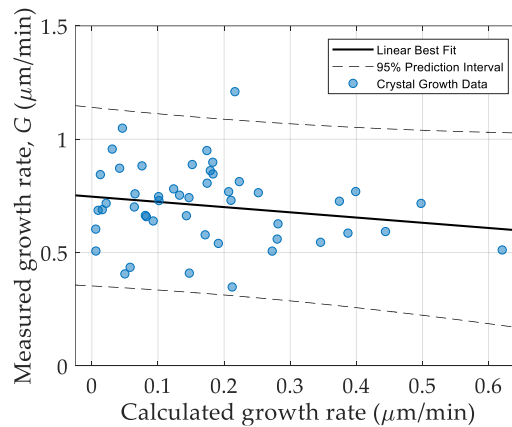


Figure 5.8. The measured growth rate of the crystals in Figure 5.7 versus the calculated growth rate of the same crystals based on the division of the image in Figure 5.7.

Previous studies have incorporated a distribution of growth rates into a population balance model to examine the effect of GRD on the CSD from a continuous crystallizer.¹⁴⁵ The population density function, n , from a mixed-suspension, mixed-product removal (MSMPR) crystallizer is given by

$$n(L) = \frac{B^o}{\int_0^\infty Gf(G)dG} \int_0^\infty f(G) \exp\left(\frac{-L}{G\tau}\right) dG \quad (5.3)$$

where B^o is the nucleation rate, $f(G)$ is the probability density function describing the growth rates of nuclei, and τ is the mean residence time of the MSMPR. To compare CSDs, it is assumed that the rate of generation of crystals, given by the suspension density M_T divided by the residence time, is the same in systems following the ΔL law and systems exhibiting GRD. M_T is defined by

$$M_T = B^o k_v \int_0^\infty L^3 n(L) dL \quad (5.4)$$

where k_v is a volumetric shape factor. With equation 5.4 the nucleation rate could be adjusted to ensure the same rate of crystal generation in any crystallizer. It was shown in Figure 5.3 (b) that the growth rates of the crystals follow a normal distribution, with a mean $\mu = 0.84 \mu\text{m}/\text{min}$ and $\sigma = 0.43 \mu\text{m}/\text{min}$, and it is assumed that this distribution is appropriate for the nuclei in the MSMPR exhibiting GRD, $f(G)$. Using these results, an MSMPR producing ampicillin by the PGA-catalyzed reactive crystallization was modeled. A residence time of 42 minutes has previously been shown to optimize yield while meeting purity constraints, therefore $\tau = 42$ was used in the model.²¹ Figure 5.9 shows the population density function of the crystals produced by an MSMPR following the ΔL law (no GRD, $\sigma = 0$) and an MSMPR with GRD. With GRD, the population density function becomes skewed towards larger crystals compared to the ΔL law growth rate; there are an order of magnitude more crystals at $400 \mu\text{m}$ length with GRD than without GRD. Such a substantial increase in large crystals could require a further processing step, such as grinding, if the process were designed to meet product size specifications with the assumption that the growth rates of all crystals are the same.

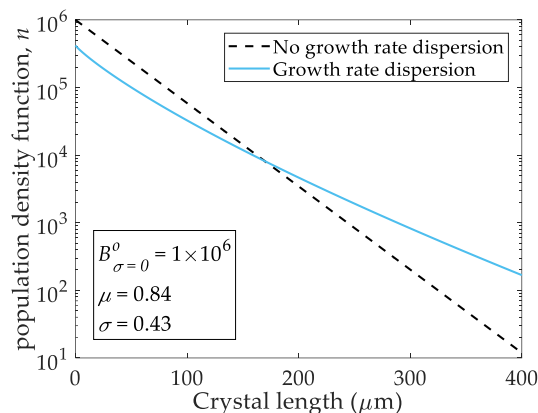


Figure 5.9. The CSD in an MSMPR producing ampicillin by PGA-catalyzed reactive crystallization. The dashed curve represents the case with no GRD and the solid blue curve shows the CSD when the growth rates follow a normal distribution as described in Figure 5.3 (b).

5.5 Conclusions

Growth rate dispersion of ampicillin trihydrate crystals was directly observed. The experimental design allowed many sources of potential differences in growth rate to be eliminated: isothermal conditions ruled out spatial differences in temperature and any Arrhenius dependence, homogeneous bulk phase ruled out mixing effects seen with anti-solvent crystallization and precipitation, quiescent conditions ruled out breakage, agglomeration, and nucleation as sources of irregularity in the CSD. Image analysis of individual crystals over time showed that the growth rate was linear and steady, ruling out the possibility of random fluctuations and size dependent growth, two theories previously advanced to explain unexpected widening of CSDs. Direct observation of growing crystals led to insight regarding the mechanism of growth rate dispersion that would not be possible with population-level measurements such as size distribution. Analysis of the spatial orientation of the crystals, in an unmixed environment, revealed that the magnitude of growth rate dispersion could not be explained by the random scattering of crystals.

Therefore, the dispersion of growth rates observed in ampicillin trihydrate crystallized in the presence of the precursors, 6-APA and PGME, is almost certainly due to properties intrinsic to each individual crystal. The correlation of growth rates and critical times required for growth to begin suggests that the most important intrinsic property is total length of growth step edge, which will be influenced by number and arrangement of screw dislocations.

CHAPTER 6. DEVELOPMENT OF A MODEL FOR IN SILICO DESIGN OF AN OPTIMAL PROCESS FOR CONTINUOUS MANUFACTURING OF BETA-LACTAMS⁵

6.1 Introduction

The preceding chapters have created the knowledgebase needed for the development of a comprehensive model of the continuous reactive crystallization of beta-lactams by penicillin G acylase. The model, to be complete, needs to consider the following kinetic phenomena: (1) the kinetics of the PGA-catalyzed reactions, (2) the kinetics of crystallization, both nucleation and growth, and (3) the kinetics of PGA deactivation. The conditions over which the kinetics need to be calculated is bounded by several factors, such as reactant solubility for concentration, enzyme activity profile for pH value, and product solubility and enzyme stability for temperature.

The model is developed from first principles, introduced in previous chapters, and fit with experimental data, also collected in previous chapters. Simplifying assumptions are used to construct attainable regions with respect to reactant conversions and mean crystal size, and Levenspiel plots are used to evaluate reactors and reactor networks. Three process attributes—conversion (X), productivity (P), and fractional yield (Φ)—are presented as a Pareto-optimal surface, i.e. the set of attribute values such that no one attribute can be improved without negatively impacting any other attribute. Attainable regions for mean

⁵ Adapted from “Computers & Chemical Engineering, 123, [McDonald, M.A.](#); Bommaris, A.S.; Rousseau, R.W.; Grover, M.A. Continuous reactive crystallization of β -lactam antibiotics catalyzed by penicillin G acylase. Part I: Model development, 331-343.” Copyright (2019), with permission from Elsevier.

crystal size with a series of mixed suspension mixed product removal reactive crystallizers (MSMPRs) are discussed. The use of classified product removal as a technique for improving the mean crystal size over the MSMPR is demonstrated. Finally, manipulating the enzyme concentration is discussed as a means of further improving the process.

6.2 Model Development

A combined model of reaction and crystallization was constructed to track the amounts of all species. Three conceptually distinct (if not physically separate) phases were considered: the crystalline phase with solid products or byproducts, the liquid phase with dissolved solutes, and the enzyme phase which could be either soluble, immobilized on a solid support, or encapsulated/recycled in some other manner. Two timescales are also considered: reaction, crystallization, and convection all occur on the single residence time timescale, while enzyme deactivation occurs over a much longer timescale.

The reaction model is based on the mechanism and resulting kinetics of PGA, elucidated in CHAPTER 3, which have previously been studied.^{32, 63, 80} As a reminder to the reader, PGA catalyzes three reactions: the desirable synthesis reaction, as well as undesirable primary hydrolysis and secondary hydrolysis reactions. The mechanism of each of these reactions can be represented by the scheme in Figure 6.1.

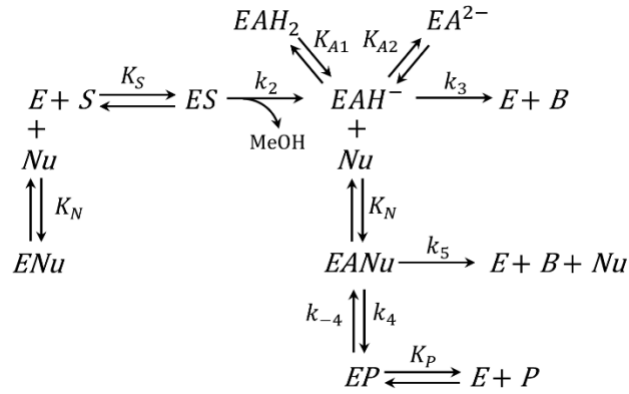


Figure 6.1. The kinetic scheme for the mechanism of PGA. E is free PGA, S is acyl-donor (HOPGME or PGME), Nu is 6-APA or 7-ADCA, B is the byproduct (HOPG or phenylglycine), P is the antibiotic, EAH is the activated acyl-enzyme complex, EA and EAH₂ are dead-end complexes due to pH equilibria, ENu is PGA bound to 6-APA or 7-ADCA, ES is PGA bound to HOPGME or PGME, EANu is acyl-enzyme complex bound to 6-APA or 7-ADCA, and EP is PGA bound to antibiotic.³²

The rates of the synthesis and hydrolysis reactions are explained in detail in CHAPTER 3 and are listed here as equations 6.1-6.5. This system of equations defines the reaction rates of production and consumption (R_P for antibiotic product, R_B for byproduct, R_S for substrate acyl-donor, and R_{Nu} for nucleophilic β -lactam core). The reaction rates are dependent on the concentration of substrate acyl-donor (c_S), nucleophilic β -lactam core (c_{Nu}), and antibiotic product (c_P), as well as the pH value and concentration of free active enzyme (c_E), defined with respect to the total enzyme concentration ($c_{E,0}$) in equation 6.5. The parameters in equations 6.1-6.5 are reported in Table 6.1.

$$R_P = \frac{dc_P}{dt} = \frac{c_E}{(k_3 K_N + k_4 c_{Nu} + k_5 c_{Nu})} \left(\frac{k_2 k_4 c_S c_{Nu}}{K_S} - \frac{k_{-4} c_P (k_3 K_N + k_5 c_{Nu})}{K_P} \right) \quad (6.1)$$

$$R_B = \frac{dc_B}{dt} = \frac{c_E (k_3 K_N + k_5 c_{Nu})}{(k_3 K_N + k_4 c_{Nu} + k_5 c_{Nu})} \left(\frac{k_2 c_S}{K_S} - \frac{k_{-4} c_P}{K_P} \right) \quad (6.2)$$

$$R_S = \frac{dc_S}{dt} = -(R_P + R_B) \quad (6.3)$$

$$R_{Nu} = \frac{dc_{Nu}}{dt} = -(R_P) \quad (6.4)$$

$$c_E = \frac{c_{E0}}{\left[1 + \frac{c_S}{K_S} + \frac{c_P}{K_P} + \frac{c_{Nu}}{K_N} + \frac{K_N}{k_3 K_N + k_4 c_{Nu} + k_5 c_{Nu}} \left(\frac{k_{-4} c_P}{K_P} + \frac{k_2 c_S}{K_S} \right) \left(1 + \frac{c_{Nu}}{K_N} + \frac{10^{-\text{pH}}}{K_{A1}} + \frac{K_{A2}}{10^{-\text{pH}}} \right) \right]} \quad (6.5)$$

Table 6.1. Values of the rate and association constants shown in Figure 6.1 and equations 6.1-6.5. Notes: ^a Youshko *et al.* 2002⁶³, ^b McDonald *et al.* 2017³², ^c values calculated from published values of α , β_0 , and γ and invariants between mechanisms (e.g. ampicillin and amoxicillin have the same nucleophile, therefore they must have the same nucleophile association constant). Discussion of α , β_0 , and γ can be found in CHAPTER 3.

Parameter	Units	Amoxicillin ^{a,c}	Ampicillin ^b	Cephalexin ^{a,c}
k_2	s ⁻¹	187	162	162
k_3	s ⁻¹	44	44	44
k_4	s ⁻¹	302	235	316
k_{-4}	s ⁻¹	217	217	217
k_5	s ⁻¹	39	9.0	6.3
K_N	mol/L	0.043	0.043	0.019
K_S	mol/L	0.38	0.38	0.38
K_P	mol/L	0.095	0.095	0.057
K_{A1}	-	10 ^{-7.52}	10 ^{-7.52}	10 ^{-7.52}
K_{A2}	-	10 ^{-8.19}	10 ^{-8.19}	10 ^{-8.19}

The driving force for crystallization and the equilibrium solute concentration depend strongly on the solubility of the species. The solubility of the crystallizing products amoxicillin, ampicillin, and cephalexin, as well as the byproducts which may crystallize and contaminate the product, HOPG and phenylglycine, are functions of pH value. The pH of the solution was solved with species and charge balances as described elsewhere.^{90, 152} Figure 6.2 shows the solubility of the antibiotics, byproducts, β -lactam cores, and acyl-donors. The solubility (c^*_j) was modeled according to equation 6.6, which captures the solubility behavior and depends on two parameters, the solubility at the isoelectric point

($c_{pI,j}^*$), and the acid dissociation constant ($pK_{a,j}$).¹⁵³ These parameter values are given in Table 6.2. The dissociation constants are also corrected for ionic strength with equation 6.7, where z_j is the charge of the conjugate base; over the pH range of interest it has a value of zero for all species except for the substrate S where $z_S = 1$.¹⁵⁴

$$c_j^* = c_{pI,j}^* \left(1 + \frac{10^{-pK_{a,j}}}{10^{-pH}} \right) \quad (6.6)$$

$$pK_{a,j} = pK_{a,j}^0 + 0.509(2z_j + 1) \left(\frac{\sqrt{I}}{1 + \sqrt{I}} - 0.2I \right) \quad (6.7)$$

In Figure 6.2.a it can be seen that amoxicillin (solid) is less soluble than ampicillin (dashed) which is less soluble than cephalixin (dash-dot) at all pH values, resulting in less antibiotic going unrecovered in the effluent stream from the amoxicillin process. The solubility of HOPG, shown in Figure 6.2.b, is also approximately three-fold greater than that of phenylglycine and is only a weak function of pH. The solubility of the β -lactam core, presented in Figure 6.2.c, can also dictate operating conditions; the low solubility of 7-ADCA compared to 6-APA indicates that 400 mM 7-ADCA cannot be used at a pH value of 7, which will result in slower synthesis of cephalixin compared to amoxicillin or ampicillin. The solubility of HOPGME, shown in Figure 6.2.d has the opposite pH dependence of the other species investigated, which requires that an HOPGME feed be slightly acidic, potentially neutralized by a slightly basic nucleophile feed. The large increase in HOPGME solubility at slightly acidic conditions motivated the two pH values (6.5 and 7.0) investigated in detail in this chapter. The solubility of PGME is greater than one molar at all investigated pH values; it is therefore not a constraint on the CM process for cephalixin. All reported solubility values, given in Table 6.2, are at 298 K.

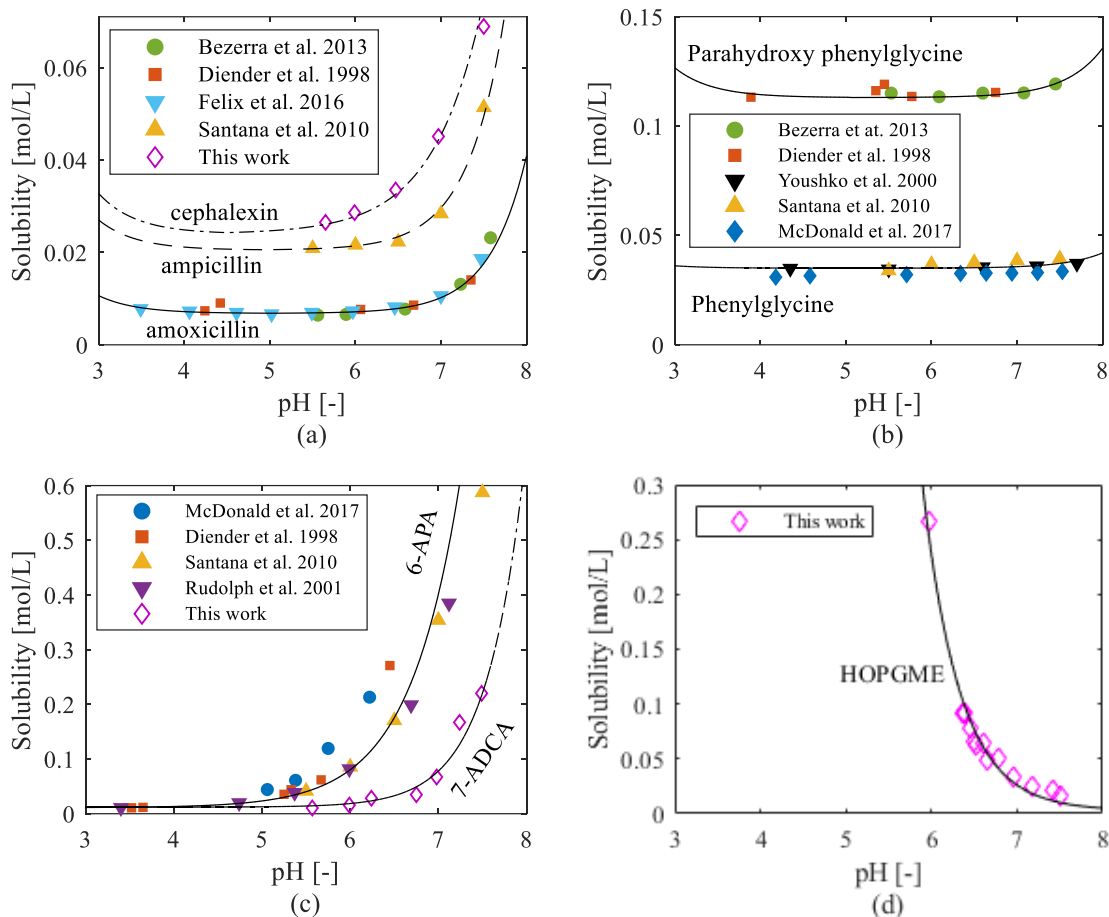


Figure 6.2. The solubility of amoxicillin (solid), ampicillin (dash), and cephalalexin (dash-dot) (a), HOPG (solid) and phenylglycine (dash) (b), 6-APA (solid) and 7-ADCA (dash-dot) (c), and HOPGME as a function of pH with experimental data from Bezerra *et al.* 2013¹⁵⁵, Diender *et al.* 1998¹⁵⁶, Felix *et al.* 2016¹⁵⁷, Santana *et al.* 2010⁴⁵, Youshko *et al.* 2000⁷⁷, McDonald *et al.* 2017³², and Rudolph *et al.* 2001²², as well as this work.

The crystallization kinetics of amoxicillin trihydrate and ampicillin trihydrate have previously been reported.^{88, 89, 151} The crystal growth rate, G , was modeled as a power law with respect to relative supersaturation, $\sigma = (c - c^*)/c^*$, and was considered to follow McCabe's ΔL rule that all crystals grow at the same rate,¹³¹ given in equation 6.8. After initial design, the known growth rate dispersion, being more computationally intensive to optimize for, was incorporated into the results (CHAPTER 5). The crystal nucleation rate, B , was modeled as the sum of the primary (B_1) and secondary nucleation (B_2) rates, shown

in equations 6.9-6.11. In addition to being a function of supersaturation, the secondary nucleation rate is also a function of the slurry density, M_T , which will be defined later in equation 6.18. Table 6.3 contains the parameter values used for these equations.

$$G = k_G \sigma^g \quad (6.8)$$

$$B_1 = k_{B1} \exp \left[\frac{-B^\circ}{\ln^2(\sigma + 1)} \right] \quad (6.9)$$

$$B_2 = k_{B2} M_T^m \sigma^b \quad (6.10)$$

$$B = B_1 + B_2 \quad (6.11)$$

Table 6.2. Summary of the parameter values used to model the solubility of amoxicillin, ampicillin, cephalixin, their precursors, and their hydrolysis products. Notes: ^a Felix *et al.* 2016¹⁵⁷, ^b Santana *et al.* 2010⁴⁵, ^c Bezerra *et al.* 2013¹⁵⁶, ^d McDonald *et al.* 2017³², ^e This work.

	Units	Amox.	Amp.	Ceph.	6-APA	7-ADCA	HOPG	PG	HOPGME
pK _a	-	7.48 ^a	7.31 ^b	7.12 ^e	4.83 ^b	6.26 ^e	9.20 ^c	9.14 ^b	7.97 ^d
c* _{pl}	mol/L	0.0068 ^c	0.021 ^d	0.024 ^e	0.020 ^d	0.012 ^e	0.113 ^c	0.035 ^d	0.010 ^d

Table 6.3. Summary of parameter values used to model the crystallization of amoxicillin and ampicillin. Notes: ^a Encarnación-Gómez *et al.* 2016⁴¹

Parameter	Units	Amoxicillin ^a
k _G	μm/min	8.95
g	-	1.87
k _{B1}	1/kg/min	5×10 ¹⁰
B ^o	-	1.27
k _{B2}	1/kg/min	2.2×10 ⁹
m	-	0.60 ^e
b	-	1.37 ^e

A reactive crystallizer network of independently sized well-mixed vessels in series was considered because a series of reactive crystallizers still requires less volume than a

single reactor and crystallizer, while potentially improving overall performance. While potentially more capital-intensive than a single reactive crystallizer, vessels in series could provide more operational freedom with reductions in operational costs that justify the increased capital expense. In this study, volume is used as a proxy for cost and a preliminary screen of process plausibility; the cost analysis required to design an optimally profitable plant is beyond the scope of this work.

Figure 6.3 shows the flowsheet used for this model. No inter-stage feeds were included, both for simplicity and to approximate industrially relevant designs. It is assumed that the enzyme separator is ideal; this model does not make any assumptions as to the form of the enzyme, such as soluble or immobilized, so a more detailed separator configuration is not presented here. In the stirred tanks, the residence time of the solids, τ_s , is independent of that for the liquid and is crystal size dependent to model fines and classified product removal. Agglomeration and breakage were considered negligible, similar to previous crystallization models of β -lactams and in accordance with our experimental observations.

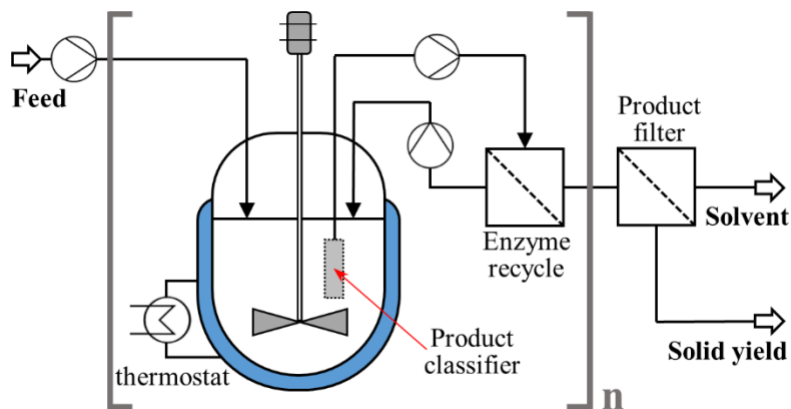


Figure 6.3. Schematic representation of the system being modeled. The product classifier allows the residence time of the crystals to be independent of the solution and vary as a function of crystal size.

The enzyme recycle is assumed to recycle a pure enzyme stream but does not affect the degradation of the enzyme.

Based on these simplifications a system of equations for the crystal size distribution was formulated, utilizing a population balance model with reaction and given below as equations 6.12-6.15. Equation 6.12 is the population balance, equation 6.13 is the solute balance, and equations 6.14 and 6.15 are boundary and initial conditions, respectively.

$$\frac{\partial n_{j,k}(L,t)}{\partial t} = \frac{n_{j,k-1}(L,t) - n_{j,k}(L,t)}{\tau_s(L)} - G_{j,k} \frac{\partial n_{j,k}(L,t)}{\partial L} \quad (6.12)$$

$$\frac{dc_{j,k}}{dt} = \frac{c_{j,k-1} - c_{j,k}}{\tau_l} - R_{j,k} - 3k_{v,j}\rho_j G_{j,k} \mu_{2,j,k} \quad (6.13)$$

$$n_{j,k}(L_0, t) = n_{j,k}^o = \frac{B_{j,k}}{G_{j,k}} \quad (6.14)$$

$$n_{j,k}(L, t_0) = 0 \quad (6.15)$$

In the above equations $n_{j,k}$ and $c_{j,k}$ represent the crystal size distribution (CSD) and solute concentrations, respectively, of component j in the k^{th} stirred tank where the 0^{th} stirred tank is the feed. τ_s and τ_l are the solids and liquids residence times, respectively. k_v and ρ are the volumetric crystal shape factor and crystal density. L and t represent the crystal length and time domains.

The moments of the CSD are defined in equation 6.16; differentiating the moments with respect to time gives equation 6.17, which can be solved with a differential equation solver as described in the Methods section below. It is also convenient to define the slurry density, $M_{T,j}$, with the third moment of the CSD, μ_3 , as shown in equation 6.18.

$$\mu_{i,j,k} = \int_0^\infty n_{j,k}(L,t) L^i dL \quad (6.16)$$

$$\frac{d\mu_{i,j,k}}{dt} = \begin{cases} B_j & i = 0 \\ iG_j \mu_{i-1,j,k} & i \geq 1 \end{cases} \quad (6.17)$$

$$M_{T,j} = k_{V,j} \rho_j \mu_{3,j} \quad (6.18)$$

In CHAPTER 2 the deactivation kinetics of PGA were determined and those findings are applied here.¹⁵⁸ Assemblase®, a commercial form of PGA used in this study, follows the Lumry-Eyring model of deactivation. In the Lumry-Eyring model⁶⁶ natively folded (active) enzyme, E , is in equilibrium with a reversibly unfolded conformation, U , which decays to an irreversibly unfolded conformation, D :



The decay (k_d) and equilibrium (K_U) constants are functions of temperature parameterized by the enthalpy and entropy of deactivation, enthalpy of reversible unfolding, and melting temperature of PGA. Equations 6.20 and 6.21 define k_d and K_U respectively (k_b is the Boltzmann constant, h is Planck's constant, and R is the gas constant). The enthalpy of deactivation (ΔH_{deact}) has a value 350 kJ/mol, the entropy of deactivation (ΔS_{deact}) has a value of 770 J/mol/K, the enthalpy of reversible unfolding (ΔH_U) has a value of 236 kJ/mol, and the melting temperature of PGA (T_m) is 328.4 K.¹⁵⁸

$$k_d = \frac{k_b T}{h} \exp\left(\frac{-\Delta H_{deact}}{RT}\right) \exp\left(\frac{\Delta S_{deact}}{R}\right) \quad (6.20)$$

$$K_U = \exp\left(\frac{\Delta H_U}{R} \left(\frac{1}{T_m} - \frac{1}{T}\right)\right) \quad (6.21)$$

The stability of PGA diminishes rapidly above ~50 °C, however, at the conditions experienced in the reactive crystallizer the amount of active PGA is practically unchanging over the course of many residence times. Equation 6.22 is the differential equation form of equation 6.19 which, in conjunction with equations 6.20 and 6.21, can be used to determine the amount of active PGA in a process of arbitrary temperature. Changing temperature is

beyond the scope of the present work, therefore equation 6.22 can be reduced to equation 6.23, where the effective decay constant ($k_{d,eff}$) has a value of $4.6 \times 10^{-9} \text{ s}^{-1}$ at 298 K (time constant of 6.7 years).

$$\frac{dc_{E,0}}{dt} = -c_{E,0} \frac{K_U k_d - \frac{dK_U}{dT} \frac{dT}{dt}}{1 + K_U} \quad (6.22)$$

$$\frac{dc_{E,0}}{dt} = -k_{d,eff} c_{E,0} \quad (6.23)$$

6.3 Methods

The model is formulated as a system of partial differential equations (PDEs) according to equation 6.12. These PDEs are reduced to a system of ordinary differential equations (ODEs) by two methods; the method of lines and the method of moments.^{159, 160} The two different methods have different qualities that make using both of them advantageous. The method of lines enables the CSD to be solved as a function of time, enabling modeling of selective removal of crystals based on size, but at a large computational cost. The method of moments uses the moments transformation to solve the PBEs with a limited number of ODEs, enabling fast solutions and large design spaces to be searched, but without the full CSD information provided by the method of lines.

With the method of lines, the crystal length domain is discretized to give a system of ODEs in the time domain that are solved with the MATLAB ODE solver *ode113*, which is an efficient ODE solver when the ODE function is expensive to evaluate. In this work, the length domain was discretized at 0.20 μm intervals from 0 to 200 μm , giving a total of 1,001 size bins. An error analysis, visualized in Figure 6.4, showed that a 1,000-bin discretization gave a smaller error than the method of moments, which only evaluates the

moments (μ_i) of the crystal size distribution, defined in equations 6.16 and 6.17, greatly reducing the number of ODEs compared to the method of lines and allowing for evaluation with the MATLAB ODE solver *ode45*. The method of moments was used to search for global optima by repeatedly running the optimization with different starting points, the method of lines was used to determine a finer-grained optimum and calculate the crystal size distribution (which the method of moments cannot do).

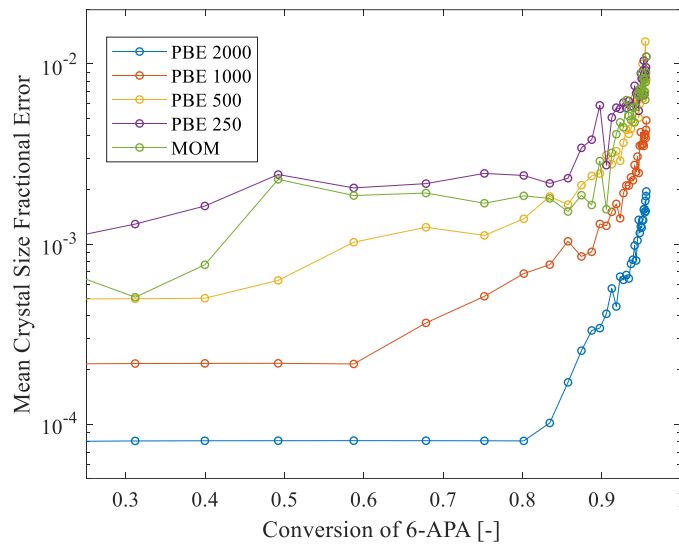


Figure 6.4. The fractional error of several different solutions to the population balance to determine mean crystal length (L_{43}) as a function of conversion. At higher conversion the error increases, however it is never more than 3%, even with the coarsest model (PBE 250) or the method of moments. In the legend, PBE indicates a complete solution of lines using the indicated number of bins to discretize the length domain. MOM indicates the method of moments

Determination of the maximum and minimum possible mean crystal sizes for reactive crystallizers in series was formulated as an optimization problem. The optimization was performed with the MATLAB nonlinear constrained optimizer *fmincon*.

Experimental solubility data, shown in Figure 6.2, were obtained by allowing a mixture with excess solids to equilibrate at constant temperature and pH before final optical rotation measurements were taken. The pH was adjusted with sodium hydroxide or

hydrochloric acid in an un-buffered solution. Ampicillin, cephalexin, 6-APA, and 7-ADCA were from TCI America, Portland OR. Phenylglycine came from Sigma-Aldrich, St. Louis MO. All chemicals were used as received.

6.4 Results and Discussion

In this section, results from the model are examined and discussed, focusing on the amoxicillin system as a case study. The attainable region for continuous reactive crystallization is compared to that for distinct reaction and separation. The attainable crystal size is determined for MSMPR units in series, and strategies for increasing crystal size are discussed. The tradeoffs between productivity and conversion are examined for reactive crystallization and the properties of the system that give rise to unique behavior are discussed. Tradeoffs between fractional yield and conversion are also discussed and used to construct a Pareto-optimal surface for all three attributes (conversion, productivity, and fractional yield). Finally, after characterizing the model with mixed-product removal and a fixed enzyme concentration, the effects of changing the product withdrawal mechanism and enzyme concentration are explored to further enhance process attributes.

6.4.1 Attainable regions

Solving the method of lines becomes computationally expensive when attempting to optimize continuous reactive crystallization over several process variables (pH, residence times, 6-APA concentration, HOPGME concentration). One method to reduce the size of this optimization problem is to construct an attainable region, a region that defines what steady state conversions of 6-APA and PGME can be achieved without

making assumptions about the underlying reactors, crystallizers, mixing and recycling, or process conditions.

To construct an attainable region for the conversion of 6-APA to amoxicillin trihydrate crystals, the reaction is assumed to be rate limiting, eliminating the need to consider the crystallization kinetics in the PBE. Accumulation of amoxicillin is kinetically controlled while crystallization of amoxicillin trihydrate can be kinetically or equilibrium controlled, depending on the slurry density or enzyme concentration. For the purpose of constructing an attainable region, it is assumed that any amoxicillin supersaturation generated by PGA is immediately incorporated into the crystal phase. Therefore, only the reaction and the solubility (crystallization equilibrium) need to be considered when determining the attainable region in conversion space (where conversion is defined as $X_{6\text{-APA}} = 1 - c_{Nu} / c_{Nu}^{feed}$, $X_{\text{HOPGME}} = 1 - c_S / c_S^{feed}$). Later, the impact of enzyme concentration will be explored, and it will be shown that these assumptions hold over a range of enzyme concentrations.

The attainable region was determined based on the geometric criteria put forth by Glasser and coworkers.¹⁶¹ At each point in HOPGME 6-APA conversion space, a reaction vector is calculated based on the rate equations 6.3 and 6.4. Only the direction of the reaction vector is important and factors that affect both reaction rates equally—the vector magnitude—such as enzyme concentration do not affect the attainable region. The attainable region is then obtained by drawing a curve from the feed conversion (in this case the origin, zero conversion) to the final steady-state conversion such that no vectors on the attainable region boundary point out of the attainable region and no reversed vectors

outside the attainable region point into the attainable region. The attainable region is then shifted to lower 6-APA conversion to account for the amoxicillin that does not crystallize and is unrecovered. The shift gives a slightly modified definition of 6-APA conversion, but for the purpose of an attainable region the shift more accurately represents the amount of amoxicillin that can be produced by a reactive crystallization process. This method is demonstrated in Figure 6.5. Figure 6.6.a shows the attainable region for a distinct reactor and separator, while Figure 6.6.b shows the same results for the reactive crystallizer.

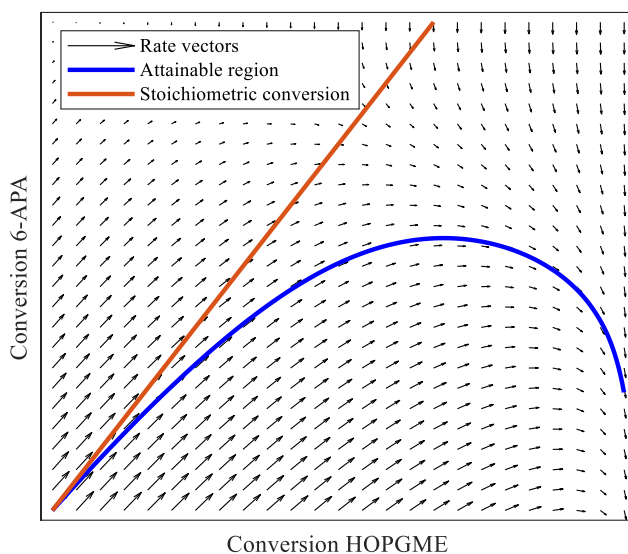


Figure 6.5. Demonstration of the geometric method for determination of the attainable region for the case of no crystallization, at pH 7 with 600 mM HOPGME and 400 mM 6-APA initially. The reaction vectors show the direction the system moves at each point in conversion space, the length of the arrow is proportional to the rate at which the system moves in that direction (however the attainable region is agnostic of rate). Only 3% of the calculated reaction vectors are shown for

readability. A line representing stoichiometric reaction of 6-APA and HOPGME is drawn to show how a perfectly selective enzyme would perform.

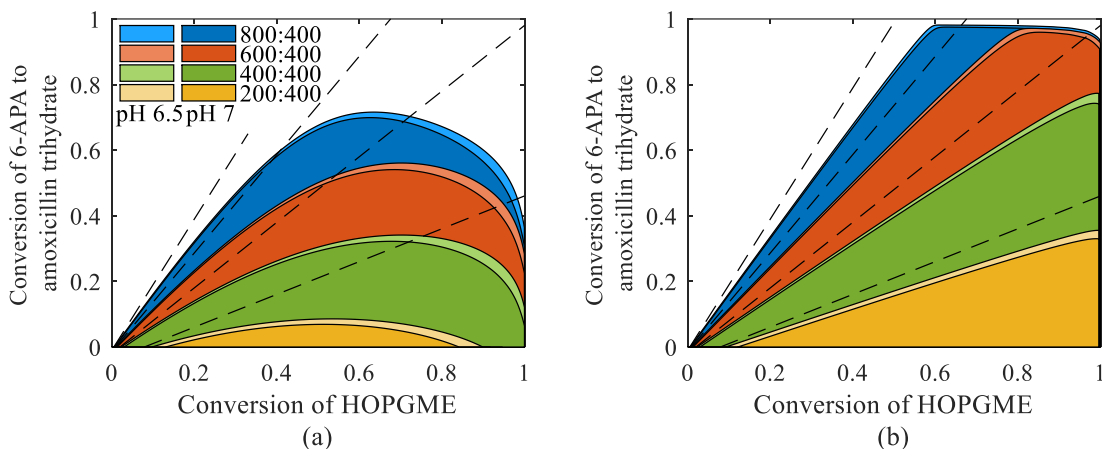


Figure 6.6. The attainable region for production of amoxicillin with PGA (a) in a distinct reactor and separator scheme and (b) with a reactive crystallizer. The attainable region is expressed in terms of HOPGME conversion and a modified 6-APA conversion that better captures how much product can actually be recovered: 6-APA converted into amoxicillin trihydrate. The 800:400 mM, 600:400 mM, 400:400 mM and 200:400 mM HOPGME:6-APA feed concentration ratios are shown in blue, red, green, and yellow, respectively. The light-colored region represents the attainable region at pH 6.5 and the dark color represents pH 7. The dashed lines represent stoichiometric conversion of HOPGME and 6-APA to amoxicillin.

The attainable region for the reactive crystallizer is larger than that for the distinct reactor and separator. The attainable region was determined for four concentration ratios of HOPGME:6-APA (200:400, 400:400, 600:400, and 800:400 mM, yellow, green, red, and blue) and at two pH values (6.5 and 7, light and dark shaded). The stoichiometric limit of 6-APA conversion is shown as a dashed line for each of the four different feed compositions; deviation below this line illustrates the imperfect selectivity of PGA. Complete conversion of HOPGME at a HOPGME: 6-APA ratio of unity is possible while complete conversion of 6-APA is not; HOPGME can hydrolyze while 6-APA can only react with HOPGME. For this reason, increasing the HOPGME:6-APA concentration ratio also increases the size of the attainable region since 6-APA generated by amoxicillin hydrolysis can be resynthesized into amoxicillin. The crystallization equilibrium also

means that amoxicillin saturation must be reached before any amoxicillin trihydrate can be formed. Therefore, at non-zero conversion of HOPGME it is possible to have zero conversion of 6-APA to amoxicillin trihydrate because amoxicillin saturation has not yet been achieved. The attainable region for the reactive crystallization process is larger because the crystallization isolates the product from the enzyme, reducing the rate of the secondary hydrolysis reaction and freeing enzyme to catalyze the desired reaction.

The attainable mean crystal size region was determined with the optimization technique developed by Vetter *et al.*¹⁶² modified to vary residence time to reach a specified conversion, rather than vary saturation concentration to reach a specified residence time. The optimization, which attempts to maximize or minimize the volume-weighted mean crystal size $\bar{L}_{43} = \mu_4 / \mu_3$, is defined in equation 6.24 below. $X_{Nu,k}$ $X_{Nu,k} = 1 - c_{Nu,k} / c_{Nu,k-1}$ is the conversion in the k^{th} reactive MSMPR, τ_k is the residence time in the k^{th} reactive MSMPR, X_{Nu} is the overall conversion, and K is the total number of MSMPRs. The maximization does not include any aggregation, as aggregation was not observed experimentally. The minimization does not include any milling or grinding, processes which could be implemented to further reduce the average crystal size. The optimization also does not consider the use of fines removal or classified product removal to further enhance product size, although this will be considered later in the paper. Figure 6.7.a shows the attainable volume-weighted mean crystal size for one, two, and three MSMPRs in series as a function of conversion for a feed composition of 800 mM HOPGME and 400 mM 6-APA.

$$\begin{aligned} & \text{maximize / minimize } \bar{L}_{43} \\ & \text{subject to } \sum_{k=1}^K X_{Nu,k} = X_{Nu} \end{aligned} \quad (6.24)$$

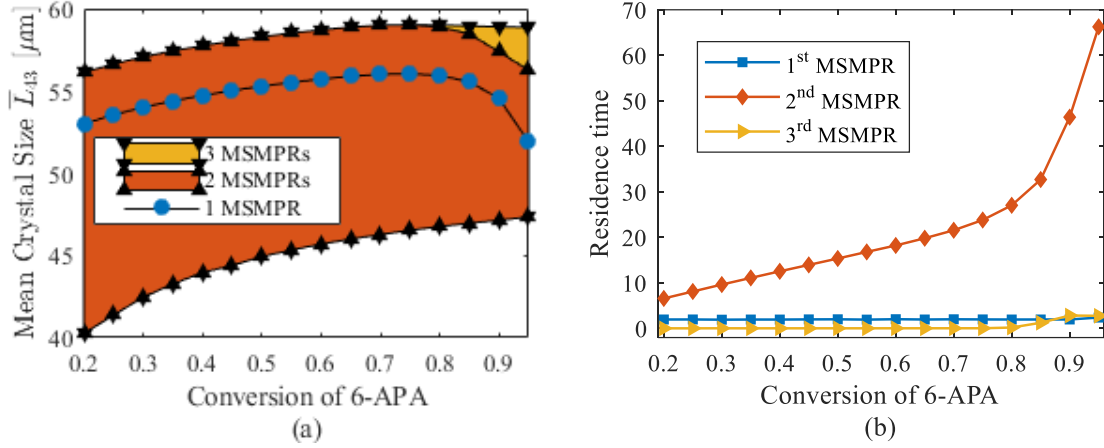


Figure 6.7. (a) the bounds of attainable mean crystal sizes for one, two, and three MSMPRs in series (● – 1 MSMPR, ▲ – 2 MSMPRs, ▼ – 3 MSMPRs). (b) the breakdown of the residence time of each MSMPR in a series of three MSMPRs (■ – 1st MSMPR, ◆ – 2nd MSMPR, ► – 3rd MSMPR) to reach the maximum mean crystal size. The feed concentrations are 800 mM HOPGME, 400 mM 6-APA, and steady state pH of 7.0.

Initially, as the conversion increases, the range of crystal sizes shifts towards larger mean size, but at high conversion the attainable region rapidly narrows. A single MSMPR has a defined mean crystal size at each conversion (shown by the blue circles in Figure 6.7.a) because there is only a single residence time that can achieve that particular conversion (there are no degrees of freedom). With two MSMPRs in series, the second residence time adds an additional degree of freedom. Figure 6.7.b shows how the residence times are allocated to meet the specified conversion to maximize the mean crystal size with three MSMPRs in series. The maximum conversion examined is 97% the maximum possible conversion determined by the attainable region in Figure 6.6.b; higher conversion requires significantly more residence time.

The crystal size is maximized when the first MSMPR operates as a seed generator with high supersaturation and short residence time. The second MSMPR operates at low supersaturation to grow the crystals and reach the desired conversion. The minimum crystal size is achieved with the opposite heuristic, with a large seed generating MSMPR and small growth MSMPR, although both phenomena occur in all MSMPRs. The addition of a third MSMPR does not significantly increase the mean crystal size at low to moderate conversion and therefore has negligible residence time over that conversion range. At high conversion the optimal configuration adds a small vessel (<5% total residence time) with higher supersaturation than the second vessel to the end of the first two vessels in series to further boost mean size. In the case of the three MSMPR cascade, two optimal solutions exist in addition to the solution shown in Figure 6.7.b. Both additional solutions are degenerate forms of the solution shown in Figure 6.7.b. In the regime where the third MSMPR has negligible volume, the three MSMPR cascade reduces to a two MSMPR cascade. The two other solutions result from the elimination of the first or second MSMPR, giving two MSMPR cascades equivalent to that shown in Figure 6.7.b. Where the third MSMPR has significant volume (conversion > 0.8) only the solution drawn in Figure 6.7.b is optimal.

6.4.2 *Pareto-optimal fronts*

To determine the bounds on productivity, selectivity, and conversion, Levenspiel plots (plots of the reciprocal reaction rate, R_p^{-1} , versus concentration or conversion) are drawn based on the reaction rate in equation 6.1.¹⁶³ The Levenspiel plot is reactor design agnostic (including whether the process is continuous or batch) and useful for visualizing

reactor sizing because the area under the curve is related to the reactor size. In Figure 6.8.a both the distinct reaction and separation (dashed curves) and reactive crystallization (solid curves) are considered for the four feed concentration ratios at pH 7. Figure 6.8.b is a zoomed-in version of Figure 6.8.a for the 800:400 mM HOPGME:6-APA curve, with additional curves drawn to highlight different aspects of the enzymatic reactive crystallization system.

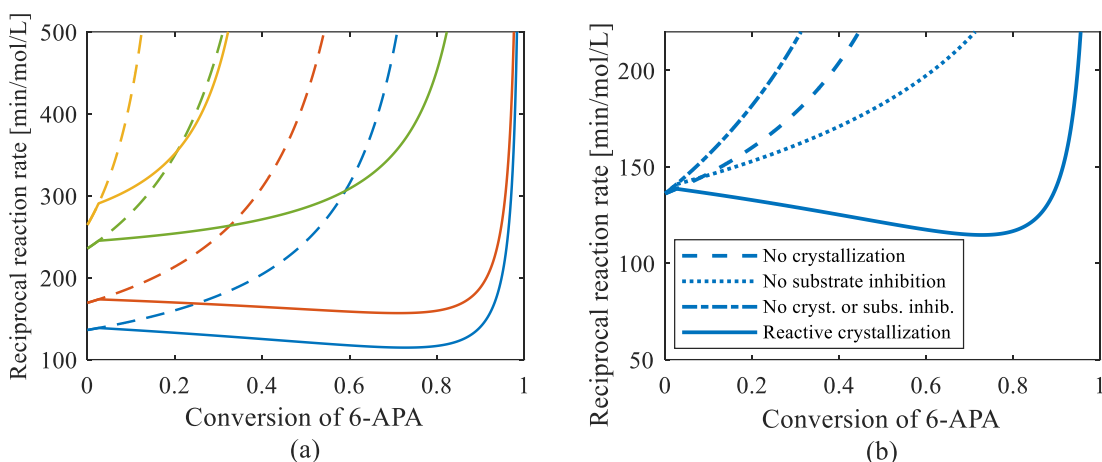


Figure 6.8. (a) the Levenspiel plot for amoxicillin production at 800:400 mM, 600:400 mM, 400:400 mM, 200:400 mM HOPGME:6-APA feed concentration ratios (blue, red, green, yellow, respectively) in a reactive crystallizer (solid curves) and a distinct reactor and separator (dashed curves). (b) Close-up of (a) for the 800:400 ratio; the dashed curve is the distinct reactor and separator, the dotted curve simulates a hypothetical variant of PGA without substrate inhibition by 6-APA, and dash-dot curve neither crystallizes nor has substrate inhibition, and the solid curve is reactive crystallization.

The reactor and reactive crystallizer have markedly different reciprocal rate curves. The reactor (dashed curves in Figure 6.8.a) shows the expected approximately first-order reaction behavior with a convex monotonic increasing reciprocal rate curve; an asymptote, corresponding to the conversion at which amoxicillin degradation outpaces amoxicillin synthesis can be seen for each curve. The reactive crystallizer has a more complex curve. At low conversion, the curves for the reactor and reactive crystallizer overlap; this beginning region represents conversion below that needed to generate amoxicillin

supersaturation and drive trihydrate crystallization. The downward sloping curve beyond the saturation concentration is the result of a combination of relief of substrate inhibition by 6-APA and relatively constant amoxicillin concentration. As 6-APA is consumed, the enzyme-nucleophile dead-end complex (see ENu in Figure 6.1) is less likely to form, increasing the concentration of free active enzyme. Additionally, the concentration of amoxicillin that can be hydrolyzed by the enzyme remains constant at the saturation concentration, resulting in less enzyme-product complex (EP) and less drag on the synthesis reaction moving forward. Figure 6.8.b shows Levenspiel plots when the substrate inhibition is removed, showing both the reactor and reactive crystallizer behaving more like first-order reactions. Both the sequestration of product in the crystal phase and the alleviation of substrate inhibition are necessary to explain the decrease in reciprocal rate at conversions between 5% and 73%. Above 73% conversion, the nucleophile concentration has been depleted to the point that substrate inhibition by 6-APA starts becoming unimportant and the rate rapidly decreases with increasing nucleophile consumption.

The results of the attainable mean crystal size region are also reflected in the Levenspiel plot results. Figure 6.9.a demonstrates how a Levenspiel plot can be used to size reactive MSMPRs (rectangles), plug flow reactors (dashed-line bounded area under the curve), and vessels in series. The vessels in series represent the reactive MSMPR series determined in Figure 6.7.b. The first reactor in the MSMPR cascade in Figure 6.7.b is small, and only handles the low conversion required to reach saturation and trigger nucleation. The second MSMPR, which is much larger, predominantly operates over the downward sloping section of the Levenspiel plot where mixing is advantageous. The third MSMPR makes use of the part of the plot where the slope switches back to being positive

and back-mixing no longer improves productivity. However, as discussed below, this arrangement of reactors does not give the optimal productivity or fractional yield, but only the maximum mean crystal size.

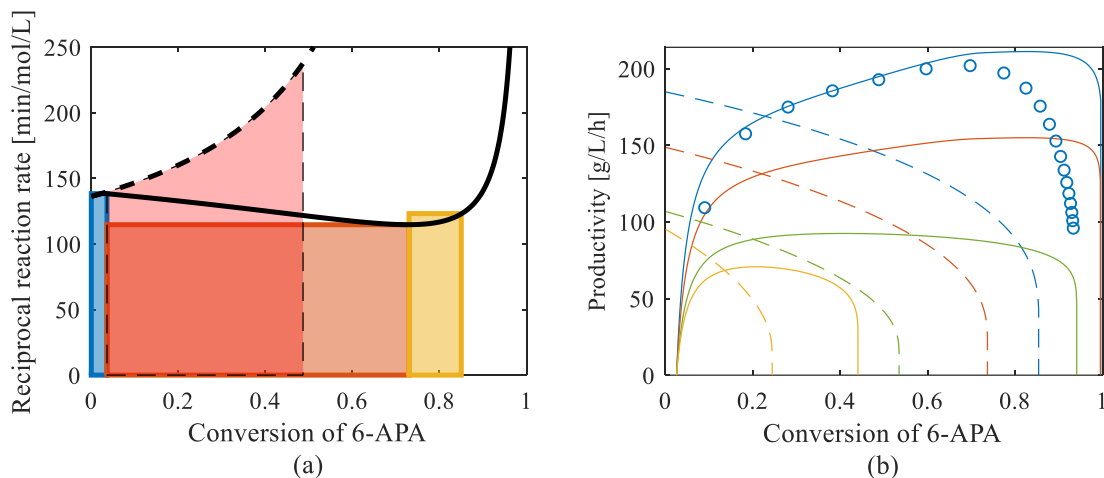


Figure 6.9. (a): Sizing a series of reactive MSMPRs, rectangles, and a plug flow reactive crystallizer, dash-outlined area under the curve, to achieve a desired conversion using the Levenspiel plots from Figure 6.8, in this case the 800:400 HOPGME:6-APA feed concentration ratio. (b) The Pareto-optimal front for productivity and conversion of 6-APA at 800:400 mM, 600:400 mM, 400:400 mM, 200:400 mM HOPGME:6-APA feed concentration ratios (blue, red, green, yellow, respectively) in a reactive crystallizer (solid lines) and a distinct reactor and separator (dashed lines). The data points are the result of solving the entire PBE for the 800:400 mM, pH 7.0 case.

The consequences of the atypical Levenspiel plot (Figure 6.9.a) manifest themselves in the Pareto front for productivity and conversion (Figure 6.9.b). As mentioned above, the reactor size is related to the area under the curve in a Levenspiel plot. The residence time of a continuous stirred tank is equal to the area of the rectangle bounded by the feed conversion, outlet conversion, abscissa, and reciprocal reaction rate at the outlet conversion. The residence time of a plug flow reactor is equal to the area under the curve bounded by the feed and outlet conversions. Therefore, a continuous stirred tank has a smaller residence time than a plug flow reactor on decreasing Levenspiel curves while the opposite is true on increasing Levenspiel curves. The Levenspiel curve decreases for reactive crystallization but increases for distinct reaction and separation, therefore a well-

mixed reactor is preferred for reactive crystallization while a plug flow reactor is more efficient when the product is not protected by crystallization. The red rectangle in Figure 6.9.a demonstrates sizing a single reactive MSMPR to achieve 70% conversion and has a residence time of 32 minutes. The red area under the curve illustrates that the same residence time as the reactive MSMPR for the distinct reaction and separation, even with the optimal plug flow reactor geometry, only reaches 48% conversion.

The minimum residence time to achieve a set conversion can be found by sizing a series of vessels (both well-mixed and plug flow) on a single Levenspiel plot and recognizing that stirred tanks are preferred on downward sloping sections and plug flow vessels are preferred on upward sloping regions. Somewhat unintuitive for an approximately first-order reaction, the well-mixed reactive crystallizer shows superior performance to that of a plug-flow reactor. This is again the result of the enzyme turning over faster at lower 6-APA concentrations and of reactive crystallization.

The Pareto front of productivity (P) and conversion (X_{Nu}) can be easily computed with the definition of productivity $P = c_{Nu}^{feed} X_{Nu} / \tau$ and the minimum residence time (τ) determined geometrically with the Levenspiel plot as a function of conversion. In Figure 6.9.b the productivity is low at low conversion, because the first 5% of 6-APA conversion goes towards saturating amoxicillin to produce amoxicillin trihydrate. At higher conversion the productivity continues to increase, uncharacteristically for a first order reaction, due to the downward sloping Levenspiel plot. For the distinct reactor and separator, the productivity is highest at low conversion; no assumption has been made about the separator. Therefore, losses to the mother liquor are not included as they are for

the reactive crystallizer (i.e. supersaturation does not need to be generated). At conversion greater than approximately 25%, even with a perfect separator, the benefits of reactive crystallization to productivity outweigh the losses of un-crystallized amoxicillin in the mother liquor.

The markers in Figure 6.9.b show that the results for the full PBE solution with the method of lines corroborated with the method of moments follow the simplified trend well up until very high conversion. Due to the values of the kinetic constants and the feed concentrations, the boundary of the attainable region is approached asymptotically despite the fact that the reaction rate (and Levenspiel curve) is defined over the entire range of conversions. At high conversions the process begins to run up against the edge of the attainable region, which is not considered when constructing the Levenspiel plot which gives the appearance that all conversions are reachable. Solving the entire PBE with the method of lines and method of moments repeatedly for all process conditions and conversions is prohibited by the large computational cost, however the attainable region has been computed for all process conditions and similar behavior is expected close to the edge of each attainable region.

Figure 6.8.a suggests that the optimal reactor for an equimolar feed or excess 6-APA (green and yellow curves) is a single plug flow geometry because the Levenspiel curves are always increasing. In practice some degree of back-mixing or recycling would greatly improve the plug flow geometry to supply seed crystals once the conversion reaches amoxicillin saturation. The optimal network of reactive crystallizers with excess HOPGME (Figure 6.8.a, blue and red curves) would consist of a MSMPR feeding a plug-flow reactive crystallizer; however, based on the attainable region determined in Figure

6.6, the addition of the plug-flow reactive crystallizer could, at best, increase the conversion another 16%. Additionally, operating MSMPRs in series would also result in sub-optimal productivity, the added volume would not be as well utilized as a plug flow reactive crystallizer based on the upward slope of the Levenspiel plot. However, the mean crystal size would increase approximately 10% with MSMPRs in series, according to Figure 6.7.a.

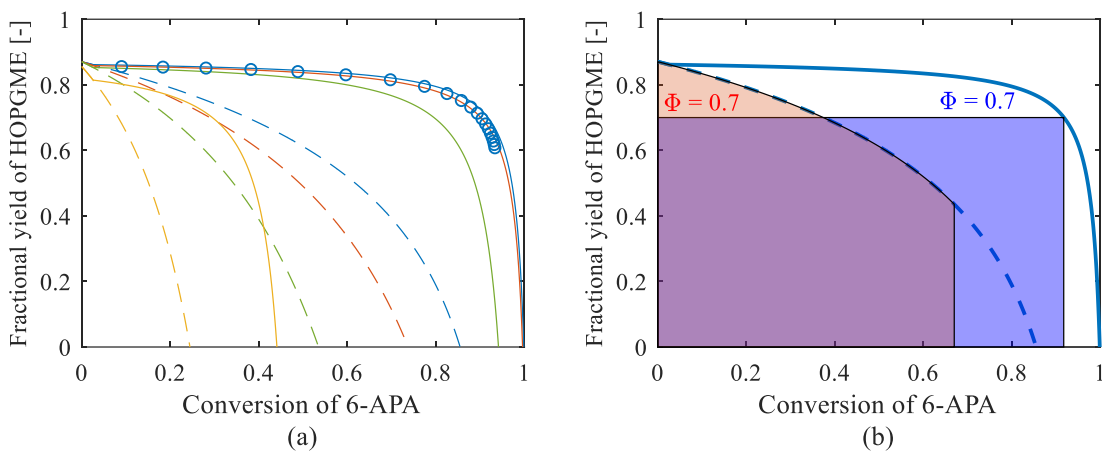


Figure 6.10. (a) fractional yield as a function of conversion for reactive crystallizers (solid curves) and distinct reactor and separators (dashed curves) at four different feed concentration ratios: 800:400 mM, 600:400 mM, 400:400 mM, 200:400 mM HOPGME:6-APA (blue, red, green, yellow, respectively). (b) reactor geometry considerations based on fractional yield of HOPGME. Solid curves are reactive crystallization, dashed curves are distinct reaction and separation.

Fractional yield can be equally as important depending on the relative cost of the reactants. If the excess reactant (HOPGME) and limiting reactant (6-APA) are costed similarly, then the fractional yield becomes an important design criterion. Even if the cost of 6-APA is much greater than HOPGME, fractional yield can play an important role in designing the process to avoid accumulation of impurities and byproducts. The overall fractional yield (Φ) is the amount of amoxicillin produced per amount of HOPGME consumed on a per mole basis. Figure 6.10.a shows the fractional yield versus conversion for reactive crystallization (solid curve) and distinct reaction and separation (dashed curve) at an initial feed concentration ratio of 800:400 mM HOPGME:6-APA. Figure 6.10.b also

demonstrates how reactor geometry considerations can be determined graphically; a reactive crystallizer with perfect back-mixing (blue rectangle) and plug-flow reactor without crystallization (red area under curve) are both sized to achieve an overall fractional yield $\Phi = 0.70$. The overall fractional conversion of the well-mixed reactive crystallizer is determined by the output conversion on the fractional yield curve, while the overall fractional yield of the plug flow reactive crystallizer is the average of the fractional yield curve over the inlet to outlet conversion range.¹⁶⁴ The plug flow geometry generally has superior overall fractional yield compared to a stirred tank when the fractional yield is monotonically decreasing with conversion, as is the case here. However, the reactive crystallization scheme shows that an MSMPR system operating at 91% conversion has the same overall fractional yield as a non-crystallizing plug flow reactor operating at 67% conversion, despite the inherent superiority of the plug flow design. Figure 6.10.a shows the fractional yield Pareto-optimal front for the other feed concentration ratios. Figure 6.10.a also shows that the results from solving the full PBE (data points) align well with the simplified calculations, only deviating at high conversion where the edge of the attainable region is not considered.

A Pareto-optimal surface can be constructed by combining the graphical approaches presented for the determination of the Pareto-optimal fronts for productivity and conversion, together with fractional yield and conversion. The blue region in Figure 6.11 represents the attainable productivity and selectivity at different 6-APA conversions, shown by the white curves, for a concentration feed ratio of 800:400 mM HOPGME:6-APA at pH 7. As was shown in Figure 6.9, the highest productivity can be attained at a 6-APA conversion between 0.7 and 0.75. The surface shows that, at a conversion of 0.75,

approximately 20 g/L/h of productivity can be sacrificed to increase the fractional yield from 81% to 84%, demonstrated by following the white curve labeled 0.75 from right to left. At high conversion (e.g. 0.875) the productivity and fractional yield can both be improved simultaneously, which is a result of requiring additional vessels in series or a plug flow reactive crystallizer to maximize productivity at high conversion (see Figure 6.8).

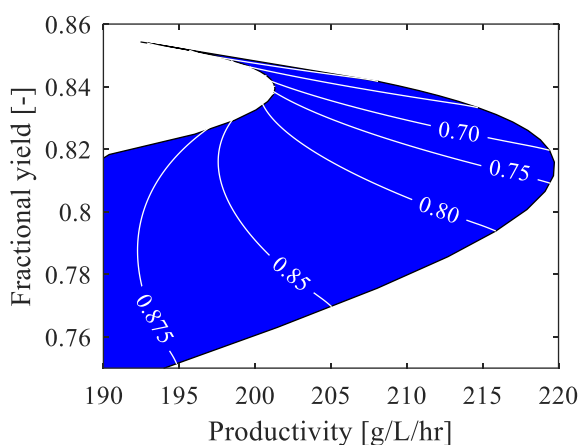


Figure 6.11. The Pareto-optimal surface for 6-APA conversion, productivity, and fractional yield for the reactive crystallization of amoxicillin. The blue region represents the attainable fractional yield as a function of productivity. The white curves represent constant conversion of 6-APA.

6.4.3 Further improvements

Two additional unexplored avenues to increase the mean crystal size are classified fines removal (CFR) and variable enzyme concentration.

The crystal residence time dependence on crystal size can be used to implement classified fines removal. By preferentially removing small crystals or fines from the crystallizer, the mean crystal size is increased significantly.^{54, 165-167} At steady state, fines are the dominant crystal based on number fraction, however, they make up only a few percent of the total mass of the crystals. Removing the crystals smaller than 10 μm at three

times the rate of crystals larger than $10\ \mu\text{m}$ increases the mean crystal size in a single vessel by 33%, from $54.0\ \mu\text{m}$ to $71.8\ \mu\text{m}$, while decreasing the yield 1.2% (this yield loss could be removed by introducing a fines dissolver and recycling the solute). Figure 6.12 shows the volume-weighted crystal size distribution with and without fines removal. A consequence of the fines removal is the broadening of the CSD, as can be seen in Figure 6.12. A compromise between large mean crystal size and narrowness of the CSD must be reached. As discussed in CHAPTER 5, the broadening of the size distribution as a result of Growth Rate Dispersion must also be considered.

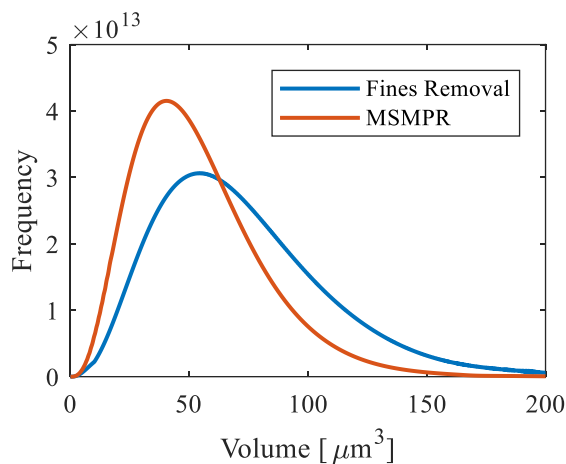


Figure 6.12. The CSD for a reactive MSMPR (red) and a reactive crystallizer with fines removal.

All of the results presented above were determined with an enzyme concentration of $5\ \mu\text{M}$. Changing the enzyme concentration could be a potential means of further improving process attributes such as fractional yield, mean crystal size, and productivity. Figure 6.13 shows that, relative to the $5\ \mu\text{M}$ standard PGA concentration, increasing the enzyme concentration further increases the mean crystal size slightly and the productivity considerably while barely decreasing the fractional yield. The increased size is a result of higher supersaturation in the reactive crystallizer (which also causes the negligible decrease

in fractional yield). The large increase in productivity is not a surprising result; if presented on a per-gram-catalyst basis the productivity is the same at all four PGA concentrations investigated. To maximize productivity on a per-liter basis the highest PGA concentration feasible should be used, however, unmodeled physical phenomena, such as enzyme separation and aggregated enzyme contamination that limit the active concentration. The enzyme is also costly, which limits how much enzyme should be used.

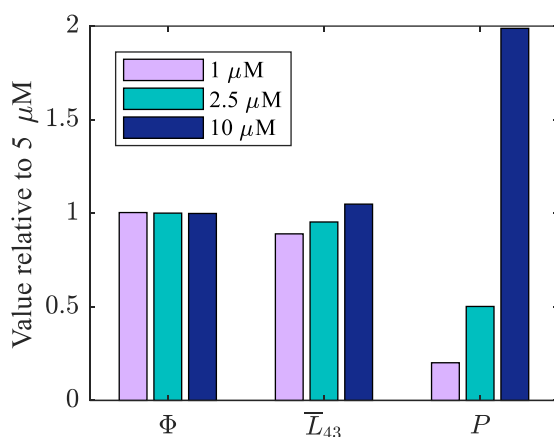


Figure 6.13. The effects of changing the enzyme concentration on the fractional yield (Φ), mean crystal size (\bar{L}_{43}), and productivity (P). The values of these attributes are shown relative to the value found with an enzyme concentration of 5 μM and a conversion of 70%. 1.0 μM , 2.5 μM , and 10 μM are shown in lavender, teal, and navy, respectively.

The concentration of active enzyme also changes with time as the enzyme decays. At the selected operating condition of 298 K the enzyme loses negligible activity over 1,000 residence times at maximum productivity (201 g/L/h at 298 K). At elevated temperatures the enzyme stability decreases but the activity increases. The half-life of the enzyme drops to only 4 days if the temperature is increased to 318 K, which could significantly increase operating costs despite the expected increase in activity.

6.5 Conclusion

A model is developed for the simulation of continuous reactive crystallization of β -lactam antibiotics catalyzed by penicillin G acylase. To the authors' knowledge, this is the first model of continuous reactive crystallization with an enzymatic reaction. Attainable regions showed that a maximum conversion of 6-APA to amoxicillin of 98% was reachable with an excess of HOPGME of 400 mM and a reactive crystallizer, while only 72% conversion of 6-APA was possible under the same reaction conditions without crystallization. Attainable crystal size regions showed that the use of MSMPR crystallizers in series could boost the mean size by 5 μm , but at the cost of increased residence time.

Classical chemical engineering techniques for process design were used to develop a more detailed understanding of the continuous reactive crystallization system. Levenspiel plots showed that an MSMPR is desired to maximize productivity when the conversion of 6-APA was between 10% and 73%, with an excess of HOPGME. The back-mixing increases productivity by two mechanisms: first by seeding the reactor so that crystallization is equilibrium controlled, and second by alleviating substrate inhibition by operating at lower 6-APA concentrations than in the feed. Interestingly, neither of these two mechanisms is substantive enough to favor a well-mixed system over a plug-flow system by themselves, but together a well-mixed reactive crystallizer becomes more productive.

A Pareto optimal surface for productivity, fractional yield, and conversion was calculated. As the 6-APA conversion is increased up to 87%, both productivity and fractional yield decrease. However, at conversions greater than 87%, the productivity and fractional yield are maximized at the same operating conditions. The Pareto optimal fronts calculated with the simplifying assumptions regarding equilibrium control of

crystallization agree well with those calculated with the computationally expensive population balance equations. The Pareto optimal surface will help inform design of an optimal operation, depending on process variables such as reactant costs, capital costs, and enzyme costs.

CHAPTER 7. IMPLICATIONS OF THE REACTIVE CRYSTALLIZER MODEL: A CASE STUDY ON PRODUCT PURITY⁶

7.1 Introduction

In the previous chapter a detailed model was built for the continuous manufacturing process for the reactive crystallization of beta-lactams. The bounds on the achievable process metrics (conversion, productivity, and fractional yield) were given in the form of a Pareto-optimal surface. However, one of the most important design constraints is missing from the discussion in CHAPTER 6, product purity. In the case of amoxicillin this is not a significant issue because, as shown in Figure 6.2, HOPG is nearly three times as soluble as phenylglycine and optimizing for the three process metrics (conversion, selectivity, and productivity) alone prevents crystallization of HOPG. This is not the case for cephalexin or the favored model beta-lactam ampicillin.¹⁵⁸ While the antibiotic could be separated from an insoluble contaminant with a downstream separation, a process design in which further purification is not required is more economical and robust.

For cephalexin the purity of the product is more difficult to ensure when optimizing for the other three process metrics. In this chapter, the design for an optimal plant producing

⁶ Adapted from “Computers & Chemical Engineering, 126, McDonald, M.A.; Bommarius, A.S.; Grover, M.A.; Rousseau, R.W. Continuous reactive crystallization of β -lactam antibiotics catalyzed by penicillin G acylase. Part II: Case study on ampicillin and product purity, 332-341.” Copyright (2019), with permission from Elsevier.

1,600 kg/day of cephalexin, roughly 10% of global demand, is developed (for reference, as of 2019 there are only three FDA-approved cephalexin manufacturers).¹⁶⁸

Continuous manufacturing is a design benefit for ensuring product quality, not a design hurdle that must be overcome. As of 2019, five drugs have received FDA approval to transition from batch to continuous manufacturing (among them, Orkambi® (lumacaftor/ivacaftor) and Symdeko® (tezacaftor/ivacaftor), both Vertex, 2015 and 2018, Prezista® (darunavir), Janssen Pharmaceuticals 2016, prexasertib and Verzenio® (abemaciclib), both Eli Lilly, 2017; improved reliability and quality were key factors in each decision.¹⁶⁹ Cephalexin, and amoxicillin, could be the next drugs to transition to CM.

The model used in this chapter is the same as the previous chapter, but complemented with a second population balance to account of the crystallization of phenylglycine. The second population balance is solved with the moment transformation because, unlike for the antibiotic product, the details of the crystal size distribution (CSD) of the byproduct are not considered. Only the operating space where phenylglycine does not crystallize is suitable for antibiotic production. The moments of the phenylglycine population balance are solved simultaneously with the moments of the ampicillin population balance. It is assumed that the crystal phases of the two species do not interact (i.e. they do not agglomerate nor does the presence of one crystal promote or inhibit nucleation or growth of the other), although rigorous experimentation should be performed to confirm the non-interaction. The crystallization parameters needed for both population balances are reported in Table 7.1 (note the ampicillin column is redundant from the previous chapter).

Table 7.1. The parameter values used to model the crystallization of ampicillin and byproduct phenylglycine.^{89, 170} Notes: ^a values for phenylalanine anhydrate used in place of phenylglycine, the

crystallization kinetics of phenylglycine anhydrate have not been published but based on experiments during the course of this thesis they can be approximated satisfactorily with the similar molecule phenylalanine.

Parameter	Ampicillin trihydrate	Phenylglycine	Units
c_{pl}^*	20.5	35.0	mmol L ⁻¹
pK_a^0	7.35	8.70	-
z	0	0	-
k_G	8.95	5.10 ^a	μm min ⁻¹
g	1.87	1.76 ^a	-
k_{B1}	5.00 × 10 ¹⁰	7.0 × 10 ^{10 a}	L ⁻¹ min ⁻¹
B^o	1.27	1.95 ^a	-
k_{B2}	2.20 × 10 ⁹	2.36 × 10 ^{8 a}	L ⁻¹ min ⁻¹
m	0.60	1.84 ^a	-
b	1.37	1.92 ^a	-
k_V	0.03	0.10	-
ρ	1.5 × 10 ⁻¹²	1.3 × 10 ⁻¹²	g μm ⁻³

7.2 Results and Discussion

7.2.1 Well-mixed enzymatic reactive crystallizer

Attainable regions for ampicillin trihydrate production were constructed to place bounds on the feasible conversion of 6-APA to antibiotic. The same methodology was used in the previous chapter, but here an additional constraint on the attainable region was added to account for potential phenylglycine crystallizing and contaminating the product stream. Briefly, a reaction vector is drawn at each point in conversion space, using equations 6.3 and 6.4, and the attainable region boundary is drawn from the feed point (in the present study, zero conversion of 6-APA or PGME) along the tangents of the rate vectors. Ampicillin produced while ampicillin is under-saturated is removed from the attainable region because it does not contribute to the production of ampicillin trihydrate

crystals. The ampicillin under-saturation region accounts for the first 5% of 6-APA conversion, therefore the entire region is then shifted 5% down in 6-APA conversion. Finally, the area where the amount of PGME converted is greater than the amount of 6-APA converted less the saturation of phenylglycine ($X_S > X_{Nu} - c_B^*/c_{S,feed}$), is removed from the attainable region because it corresponds to the phenylglycine supersaturation region.

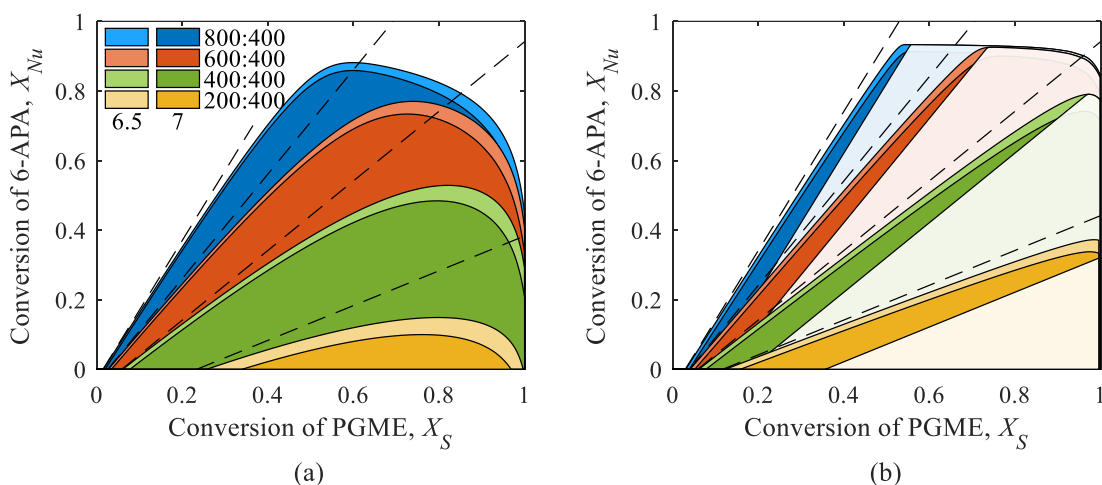


Figure 7.1. The attainable regions, in the PGME 6-APA conversion space, for ampicillin produced without *in situ* crystallization (a) and ampicillin produced by reactive crystallization (b). The blue, red, green, and yellow regions represent 800:400, 600:400, 400:400, and 200:400 mM PGME:6-APA initial/feed concentrations. The light-colored regions are at pH 6.5 and the dark colored regions are at pH 7.0. The dashed black lines represent stoichiometric conversion of PGME and 6-APA to ampicillin. The white-washed (lightest colored) regions on the right represent the regime in which phenylglycine and ampicillin crystallize simultaneously, jeopardizing product purity.

In Figure 7.1, the attainable region for ampicillin synthesis by PGA without *in situ* crystallization (left) is much larger than that for reactive crystallization (right), in contrast to the result for amoxicillin (CHAPTER 6). The large size of the non-crystallizing attainable regions (compared to that for amoxicillin) can be attributed to the slower rate of hydrolysis of ampicillin compared to amoxicillin. The small size of the reactive

crystallization attainable region is the result of the low solubility of phenylglycine (35 and 36 mM at pH 6.5 and 7, respectively). No assumption is made regarding the separation of ampicillin in the non-reactive-crystallizing system, therefore, the potential crystallization of phenylglycine is not considered a restriction on the non-crystallizing attainable region (e.g. phenylglycine crystallization may not effect membrane-based purification of ampicillin¹⁷¹). As the maximum conversion of 6-APA is similar in both Figure 7.1.a and 2.b (88% versus 93%), the advantages of reactive crystallization for ampicillin synthesis are rooted in productivity and simplicity of process design as opposed to improved conversion/yield, as was the case for amoxicillin (CHAPTER 6).

Previously, it was shown that the productivity of amoxicillin is optimized with a single well-mixed reactive crystallizer tuned to a specific residence time and enzyme concentration.²¹ A similar setup can be sized for ampicillin, which due to small differences in the enzyme reaction kinetics, has a slightly different optimal residence time. In Figure 7.2, a plot of productivity versus residence time of a single reactive MSMR (at a fixed enzyme concentration) shows that a maximum productivity of 191 g/L/h is attained at a residence time of 42.0 minutes for a PGME:6-APA feed concentration ratio of 800:400 mM. For comparison, amoxicillin productivity under the same conditions is 6% greater on a per mole basis at a residence time of 38.0 minutes. The dashed lines in Figure 7.2 denote the productivity of the distinct reactor and separator; no assumptions about the method of separation are made, perfect separation is assumed here. Therefore, no loss of ampicillin to the spent solvent (which results in the initial lack of productivity for reactive crystallization) is included in the distinct reactor and separator.

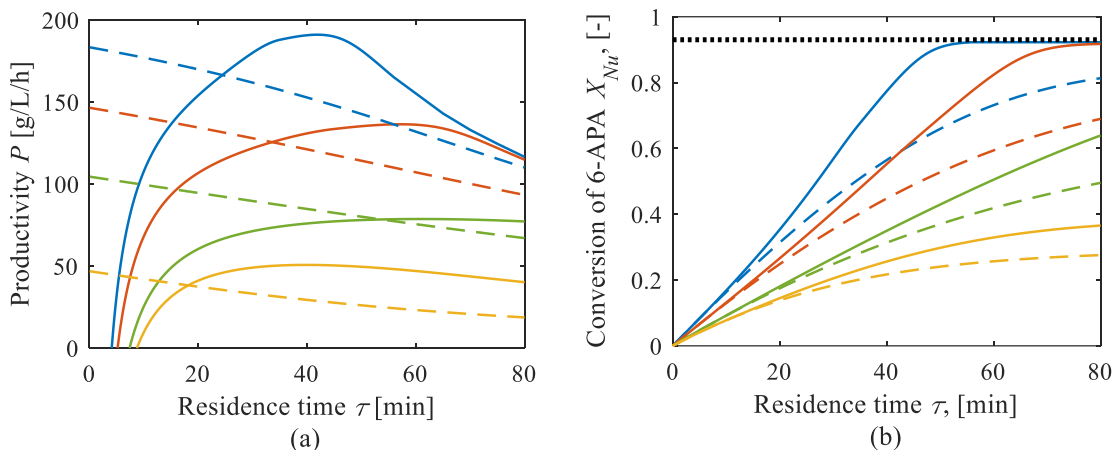


Figure 7.2. (a) the productivity of a reactive MSMPR (solid) and non-crystallizing well-mixed reactor (dashed) for different residence times and feed concentration ratios. (b) the conversion of 6-APA in a reactive MSMPR (solid) and non-crystallizing well-mixed reactor (dashed) for different residence times and feed concentration ratios (blue 800:400, red 600:400, green 400:400, yellow 200:400 mM PGME:6-APA). The black dotted line represents the maximum conversion, as shown in Figure 7.1.

Figure 7.2.a shows that the productivity in a reactive MSMPR for the 800:400 mM ratio is 40% higher than the 600:400 feed ratio and 140% higher than the 400:400 feed ratio. Figure 7.2.b shows that, while both the 800:400 and 600:400 feed ratio reach the maximum conversion in a reactive MSMPR (dotted black line), the 800:400 feed ratio reaches maximum conversion appreciably faster. From this point forward only the highest feed concentration ratio of PGME to 6-APA, 800:400 mM, will be considered because it gives the highest productivity and yield in a reactive MSMPR.

However, Figure 7.1.b showed that the attainable region for 800:400 PGME:6-APA only extends to 55% conversion of PGME. Therefore, a significant amount of the feed PGME will go unreacted in favor of high conversion of 6-APA, good productivity, and >99.99% purity. A possible process improvement not considered in the present study would be to recycle the unreacted PGME. A PGME recycle would enable part of the unreacted 45% of PGME to be used to convert additional 6-APA. This would enable the

process to use a smaller excess of PGME while still maintaining the reactive crystallization benefits of an 800:400 PGME:6-APA ratio. While the means of PGME recycle has not been studied here, selective removal of the phenylglycine, possibly by crystallization, could enable reuse of the PGME-containing mother liquor, which would have the added benefit of recovering additional antibiotic from the mother liquor as well. Both the productivity and conversion (Figure 7.2.a and 3.b) should be considered in the final design of a continuous process, which metric is more important depends on specific economics.

The optimal conditions are also sensitive to variations in operating conditions. Tight process control, particularly on temperature and residence time, which have an outsized impact on the process metrics, is recommended to maintain optimal steady state performance. For instance, at elevated temperature, the reaction rate increases, increasing the optimal productivity, however the solubility also increases, decreasing the optimal conversion. Purity, which is the most important process metric, can take on multiple steady states if the process is not adequately controlled.

7.2.2 Steady state multiplicity in reactive MSMPRs

In many cases, a supersaturated solution of phenylglycine exits the reactive MSMPR, and the relationship between that supersaturation and phenylglycine nucleation kinetics determines the state of the system. If the phenylglycine suspension density is negligible (say < 0.03 g/L), new crystals will be formed predominantly by primary nucleation and removed from the crystallizer without the formation of substantial crystal mass. On the other hand, a significant phenylglycine suspension density increases the rate of secondary nucleation, which will generate phenylglycine crystals to accommodate the

rate at which they are removed. In the latter of these two cases, an impure product stream will ensue. While both steady states are stable, it is possible for a disruption to trigger the process to transition from the favorable to the unfavorable steady state. Reverting from the unfavorable back to the favorable steady state is difficult because a large mass of phenylglycine crystals must be washed out of the crystallizer. External disturbances, as well as uncertainty in parameter estimation, require the design of a robust process for pure ampicillin production.

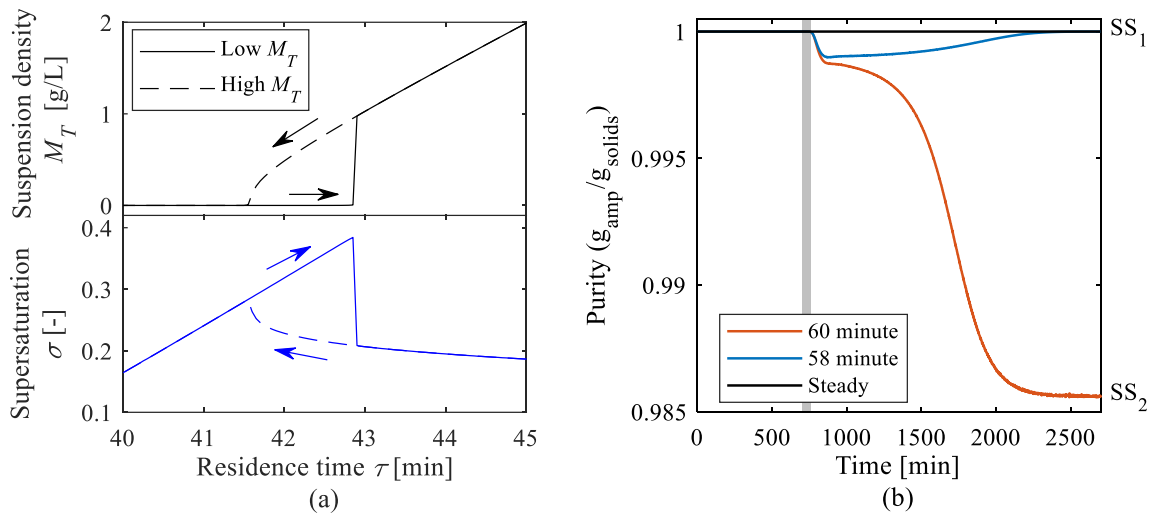


Figure 7.3. (a) The coexistence of two steady states over the range of residence times from 41.5 to 43 minutes, demonstrated by the hysteresis of the phenylglycine suspension density, M_T (top) and supersaturation, σ (bottom). The solid curves were generated by reaching steady state from a low suspension density initial state, and the dashed curves are from a high suspension density initial state. (b) A perturbation in the residence time of 5%, lasting 58 minutes and 60 minutes, leading the process to slowly decay back to the high-purity steady state and jump to the low-purity steady state, respectively. The noise at the second steady state in (b) stems from how the differential equation solver handles stiffness; solving for the steady state explicitly (by finding the roots of the equation) shows that the steady state is exactly 0.9856.

Figure 7.3.a demonstrates how two stable steady states exist for an ampicillin-producing reactive MSMPR with a feed concentration ratio of 800:400 mM PGME:6-APA. The solid and dashed curves represent the two different steady states; a hysteresis occurs where the low suspension density (solid curve) steady state prevails when increasing the

residence time while the high suspension density (dashed curve) steady state is dominant when decreasing the residence time. The coexistence of two steady states depends on both supersaturation as well as residence time; therefore, at some shorter residence times, one value of supersaturation results in a pure effluent while the same supersaturation at a longer residence time results in an impure effluent (physical mixture of ampicillin and phenylglycine crystals). Tavare and Garside developed a concentration criterion for an MSMPR, which has been adapted here for a reactive MSMPR, to determine whether a steady state is unique.¹⁷² Defined in equation 7.1, this criterion limits the steady-state concentration of a crystallizing solute and informs further process design (the derivation of this criterion is given in section 7.4). In the example in Figure 7.3.b ($\tau = 42$, $c_{s,0} = 800$ mM, $c_{Nu,0} = 400$ mM, pH = 7.0) the criterion has a value of 45.9 mM and the steady state concentration is 47.1 mM for phenylglycine.

$$c_j < \frac{R_j \tau (3g_j + b_j) + c_j^* (m_j - 1)}{3g_j + b_j + m_j - 1} \quad (7.1)$$

This criterion only considers secondary nucleation because of the stochastic nature of primary nucleation. Assuming that primary nucleation occurs at a deterministic rate governed by classical nucleation theory, a modified stability criterion can be developed, however a simple analytical representation similar to that given in equation 7.1 is not obtainable. Including primary nucleation does not noticeably change the value of the criterion in equation 7.1 because secondary nucleation is responsible for the formation of the overwhelming majority of crystals (see Figure 7.9). Inclusion of primary nucleation does shift the “pure” steady state (SS1 in Figure 7.3.b) to a negligibly lower purity (from

100% to >99.99%), but the stochastic nature of primary nucleation indicates that this is the expected value over many perturbations.

Figure 7.3.b demonstrates how a perturbation can take the reactive crystallizer to the second steady state where the amount of solid phenylglycine in the effluent results in the purity of ampicillin decreasing from >99.99% to 98.56%. In Figure 7.3.b, the residence time of the reactive crystallizer is increased 5% (from 42 minutes to 44 minutes) for approximately one hour. Disturbances lasting less than an hour do not result in a change of steady state, while those lasting an hour or longer trigger the system to switch to the impure steady state. The transition to the new steady state, or the return to the original steady state, is gradual, taking tens of residence times, making the transition hard to observe. It is therefore important to build a process where the risk of an impure steady state is negligible.

7.2.3 Reactive crystallizers in series for robust purity

The purity constraint elevates the importance of the fractional yield (Φ). Fractional yield, defined as the amount of ampicillin produced over the amount of ampicillin and phenylglycine produced, as a function of conversion, determines the maximum conversion possible while maintaining purity. The light gray shaded region in Figure 7.4 indicates the region where a reactive MSMPR producing ampicillin has multiple steady states, at least one with purity > 99.99% and one with untenable phenylglycine impurity greater than 1.0%. The dark shaded region in Figure 7.4 shows the region where only a single impure steady state exists and phenylglycine *will* crystallize and contaminate the ampicillin trihydrate product.

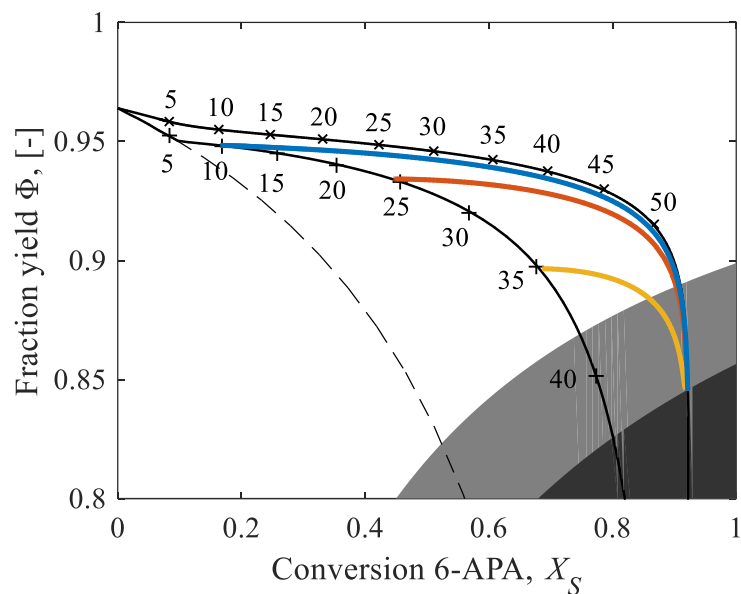


Figure 7.4. The operating curves in fractional yield versus conversion space for a plug-flow reactive crystallizer (top solid curve, \times) and a well-mixed reactive crystallizer (bottom solid curve, $+$) with feed concentration of 800 mM PGME and 400 mM 6-APA. The dashed curve represents a well-mixed reactor (no crystallization). The light shaded area is the region where reactive MSMPRS exhibit steady-state multiplicity and the dark shaded area is the region where primary nucleation results in impure ampicillin product regardless of reactor design. The labeled markers represent the residence time needed to reach the specified conversion and fractional yield in a plug flow (\times) and well-mixed reactive crystallizer ($+$). The blue, red, and yellow curves are plug-flow reactive crystallizer operating curves that are fed by reactive MSMPRS with residence times of 10, 25, and 35 minutes, respectively.

In section 6.4.1 of this thesis, well-mixed vessels in series were considered for a β -lactam antibiotic producing process; in this section the plug-flow reactive crystallizer (PFRC) is introduced because it can achieve superior fractional yields. However, the PFRC requires seed crystals during steady state operation to function effectively because nucleation predominantly occurs via primary nucleation¹⁷³, which is orders of magnitude slower than secondary nucleation. To address the seeding issue, a reactive MSMPR, which at steady state is self-seeding, can generate nuclei, predominantly via secondary nucleation, and feed the PFRC. The population balance equation for the plug flow reactive crystallizer is expressed as

$$\frac{\partial n_j(L, y)}{\partial z} = -\frac{G_j}{u_y} \frac{\partial n_j(L, y)}{\partial L} \quad (7.2)$$

where y is the axial coordinate of the PFR and u_y is the velocity in the axial direction. The nucleation boundary condition is $n_j(0, z) = B_{1j}/G_j$, note that only primary nucleation is considered because diminished mixing in plug flow decreases the secondary nucleation rate.^{174, 175} The inlet boundary condition, $n_j(L, 0)$, is the outlet from a reactive MSMPR, see equation 6.12. The solute balance is given by

$$u_y \frac{dc_j}{dy} = -R_j - 3k_{v,j} \rho_j G_j \mu_{2,j} \quad (7.3)$$

where the boundary condition is again the outlet from a reactive MSMPR, as described in the previous chapter equation 6.13.

In Figure 7.4, the PFRC and MSMPR operating curves form the upper and lower bounds on the achievable fractional yield as a function of conversion (the solid black curves marked with \times and $+$, respectively). The lack of back-mixing in the PFRC means that only a single steady state is possible, and therefore a PFRC can operate up to the dark shaded region and maintain less than 1.0% phenylglycine impurity. On the other hand, the MSMPR can only operate up to the lightly shaded region before the risk of the process being perturbed to an impure steady state arises.

The blue, red, and yellow curves represent PFRC operating curves fed by reactive MSMPRs with residence times of 10, 25, and 35 minutes in the MSMPR, respectively. These three operating curves, together with the MSMPR operating curve up to the feed point, will be referred to as Designs 1, 2 and 3, respectively. The number labels on the

PFRC and MSMPR operating curves are the residence times (in minutes) required for a PFRC or MSMPR to reach that conversion and fractional yield. As can be seen, the MSMPR reaches higher conversions with shorter residence times than the PFRC, as was expected based on the results for amoxicillin in the previous chapter. Design 1 achieves 18% conversion in the MSMPR, Design 2 achieves 44% conversion in the MSMPR, and Design 3 achieves 67% conversion in the MSMPR. Figure 7.5 shows the reaction rate in the MSMPR for each design, as well as the reaction rate along the length of the PFRC. The size of the MSMPR markers is proportional to the volume needed to achieve that conversion. It also shows that with crystallization (solid), the reaction rate is always higher than without crystallization (dashed), due to lower hydrolysable antibiotic concentration, as ampicillin is sequestered in the trihydrate crystal (discussed in detail in CHAPTER 6).

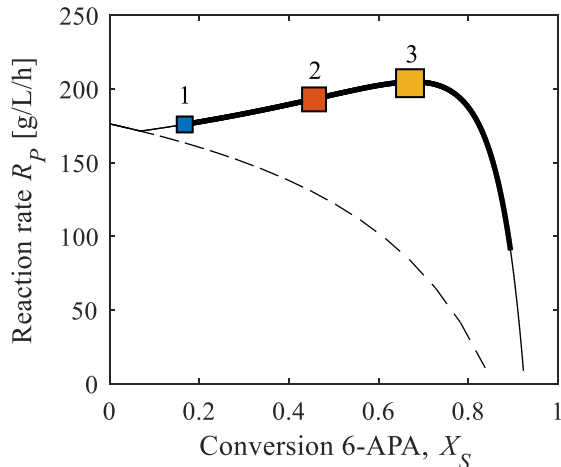


Figure 7.5. The solid curve shows the reaction rate with *in situ* crystallization while the dashed line shows the reaction rate without crystallization. The colored squares are the reactive MSMPRs operating at the specified conversion with size proportional to the MSMPR volume. The bolded solid line represents the range of conversion that occurs over the length of the PFRC, fed by each of the MSMPRs.

It has already been shown for amoxicillin that the reaction kinetics favor implementation of a reactive MSMPR over a PFRC to maximize productivity from 5% to

73% conversion, but the benefit of an MSMPR over a PFRC decreases above 73% conversion.²¹ Applying the same findings to ampicillin production suggests that the nuclei-generating MSMPR should be operated up to the largest conversion possible such that the maximum yield of the PFRC is not significantly impacted. The yellow curve in Figure 7.4 shows that as long as the MSMPR does not go beyond 70% conversion, the maximum possible conversion still reaches 98% of the theoretical maximum before contamination greater than 0.5% becomes certain—in the dark shaded region. Whether a disturbance can cause MSMPR operation to enter the light shaded region, or PFRC operation to enter the dark shaded region, needs to be considered for a robust process.

The spatial distribution of productivity throughout the reactor network is shown in Figure 7.6. In Figure 7.6, the size of the square is proportional to the residence time of the reactive MSMPR and the length of the rectangle is proportional to the residence time of the plug flow reactive crystallizer. The color indicates the space time yield, which is the productivity of the vessel distributed across its volume (reactive MSMPRs, being well mixed, are uniformly colored). The last 5–10 minutes of the plug flow reactive crystallizer is not very productive but is necessary to reach high conversion. The plug flow reactive crystallizers can be shortened to further improve productivity if single pass conversion is not as important (e.g. if unused reactants can be efficiently recycled).

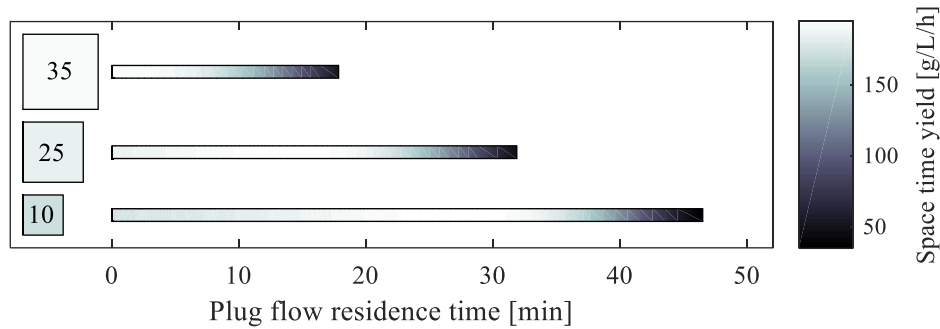


Figure 7.6. The productivity of the reactive MSMPR fed plug flow reactive crystallizer is shown by the degree of shading (lighter hues indicating greater productivity) in the well-mixed vessel (square) and the plug flow vessel (rectangle). The area of the square and rectangle are proportional to the volume of each vessel. The residence time of the reactive MSMPR is labeled in the square, the residence time of each plug flow reactive crystallizer is shown on the abscissa. The top, middle, and bottom reactors represent Designs 3, 2, and 1, the yellow, red, and blue operating curves in Figure 7.4.

The CSD from each of these reactor configurations also differs significantly. Plug flow crystallizers produce desirable narrow size distributions because all crystals have the same residence time, and therefore grow by the same amount. MSMPRs produce wide CSDs because of their exponential residence time distribution. Additionally, secondary nucleation is not considered in plug flow crystallizers because mixing is weakened. Figure 7.7 shows the volume-weighted size distributions from Designs 1, 2, and 3. The area under each CSD is the same, confirming that each design gives the same conversion of 6-APA. Design 1 has the narrowest size distribution and a volume-weighted mean crystal size $\bar{L}_{4,3}$ of 54.5 μm . Designs 2 and 3 have very similar, but wider, size distributions and volume weighted mean sizes of 50.5 and 51.5 μm , respectively, suggesting that most of the growth is occurring in the MSMPR. Depending on the form factor of the final product (powder for suspension, capsule, etc.), the CSD shape may be as important as or even more important than economic criteria such as conversion and productivity.

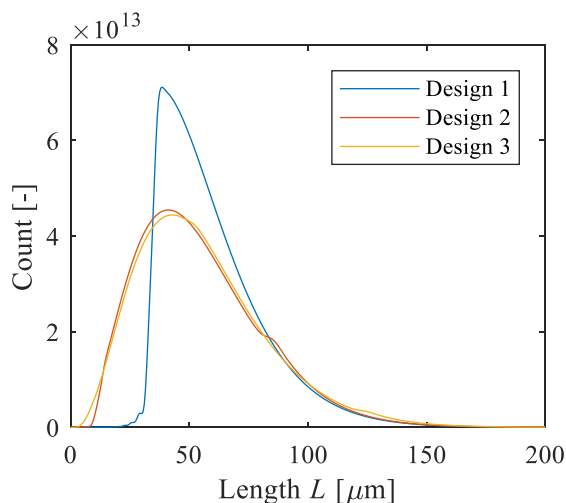


Figure 7.7. The volume weighted CSD of ampicillin trihydrate resulting from the blue, red, and yellow operating lines in Figure 7.4.

7.2.4 Evaluation of process robustness

The most favorable process will be one that is robust despite uncertainty. In the present study two sources of uncertainty are considered: uncertainty in parameter values and variability of operating conditions. The first could be the result of poor model calibration, but it is equally plausible that slight impurities in the feed could change the values of the kinetics parameters used in the model. The second source of uncertainty accounts for environmental fluctuations that cannot be controlled. To demonstrate this uncertainty, and the robustness of the MSMPR-fed PFRCs compared to a single optimized reactive MSMPR, we simulate a 10% decrease in the solubility of phenylglycine at the isoelectric point (c^*) as well as a 2 °C increase in temperature from 25 °C to 27 °C.

The decrease in solubility was selected as the source of “parameter uncertainty” because a change in solubility effects the driving force of crystallization, impacting growth and nucleation kinetics, combining for a larger purity deviation than an aberration in

growth or nucleation alone. The change in temperature was chosen to illustrate how a source of “operational uncertainty” affects the optimized process because as the scale is increased temperature control becomes increasingly difficult, and the solubility and reaction rates are strongly temperature dependent. While one can imagine other possible operational deviations, such as a change in flow rate, maintaining a uniform temperature in a scaled-up process poses one of the biggest challenges.

Figure 7.8.a demonstrates the robustness of the purity of the effluent from the MSMPR-fed PFRCs. A single reactive MSMPR generates a 98.8% pure ampicillin trihydrate effluent when the solubility of the primary byproduct, phenylglycine, decreases 10% compared to the value used in the above analysis (see Table 7.1). Under the same conditions, the purity of Designs 1, 2, and 3 remains at >99.99%. When the temperature of the reactive crystallizer is increased by 2 °C, the single reactive MSMPR purity drops to 95.9%. The purity of Design 3 also decreases to 98.8%, but the two smaller MSMPR designs continue to yield >99.99% pure ampicillin trihydrate. In fact, Design 1 never reaches phenylglycine supersaturation, all but guaranteeing purity, even with the possibility that phenylglycine crystallization could be catalyzed by the presence of the ampicillin trihydrate (i.e. nucleates on the crystal surface), though we have not observed this experimentally.

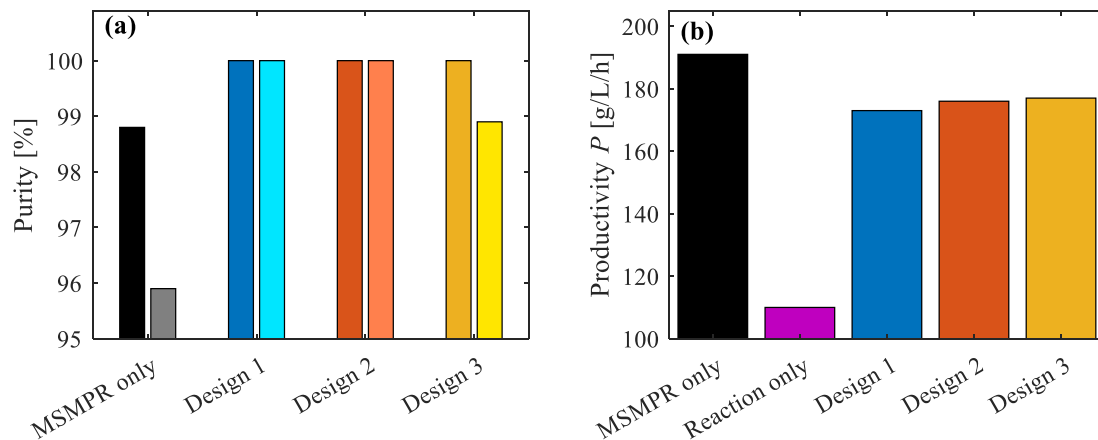


Figure 7.8. (a) The purity of the effluent crystals from the different reactive crystallizer designs with a 10% decrease in phenylglycine solubility (darker shades) and 2 °C increase in temperature (light shades). (b) The productivity of the different reactive crystallizer configurations as well as a non-crystallizing well-mixed reactor at the same final 6-APA conversion of 90%.

To design the optimal process for the continuous synthesis of ampicillin trihydrate, robust purity needs to be weighed against economic factors such as yield and productivity, which are proxies for materials and capital costs. Figure 7.8.a and 9.b taken together can help inform design. Based on the purity robustness and good productivity, Design 2 is recommended. Confidence in tight process control could, however, make a single reactive MSMPR the favored design.

As stated previously, ampicillin is a favorite model β -lactam, therefore, parameters used in the present study can be sourced from the literature for ampicillin but are not available for the far more important β -lactam cephalexin. Because of the similarity of ampicillin and cephalexin—they both have phenylglycine as a primary byproduct and are synthesized with PGA—the results for ampicillin trihydrate are generalized here to cephalexin for the purpose of sizing a production plant. It is likely that the kinetics for cephalexin will differ from those for ampicillin, and therefore the calculations may need to

be rerun with updated kinetic constants to predict exact values of process metrics such as productivity and conversion for cephalexin. However, for the purposes of purity, both medicines have similar solubility and the same risk of phenylglycine contamination and are therefore suitable analogs for an illustrative sizing for production of a clinically vital drug; cephalexin.

The global demand for cephalexin is approximately 6,000 tons per annum. To meet 10% of this demand using the proposed continuous enzymatic reactive crystallizer system, assuming 10% annual downtime, a 430-L total-volume reactive crystallizer would be needed. While 10% downtime is assumed, the actual time required for startup and shutdown has not been calculated. According to Design 2, the reactive crystallizer should consist of a 205-L reactive MSMPR and a 225-L plug flow reactive crystallizer in series and should be fed with 800 mM PGME and 400 mM 6-APA at a rate of 5.8 L min^{-1} . Sizing a reactive plug flow crystallizer is non-trivial, the diameter must be small enough for turbulent flow to keep the crystals from settling but large enough to prevent the crystals from clogging. A computational fluid dynamics simulation could assist in the design of such an apparatus; a rough calculation indicates that the plug flow tube would have to be on the order of 100 meters long and several centimeters in diameter, static mixers could help maintain the suspension.

7.3 Conclusions

Using the model developed in CHAPTER 6, a process for the production of ampicillin was designed.²¹ Combined reaction and crystallization is shown to increase conversion and productivity of β -lactams, as well as reduce the risk of β -lactam

contamination in other drugs. Given the goal increased efficiency by process intensification, an additional purification step is undesired; therefore, purity of the effluent crystals is a paramount consideration in designing the process. The single well-mixed reactive crystallizer design that had been employed for amoxicillin in CHAPTER 6 is not effective for ampicillin (or cephalexin) because phenylglycine, the byproduct of ampicillin (or cephalexin), is only slightly soluble, and its potential crystallization can contaminate the product. With ampicillin, the single reactive MSMPR has at least two steady-state conditions, one of which produces low-purity ampicillin trihydrate. Perturbations in the process can cause the system to change from one steady state to the other. A plug-flow reactive crystallizer has higher fractional yield, leading to less accumulation of phenylglycine and reduced risk of the product being contaminated. However, a PFRC has lower productivity and detrimentally slow crystal nucleation kinetics compared to a reactive MSMPR. A reactive MSMPR-fed PFRC can combine the strengths of both reactor/crystallizer types.

Three different MSMPR-fed PFRCs were considered: a reactive MSMPR with 10 minutes, 25 minutes, or 35 minutes residence time followed by a plug flow reactive crystallizer with enough volume to reach 98% of the maximum possible conversion (as determined from the attainable regions, and equivalent to the conversion in a single optimized reactive MSMPR). Designs 1, 2, and 3 are 94%, 95%, and 96% as productive as and 30%, 27%, and 26% larger than the MSMPR alone. All proposed designs have productivity 50% greater than a non-crystallizing reactor. The MSMPR-fed PFRC demonstrates much better robustness in the face of parameter uncertainty and operational variability than the MSMPR alone. Designs 1 and 2 produce >99.99% pure ampicillin with

a 10% error in modeled phenylglycine solubility and 2 °C increase in process temperature. Additionally, Design 1 never generates any phenylglycine supersaturation, ensuring purity if phenomena not captured by the model cause phenylglycine crystallization (e.g. nucleation catalyzed by the presence of ampicillin crystals). Adapting Design 2 to meet 10% of the annual demand for cephalexin yielded a realistic blueprint for a new continuous β -lactam producing plant.

7.4 Derivation of steady state uniqueness criterion in a reactive MSMPR

Steady state multiplicity in well-mixed continuous crystallizers was studied by Tavare and Garside in 1985.¹⁷² The framework they established is modified here to determine steady state multiplicity in reactive crystallizers. A solute balance for the reaction product in a well-mixed reactive crystallizer (assuming no solute in the feed) is given by:

$$M_T = R\tau - c \quad (7.4)$$

where M_T is the suspension density, R is the reaction rate, τ is the mean residence time, and c is the solute concentration. Crystal growth rate (G) and nucleation rate (B) are represented by a power laws; growth is independent of crystal size, and nucleation occurs predominantly through secondary nucleation, as shown in equations 7.5 and 7.6:

$$G = k_G (S - 1)^g \quad (7.5)$$

$$B = k_B M_T^m (S - 1)^b \quad (7.6)$$

with rate coefficients k_G and k_B , exponents g and b , and supersaturation ratio $S = c/c^*$. The assumption that primary nucleation is unimportant for this analysis is justified by the fact that secondary nucleation is orders of magnitude faster in the presence of any other crystals;

Figure 7.9 shows the primary and secondary nucleation rates with a very low suspension density of $M_T = 0.01$ g/L.

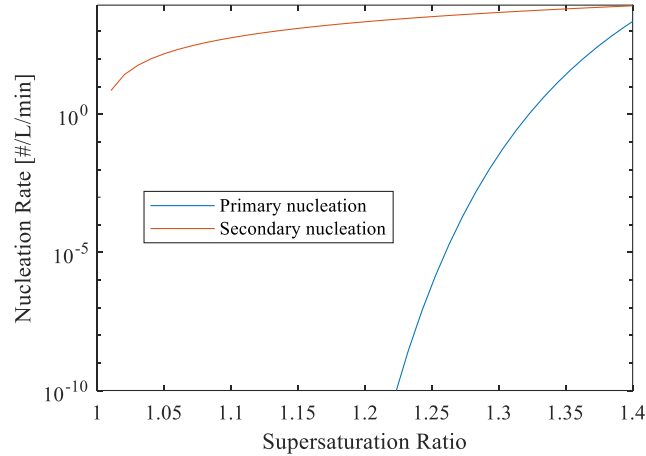


Figure 7.9. The primary (blue) and secondary (red) nucleation rates of phenylglycine with a suspension density of 0.01 g/L.

At steady state, the method of moments can be used to show that the suspension density is proportional to the residence time, growth rate, and nucleation rate, according to equation 7.7.

$$M_T = 6k_V \rho \tau^4 G^3 B \quad (7.7)$$

where k_V is the volumetric shape factor and ρ is the crystal density. Equations 7.5-7.7 can be made dimensionless with a dimensionless concentration, $x = c/R\tau$, and dimensionless saturation concentration, $\xi = c^*/R\tau$. Substituting equations 7.5-7.7 into the solute balance 7.4 gives:

$$(1-x)^{m-1} (x-\xi)^q = \frac{1}{\alpha} \quad (7.8)$$

where

$$q = 3g + b \quad (7.9)$$

and

$$\alpha = 6k_v \rho \tau^4 k_G^3 k_B (R\tau)^{q+m-1} (c^*)^{-q} \quad (7.10)$$

On the physically relevant interval of $\xi < x < 1$ (i.e. between 100% and 0% consumption of supersaturation), whether equation 7.8 has one or more additional roots determines whether there are multiple steady states. The mean value theorem states that for a continuous function to have two roots, the derivative of the function must equal zero somewhere on the interval between the roots. The system bifurcates when the parameters result in the derivative of equation 7.8 with respect to the dimensionless concentration (x), shown in equation 7.11, being equal to zero. A unique steady state is guaranteed when the derivative is greater than zero, and multiple steady states arise when the derivative takes on values less than zero.

$$q(1-x)^{m-1} (x-\xi)^{q-1} - (m-1)(1-x)^{m-2} (x-\xi)^q > 0 \quad (7.11)$$

Rearranging leads to a uniqueness criterion for x based on system parameters:

$$x < \frac{q + \xi(m-1)}{q + m - 1} \quad (7.12)$$

An analytical uniqueness criterion for the ampicillin continuous reactive crystallization system does not exist because the rate of make, R , and solute concentration, c , depend on the residence time (the saturation concentration, c^* , is also weakly dependent on the residence time because changes in residence time affect the steady state pH value, which affects the saturation concentration). In the example given in Figure 7.3, the uniqueness criterion, 7.12, has a value of 0.975 and the dimensionless concentration, x , is

0.999. Since $x \approx 1$ (and cannot be greater than 1), it is prudent to design a process where the criterion is always greater than unity. Figure 7.10 shows the value of the uniqueness criterion versus the residence time of a single well-mixed reactive crystallizer. Using the same analysis as above for ampicillin showed gives a uniqueness criterion greater than unity for all relevant process conditions (conditions that give appreciable yield and productivity), indicating a unique steady state for ampicillin suspension density always exists.

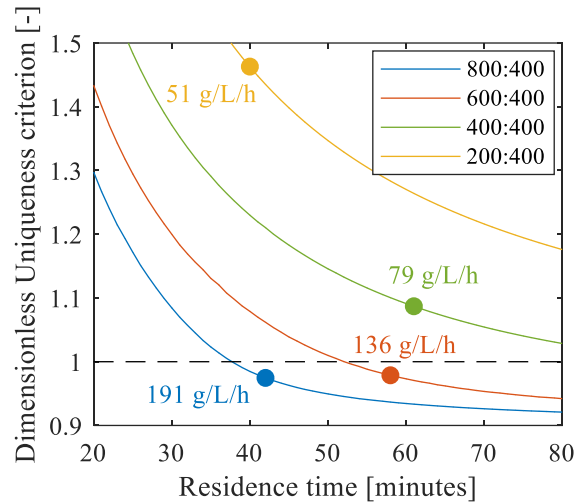


Figure 7.10. The uniqueness criterion defined in equation (9) versus the residence time in a well-mixed reactive crystallizer with four different feed compositions (blue- 800:400 mM PGME:6-APA, red- 600:400 mM PGME:6-APA, green- 400:400 mM PGME:6-APA, and yellow- 200:400 mM PGME:6-APA). The points represent the residence time that gives the maximum productivity and are labeled with that productivity. Below the black dashed line is the region where steady state multiplicity can arise.

Casting the dimensionless uniqueness criterion 7.12 back into dimensional terms gives equation 7.1.

CHAPTER 8. PROCESS ANALYTICAL TECHNOLOGY FOR CONTINUOUS MANUFACTURE OF BETA-LACTAMS

8.1 Introduction

Quality by Design (QbD) is one of the main pillars of the FDA's current manufacturing best practices. The crux of QbD is that medicines and the process used to manufacture them should be designed to minimize risk, and where risk is identified measures are taken to mitigate it.¹⁷⁶ Testing cannot make up for poor process design. QbD therefore requires a detailed understanding of the properties of the product as well as of the manufacturing process.^{177, 178} These properties are termed Critical Quality Attributes (CQAs) and Critical Process Parameters (CPPs) in FDA parlance.¹⁷⁹ The goal of PAT is to guarantee that CQAs are met upon completion of processing. Ideal PAT can be implemented in an online configuration, such that sampling is not required. PAT enables real time monitoring and control of CPPs and is key to mitigating known risks.¹⁷ Validation is a key part of QbD, both for the manufacturing process, which must have validated performance, and for the PAT, which must be reliable and give useful information.^{16, 180}

For the CM enzymatic reactive crystallization of beta-lactams several different PATs have been tested, including polarimetry, attenuated total reflectance Fourier transformed infrared spectroscopy (ATR-FTIR), focused beam reflectance measurement (FBRM), and *in situ* microscopy. Polarimetry measures solution concentrations but is easily confounded by the presence of solids, which obscure the path of the polarized light. ATR-FTIR also measures solution concentrations, with less sensitivity than polarimetry

but robustness against suspended solids. FBRM measures the chord length distribution (CLD) of a crystal population, which can be used as a proxy for the crystal population density function. *In situ* microscopy uses nanosecond laser pulses to capture still images of crystals in suspension; paired with image analysis, information regarding the crystal population can be extracted.

In this chapter each of these PAT is discussed in the context of the CM beta-lactam process. While most of these tools have been mentioned in the preceding chapters, the work required to monitor a CM process is still underway. Large strides have been made towards using each of these PAT in the final pilot plant. Validation, including construction of calibration curves, and quantification of the limits of detection (LoD), limits of quantification (LoQ), bias, and root-mean-square error of prediction (RMSEP), is also necessary for a QbD process. The LoD is defined as three standard deviations of the blank sample, the LoQ is ten standard deviations. The bias is the average amount by which the concentration derived from the calibration model deviates from the true concentration. The RMSEP is defined by the equation below

$$\text{RMSEP} = \sqrt{\frac{\sum_{i=1}^N (x_i - x_{i,\text{prediction}})^2}{N}}$$

where N is the number of tests, x_i is the measured value, and $x_{i,\text{prediction}}$ is the predicted value from the calibration model.¹⁵

8.2 Polarimetry

Polarimetry works by measuring the rotation of polar light by chiral molecules in solution. The optical rotation of a solution is the linear combination of the optical rotations

of the dissolved species weighted by their concentrations.⁸⁹ Figure 8.1 demonstrates how the polarimeter works; a polarizer at one end allows only plane polarized light into the cuvette, at the other end a second polarizer is rotated to allow the maximum amount of light through, the angle between the polarizers is the polarimeter output. As the antibiotics, their precursors, and byproducts are all chiral, do not undergo any racemizing reactions, and have distinct specific optical rotations, the measured optical rotation, along with the known reaction stoichiometry and starting concentrations, can be used to determine the solution concentration. This was the basis for measuring enzyme deactivation in CHAPTER 2, using an Anton Paar MCP 500 polarimeter. In Figure 8.2 the calibration curves for the ampicillin system are shown, demonstrating how each species has a unique specific optical rotation, enabling determination of conversion.

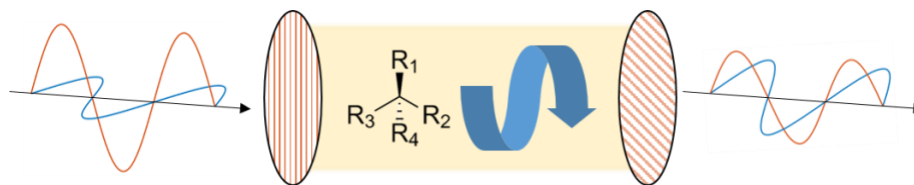


Figure 8.1. A polarimeter measures the optical rotation of a solution caused by chiral solutes by measuring the angle between two polarizers such that the maximum amount of light is allowed through.

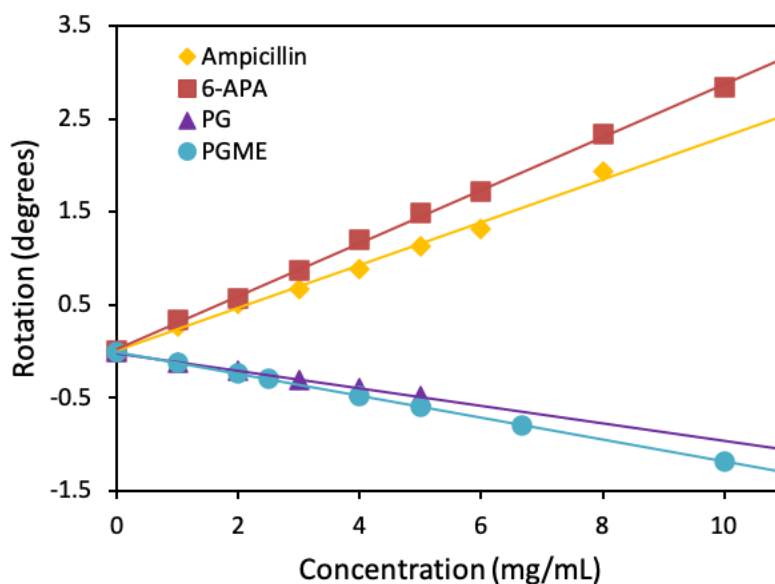


Figure 8.2. The calibration curves for determination of the specific optical rotation of the species involved in ampicillin synthesis. The optical rotation was measured in water at 20 °C, at 589 nm, and in a 100 mm cuvette.

A linear model of the form $c_i = a_i\theta$, where c_i is the concentration, a_i is the specific rotation of species i , and θ is the measured rotation, was found to be sufficient. The model was evaluated, and the relevant parameters and validation metrics are given in Table 8.1. The calibration data were randomly divided into two subsets, one for calibration model fitting, and the other for calibration model validation.

Table 8.1. Evaluation of the simple linear model of optical rotation dependence on concentration. Specific rotation for a 10 cm cuvette at 20 °C at a wavelength of 589 nm, $\pm 95\%$ confidence interval.

Compound	Ampicillin	6-APA	Phenylglycine	PGME
Specific Rotation ($^{\circ}$ /mol/L)	96.8 ± 1.8	61.6 ± 1.7	-14.2 ± 0.7	-22.1 ± 2.3
LoD (mol/L) $\times 10^{-6}$	31	49	211	136
LoQ (mol/L) $\times 10^{-6}$	103	162	704	452
Bias (mol/L) $\times 10^{-3}$	-0.77	-0.45	1.2	1.5
RMSEP	0.0053	0.0013	0.0020	0.0039

Polarimetry is by far the simplest of the PAT evaluated in this thesis. The polarimeter reports a scalar quantity, the optical rotation at a fixed wavelength, which when combined with process knowledge, such as stoichiometry and initial conditions, can be used to determine concentrations. It is also incapable of monitoring slurries as the solids immediately obstruct the very long path length needed for accurate measurements. Going forward, each additional PAT requires more effort to extract useful low-dimensional process information (such as concentrations) from instruments that generate high-dimensional data (such as spectra).

8.3 Attenuated total reflectance Fourier transform infrared spectroscopy

Extracting the maximum amount of actionable information possible from ATR-FTIR and other spectra collected *in situ* has been the subject of many papers, including those by Griffin^{55, 103, 181, 182} and Kocевska *et al.*¹⁸³ The principle of ATR-FTIR is a simple variation on standard Fourier transform infrared spectroscopy, shown in Figure 8.3. The IR laser is reflected within an ATR crystal (diamond), with each reflection producing an evanescent wave reaching only two micrometers outside the ATR crystal. By contacting

the ATR crystal with the slurry, one can take advantage of hydrodynamics hindering crystals from entering the sampled region, thereby producing a signal predominantly from the solution. One caveat is crystal growth on the probe window produces a signal from the crystal only.

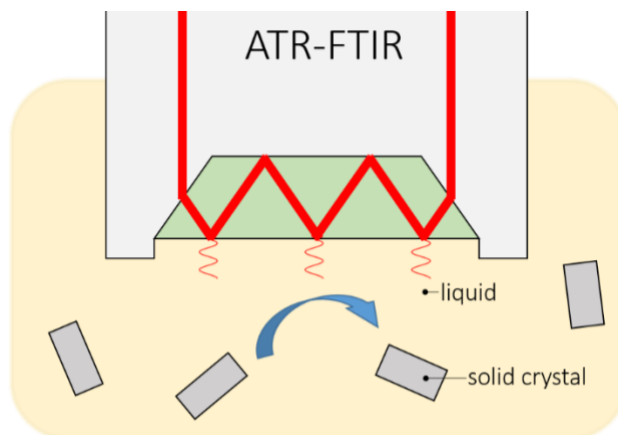


Figure 8.3. In ATR-FTIR evanescent waves are generated during the internal total reflection of the IR laser (red) in the ATR crystal (green). The evanescent waves only penetrate a few micrometers into the solution, such that hydrodynamics prevent crystals from being ‘seen’ by the laser.

In CHAPTER 4 ATR-FTIR was used to measure concentration of cephalexin. A linear calibration model of the form $c = a(h_{1369} - h_{1305}) + b$ was used, where h_N represents the height of the peak at wavenumber N . The peak at 1369 cm^{-1} was chosen because it proved to be most robust against the presence of other species, 1305 cm^{-1} was used to baseline the peak height. Figure 8.4 shows the IR spectrum of cephalexin and the calibration curve used in CHAPTER 4. In Table 8.2 the parameters for the calibration model for cephalexin and other single species are presented, with different wavenumbers used for different compounds. Cephalexin was calibrated from zero to 100 mM while 7-ADCA and PGME were both calibrated through 200 mM, reflecting the expected ranges

of concentrations in the final process. The instruments used were Mettler-Toledo's ReactIR iC10 and ReactIR 702L.

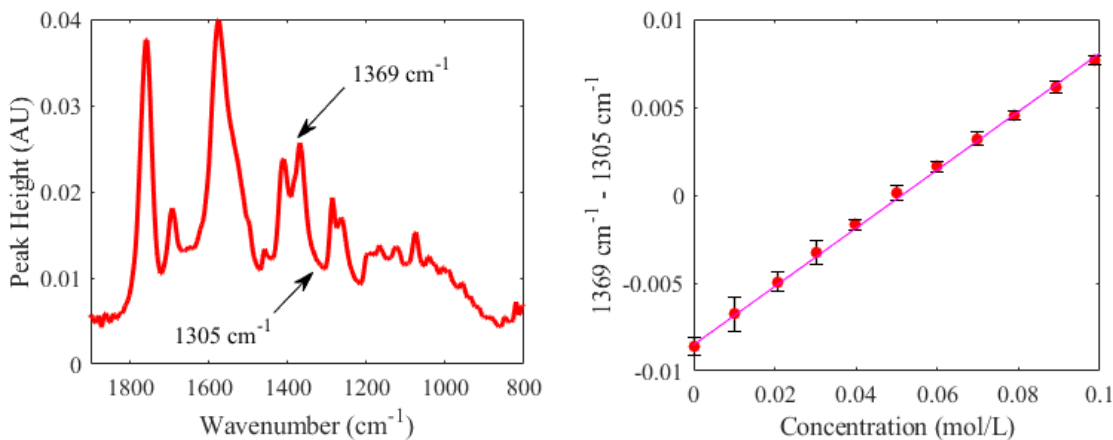


Figure 8.4. The IR spectrum of cephalixin (left) and the linear calibration model used to convert the 1369 cm⁻¹ peak height to concentration (right). Error bars represent standard deviation of $n = 38$ samples.

Table 8.2. Summary of IR calibration models and validation for single species. *Data collected on ReactIR iC10 with 30 second scan time, all others collected on ReactIR 702L with 60 second scan time.

Compound (peak – trough)	Cephalixin* (1369 – 1305)	7-ADCA (1744 – 1820)	PGME (1252 – 1212)
a (mol/L/cm ⁻¹)	6.021 ± 0.031	2.474 ± 0.012	4.524 ± 0.046
b (mol/L)	0.0513 ± 0.0002	-0.1873 ± 0.0015	-1.155 ± 0.013
LoD (mol/L) $\times 10^{-3}$	1.51	1.21	0.67
LoQ (mol/L) $\times 10^{-3}$	5.04	4.05	2.22
Bias (mol/L) $\times 10^{-3}$	0.54	-1.84	3.61
RMSEP	0.0012	0.0014	0.0028

For single compounds the linear models of concentration are sufficient. Baselineing can be used to remove the spectrum of second (or more) dissolved species, provided the concentration of the additional species is constant. However, once the concentration of

multiple species begins changing in tandem, the simple models used thus far are no longer accurate. To monitor the changes in concentration of several species more advanced methods are required. One group of methods involves reducing the dimensionality of the data to give only one dimension for each independent concentration (dependent concentrations would be, for example, the concentrations of A and B in the reaction $A + B \rightarrow C$; A and B decrease in concentration at equal rates). This approach was implicitly used in the single species models, as only a single wavenumber was chosen to represent the species. Since spectra of the acyl-donors, by products, beta-lactam cores, and antibiotics overlap considerably the reduced dimensions may not be individual wavenumbers but some combination of them instead. This remains an active area of work for the CM process.

While tracking changes in the concentration of many different species with ATR-FTIR may be difficult for the beta-lactam chemistry, CM simplifies monitoring immensely. In a CM process at steady state, the concentrations of each species are by definition not changing; therefore, to monitor the process by IR, all one needs is a spectrum representing the desired steady state. Deviations in the measured spectrum from the desired spectrum indicate a change in the process and could be turned into actionable information with empirical correlations. For example, if a decrease in signal in a certain range of spectrum can be correlated to a decrease in purity, then an excursion in that range would signal to the operator or controller that action must be taken to segregate material flowing out of the reactive crystallizer at that time, so as not to contaminate the pure product with impure product. In this manner the ATR-FTIR produces actionable information without intricate models for deconvolution of complex signals. The most conservative approach, applying

statistical process control,¹⁸⁴ would be to divert the product line upon any deviation from the desired spectrum, as potentially measured by Pearson correlation coefficient.¹⁸⁵ More nuanced approaches, which should be pursued once steady state operation has been achieved and intentional perturbations studied, could use principle components analysis (PCA) to correlate specific changes in the principle components of the spectrum to changes in the CQAs. With a known correlation, designer and operator insight could enable corrective action to avoid wasted product.

The main challenges with further developing ATR-FTIR for use in the CM reactive crystallization of beta-lactam antibiotics are: (1) complex non-linear phenomena, (2) low concentrations and therefore signals, (3) probe fouling, and (4) probe variability. The first challenge cannot be changed as crystal nucleation is a non-linear phenomenon. Linearization of the process model around the steady state set point can simplify control, and design choices can be made to make sure that no actions are taken that result in significant system changes faster than the ATR-FTIR sampling rate (order one sample per minute). The second challenge is also inherent to the system and will require large amounts of calibration data such that small changes in signal can be quantifiably related to changes in the solution. The signal to noise ratio can also be improved by increasing the sampling time and averaging over more scans. The third challenge is addressable by process design and operation. Rapid generation of supersaturation and free PGA have been shown to foul the probe. Figure 8.5 shows the apparent concentration of amoxicillin increasing indefinitely during a pH-swing crystallization (left) with high supersaturation and an enzymatic crystallization (right) with soluble PGA. QbD requires that the process be designed to maximize real time process analysis, therefore immobilized PGA should be

used with a large enough reactor residence time to keep the supersaturation to a minimum. The fourth challenge relates to smaller but significant differences in the optical properties of different probes or even the same probe in different positions. Griffin *et al.* previously addressed this issue;¹⁰³ in addition to implementing their solution based on preferentially weighting stable parts of the spectrum, the position of the probe can also be stabilized as much as possible.

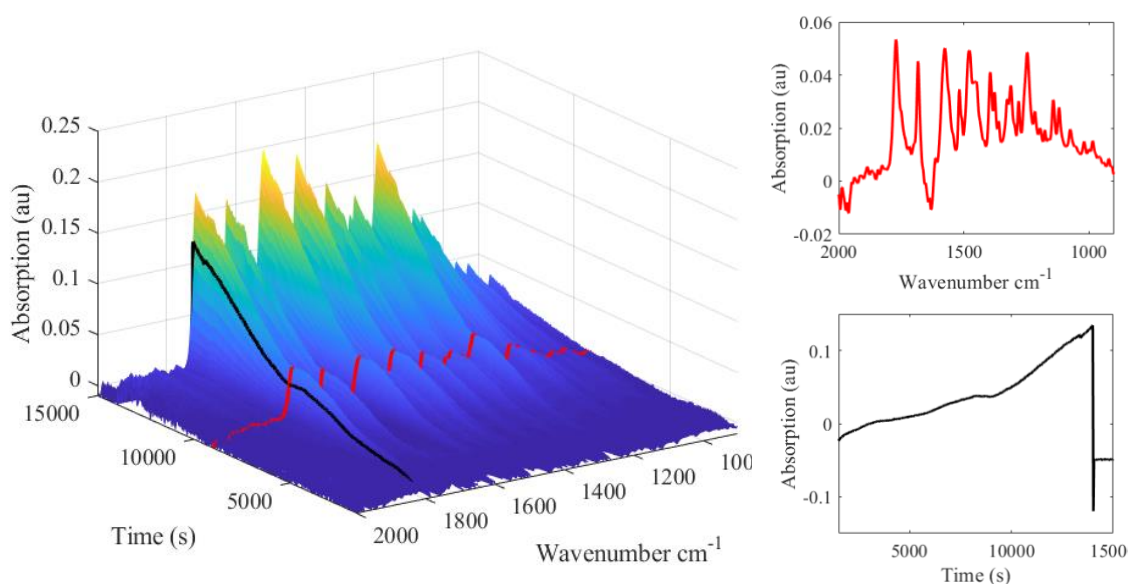


Figure 8.5. The FTIR signal from a continuous amoxicillin crystallization experiment with spectrum trace (red) and progression trace (black), highlighted in the insets to the right, showing an increasing signal as amoxicillin crystallizes over the probe window. At approximately 14000 seconds the probe was removed, cleaned, and reinserted into the crystallizer, resulting in the drop in peak height visible in the black progression trace.

8.4 Focused Beam Reflectance Measurement

Focused beam reflectance measurement gives a signature of the crystal population which measured over time can be indicative of certain underlying processes. The instrument used is a Mettler-Toledo G400. The apparatus works by spinning a focused laser through a crystal slurry at 2.0 m/s (significantly less than the impeller tip speed, approximately 1.0 m/s). The focus of the laser is several micrometers into the slurry such

that the probe can ‘see’ the particles in front of it, unlike for ATR-FTIR, but not particles far from the probe window. When the laser scans over a crystal, which is standing relatively still compared to the laser speed of 2.0 m/s, the beam is reflected back into the probe, where the duration of the backscattering event is recorded. Based off the laser speed the reflectance durations are transformed into lengths, and the lengths are binned into a size histogram. The working principles are illustrated in Figure 8.6.

The histogram, or chord length distribution (CLD), is representative of the crystal population, but is not the same as the CSD (which is an important CQA). Larger crystals are more likely to be scanned by the laser, but they may not give longer chords if they are needle-shaped, as with amoxicillin and cephalexin. The CLD is often weighted by the square of the bin size to transform from a number-based distribution to a volume or mass-based distribution. The FBRM can also miss larger particles due to what has been termed the snowstorm effect, observed with cephalexin experimentally in Figure 8.7, whereby a great number of small crystals (snowflakes) obscure the larger crystals.¹⁸⁶ Other factors that increase variability include probe orientation relative to the flow, mixing intensity, small differences in the optics between different probes, and properties affecting crystal reflectivity (refractive index, surface roughness, etc.).¹⁸⁷

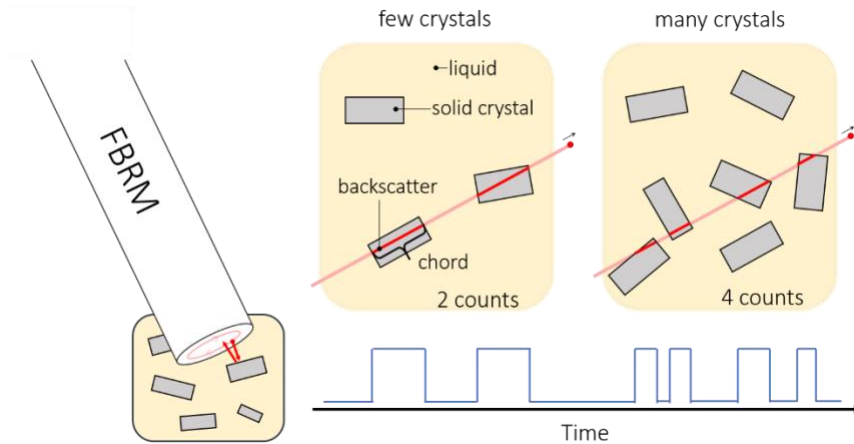


Figure 8.6. The working principle of FBRM is illustrated. Large crystals are more likely to be ‘seen’ by the probe, but even large crystals can produce short chords, especially if they are high aspect ratio crystals like those of amoxicillin and cephalixin.

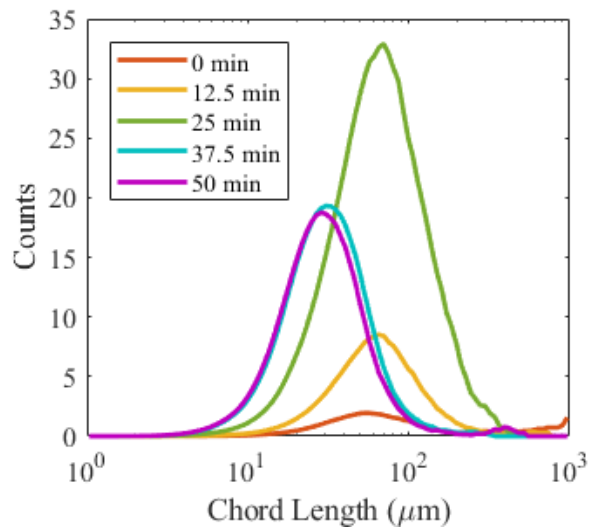


Figure 8.7. The snowstorm effect observed during the crystallization of cephalixin. Beginning with a small number of seed crystals (red), the initial population grows and breeds new crystals (yellow) until a maximum appears for chords 100 μm in length (green). Continued crystallization creates many fines, obscuring the large ($\sim 100 \mu\text{m}$) chords and shifting the mode of the distribution down to $\sim 25 \mu\text{m}$ (blue and purple).

Reconstructing the CSD from the CLD has been the topic of several studies and been approached with several methods. Ruf *et al.* rigorously modeled the CLDs of ellipsoids and cuboids of different sizes and experimented with spheres precisely

positioned in front of the probe to understand exactly what aspects of the crystal are captured in the CLD.¹⁸⁸ Barthe *et al.* moved more towards empirical experimental characterization of FBRM by observing paracetamol crystallization and modeling of the FBRM mechanism by simplifying the crystals as two dimensional projections of octahedra and using PCA to reconstruct the population.^{189, 190} Li *et al.* moved to complete empiricism, also for modeling paracetamol crystallization, by taking well specified crystal populations and measuring their CLDs (termed fingerprints), then reconstructing complex populations by fitting their CLDs to linear combinations of the fingerprints.^{109, 110} There are many frameworks within which to utilize FBRM, but as was the case with ATR-FTIR, but each of them requires significant effort and may not be helpful in quantifying CQAs.

In a CM process at steady state the CLD should not change with time, similar to how the ATR-FTIR spectra should not change with time. Therefore, the greatest strength of FBRM may be ensuring steady operation rather than determining crystal size distributions. A CLD representing the desired steady state can be determined, and then deviations from that CLD can be used to indicate excursions from the operating point. An even simpler approach is to add all bins, or certain subsets of bins, together and observe the change in total counts over time. It may also be possible to correlate certain types of excursions, such as a proportional increase in number of chords in all bins, to pilot plant issues, such as clogging. However, a significant effort will have to be invested to turn CLDs into actionable data for more complex operations such as manipulating the CSD.

A possible application of FBRM specific to the cephalexin system is the detection of phenylglycine crystallization. To maximize process metrics (conversion, yield, and productivity) the concentration of the phenylglycine byproduct must approach its solubility

limit. A perturbation causing phenylglycine crystallization would contaminate the solid cephalixin product, therefore detecting phenylglycine solids is of paramount importance. Measuring the concentration of phenylglycine with ATR-FTIR and ensuring that it remains below the solubility limit could guarantee purity, but the precision of such measurements is (presently) insufficient as the solubility of phenylglycine is approximately 30 mmol/L. Likewise, detecting the decrease in phenylglycine concentration upon crystallization with ATR-FTIR is also impractical. Ongoing work is investigating the efficacy of FBRM in this role. If a model that successfully identifies phenylglycine is constructed it will be validated in the same manner as the IR and optical rotation concentration models, i.e. the LoD, LoQ, bias, and RMSEP will be evaluated, with particular emphasis on LoD as any amount of solid phenylglycine is considered unacceptable. An alternative approach would be to measure the phenylglycine concentration with ATR-FTIR and ensure that it remains below the solubility limit, but so far it has not

8.5 Particle Vision and Measurement

The final PAT planned for use in the CM pilot plant is *in situ* microscopy with particle vision and measurement (PVM). The instrument used is a Mettler-Toledo EasyViewer 100. PVM allows one to see phenomena (such as growth, nucleation, agglomeration, etc.) as they occur in the crystallizer while with FBRM one has to infer the occurrence of such phenomena from CLD trends, which is not a trivial exercise. Figure 8.8 shows PVM images of amoxicillin, cephalixin, and phenylglycine; it is immediately obvious that each crystal is distinct with very different optical properties. An advantage of FBRM over PVM is that confirming steady state operation is more difficult with a series of images than a series of CLDs. One technique to overcome this disadvantage is to use

computer vision to extract size distributions, or even CLDs, from the images to compare over time. Simpler yet, the turbidity can be computed from the average pixel intensity, giving a scalar quantity to be tracked over time.

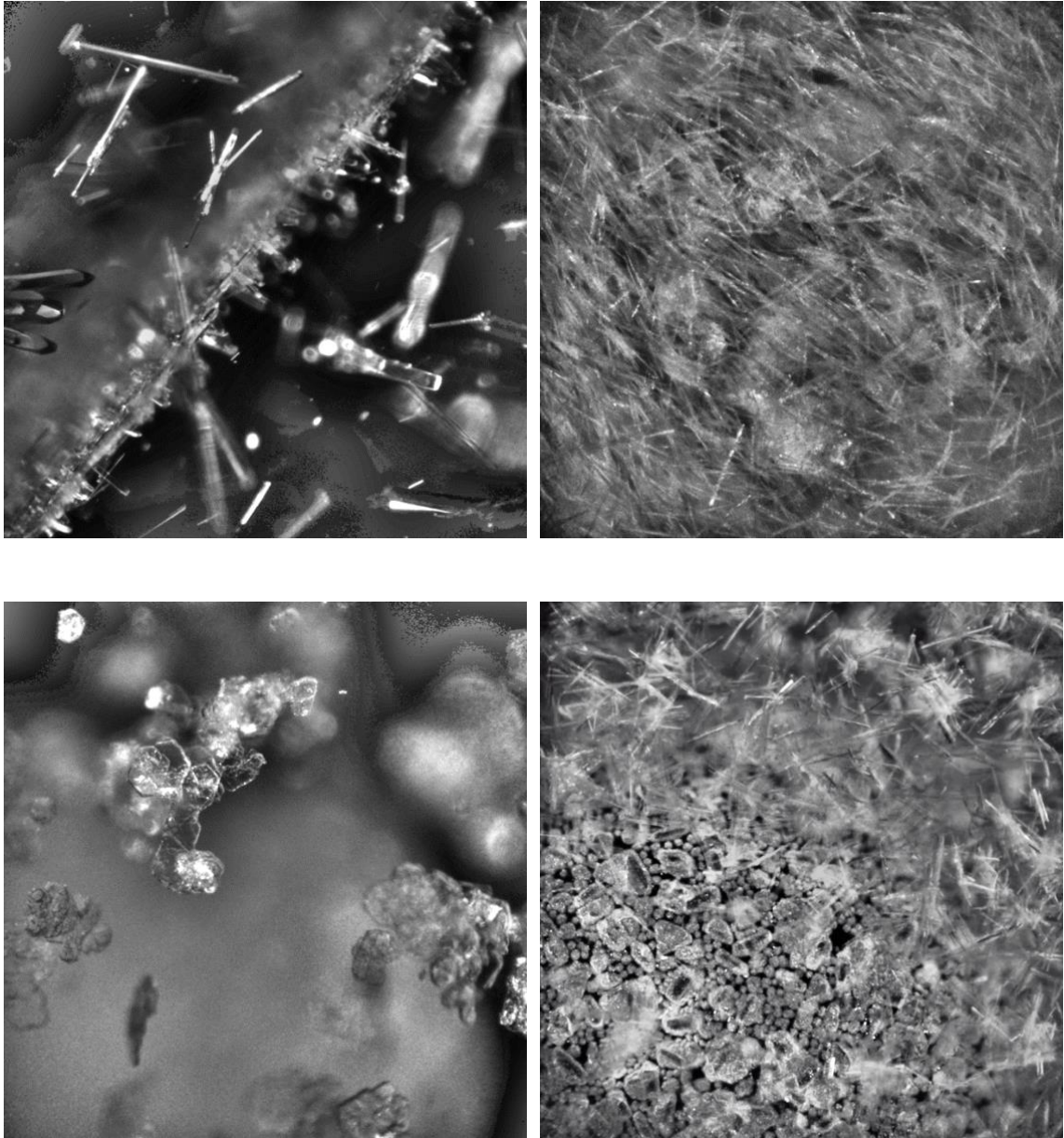


Figure 8.8. Top left: Amoxicillin trihydrate. Top right: Cephalexin monohydrate. Bottom left: Phenylglycine. Bottom right: Cephalexin and phenylglycine, both produced curing a batch enzymatic reactive crystallization. Each image is 1.0 mm × 1.0 mm.

The range of applications of computer vision, and the resulting tools available for analyzing large sets of images, means that PVM may be better suited to directly measuring certain CQAs than FBRM. Measuring the crystal size distribution for needle-shaped crystals has been demonstrated for other systems, and may be plausible here as well.^{48, 191-193} There is also of interest in training a computer to recognize phenylglycine crystals in a slurry of cephalexin crystals, which may be a powerful application of machine learning and big data for the successful operation of the CM pilot plant. Convolutional neural networks have proven adept at image classification and could be trained on large data sets collected with PVM.¹⁹⁴ The challenges associated with such an approach include the typical challenges of preventing probe fouling and properly sampling the slurry, as well as the challenges of running computationally expensive image analysis in real time.

8.6 Other Process Analytical Technology

It is worth noting that many other PAT were considered for this project; many have been implemented but are common analytical techniques not requiring further elaboration, e.g. HPLC and pH measurement, while others are powerful tools but were deemed unsuitable for this project.¹⁷ For completeness, it should be mentioned that refractometry, UV-vis spectroscopy, and Raman spectroscopy were all investigated as additional online PATs. Refractometry gives additional information about the total amount of dissolved content in the solution, which is valuable information when measuring crystallization extent. However, the refractometer (Anton Paar Abbemat 500) is very sensitive to changes in flow rate, which are inevitable as peristaltic pumps produce pulsating flow (see next

chapter). UV-vis spectroscopy was not sensitive to changes in relative amounts of reactants and products while keeping the total concentration constant, which would serve to measure reaction conversion. Use of a chromophore derivatizing agent, namely *p*-dimethyl amino-benzaldehyde, enabled quantification of 7-ADCA by UV-vis spectroscopy, but online implementation is not feasible.¹⁹⁵ Raman spectroscopy was promising as it probes the composition of both the solution and crystalline phases, however the signal-to-noise ratio for the Raman spectrometer (Mettler-Toledo ReactRaman 785) in an antibiotic slurry was very low and not quantifiable.

CHAPTER 9. THE PILOT PLANT: PROGRESS TOWARDS OPERATION OF A CONTINUOUS PROCESS FOR THE MANUFACTURE OF AMOXICILLIN AND CEPHALEXIN

9.1 Introduction

Demonstration of the continuous manufacture of beta-lactam antibiotics by enzymatic reactive crystallization in a lab scale pilot plant is the primary goal of this work. Recently, academic and industrial labs have published numerous examples of pilot plants for specific CM processes. The motivations for utilizing CM in pilot plants have varied, including containing potent materials,^{9, 10} providing a variety of drugs on demand,^{12, 19, 97} and simplifying operation and control of crystallizers compared to batch.^{14, 196, 197} Each of the motivations cited above are also reasons to construct a pilot plant for the CM of beta-lactams. Beta-lactams are known to be highly allergenic, requiring hospitalization upon exposure in 0.1-0.5% of the population, and the FDA now requires that they be produced in standalone facilities; CM would provide an additional layer of containment.^{6, 8, 198} Beta-lactams, particularly amoxicillin and cephalexin, are produced on a huge scale, approximately 20,000 and 6,000 tons per year, respectively,¹ and are often subject to shortages, especially when disruptions in highly optimized supply lines, dependent on single nations, are caused by unforeseeable events. Continuous manufacturing could abate the cost of operating new plants with the flexibility to shore up delicate supply networks.^{3, 199-201} Control of the batch process is also a concern for reactive crystallization; maintaining a low but productive level of supersaturation is critical to produce quality crystals,

particularly for cephalexin, and is comparatively easier in an MSMPR crystallizer where a population of crystals exists to consume the generated supersaturation.^{99, 202}

In this chapter the various parts of the pilot plant are discussed individually, the results of extensive modeling of the pilot plant with the models built in CHAPTER 6 are shown, and the future directions for the pilot plant are explored in depth, as there is still much to be done in the coming years. The pilot plant is planned to be built in two iterative phases; the first phase, termed the basic pilot plant, has been assembled and undergone some testing while the second phase, termed the optimized pilot plant, will be built around the skeleton of the basic pilot plant. The differences between the two phases is shown in Figure 9.1, where additional elements in the optimized pilot plant are shown in green in the simplified schematic of the plant.

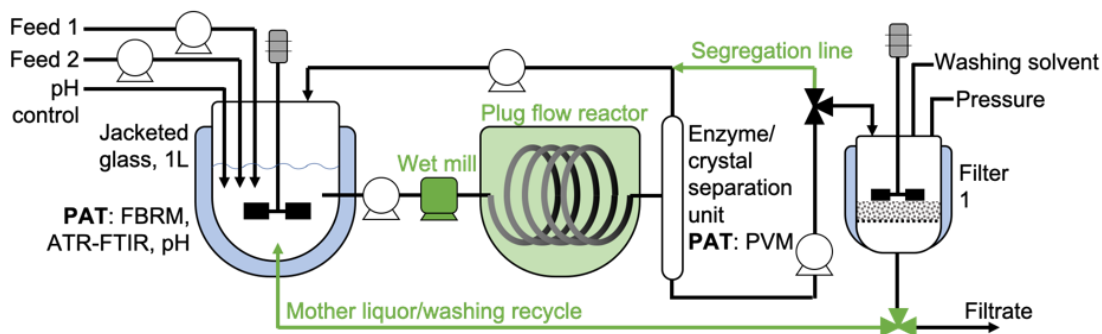


Figure 9.1. Basic pilot plant elements in blue/black, optimal design elements shown in green.

9.2 Reaction and Crystallization

The modeling conducted in CHAPTER 6 suggested that a mixed suspension mixed product removal reactive crystallizer (MSMPR), leftmost vessel in Figure 9.1, followed by a plug flow reactive crystallizer (PFRC), center vessel, would optimize the three process metrics (conversion, selectivity, and productivity). The benefits of this reactor combination

are: self-seeding, low substrate concentrations, and ease of PAT implementation.²⁰³ In the basic pilot plant phase only the MSMPR-RC will be included, the PFRC is one of the additions for the optimized pilot plant.

9.2.1 *Mixed-suspension Mixed-product-removal Reactive Crystallizer*

The MSMPR-RC is the equivalent of the continuous stirred tank reactor for crystallizers, the effluent slurry is representative of the reactor contents. MSMPR-RCs have been used extensively in the chemical industry,^{126, 137, 143, 204, 205} and are now making their way to pharmaceuticals as continuous manufacturing gains traction in the industry.^{9, 206-210} The setup is simple, a jacketed glass vessel with ports for PAT probes and feed and effluent streams. An overhead stirrer keeps the slurry suspended while PGA, immobilized on high surface area beads, is also mixed and generates supersaturation. The simple design allows representative sampling of the entire crystal population by FBRM and PVM and accurate concentration measurements by ATR-FTIR in the MSMPR-RC. In this section, relevant research on the MSMPR-RC is introduced, the predicted behavior of the enzymatic MSMPR-RC from the models built in CHAPTER 6 is discussed, and the challenges anticipated with the MSMPR-RC, along with potential solutions, are enumerated.

In the 1970s and 80s the fundamental behaviors of the MSMPR was an active area for researchers combining vast experimental data sets with newfound computational resources. Topics included hydrodynamics,¹²³ secondary nucleation,²¹¹ sustained oscillatory behaviors,^{212, 213} growth rate dispersion,^{133, 143, 214} but perhaps the most relevant here is steady state multiplicity, and so it is revisited. Like the CSTR, a multiplicity of temperature steady states may exist based on the heat of crystallization and temperature

dependent crystal growth rates.²¹⁵ The enzymatic reactive crystallization process is planned to be isothermal (25 °C) and has very low heats of crystallization and reaction, which should eliminate the possibility of temperature steady state multiplicity, however steady state multiplicity may arise from size distributions alone.¹⁷² Furthermore, when coupled to reaction kinetics that depend on product concentrations, the possibility of multiple steady states increases further.²¹⁶ Figure 9.2 shows how multiple steady state arise. Secondary nucleation (the dominant nucleation pathway in MSMPRs)²⁰⁴ and crystal withdrawal are both functions of suspension density; if they have different orders in the power laws used to describe them, then a multiplicity of steady states may arise. In designing the pilot plant, the reaction rate should be selected such that a stable population of cephalixin crystals exists but any population of phenylglycine crystals wash out, otherwise the concentration of phenylglycine must be kept below the solubility limit.

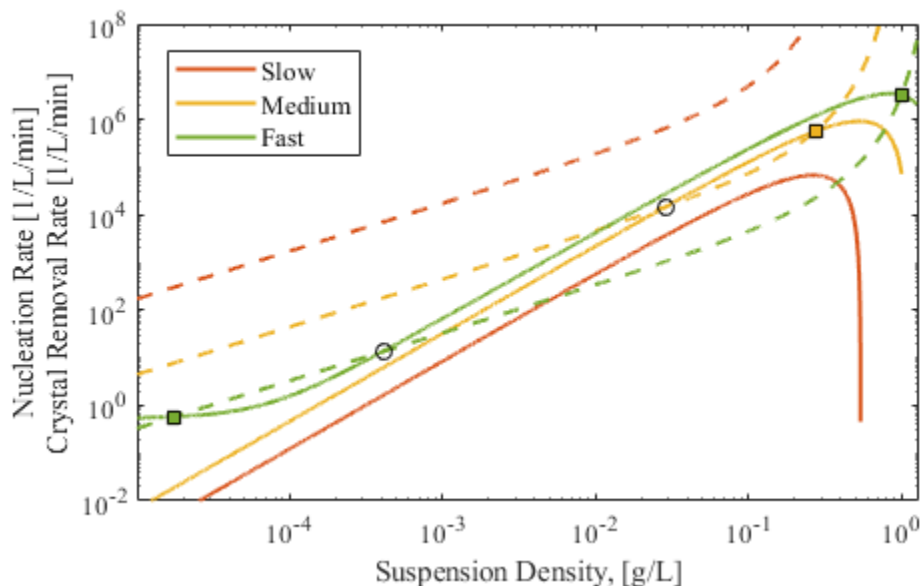


Figure 9.2. A diagram depicting how a multiplicity of steady states arise in an MSMPR-RC, based on the nucleation rate (solid curve) and crystal removal rate (dashed curve) dependence on suspension density. For a slow reaction (red curves) the removal rate is greater than the nucleation rate at all suspension densities; the reaction is not fast enough to sustain a crystal population, a condition

known as wash out. For a medium speed reaction (yellow curves) two stable steady states exist, one with a stable crystal population (yellow square) and one with no crystal population. Systems to the left of the circle eventually converge to the wash out condition while systems to the right of the circle converge to the stable population. For the fast reaction (green curves) the behavior is the same as the medium speed reaction, except there is no wash out condition as the fast reaction generates enough supersaturation to sustain a population of primary nucleated crystals, hence the significant nucleation rate at low suspension density. This plot was created with the model from CHAPTER 7.

The MSMPR has recently gained traction in numerous industries, with publications describing myriad improvements and alterations. In the pharmaceutical industry in particular the MSMPR has been improved by cascading multiple vessels together to reduce supersaturation,^{105, 106, 202, 217} incorporating membranes to remove impurities,²¹⁸⁻²²⁰ and combining different modes of crystallization (e.g. cooling and antisolvent) to enhance yield.²²¹ There has also been work taking advantage of the well-defined residence time of MSMPRs for producing metastable crystal forms or polymorphs.^{106, 222-224} The MSMPR has also found use for deracemizing conglomerate forming enantiomers.²²⁵⁻²²⁷ That so many improvements have been made to, and so many difficult processes been achieved with, the MSMPR speaks volumes to its important role in continuous manufacturing.

The expected behavior of the pilot plant MSMPR-RC has been modeled in CHAPTER 6 and CHAPTER 7. The MSMPR-RC will be operated with the inputs summarized in Table 9.1 for the two different antibiotics. These parameters were chosen to give optimal performance in terms of conversion, selectivity, and productivity. The expected performance of the MSMPR-RC in the basic pilot plant is given in

Table 9.2 for both antibiotics, operating under the conditions set out in Table 9.1.

Table 9.1. Summary of design conditions for reactor sizing, feed concentrations, and flow rates.

Residence time (min), Volume (mL)	Amoxicillin	Cephalexin
MSMPR-RC	120 min, 600 mL	70 min, 350 mL
PFRC	20 min, 105 mL	30 min, 160 mL
Feed (flow rate, concentration, pH)		
Feed 1 (4-HPGME/PGME)	3 mL/min, 0.5 M, pH 4	1.5 mL/min, 1.1 M, pH 4
Feed 2 (6-APA/7-ADCA)	2 mL/min, 0.6 M, pH 7	3.5 mL/min, 0.37 M, pH 7
pH value, temperature, PGA conc.	pH 6.5, 25 °C, 5 μ M	pH 6.5, 25 °C, 5 μ M

Table 9.2. Summary of expected performance of the basic pilot plant based on modeling and the values in Table 9.1.

Basic pilot plant	Conversion w.r.t. 6-APA or 7-ADCA	Selectivity (antibiotic/byproduct)	Productivity (g_{API}/h)
Amoxicillin	80%	3.73	23.2
Cephalexin	65%	5.15	15.7

There are several aspects of the design, implied in Figure 9.1 and Table 9.1 that are worth pointing out. First is the separation of the precursors into two separate feeds with different conditions. For amoxicillin, the solubility of HPGME is less than 100 mM at MSMPR-RC conditions (pH value of 6.5) but increases rapidly at lower pH values, while the solubility of 6-APA decreases rapidly at lower pH values. There is no single feed condition that results in completely dissolved reactants, necessitating two feeds. Upon dilution into the MSMPR-RC the HPGME remains dissolved. The same is true of 7-ADCA for cephalexin: it requires a neutral pH value (basic conditions result in degradation) but remains in solution upon dilution in the MSMPR-RC. This could pose an additional challenge during startup, it is recommended that the reactor be initially charged with a

solution saturated with beta-lactam nucleophile, acyl donor, and antibiotic, then seeded with antibiotic crystals before adding PGA, after which feeding can begin.

The second point is that the volume of the MSMPR-RC is different between the two antibiotics. This stems from cephalexin requiring greater selectivity than amoxicillin because the byproduct from cephalexin hydrolysis is much less soluble than the byproduct of amoxicillin hydrolysis. Selectivity decreases with residence time in the MSMPR-RC, so cephalexin achieves proportionally more conversion in the PFRC compared to amoxicillin. The volumes are close enough that the same vessel will be used for both antibiotics.

The MSMPR-RC, while easier to implement than the PFRC, is not without its own challenges. Fouling remains a significant concern in the MSMPR-RC. As discussed in CHAPTER 8 the PAT probes are subject to fouling, making process control difficult. The simplest solution is to decrease the supersaturation of the system. The supersaturation can be decreased by increasing the MSMPR-RC volume while holding all other design variables constant (feed rate, concentration, enzyme concentration); the rate of antibiotic formation is the same but the crystal population surface area is greater enabling faster depletion of any accumulated supersaturation. Another source of potential fouling comes from the tendency for amoxicillin and cephalexin crystals to form spherulites, shown in Figure 9.3. Spherulites clog tubing, often forming log jams at the crystallizer outlet port. Solutions again include decreased supersaturation, as well as milling to break up large particles, and periodic back pumping to clear clogged inlet. Decreasing supersaturation has the added benefit of making cephalexin crystals less needle-like,²²⁸ the impact of supersaturation on amoxicillin has not been studied.

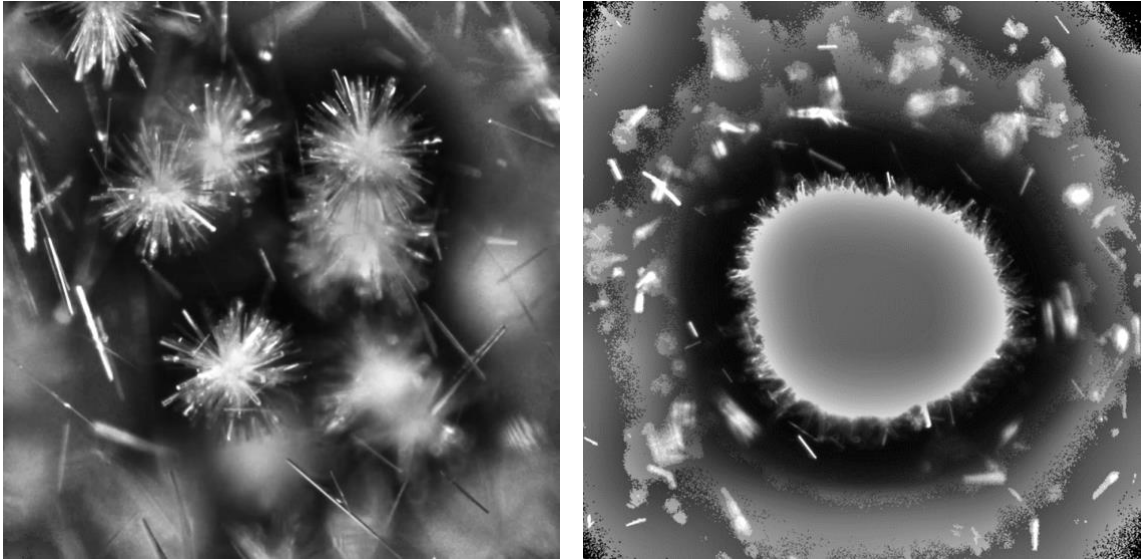


Figure 9.3. PVM images of amoxicillin (left) and cephalixin (right) spherulites. Both images are 1.0 mm².

9.2.2 Plug Flow Reactive Crystallizer

The plug flow reactive crystallizer is equivalent to a batch crystallizer in that the residence time distribution is, ideally, a delta function. Some non-ideal dispersion and mixing ultimately result in a narrow residence time distribution. Less research has been conducted on the PFRC than the MSMPR-RC, however there have still been several important studies on controlling crystal size in a PFRC,^{162, 167, 229} preventing particle settling due to insufficient mixing in a PFRC,^{173, 230} and monitoring crystals in a PFRC.^{231, 232} There has also been a large amount of work with continuous oscillatory baffle crystallizers (COBCs) which seek to mimic the performance of the PFRC with a long series of very small compartments separated by baffles and agitated by oscillatory flow.^{206, 233-236} Some work with modeling COBCs has even involved reactive crystallization (of paracetamol)²³⁶ which is highly relevant to the current process.

The PFRC in this process will receive a feed directly from the MSMPR-RC effluent, avoiding the difficulties associated with seeding and primary nucleation.^{230, 232} The PFRC will operate according to the parameters in Table 9.1 with expected performance outlined in Table 9.3. The design of the PFRC is not as straight forward as for the MSMPR-RC, the length and diameter of the tubing have to be considered. To avoid clogging the diameter must be large enough to accommodate the largest crystals, the particles need to remain suspended, the length must short enough to avoid large pressure drops, and the volumetric throughput must be equal to (or greater than, with recycling of the PFRC products) that of the MSMPR-RC. The tubing must have an inner diameter of at least 1.5 mm as the largest crystals can reach lengths of almost 1.0 mm. The critical velocity (v_c) required to keep the particles suspended can be estimated with the equation below and is found to be 1.96 cm/s.²³⁷

$$v_c = \sqrt{gd(s-1)} \left\{ \frac{5C(1-C)^{2n-1}}{x} \left(\frac{D}{d} \right) \left(\frac{D\rho_l \sqrt{gd(s-1)}}{\mu} \right)^{1/8} \right\}^{8/15} \quad (9.1)$$

where g is the acceleration due to gravity, d is the average particle diameter, s is the ratio of the solid to liquid densities, C is the volume fraction of particles in the slurry, n determines the order of the dependence of the hindered settling velocity on particle concentration and ranges from 4.5 at low Reynolds number to 2.5 at high Reynolds number, x is the fraction of eddies with velocity greater than the hindered settling velocity and typically takes a value between 0.95-1.0, D is the diameter of the tubing, ρ_l is the liquid density, and μ is the viscosity. Putting all the design requirements together, and searching through available inner diameters for pharmaceutical compatible tubing, one determines

that the PFRC should consist of Tygon E-3606 I.D. 2.0 mm with a length of 32 m for amoxicillin and 50 m for cephalixin with a velocity $v = 2.67$ cm/s. While $v > v_c$ it is possible that some settling may occur, in which case pulsed flow, with an average velocity of v but an instantaneous velocity $v_i > v$ may enable steady flow. The pulsation could also improve the performance of the MSMPR-RC by ensuring true mixed product removal.

Table 9.3. Summary of expected performance of the optimized pilot plant based on extensive modeling and the inputs from Table 9.1.

Optimal pilot plant	Conversion w.r.t. 6-APA or 7-ADCA	Selectivity (antibiotic/byproduct)	Productivity (g _{API} /h)
Amoxicillin	89%	3.60	27.0
Cephalixin	80%	5.07	18.0

9.3 Enzyme crystal separation

In Figure 9.1 the enzyme crystal separator is shown after the reactor(s) with two outlets, an enzyme rich retentate and enzyme free permeate. The terms retentate and permeate are borrowed from membrane literature as one of the means of retaining the enzyme is by using an ultrafiltration membrane and soluble PGA, however, initial tests showed low throughput with high fouling potential; not suitable for a continuous process. Rather the separation is conducted based on differences in the properties of the crystals and enzyme carrier. While the design is far from finalized, a promising candidate is the use of a magnetic carrier particle upon which PGA is immobilized and subsequently recovered by application of a magnetic field.

Immobilization of enzymes on magnetic particles is not new, however, so far there have not been any published studies demonstrating continuous recovery of a magnetic biocatalyst, only batch recovery.²³⁸⁻²⁴⁰ Additionally, those examples are limited to liquid phase reactions, magnetic biocatalysts have not been used to recover the catalyst from a product slurry. The inspiration for a continuous magnetic biocatalyst recovery system comes from continuous cell sorting, where antibodies conjugated to magnetic particles bind specific cells. The cells are then sorted by magnetophoresis, or the movement perpendicular to the flow of the medium due to the application of a magnetic field.²⁴¹ Figure 9.4 shows the basic layout, a rectangular compartment with an inlet on the left from the reactor (green) and two outlets on the right, one for the permeate (purple) and a second for the retentate (yellow). A sweeping solution may be optionally included (blue) to improve the separation efficiency. Magnetic particles accumulate above the magnet before being swept into the retentate whereas nonmagnetic particles are free to enter either outlet. It does not matter if there is a significant population of crystals in the retentate as they will be recycled back into the reactor with the biocatalyst. In fact, recycling of crystals increases the suspension density in the crystallizer and may have benefits similar to those found in double draw off crystallizers, namely increased capacity to consume low levels of supersaturation.^{165, 242}

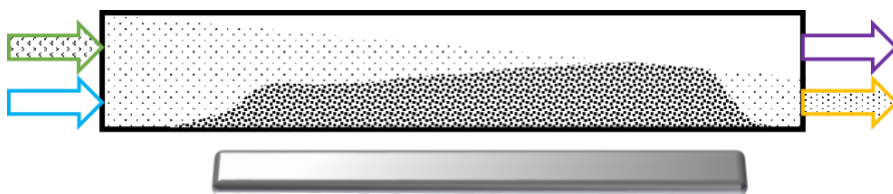


Figure 9.4. Schematic of magnetic separation device. Green arrow, crystallizer effluent containing crystals and biocatalyst. Blue arrow, sweep solution. Purple arrow, permeate, to filtration units. Yellow arrow, retentate, recycled back to reactor. Magnetic particles accumulate above the bar

magnet before being swept into the retentate stream. The scale of the device is <1 cm wide and <15 cm long.

Computational fluid dynamics are used to model the separation factor for magnetic beads before testing in the lab. The magnetic separation system is an ideal application of rapid prototyping by 3-D printing. The initial device, refined from Figure 9.4, is modeled in Figure 9.5. Simulations have shown that laminar flow is key to good separation, but not necessary for high biocatalyst recovery, i.e. to avoid dispersion of the crystals smooth flow is required, otherwise the concentration of crystals is approximately equal in both outlets. Figure 9.5 shows the development of laminar flow with a gentle velocity gradient in the initial section of the device, viewed from the top down (a) and at two slices, one just after the inlets and one near the outlets (b). Experiments with the initial prototype, where retention >95% was achieved at all flow rates (2-5 cm/s) and inert magnetic beads 212-250 μm in diameter, informed the second iteration of the device.

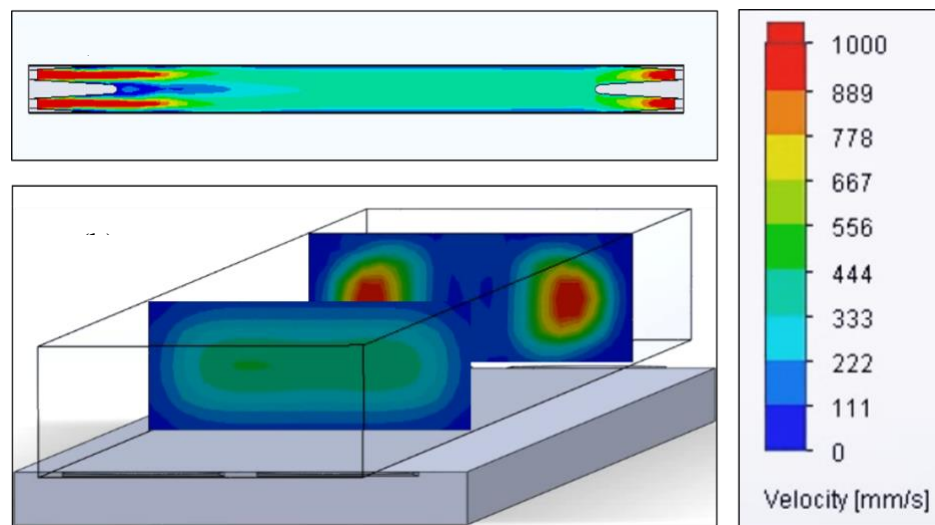


Figure 9.5. Computational fluid dynamics analysis of a continuous magnetic particle separating device. The device, shown as seen from the top in (a), is a rectangular body with two inlets at one end

and two outlets at the other. A magnet is placed parallel to the length of the separator body, pulling magnetic particles to that side. Two slices of the flow field are shown in (b), with velocity scale in (c).

The next steps in the development of the crystal enzyme separator involve scaling the device to work with smaller (2-5 μm) functionalized magnetic beads, conjugated to PGA. Smaller beads are required to achieve a practical enzyme loading per gram of catalyst as the beads are non-porous. A Buckingham Pi analysis, whereby the relevant dimensions are used to infer relevant criteria for good separation, will help to ensure reproducibility with scaled down particles. The relevant dimensionless groups deal with flow rate, magnetic field strength, and solids concentrations; it is expected that particle shape and size should not have too great an impact as long as the flow regime and drag regime are the same across scales.

9.4 Filtration and washing

The final operation in the pilot plant is the combined washing and filtration step. The product will be continuously collected from the permeate stream of the enzyme crystal separator and fed to one of two (or more) batch filtration units. While one filter is collecting material, the material in the other filter is re-suspended with washing solvent and re-filtered, by application of pressure, to give a pure product. When the collection filter is filled, the two filters' roles are switched. Drying is considered beyond the scope of this thesis, being complicated by the product taking the form of a hydrated crystal. However, it can be noted now that too much drying will dehydrate the crystal, compromising product quality.

Filtration is a significant bottleneck in many solids-handling processes.^{243, 244}

Darcy's law for flow through porous media states that the flow rate $Q = \frac{kA}{\mu h} \Delta p$ where k is the cake permeability, A is the filter area, μ is the solution viscosity, h is the filter cake height, and Δp is the pressure differential across the filter. The cake permeability k is highly sensitive to particle attributes such as shape, size distribution, and suspension density. It has been shown that more needle-like particles and smaller particles filter more slowly, having greater filter cake resistances.²⁴⁵ The same trend was observed for cephalexin at small scale, the solution containing a slurry of very high aspect ratio cephalexin crystals filtered at a rate of about 10 mL/min while that containing low aspect ratio cephalexin crystals filtered at nearly 100 mL/min. Figure 9.6 shows the filtration of the two different samples of cephalexin at a suspension density of 100 g/L with vacuum pressure pulling solution through the filter cake.

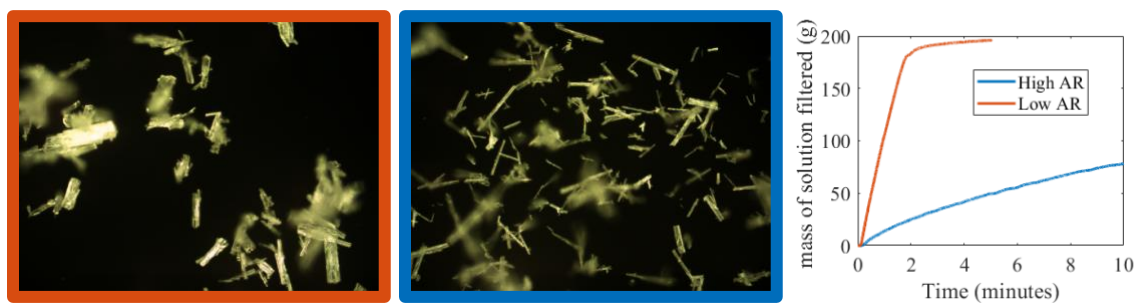


Figure 9.6. The filtration rate of low (left) and high (right) aspect ratio (AR) cephalexin crystals, as measured by the time required to collect the solution in which the crystals were suspended. IN the case of the low AR crystals, complete filtration took less than two minutes, the sharp decrease in mass of collected solution is a result of deliquoring the filter cake.

The pilot plant requires a filtration rate of 5 mL/min, which both samples achieved in this small scale test, however, extrapolating the decreasing rate of filtration seen for the high aspect ratio sample to several hours indicates that these filtration conditions (filter

area, pressure, crystal size and shape) will not suffice. The filter to be used in the pilot plant has approximately twice as much surface area and the capacity for three times as much pressure to drive fluid flow. Still, optimizing the MSMPR-RC and PFRC to grow low aspect ratio crystals will further reduce the risk of a filtration bottleneck. It has been shown that producing cephalexin with a large amount of seed crystals (as would be present in an MSMPR) and at a very low supersaturation, which has previously been advocated for several reasons, can reduce the aspect ratio.²²⁸

Similar filtration experiments were conducted with amoxicillin. A mixture of amoxicillin trihydrate crystals produced under different conditions, to simulate the product from an MSMPR-RC, were suspended and filtered in the same filter to be used in the pilot plant. Complete filtration of 750 mL of suspension took less than four minutes with the application of 15 psi of air pressure pushing solution through the filter cake. While it is possible to model filter performance, based on preliminary results it is not clear that modeling is needed at this time.

Washing, which entails resuspending the filter cake in a non- or poor-solvent, is necessary to both remove entrained reaction solution and reduce adsorbed contaminants from the crystal surface. At present cold water is the intended washing solvent, however, preliminary studies of alcohols and glycols also show promise. A good washing solvent is non-toxic/benign, environmentally friendly, miscible with the aqueous reaction solution, a poor solvent for the antibiotics, a good solvent for the reactants and byproducts, and has high enough water activity to avoid dehydrating the product crystals. The amount of washing solvent, duration of washing, and temperature of washing also need to be

determined. Washing with water would simplify waste treatment and raise the possibility of wash recycling, assuming the primary contaminants are in fact reactants.

9.5 Control

The performance of the process plant is measured in terms of conversion, selectivity, and productivity, while maintaining that purity is more important than any of the performance metrics. Process control should therefore work to keep conversion, selectivity, and productivity at their optimal values without compromising purity, or taking prompt action to uphold high product purity. The process has been designed such that the optimal state is stable, however, large perturbations can cause a very slow return to the controlled state or worse, in the case of the MSMPR-RC, settling into a new steady state, see Figure 9.2. The desired steady state results in pure antibiotic product, but the undesired steady states may not. A process control system that helps keep the system at steady state is therefore highly desirable. It should also be mentioned that additional product specifications, e.g. crystal size, are not yet defined for this process, but some form of active control could enable those specifications to be met as well.

For the dependent variables of purity, conversion, selectivity, and productivity, there are independent variables of flow rates of both the feeds (see Figure 9.1), pH value in the MSMPR-RC, total residence time, and wet-milling intensity. The first four independent variables have well quantified impacts on the dependent variables; their effects are captured by the model developed in CHAPTER 6. Wet-milling, however, is still an area of active research, it has been shown to increase nucleation rates and to significantly decrease crystal length and aspect ratio, enabling control of particle size.²⁴⁶⁻²⁴⁹ The simplest

implementation for control would be to linearize the models around the desired steady state and use PID control based on just one of the independent variables. Complexity could be added by manipulating multiple independent variables. Crystal size control by wet-milling is possible but not a primary aim of the initial pilot plant.²⁴⁸

An important consideration for process control is the ability of PAT to accurately measure the process metrics. In the previous chapter the relevant PAT were evaluated and validated. Concentration measurements from ATR-FTIR, paired with knowledge of the feed concentrations and MSM-RC pH value, can be used to determine conversion, selectivity, and productivity for the basic pilot plant. Estimating crystal size and purity is more difficult. The FBRM signature of the desired crystal size distribution and suspension density could be measured and an empirical relation to wet-milling intensity developed. The presence of phenylglycine crystals should be detectable with PVM, but the controller action will be difficult, as the phenylglycine crystal population would be washed out of the reactor. The difficulty of process monitoring complicates process control and is an additional consideration for estimated controller performance.

9.6 Conclusion

Figure 9.7 shows the progress to date on the basic pilot plant. The entire plant is housed in a fume hood, with temperature control of the feeds, reactor(s), and filters, shown as blue, yellow, and orange jacketed vessels in Figure 9.7. Figure 9.7 has a schematic overlay to make the pilot plant parts recognizable, but what is clear even without labeling is the compactness of the plant, with ample room for upgrading to the optimized pilot plant all within a footprint of less than 20 square feet.

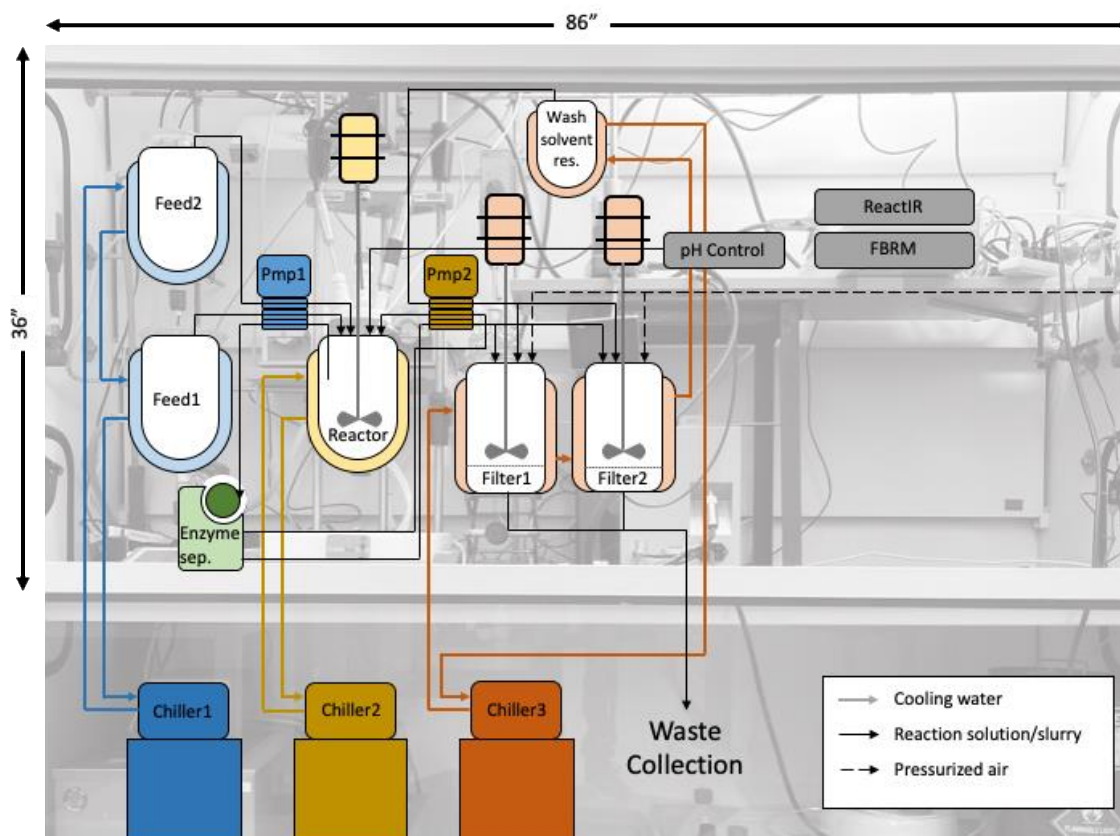


Figure 9.7. Basic pilot plant as of July 2020, with schematic overlay. Prepared for first rounds of testing imminent. Ample space for expansion to the optimal pilot plant can be seen on the right side of the fume hood. The Chillers are color coded to their respective unit operation. PAT are shown in gray

Before attempting the continuous enzymatic reactive crystallization, the pilot plant will be run through a series of tests to ensure successful continuous operation and validity of results. The planned tests are listed below, with the aspects of the plant being tested briefly described. Robust testing is vital to successful implementation of the entire process but is not often discussed

1. Water only: identify leaks, unsteady behavior, verify pump performance, temperature control
2. Reactants (no enzyme): Solution PAT, pH control, stability
3. Non-reacting slurry: slurry transfer, clogging, mixing, particle PAT, filtration
4. Reactive crystallization no separator: verify performance, reclaim catalyst by dissolving product, evaluate catalyst fouling
5. Separator efficacy > 99.9%: continued development alongside reactor testing

In the coming year it is planned to produce kilogram quantities of amoxicillin trihydrate and cephalexin monohydrate in a biocatalytic CM reactive crystallization process for the first time.

CHAPTER 10. FUTURE DIRECTIONS AND PAST REFLECTIONS

In this chapter, the preceding studies are summarized from the perspective of how they add to the scientific knowledgebase. Additional work that could further develop the knowledge generated during these studies is discussed as well.

The first chapter was spent motivating this thesis. While the motivation provides the necessary background to understand the results discussed in the later chapters, there are still facets of the background that are worth mentioning or expanding on here.

First is the issue of antibiotic resistance. CM for beta-lactam antibiotics could potentially contribute to antibiotic resistance if not implemented properly; if done correctly, CM could lead to decreased antibiotic resistance even with a corresponding increase in antibiotic production. It has been shown that many pathogens develop resistance in pharmaceutical wastewater treatment facilities.²⁵⁰ A very recent metagenomics study of 16 European wastewater treatment plants found that the concentration of antibiotic resistance genes downstream of the plant discharge was significantly greater than the concentration in the water upstream of the plant, with beta-lactamase genes (providing bacterial defense against beta-lactams) being some of the most prevalent.²⁵¹ The story is worse in China, where >20% of bacteria isolated from a penicillin producing factory's wastewater treatment plant were resistant to eight beta-lactams at concentrations greater than 1 g/L, significantly higher than the therapeutic concentration in a patient's blood.²⁵²

The effluent is discharged to a river, where its spread and exposure to downstream populations is easily conceivable.

By using CM, the production of wastewater associated with antibiotic manufacture can be decreased. The productivity per liter is significantly higher for the CM process compared to batch, decreasing the amount of solvent needed. Furthermore, by using biocatalysis, fewer steps are needed and no solvent changes are required, reducing the amount of solvent requiring treatment.²⁰ A potential pilot plant improvement is to recycle the mother liquor; it is conceivable that the solvent could be recycled more or less indefinitely, producing no wastewater. For this to happen the following adjustments must be made: (1) powder feeding of reactants, (2) removal of built-up sodium and chloride, possibly by ion exchange, (3) removal of methanol, possibly by evaporation, and (4) removal of (4-hydroxy-) phenylglycine, ideally by crystallization. The last point, phenylglycine crystallization has already been investigated within this thesis. It has been repeatedly observed that phenylglycine crystals adhere to air-water interfaces, see Figure 10.1, and it may be possible to separate the phenylglycine crystals by taking advantage of their hydrophobicity.²⁵³ Doing so continuously would be novel and allow conversion (w.r.t 6-APA or 7-ADCA) to reach nearly 100%, without regard for the selectivity, and at double the productivity. A process producing no liquid waste (that had contacted antibiotics) would halt the spread of resistance in industrial and urban environments, especially since the industrially practiced method of treatment for amoxicillin manufacturing discharge (alkaline degradation, also practiced in this study) has been shown to be insufficient.²⁵⁴

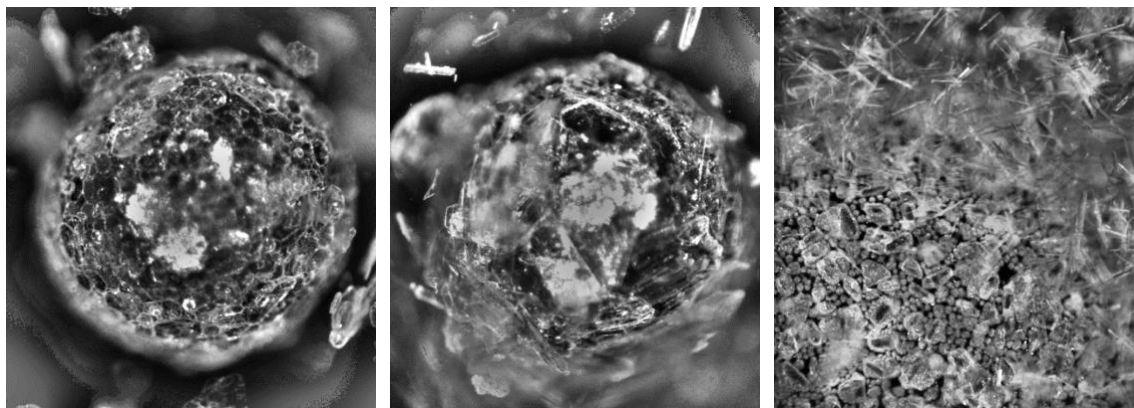


Figure 10.1. PVM images of phenylglycine crystals adhered to bubbles. Left phenylglycine as received, middle pure phenylglycine during recrystallization, right phenylglycine crystallized during cephalixin synthesis (needle shaped crystals are cephalixin). All images are 1.0 mm².

It is beyond the scope of this thesis to address the spread of resistance in other settings, such as hospitals and farms, but it is encouraging to see that use is trending downwards in developed countries. This project could help equalize access to medicines in all countries, but it is up to doctors and veterinarians to dampen the spread of resistance in medical and pastoral settings.

The second background point is related to safety and drug availability. Penicillins, such as amoxicillin, are notoriously potent allergens. The FDA requirement that penicillins be produced in stand-alone facilities (a practice also recommended for cephalosporins) has concentrated production in only a handful of plants worldwide. This concentration of production can and has led to supply chain issues and drug shortages. With this project, the potential exists to create a small, scalable, hypothetically portable, process to provide local access to key drugs on demand.

Moving on to CHAPTER 2, the stability of the biocatalyst was examined. In the frame of the CM process, the exact stability numbers for PGA are most important. However

from a wider lens the scientifically novel contribution here is a method with which to rapidly evaluate biocatalysts. The thermal deactivation properties of almost any enzyme can be modeled and computed within a few hours; orders of magnitude less time than would traditionally be needed. The assay could be further developed by subjecting a variety of enzymes to the temperature profiles used to create a model of PGA deactivation. It would be particularly interesting to manipulate pH value rather than temperature. The same principles, but implemented with adjustable rates of feeding reactants in different pH buffers, could lead to pH specific deactivation models in only hours, again applicable to a wide range of enzymes. The requirement that the reaction produce a change in optical rotation is also unnecessary, different sensors, such as flow ATR-FTIR, flow Raman spectroscopy, flow UV-vis, flow refractometry, or any other online PAT could be used.

In CHAPTER 3 the kinetics of PGA were determined for ampicillin and cephalexin. The feasibility of crystallizing ampicillin by the action of PGA alone, without simultaneous precipitation of phenylglycine was shown for the first time. The activity dependence on pH value was also captured and modeled, expanding on a model published for similar reactions and applied to PGA.²⁵⁵ One key assumption required for fitting the model parameters was that the equilibrium constant for binding the nucleophile (6-APA or 7-ADCA) to the free enzyme and the acyl-enzyme complex was the same. Few report that the nucleophile binds the free enzyme, but the inhibitory effects of excess nucleophile indicates such binding is significant. Since the inhibition is relatively weak this assumption has not impacted any pilot plant models discussed and no results have disproved this assumption. Still, it would further strengthen the expanded model if both constants were quantified independently, to confirm the assumption. A simple experiment would be to measure the inhibition of

cephalexin hydrolysis by 6-APA and the inhibition of ampicillin hydrolysis by 7-ADCA. For example, with cephalexin, phenylglycine, 7-ADCA, and ampicillin would be produced while cephalexin and 6-APA are consumed, as shown in Figure 10.2. Measuring the concentrations of all five species would add significant confidence to the models developed for each antibiotic system alone.

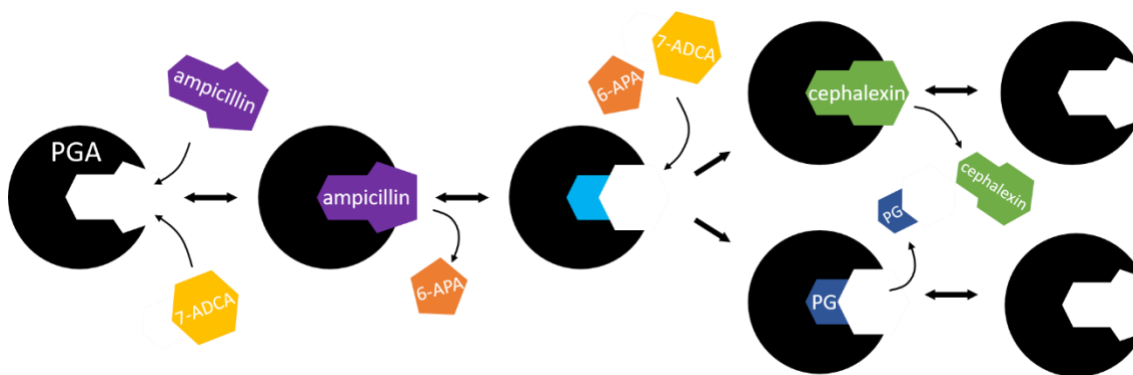


Figure 10.2. Scheme depicting the reaction of ampicillin to cephalexin, and the possible conformation change induced by the acyl-donor.

While the kinetics of enzyme-catalyzed reactions can be very complex, the kinetics of crystallization may be even more so. In CHAPTER 4 it was found that growth is inhibited by the presence of other species, however nucleation is unaffected, only limited to the extent that secondary nucleation depends on suspension density which in turn is determined by total crystal growth. The exact mechanism of inhibition was shown to be adsorption of impurities onto the growing surface, preventing the spread of new growth layers by the inhibition concentration dependence following a Langmuir isotherm. The specific inhibitory effect was stronger for 7-ADCA than PGME, but exactly why is uncertain. A crystal structure of cephalexin could elucidate how each co-solute binds the growing crystals, however no crystal structure of cephalexin monohydrate has been published. Determination of the crystal structure of cephalexin monohydrate presents an

additional opportunity to add to the scientific literature surrounding beta-lactam antibiotics. In any case, knowledge of the impact of the reactants on the crystallization kinetics of cephalexin will decrease the unknowns faced when starting the pilot plant.

The modification of cephalexin crystal shape could also be studied further; it has been reported and observed during this thesis that lower aspect ratio cephalexin is produced at low supersaturation.²²⁸ It might also be possible to modify the shape with additives that either affect supersaturation or inhibit specific faces from growing.²⁵⁶⁻²⁵⁹ It may be possible to take advantage of the difference in binding to cephalexin crystals between 7-ADCA and PGME to create crystals of a more desirable shape. Cephalexin is also known to form low-solubility complexes with several compounds, including parabens, which are already used as preservatives in pharmaceutical formulations.²⁶⁰ Adding a complexing agent could improve crystal shape while increasing yield by sequestering more of the antibiotic in the complex than would otherwise be sequestered by crystallization, preventing undue secondary hydrolysis.

CHAPTER 5 was a slight departure from the main goals of this thesis. The insights into growth rate dispersion are certainly useful and will help to interpret the crystal size distributions measured in the pilot plant. However, as a target size distribution has not yet been determined, knowing fine details such as the degree of growth rate dispersion in a population of ampicillin crystals does not have a tremendous impact on how the pilot plant will be operated. In the future this will not be the case when a size distribution CQA is determined.

Instead the growth rate dispersion study has the most value as a new tool for measuring difficult-to-measure properties of crystal populations. With only a microscope, the differences in growth rates between individual crystals can be quantified without concerns of mass and heat transfer limitations or nucleation. Repeating this study with cephalexin and amoxicillin could increase understanding of growth rate dispersion, which presently is best explained as nebulous differences in surface structure and crystal perfection. An improved experiment would be able to measure the rates of surface repair, the growth rates of each end of the needle independently, and how fast non-equilibrium faces (i.e. those that are only exposed by crystal breakage) grow. Broken crystals grew faster to return to their unbroken shape, and this repair has been interpreted as a cause of growth rate dispersion in other studies.^{261, 262} This finding is consistent with observations of face specific growth rates and even solubilities,^{263, 264} but the implications and applications of confirming this phenomenon, e.g. enhanced crystallization rate by grinding, have not been explored.

There are very few experimental examples of reactive crystallization models with defined reaction kinetics (i.e. reactions that are not modeled as instantaneous)²⁶⁵ despite the thorough theoretical groundwork laid by Kelkar and Ng.²⁶⁶ In this respect, the modeling in CHAPTER 6 stands out as unique but could easily be applied to many other systems with similar features, particularly in the realm of biocatalytic reactions. By undertaking such detailed modeling of the reaction, crystallization, and catalyst deactivation kinetics, bounds have been placed on the performance of the system, with guidance on how to reach those bounds. The model is being further improved to consider mass transfer resistances and immobilized biocatalysts.²⁶⁷ Applying the models to simulate other systems could

assist in evaluating the feasibility of using biocatalysis in other applications typically conducted with more traditional and environmentally taxing chemistry. One could also continue to expand on the present models to include phenomena such as breakage, face specific growth rates, and crystal habit modification. Such upgrades to the model may uncover additional operational modes not accessible with the present model but physically realizable and possibly more desirable. CHAPTER 7 was a natural continuation of CHAPTER 6, addressing the more challenging aspects of the pilot plant design for high conversion, selectivity, and productivity while maintaining purity.

In CHAPTER 8 the value of PAT was discussed in the context of building a pilot plant within the quality-by-design framework. With advanced PAT the pilot plant could, in theory, achieve conversion, selectivity, and productivity beyond the bounds set in CHAPTER 6. In that chapter, the pilot plant was evaluated only at steady state; with PAT and the necessary control, one can imagine operating at an unsteady state or periodic steady state that gives even higher yields.^{213, 268} The work required to examine the infinite design space of unsteady operation is daunting and beyond this thesis, however some observations motivate further investigation. When modeling reactor startup the concentration goes through oscillations, which is a result of the feedback between reactant concentration, reaction rate, crystal nucleation rate, and crystal growth rate. During startup, transient peaks in phenylglycine concentration cause the formation of a sustained phenylglycine crystal population. However, the appearance of the phenylglycine crystal population is delayed (relative to the peak phenylglycine concentration) due to the kinetics of nucleation and growth. It is possible that there is a periodic operating regime where the phenylglycine peak concentration becomes very high but is corrected for before the phenylglycine crystal

population appears; a process only needs to be in a well-controlled state, not a steady state. The increased ceiling on phenylglycine concentration would loosen the selectivity constraint and enable higher conversion and productivity. However, running a pilot plant under these conditions would require more accurate concentration measurements and the ability to pick out phenylglycine crystals from a cephalexin slurry in the ppm range. For that, improved IR concentration measurements and PVM/FBRM solids characterization is needed.

Finally, in CHAPTER 9, the completed pilot plant is discussed. Producing kilogram quantities of amoxicillin and cephalexin in days long continuous campaigns, as well as the challenges, knowledge, and experience that is sure to come from such an undertaking, will surely warrant excitement from the chemical engineering community.

REFERENCES

- [1] Organization, W. H. (2018) WHO report on surveillance of antibiotic consumption: 2016-2018 early implementation.
- [2] Klein, E. Y., Van Boeckel, T. P., Martinez, E. M., Pant, S., Gandra, S., Levin, S. A., Goossens, H., and Laxminarayan, R. (2018) Global increase and geographic convergence in antibiotic consumption between 2000 and 2015, *Proceedings of the National Academy of Sciences* 115, E3463-E3470.
- [3] Roland, D., and Hopkins, J. S. (2020) FDA Cites Shortage of One Drug, Exposing Supply-Line Worry, In *Wall Street Journal*, New York.
- [4] Jiménez-González, C., Poechlauer, P., Broxterman, Q. B., Yang, B.-S., Am Ende, D., Baird, J., Bertsch, C., Hannah, R. E., Dell’Orco, P., and Noorman, H. (2011) Key green engineering research areas for sustainable manufacturing: A perspective from pharmaceutical and fine chemicals manufacturers, *Organic Process Research & Development* 15, 900-911.
- [5] McDonald, M. A., Salami, H., Lagerman, C. E., Harris, P. R., Bommarium, A. S., Grover, M. A., and Rousseau, R. W. (2020) Reactive Crystallization: A Review, *Reaction Chemistry & Engineering*.
- [6] Albin, S., and Agarwal, S. (2014) Prevalence and characteristics of reported penicillin allergy in an urban outpatient adult population, *Allergy and Asthma Proceedings* 35, 489-494.
- [7] (2015) 21 C.F.R § 211.42 (The Code of Federal Regulations of the United States), (Food & Drug Administration).
- [8] (2013) Guidance for Industry: Non-Penicillin Beta-Lactam Drugs: A CGMP Framework for Preventing CrossContamination, (Administration, U. S. F. a. D., Ed.), Center for Drug Evaluation and Research, Silver Spring, MD.
- [9] Cole, K. P., Groh, J. M., Johnson, M. D., Burcham, C. L., Campbell, B. M., Diseroad, W. D., Heller, M. R., Howell, J. R., Kallman, N. J., Koenig, T. M., May, S. A., Miller, R. D., Mitchell, D., Myers, D. P., Myers, S. S., Phillips, J. L., Polster, C. S., White, T. D., Cashman, J., Hurley, D., Moylan, R., Sheehan, P., Spencer, R. D., Desmond, K., Desmond, P., and Gowran, O. (2017) Kilogram-scale prexasertib monolactate monohydrate synthesis under continuous-flow CGMP conditions, *Science* 356, 1144.
- [10] Cole, K. P., Reizman, B. J., Hess, M., Groh, J. M., Laurila, M. E., Cope, R. F., Campbell, B. M., Forst, M. B., Burt, J. L., Maloney, T. D., Johnson, M. D., Mitchell, D., Polster, C. S., Mitra, A. W., Boukerche, M., Conder, E. W., Braden, T. M., Miller, R. D., Heller, M. R., Phillips, J. L., and Howell, J. R. (2019) Small-

Volume Continuous Manufacturing of Merestinib. Part 1. Process Development and Demonstration, *Organic Process Research & Development*.

- [11] Reizman, B. J., Cole, K. P., Hess, M., Burt, J. L., Maloney, T. D., Johnson, M. D., Laurila, M. E., Cope, R. F., Luciani, C. V., Buser, J. Y., Campbell, B. M., Forst, M. B., Mitchell, D., Braden, T. M., Lippelt, C. K., Boukerche, M., Starkey, D. R., Miller, R. D., Chen, J., Sun, B., Kwok, M., Zhang, X., Tadayon, S., and Huang, P. (2019) Small-Volume Continuous Manufacturing of Merestinib. Part 2. Technology Transfer and cGMP Manufacturing, *Organic Process Research & Development*.
- [12] Mascia, S., Heider, P. L., Zhang, H., Lakerveld, R., Benyahia, B., Barton, P. I., Braatz, R. D., Cooney, C. L., Evans, J., and Jamison, T. F. (2013) End-to-End Continuous Manufacturing of Pharmaceuticals: Integrated Synthesis, Purification, and Final Dosage Formation, *Angewandte Chemie International Edition* 52, 12359-12363.
- [13] Lee, S. L. (2017) Modernizing the Way Drugs Are Made: A Transition to Continuous Manufacturing, U.S. FDA, Silver Spring, MD.
- [14] Wood, B., Girard, K. P., Polster, C. S., and Croker, D. M. (2019) Progress to Date in the Design and Operation of Continuous Crystallization Processes for Pharmaceutical Applications, *Organic Process Research & Development* 23, 122-144.
- [15] Acevedo, D., Yang, X., Mohammad, A., Pavurala, N., Wu, W.-L., O'Connor, T. F., Nagy, Z. K., and Cruz, C. N. (2018) Raman Spectroscopy for Monitoring the Continuous Crystallization of Carbamazepine, *Organic Process Research & Development* 22, 156-165.
- [16] Liu, Y. C., Acevedo, D., Yang, X., Naimi, S., Wu, W.-L., Pavurala, N., Nagy, Z. K., and O'Connor, T. F. (2020) Population Balance Model Development Verification and Validation of Cooling Crystallization of Carbamazepine, *Crystal Growth & Design*.
- [17] Simon, L. L., Pataki, H., Marosi, G., Meemken, F., Hungerbühler, K., Baiker, A., Tummala, S., Glennon, B., Kuentz, M., Steele, G., Kramer, H. J. M., Rydzak, J. W., Chen, Z., Morris, J., Kjell, F., Singh, R., Gani, R., Gernaey, K. V., Louhi-Kultanen, M., O'Reilly, J., Sandler, N., Antikainen, O., Yliruusi, J., Frohberg, P., Ulrich, J., Braatz, R. D., Leyssens, T., Von Stosch, M., Oliveira, R., Tan, R. B. H., Wu, H., Khan, M., O'Grady, D., Pandey, A., Westra, R., Delle-Case, E., Pape, D., Angelosante, D., Maret, Y., Steiger, O., Lenner, M., Abbou-Oucherif, K., Nagy, Z. K., Litster, J. D., Kamaraju, V. K., and Chiu, M.-S. (2015) Assessment of Recent Process Analytical Technology (PAT) Trends: A Multiauthor Review, *Organic Process Research & Development* 19, 3-62.
- [18] Azad, M. A., Osorio, J. G., Brancazio, D., Hammersmith, G., Klee, D. M., Rapp, K., and Myerson, A. (2018) A compact, portable, re-configurable, and automated

system for on-demand pharmaceutical tablet manufacturing, *International Journal of Pharmaceutics* 539, 157-164.

- [19] Rogers, L., Briggs, N., Achermann, R., Adamo, A., Azad, M., Brancazio, D., Capellades, G., Hammersmith, G., Hart, T., Imbrogno, J., Kelly, L. P., Liang, G., Neurohr, C., Rapp, K., Russell, M. G., Salz, C., Thomas, D. A., Weimann, L., Jamison, T. F., Myerson, A. S., and Jensen, K. F. (2020) Continuous Production of Five APIs in Flexible Plug-and-Play Modules - A Demonstration Campaign, *Organic Process Research & Development*.
- [20] Elander, R. P. (2003) Industrial production of β -lactam antibiotics, *Applied Microbiology and Biotechnology* 61, 385-392.
- [21] McDonald, M. A., Bommarius, A. S., Rousseau, R. W., and Grover, M. A. (2019) Continuous reactive crystallization of β -lactam antibiotics catalyzed by penicillin G acylase. Part I: Model development, *Computers & Chemical Engineering* 123, 331-343.
- [22] Rudolph, E., Zomerdijk, M., Ottens, M., and van der Wielen, L. (2001) Solubilities and partition coefficients of semi-synthetic antibiotics in water+ 1-butanol systems, *Industrial & Engineering Chemistry Research* 40, 398-406.
- [23] Wang, S., Li, Q.-S., and Li, Y.-L. (2006) Solubility of D-p-hydroxyphenylglycine in water, methanol, ethanol, carbon tetrachloride, toluene, and N, N-dimethylformamide between 278 K and 323 K, *Journal of Chemical & Engineering Data* 51, 2201-2202.
- [24] Srirangan, K., Orr, V., Akawi, L., Westbrook, A., Moo-Young, M., and Chou, C. P. (2013) Biotechnological advances on Penicillin G acylase: Pharmaceutical implications, unique expression mechanism and production strategies, *Biotechnology Advances* 31, 1319-1332.
- [25] Guisán, J. M., Alvaro, G., Fernandez-Lafuente, R., Rosell, C. M., Garcia, J. L., and Tagliani, A. (1993) Stabilization of heterodimeric enzyme by multipoint covalent immobilization: penicillin G acylase from *Kluyvera citrophila*, *Biotechnology and Bioengineering* 42, 455-464.
- [26] Abian, O., Grazú, V., Hermoso, J., González, R., García, J. L., Fernández-Lafuente, R., and Guisán, J. M. (2004) Stabilization of penicillin G acylase from *Escherichia coli*: site-directed mutagenesis of the protein surface to increase multipoint covalent attachment, *Applied and Environmental Microbiology* 70, 1249-1251.
- [27] Flores, G., Soberón, X., and Osuna, J. (2004) Production of a fully functional, permuted single-chain penicillin G acylase, *Protein Science* 13, 1677-1683.
- [28] Kallenberg, A. I., van Rantwijk, F., and Sheldon, R. A. (2005) Immobilization of penicillin G acylase: the key to optimum performance, *Advanced Synthesis & Catalysis* 347, 905-926.

- [29] Cai, G., Zhu, S., Yang, S., Zhao, G., and Jiang, W. (2004) Cloning, overexpression, and characterization of a novel thermostable penicillin G acylase from *Achromobacter xylosoxidans*: probing the molecular basis for its high thermostability, *Applied and Environmental Microbiology* 70, 2764-2770.
- [30] de los Ríos, A. P., Hernández-Fernández, F. J., Rubio, M., Gómez, D., and Villora, G. (2007) Stabilization of native penicillin G acylase by ionic liquids, *Journal of Chemical Technology and Biotechnology* 82, 190-195.
- [31] Kazan, D., and Erarslan, A. (1997) Stabilization of *Escherichia coli* penicillin G acylase by polyethylene glycols against thermal inactivation, *Applied biochemistry and biotechnology* 62, 1-13.
- [32] McDonald, M. A., Bommarius, A. S., and Rousseau, R. W. (2017) Enzymatic reactive crystallization for improving ampicillin synthesis, *Chemical Engineering Science* 165, 81-88.
- [33] Henderson, R. K., Jiménez-González, C., Preston, C., Constable, D. J., and Woodley, J. M. (2008) EHS & LCA assessment for 7-ACA synthesis: a case study for comparing biocatalytic & chemical synthesis, *Industrial Biotechnology* 4, 180-193.
- [34] Youshko, M. I., van Langen, L. M., de Vroom, E., Moody, H. M., van Rantwijk, F., Sheldon, R. A., and Švedas, V. K. (2000) Penicillin acylase-catalyzed synthesis of ampicillin in “aqueous solution–precipitate” systems. High substrate concentration and supersaturation effect, *Journal of Molecular Catalysis B: Enzymatic* 10, 509-515.
- [35] Pan, X., Wang, L., Ye, J., Qin, S., and He, B. (2018) Efficient synthesis of β -lactam antibiotics with very low product hydrolysis by a mutant *Providencia rettgeri* penicillin G acylase, *Applied Microbiology and Biotechnology* 102, 1749-1758.
- [36] Ferreira, A. L., Giordano, R. L., and Giordano, R. C. (2007) Nonconventional reactor for enzymatic synthesis of semi-synthetic β -lactam antibiotics, *Industrial & Engineering Chemistry Research* 46, 7695-7702.
- [37] Hernandez-Justiz, O., Fernandez-Lafuente, R., Terreni, M., and Guisan, J. M. (1998) Use of aqueous two-phase systems for in situ extraction of water soluble antibiotics during their synthesis by enzymes immobilized on porous supports, *Biotechnology and Bioengineering* 59, 73-79.
- [38] Wang, K. Y., and Chung, T.-S. (2005) The characterization of flat composite nanofiltration membranes and their applications in the separation of Cephalexin, *Journal of Membrane Science* 247, 37-50.
- [39] Schroën, C., Nierstrasz, V. A., Bosma, R., Kemperman, G. J., Strubel, M., Ooijkaas, L. P., Beeftink, H. H., and Tramper, J. (2002) In situ product removal during enzymatic cephalosporin synthesis by complexation, *Enzyme and Microbial Technology* 31, 264-273.

- [40] Schroën, C., Nierstrasz, V., Kroon, P., Bosma, R., Janssen, A., Beeftink, H., and Tramper, J. (1999) Thermodynamically controlled synthesis of β -lactam antibiotics. Equilibrium concentrations and side-chain properties, *Enzyme and Microbial Technology* 24, 498-506.
- [41] Encarnación-Gómez, L. G., Bommarius, A. S., and Rousseau, R. W. (2016) Reactive crystallization of β -lactam antibiotics: strategies to enhance productivity and purity of ampicillin, *Reaction Chemistry & Engineering* 1, 321-329.
- [42] Söhnel, O., and Mullin, J. W. (1978) Expressions of supersaturation for systems containing hydrates, partially dissociated electrolytes and mixtures of electrolytes, *Chemical Engineering Science* 33, 1535-1538.
- [43] Mullin, J. W. (2001) *Crystallization*, Fourth edition ed., Butterworth-Heinemann.
- [44] Urbanus, J., Roelands, C., Verdoes, D., and ter Horst, J. (2012) Intensified crystallization in complex media: Heuristics for crystallization of platform chemicals, *Chemical Engineering Science* 77, 18-25.
- [45] Santana, M., Ribeiro, M., Leite, G. A., Giordano, R. L., Giordano, R. C., and Mattedi, S. (2010) Solid-liquid equilibrium of substrates and products of the enzymatic synthesis of ampicillin, *AIChE Journal* 56, 1578-1583.
- [46] Yu, W., Muteki, K., Zhang, L., and Kim, G. (2011) Prediction of Bulk Powder Flow Performance Using Comprehensive Particle Size and Particle Shape Distributions, *Journal of Pharmaceutical Sciences* 100, 284-293.
- [47] Pudasaini, N., Upadhyay, P. P., Parker, C. R., Hagen, S. U., Bond, A. D., and Rantanen, J. (2017) Downstream Processability of Crystal Habit-Modified Active Pharmaceutical Ingredient, *Organic Process Research & Development* 21, 571-577.
- [48] Wang, X., De Anda, J. C., and Roberts, K. (2007) Real-time measurement of the growth rates of individual crystal facets using imaging and image analysis: a feasibility study on needle-shaped crystals of L-glutamic acid, *Chemical Engineering Research and Design* 85, 921-927.
- [49] Leyssens, T., Baudry, C., and Escudero Hernandez, M. L. (2011) Optimization of a crystallization by online FBRM analysis of needle-shaped crystals, *Organic Process Research & Development* 15, 413-426.
- [50] Ochsenbein, D. R., Vetter, T., Morari, M., and Mazzotti, M. (2015) Agglomeration of needle-like crystals in suspension. II. Modeling, *Crystal Growth & Design* 15, 4296-4310.
- [51] Ochsenbein, D. R., Vetter, T., Schorsch, S., Morari, M., and Mazzotti, M. (2015) Agglomeration of Needle-like Crystals in Suspension: I. Measurements, *Crystal Growth & Design* 15, 1923-1933.

- [52] Szilágyi, B., Agachi, P. Ş., and Lakatos, B. G. (2015) Numerical analysis of crystallization of high aspect ratio crystals with breakage, *Powder Technology* 283, 152-162.
- [53] Li, H., and Yang, B.-S. (2019) Model evaluation of particle breakage facilitated process intensification for Mixed-Suspension-Mixed-Product-Removal (MSMPR) crystallization, *Chemical Engineering Science* 207, 1175-1186.
- [54] Saleemi, A., Rielly, C., and Nagy, Z. K. (2012) Automated Direct Nucleation Control for In Situ Dynamic Fines Removal in Batch Cooling Crystallization, *CrystEngComm* 14, 2196-2203.
- [55] Griffin, D. J., Grover, M. A., Kawajiri, Y., and Rousseau, R. W. (2015) Mass-count plots for crystal size control, *Chemical Engineering Science* 137, 338-351.
- [56] Szilágyi, B., and Nagy, Z. K. (2018) Population Balance Modeling and Optimization of an Integrated Batch Crystallizer–Wet Mill System for Crystal Size Distribution Control, *Crystal Growth & Design* 18, 1415-1424.
- [57] Alvaro, G., Fernandez-Lafuente, R., Blanco, R. M., and Guisán, J. M. (1990) Immobilization-stabilization of penicillin G acylase from *Escherichia coli*, *Applied Biochemistry and Biotechnology* 26, 181-195.
- [58] Illanes, A., Altamirano, C., and Zuñiga, M. E. (1996) Thermal inactivation of immobilized penicillin acylase in the presence of substrate and products, *Biotechnology and Bioengineering* 50, 609-616.
- [59] Rogers, T. A., and Bommarius, A. S. (2010) Utilizing simple biochemical measurements to predict lifetime output of biocatalysts in continuous isothermal processes, *Chemical Engineering Science* 65, 2118-2124.
- [60] Schokker, E. P., and van Boekel, A. (1997) Kinetic modeling of enzyme inactivation: Kinetics of heat inactivation at 90– 110° C of extracellular proteinase from *Pseudomonas fluorescens* 22F, *Journal of Agricultural and Food Chemistry* 45, 4740-4747.
- [61] Rogers, T. A. (2010) Long-term biocatalyst performance via heuristic and rigorous modeling approaches, In *School of Chemical and Biomolecular Engineering*, Georgia Institute of Technology.
- [62] Rogers, T. A., Daniel, R. M., and Bommarius, A. S. (2009) Deactivation of TEM-1 β -Lactamase Investigated by Isothermal Batch and Non-Isothermal Continuous Enzyme Membrane Reactor Methods, *ChemCatChem* 1, 131-137.
- [63] Youshko, M. I., Chilov, G. G., Shcherbakova, T. A., and Švedas, V. K. (2002) Quantitative characterization of the nucleophile reactivity in penicillin acylase-catalyzed acyl transfer reactions, *Biochimica et Biophysica Acta (BBA)-Proteins and Proteomics* 1599, 134-140.

- [64] Alkema, W. B. L., de Vries, E., Floris, R., and Janssen, D. B. (2003) Kinetics of enzyme acylation and deacylation in the penicillin acylase-catalyzed synthesis of beta-lactam antibiotics, *European Journal of Biochemistry* 270, 3675-3683.
- [65] Daniel, R. M., Danson, M. J., Eisenthal, R., Lee, C., and Peterson, M. E. (2007) New parameters controlling the effect of temperature on enzyme activity, Portland Press Limited.
- [66] Lumry, R., and Eyring, H. (1954) Conformation changes of proteins, *The Journal of Physical Chemistry* 58, 110-120.
- [67] Sanchez-Ruiz, J. M. (1992) Theoretical analysis of Lumry-Eyring models in differential scanning calorimetry, *Biophysical Journal* 61, 921-935.
- [68] Peterson, M. E., Daniel, R. M., Danson, M. J., and Eisenthal, R. (2007) The dependence of enzyme activity on temperature: determination and validation of parameters, *Biochemical Journal* 402, 331-337.
- [69] Mazurenko, S., Kunka, A., Beerens, K., Johnson, C. M., Damborsky, J., and Prokop, Z. (2017) Exploration of Protein Unfolding by Modelling Calorimetry Data from Reheating, *Scientific Reports* 7, 16321.
- [70] Burnham, K. P., and Anderson, D. R. (2004) Multimodel Inference: Understanding AIC and BIC in Model Selection, *Sociological Methods & Research* 33, 261-304.
- [71] Burnham, K. P., and Anderson, D. R. (2003) *Model selection and multimodel inference: a practical information-theoretic approach*, Springer Science & Business Media.
- [72] Daniel, R. M., Danson, M. J., and Eisenthal, R. (2001) The temperature optima of enzymes: a new perspective on an old phenomenon, *Trends in Biochemical Sciences* 26, 223-225.
- [73] Peterson, M. E., Eisenthal, R., Danson, M. J., Spence, A., and Daniel, R. M. (2004) A new intrinsic thermal parameter for enzymes reveals true temperature optima, *Journal of Biological Chemistry* 279, 20717-20722.
- [74] Rodriguez-Larrea, D., Ibarra-Molero, B., de Maria, L., Borchert, T. V., and Sanchez-Ruiz, J. M. (2008) Beyond Lumry-Eyring: An unexpected pattern of operational reversibility/irreversibility in protein denaturation, *Proteins: Structure, Function, and Bioinformatics* 70, 19-24.
- [75] Anfinsen, C. B. (1973) Principles that govern the folding of protein chains, *Science* 181, 223-230.
- [76] Grinberg, V. Y., Burova, T. V., Grinberg, N. V., Shcherbakova, T. A., Guranda, D. T., Chilov, G. G., and Švedas, V. K. (2008) Thermodynamic and kinetic stability

of penicillin acylase from *Escherichia coli*, *Biochimica et Biophysica Acta (BBA)-Proteins and Proteomics* 1784, 736-746.

- [77] Youshko, M., and Švedas, V. (2000) Kinetics of ampicillin synthesis catalyzed by penicillin acylase from *E. coli* in homogeneous and heterogeneous systems. Quantitative characterization of nucleophile reactivity and mathematical modeling of the process, *Biochemistry (Moscow)* 65, 1367-1375.
- [78] Illanes, A., Anjarí, S., Arrieta, R., and Aguirre, C. (2002) Optimization of yield in kinetically controlled synthesis of ampicillin with immobilized penicillin acylase in organic media, *Applied Biochemistry and Biotechnology* 97, 165-179.
- [79] Illanes, A., Wilson, L., Corrotea, O., Tavernini, L., Zamorano, F., and Aguirre, C. (2007) Synthesis of cephalexin with immobilized penicillin acylase at very high substrate concentrations in fully aqueous medium, *Journal of Molecular Catalysis B: Enzymatic* 47, 72-78.
- [80] Giordano, R. C., Ribeiro, M. P., and Giordano, R. L. (2006) Kinetics of β -lactam antibiotics synthesis by penicillin G acylase (PGA) from the viewpoint of the industrial enzymatic reactor optimization, *Biotechnology Advances* 24, 27-41.
- [81] Gonçalves, L. R., Fernandez-Lafuente, R., Guisan, J. M., Giordano, R. L., and Giordano, R. C. (2003) Inhibitory effects in the side reactions occurring during the enzymic synthesis of amoxicillin: p-hydroxyphenylglycine methyl ester and amoxicillin hydrolysis, *Biotechnology and Applied Biochemistry* 38, 77-85.
- [82] Gonçalves, L. R. B., Giordano, R. L. C., and Giordano, R. C. (2005) Mathematical modeling of batch and semibatch reactors for the enzymic synthesis of amoxicillin, *Process Biochemistry* 40, 247-256.
- [83] Gonçalves, L. R. B., Sousa, R., Fernandez-Lafuente, R., Guisan, J. M., Giordano, R. L. C., and Giordano, R. C. (2002) Enzymatic synthesis of amoxicillin: avoiding limitations of the mechanistic approach for reaction kinetics, *Biotechnology and Bioengineering* 80, 622-631.
- [84] Blum, J. K., Deaguero, A. L., Perez, C. V., and Bommarius, A. S. (2010) Ampicillin Synthesis Using a Two-Enzyme Cascade with Both α -Amino Ester Hydrolase and Penicillin G Acylase, *ChemCatChem* 2, 987-991.
- [85] Deng, S., Ma, X., Sun, M., Wei, D., and Su, E. (2016) Efficient enzymatic synthesis of ampicillin using mutant Penicillin G acylase with bio-based solvent glycerol, *Catalysis Communications* 79, 31-34.
- [86] Blum, J. K. (2011) Broadening the application of enzyme-catalyzed synthesis of semi-synthetic antibiotics, In *School of Chemical and Biomolecular Engineering*, p 197, Georgia Institute of Technology, Atlanta, Georgia.

- [87] Youshko, M. I., van Langen, L. M., de Vroom, E., van Rantwijk, F., Sheldon, R. A., and Švedas, V. K. (2002) Penicillin acylase-catalyzed ampicillin synthesis using a pH gradient: A new approach to optimization, *Biotechnology and Bioengineering* 78, 589-593.
- [88] Ottens, M., Lebreton, B., Zomerdijk, M., Rijkers, M., Bruinsma, O. S. L., and Van der Wielen, L. A. M. (2001) Crystallization kinetics of ampicillin, *Industrial & Engineering Chemistry Research* 40, 4821-4827.
- [89] Encarnación-Gómez, L. G., Bommarius, A. S., and Rousseau, R. W. (2016) Crystallization Kinetics of Ampicillin Using Online Monitoring Tools and Robust Parameter Estimation, *Industrial & Engineering Chemistry Research* 55, 2153-2162.
- [90] Volcke, E. I. P., Van Hulle, S., Deksissa, T., Zaher, U., and Vanrolleghem, P. A. (2005) Calculation of pH and concentration of equilibrium components during dynamic simulation by means of a charge balance, BIOMATH Tech. Report, Ghent University, Ghent, Belgium.
- [91] Lange, L., Lehmkemper, K., and Sadowski, G. (2016) Predicting the Aqueous Solubility of Pharmaceutical Cocrystals As a Function of pH and Temperature, *Crystal Growth & Design* 16, 2726-2740.
- [92] Erarslan, A. (1993) The effect of pH on the kinetics of penicillin G acylase obtained from a mutant of Escherichia coli ATCC 11105, *Process Biochemistry* 28, 319-324.
- [93] Ospina, S., Barzana, E., Ramírez, O. T., and López-Munguía, A. (1996) Effect of pH in the synthesis of ampicillin by penicillin acylase, *Enzyme and Microbial Technology* 19, 462-469.
- [94] Gololobov, M. Y., Borisov, I. L., and Svedas, V. K. (1989) Acyl group transfer by proteases forming an acylenzyme intermediate - kinetic-model analysis (including hydrolysis of acylenzyme-nucleophile complex), *Journal of Theoretical Biology* 140, 193-204.
- [95] Silva, J. A., Neto, E. H. C., Adriano, W. S., Ferreira, A. L. O., and Gonçalves, L. R. B. (2008) Use of neural networks in the mathematical modelling of the enzymic synthesis of amoxicillin catalysed by penicillin G acylase immobilized in chitosan, *World Journal of Microbiology and Biotechnology* 24, 1761-1767.
- [96] Gololobov, M. Y., Kozlova, E. V., Borisov, I. L., Schellenberger, U., Schellenberger, V., and Jakubke, H. D. (1992) How to predict product yield in kinetically controlled enzymatic peptide synthesis, *Biotechnology and Bioengineering* 40, 432-436.
- [97] Adamo, A., Beingessner, R. L., Behnam, M., Chen, J., Jamison, T. F., Jensen, K. F., Monbaliu, J.-C. M., Myerson, A. S., Revalor, E. M., and Snead, D. R. (2016) On-

demand continuous-flow production of pharmaceuticals in a compact, reconfigurable system, *Science* 352, 61-67.

- [98] Jolliffe, H. G., and Gerogiorgis, D. I. (2016) Plantwide design and economic evaluation of two Continuous Pharmaceutical Manufacturing (CPM) cases: Ibuprofen and artemisinin, *Computers & Chemical Engineering* 91, 269-288.
- [99] McDonald, M. A., Marshall, G. D., Bommarius, A. S., Grover, M. A., and Rousseau, R. W. (2019) Crystallization Kinetics of Cephalexin Monohydrate in the Presence of Cephalexin Precursors, *Crystal Growth & Design* 19, 5065-5074.
- [100] Kubota, N., Yokota, M., and Mullin, J. (1997) Supersaturation dependence of crystal growth in solutions in the presence of impurity, *Journal of Crystal Growth* 182, 86-94.
- [101] Kubota, N. (2001) Effect of impurities on the growth kinetics of crystals, *Crystal Research and Technology* 36, 749-769.
- [102] Fevotte, F., and Fevotte, G. (2010) A method of characteristics for solving population balance equations (PBE) describing the adsorption of impurities during crystallization processes, *Chemical Engineering Science* 65, 3191-3198.
- [103] Griffin, D. J., Grover, M. A., Kawajiri, Y., and Rousseau, R. W. (2014) Robust multicomponent IR-to-concentration model regression, *Chemical Engineering Science* 116, 77-90.
- [104] Griffin, D. J., Grover, M. A., Kawajiri, Y., and Rousseau, R. W. (2015) Combining ATR-FTIR and FBRM for feedback on crystal size, In *2015 American Control Conference (ACC)*, pp 4308-4313, IEEE.
- [105] Li, J., Trout, B. L., and Myerson, A. S. (2015) Multistage Continuous Mixed-Suspension, Mixed-Product Removal (MSMPR) Crystallization with Solids Recycle, *Organic Process Research & Development* 20, 510-516.
- [106] Lai, T.-T. C., Cornevin, J., Ferguson, S., Li, N., Trout, B. L., and Myerson, A. S. (2015) Control of Polymorphism in Continuous Crystallization via Mixed Suspension Mixed Product Removal Systems Cascade Design, *Crystal Growth & Design* 15, 3374-3382.
- [107] Li, H., Kawajiri, Y., Grover, M. A., and Rousseau, R. W. (2017) Modeling of nucleation and growth kinetics for unseeded batch cooling crystallization, *Industrial & Engineering Chemistry Research* 56, 4060-4073.
- [108] Abu Bakar, M. R., Nagy, Z. K., and Rielly, C. D. (2010) Investigation of the Effect of Temperature Cycling on Surface Features of Sulfathiazole Crystals during Seeded Batch Cooling Crystallization, *Crystal Growth & Design* 10, 3892-3900.

- [109] Li, H., Grover, M. A., Kawajiri, Y., and Rousseau, R. W. (2013) Development of an Empirical Method Relating Crystal Size Distributions and FBRM Measurements, *Chemical Engineering Science* 89, 142-151.
- [110] Li, H., Kawajiri, Y., Grover, M. A., and Rousseau, R. W. (2014) Application of an Empirical FBRM Model to Estimate Crystal Size Distributions in Batch Crystallization, *Crystal Growth & Design* 14, 607-616.
- [111] Maggioni, G. M., and Mazzotti, M. (2015) Modelling the stochastic behaviour of primary nucleation, *Faraday Discussions* 179, 359-382.
- [112] Maggioni, G. M., Bosetti, L., dos Santos, E., and Mazzotti, M. (2017) Statistical Analysis of Series of Detection Time Measurements for the Estimation of Nucleation Rates, *Crystal Growth & Design* 17, 5488-5498.
- [113] Burton, W.-K., Cabrera, N., and Frank, F. (1951) The growth of crystals and the equilibrium structure of their surfaces, *Philosophical Transactions of the Royal Society of London A: Mathematical, Physical and Engineering Sciences* 243, 299-358.
- [114] Barthe, S. C., Grover, M. A., and Rousseau, R. W. (2008) Observation of polymorphic change through analysis of FBRM data: Transformation of paracetamol from form II to form I, *Crystal Growth & Design* 8, 3316-3322.
- [115] Hutton, K., Mitchell, N., and Frawley, P. J. (2012) Particle size distribution reconstruction: The moment surface method, *Powder Technology* 222, 8-14.
- [116] Wold, S., Sjöström, M., and Eriksson, L. (2001) PLS-Regression: a Basic Tool of Chemometrics, *Chemometrics and Intelligent Laboratory Systems* 58, 109-130.
- [117] Bada, J. L. (1969) The pKa of a weak acid as a function of temperature and ionic strength: An experiment using a pH meter, *Journal of Chemical Education* 46, 689.
- [118] Xiao, Y., Tang, S. K., Hao, H., Davey, R. J., and Vetter, T. (2017) Quantifying the Inherent Uncertainty Associated with Nucleation Rates Estimated from Induction Time Data Measured in Small Volumes, *Crystal Growth & Design* 17, 2852-2863.
- [119] Kennedy, A. R., Okoth, M. O., Sheen, D. B., Sherwood, J. N., Teat, S. J., and Vrcelj, R. M. (2003) Cephalexin: a channel hydrate, *Acta Crystallographica Section C: Crystal Structure Communications* 59, o650-o652.
- [120] Davison, A. C., and Hinkley, D. V. (1997) *Bootstrap methods and their application*, Vol. 1, Cambridge university press.
- [121] Lacmann, R., Herden, A., and Mayer, C. (1999) Kinetics of nucleation and crystal growth, *Chemical Engineering & Technology: Industrial Chemistry-Plant Equipment-Process Engineering-Biotechnology* 22, 279-289.

- [122] Armenante, P. M., Mazzarotta, B., and Chang, G.-M. (1999) Power consumption in stirred tanks provided with multiple pitched-blade turbines, *Industrial & engineering chemistry research* 38, 2809-2816.
- [123] Ayazi Shamlou, P., Jones, A. G., and Djamarani, K. (1990) Hydrodynamics of secondary nucleation in suspension crystallization, *Chemical Engineering Science* 45, 1405-1416.
- [124] Sinnott, R. K. (1993) CHAPTER 10 - Equipment Selection, Specification and Design, In *Coulson and Richardson's Chemical Engineering (Second Edition)* (Sinnott, R. K., Ed.), pp 352-438, Pergamon, Amsterdam.
- [125] Alargova, R. G., Warhadpande, D. S., Paunov, V. N., and Veleev, O. D. (2004) Foam superstabilization by polymer microrods, *Langmuir* 20, 10371-10374.
- [126] Garside, J., Rusli, I., and Larson, M. A. (1979) Origin and size distribution of secondary nuclei, *AIChE Journal* 25, 57-64.
- [127] Tai, C. Y., Wu, J.-F., and Rousseau, R. W. (1992) Interfacial supersaturation, secondary nucleation, and crystal growth, *Journal of Crystal Growth* 116, 294-306.
- [128] Kubota, N., and Mullin, J. (1995) A kinetic model for crystal growth from aqueous solution in the presence of impurity, *Journal of Crystal Growth* 152, 203-208.
- [129] Albon, N., and Dunning, W. (1962) Growth of sucrose crystals: determination of edge energy from the effect of added impurity on rate of step advance, *Acta Crystallographica* 15, 474-476.
- [130] Parker, R. L. (1970) Crystal Growth Mechanisms: Energetics, Kinetics, and Transport, In *Solid State Physics* (Ehrenreich, H., Seitz, F., and Turnbull, D., Eds.), pp 151-299, Academic Press.
- [131] McCabe, W. L. (1929) Crystal growth in aqueous solutions I: I—Theory, *Industrial & Engineering Chemistry* 21, 30-33.
- [132] Ulrich, J. (1989) Growth rate dispersion — a review, *Crystal Research and Technology* 24, 249-257.
- [133] Girolami, M. W., and Rousseau, R. W. (1985) Size-dependent crystal growth—A manifestation of growth rate dispersion in the potassium alum-water system, *AIChE Journal* 31, 1821-1828.
- [134] Randolph, A. D., and White, E. T. (1977) Modeling size dispersion in the prediction of crystal-size distribution, *Chemical Engineering Science* 32, 1067-1076.
- [135] Garside, J., and Ristić, R. I. (1983) Growth rate dispersion among ADP crystals formed by primary nucleation, *Journal of Crystal Growth* 61, 215-220.

- [136] Zumstein, R. C., and Rousseau, R. W. (1989) Anomalous growth of large and small copper sulfate pentahydrate crystals, *Industrial & Engineering Chemistry Research* 28, 289-297.
- [137] Budz, J., Jones, A., and Mullin, J. (1987) On the shape-size dependence of potassium sulfate crystals, *Industrial & Engineering Chemistry Research* 26, 820-824.
- [138] Sahin, Ö., and Nusret Bulutcu, A. (2002) Effect of surface charge distribution on the crystal growth of sodium perborate tetrahydrate, *Journal of Crystal Growth* 241, 471-480.
- [139] Botsaris, G. D., Ersan Denk, G., and Shelden, R. A. (1973) Oscillating crystal growth rates, *Kristall und Technik* 8, 769-778.
- [140] Woo, X. Y., Nagy, Z. K., Tan, R. B. H., and Braatz, R. D. (2009) Adaptive Concentration Control of Cooling and Antisolvent Crystallization with Laser Backscattering Measurement, *Crystal Growth & Design* 9, 182-191.
- [141] Tavare, N. S. (1986) Mixing in continuous crystallizers, *AIChE Journal* 32, 705-732.
- [142] Bobo, E., Petit, S., and Coquerel, G. (2015) Growth Rate Dispersion at the Single-Crystal Level, *Chem. Eng. Technol.* 38, 1011-1016.
- [143] Berglund, K., and Larson, M. (1984) Modeling of growth rate dispersion of citric acid monohydrate in continuous crystallizers, *AIChE Journal* 30, 280-287.
- [144] Srisanga, S., Flood, A. E., Galbraith, S. C., Rugmai, S., Soontaranon, S., and Ulrich, J. (2015) Crystal growth rate dispersion versus size-dependent crystal growth: Appropriate modeling for crystallization processes, *Crystal Growth & Design* 15, 2330-2336.
- [145] Zumstein, R., and Rousseau, R. (1987) Growth rate dispersion by initial growth rate distributions and growth rate fluctuations, *AIChE Journal* 33, 121-129.
- [146] Zumstein, R. C., and Rousseau, R. W. (1987) Growth rate dispersion in batch crystallization with transient conditions, *AIChE Journal* 33, 1921-1925.
- [147] Persson, N. E., McBride, M. A., Grover, M. A., and Reichmanis, E. (2016) Automated Analysis of Orientational Order in Images of Fibrillar Materials, *Chemistry of Materials* 29, 3-14.
- [148] Persson, N., Rafshoon, J., Naghshpour, K., Fast, T., Chu, P.-H., McBride, M., Risteen, B., Grover, M. A., and Reichmanis, E. (2017) High-throughput Image Analysis of Fibrillar Materials: A Case Study on Polymer Nanofiber Packing, Alignment, and Defects in OFETs, *ACS Applied Materials & Interfaces*.

- [149] Lilliefors, H. W. (1967) On the Kolmogorov-Smirnov test for normality with mean and variance unknown, *Journal of the American statistical Association* 62, 399-402.
- [150] Ottens, M., Lebreton, B., Zomerdijk, M., Rijkers, M., Bruinsma, O. S. L., and van der Wielen, L. M. (2004) Impurity effects on the crystallization kinetics of ampicillin, *Industrial & Engineering Chemistry Research* 43, 7932-7938.
- [151] Feng, S., Shan, N., and Carpenter, K. J. (2006) Crystallization of amoxicillin trihydrate in the presence of degradation products, *Organic process research & development* 10, 1212-1218.
- [152] Diender, M. B., Straathof, A. J. J., Van der Does, T., Zomerdijk, M., and Heijnen, J. J. (2000) Course of pH during the formation of amoxicillin by a suspension-to-suspension reaction, *Enzyme and Microbial Technology* 27, 576-582.
- [153] Rose, H. B., Greinert, T., Held, C., Sadowski, G., and Bommarius, A. S. (2018) Mutual Influence of Furfural and Furancarboxylic Acids on Their Solubility in Aqueous Solutions: Experiments and Perturbed-Chain Statistical Associating Fluid Theory (PC-SAFT) Predictions, *Journal of Chemical & Engineering Data* 63, 1460-1470.
- [154] Paye, M. F., Rose, H. B., Robbins, J. M., Yunda, D. A., Cho, S., and Bommarius, A. S. (2018) A high-throughput pH-based colorimetric assay: application focus on alpha/beta hydrolases, *Analytical Biochemistry* 549, 80-90.
- [155] Bezerra, I., Chiavone-Filho, O., and Mattedi, S. (2013) Solid-liquid equilibrium data of amoxicillin and hydroxyphenylglycine in aqueous media, *Brazilian Journal of Chemical Engineering* 30, 45-54.
- [156] Diender, M., Straathof, A., Van der Wielen, L., Ras, C., and Heijnen, J. (1998) Feasibility of the thermodynamically controlled synthesis of amoxicillin, *Journal of Molecular Catalysis B: Enzymatic* 5, 249-253.
- [157] Felix, I., Moreira, L., Chiavone-Filho, O., and Mattedi, S. (2016) Solubility measurements of amoxicillin in mixtures of water and ethanol from 283.15 to 298.15 K, *Fluid Phase Equilibria* 422, 78-86.
- [158] McDonald, M. A., Bromig, L., Grover, M. A., Rousseau, R. W., and Bommarius, A. S. (2018) Kinetic model discrimination of penicillin G acylase thermal deactivation by non-isothermal continuous activity assay, *Chemical Engineering Science* 187, 79-86.
- [159] Yang, Y., and Nagy, Z. K. (2015) Advanced control approaches for combined cooling/antisolvent crystallization in continuous mixed suspension mixed product removal cascade crystallizers, *Chemical Engineering Science* 127, 362-373.

- [160] Schiesser, W. E., and Griffiths, G. W. (2009) *A compendium of partial differential equation models: method of lines analysis with Matlab*, Cambridge University Press.
- [161] Glasser, D., Crowe, C., and Hildebrandt, D. (1987) A geometric approach to steady flow reactors: the attainable region and optimization in concentration space, *Industrial & Engineering Chemistry Research* 26, 1803-1810.
- [162] Vetter, T., Burcham, C. L., and Doherty, M. F. (2014) Regions of attainable particle sizes in continuous and batch crystallization processes, *Chemical Engineering Science* 106, 167-180.
- [163] Levenspiel, O. (1972) *Chemical reaction engineering*, Vol. 2, Wiley New York etc.
- [164] Levenspiel, O., and Bischoff, K. B. (1959) Backmixing in the design of chemical reactors, *Industrial & Engineering Chemistry* 51, 1431-1434.
- [165] Juzaszek, P., and Larson, M. A. (1977) Influence of fines dissolving on crystal size distribution in an MSMPR crystallizer, *AIChE Journal* 23, 460-468.
- [166] Nagy, Z. K., Aamir, E., and Rielly, C. D. (2011) Internal fines removal using population balance model based control of crystal size distribution under dissolution, growth and nucleation mechanisms, *Crystal Growth & Design* 11, 2205-2219.
- [167] Majumder, A., and Nagy, Z. K. (2013) Fines removal in a continuous plug flow crystallizer by optimal spatial temperature profiles with controlled dissolution, *AIChE Journal* 59, 4582-4594.
- [168] Alpern, J. D., Zhang, L., Stauffer, W. M., and Kesselheim, A. S. (2017) Trends in Pricing and Generic Competition Within the Oral Antibiotic Drug Market in the United States, *Clinical Infectious Diseases* 65, 1848-1852.
- [169] Yu, L. (2016) Continuous Manufacturing Has a Strong Impact on Drug Quality, In *FDA Voice* (US Food and Drug Administration).
- [170] Kee, N. C. S., Arendt, P. D., Goh, L. M., Tan, R. B. H., and Braatz, R. D. (2011) Nucleation and growth kinetics estimation for L-phenylalanine hydrate and anhydrate crystallization, *CrystEngComm* 13, 1197-1209.
- [171] Rindfleisch, D., Syska, B., Lazarova, Z., and Schügerl, K. (1997) Integrated membrane extraction, enzymic conversion and electrodialysis for the synthesis of ampicillin from penicillin G, *Process Biochemistry* 32, 605-616.
- [172] Tavaré, N. S., and Garside, J. (1985) Multiplicity in continuous MSMPR crystallizers. Part I: Concentration multiplicity in an isothermal crystallizer, *AIChE Journal* 31, 1121-1127.

- [173] Alvarez, A. J., and Myerson, A. S. (2010) Continuous plug flow crystallization of pharmaceutical compounds, *Crystal Growth & Design* 10, 2219-2228.
- [174] Zauner, R., and Jones, A. G. (2002) On the influence of mixing on crystal precipitation processes—application of the segregated feed model, *Chemical Engineering Science* 57, 821-831.
- [175] O’Grady, D., Barrett, M., Casey, E., and Glennon, B. (2007) The Effect of Mixing on the Metastable Zone Width and Nucleation Kinetics in the Anti-Solvent Crystallization of Benzoic Acid, *Chemical Engineering Research and Design* 85, 945-952.
- [176] Moore, C. M. V. (2012) Quality by Design - FDA Lessons Learned and Challenges for International Harmonization, In *International Conference on Drug Development*, Houston, TX.
- [177] Yang, X., Acevedo, D., Mohammad, A., Pavurala, N., Wu, H., Brayton, A. L., Shaw, R. A., Goldman, M. J., He, F., Li, S., Fisher, R. J., O’Connor, T. F., and Cruz, C. N. (2017) Risk Considerations on Developing a Continuous Crystallization System for Carbamazepine, *Organic Process Research & Development* 21, 1021-1033.
- [178] Fysikopoulos, D., Benyahia, B., Borsos, A., Nagy, Z. K., and Rielly, C. D. (2018) A framework for model reliability and estimability analysis of crystallization processes with multi-impurity multi-dimensional population balance models, *Computers & Chemical Engineering*.
- [179] Lee, S. L., O’Connor, T. F., Yang, X., Cruz, C. N., Chatterjee, S., Madurawe, R. D., Moore, C. M. V., Yu, L. X., and Woodcock, J. (2015) Modernizing Pharmaceutical Manufacturing: from Batch to Continuous Production, *Journal of Pharmaceutical Innovation* 10, 191-199.
- [180] Kalbasenka, A., Huesman, A., and Kramer, H. (2011) Modeling batch crystallization processes: Assumption verification and improvement of the parameter estimation quality through empirical experiment design, *Chemical Engineering Science* 66, 4867-4877.
- [181] Griffin, D. J., Kawajiri, Y., Grover, M. A., and Rousseau, R. W. (2014) Feedback control of multicomponent salt crystallization, *Crystal Growth & Design* 15, 305-317.
- [182] Griffin, D. J., Grover, M. A., Kawajiri, Y., and Rousseau, R. W. (2016) Data-Driven Modeling and Dynamic Programming Applied to Batch Cooling Crystallization, *Industrial & Engineering Chemistry Research* 55, 1361-1372.
- [183] Maggioni, G. M., Kocavska, S., Grover, M. A., and Rousseau, R. W. (2019) Analysis of Multicomponent Ionic Mixtures Using Blind Source Separation: A Processing Case Study, *Industrial & Engineering Chemistry Research* 58, 22640-22651.

- [184] Seborg, D. E., Mellichamp, D. A., Edgar, T. F., and Doyle III, F. J. (2010) *Process dynamics and control*, John Wiley & Sons.
- [185] Varmuza, K., Karlovits, M., and Demuth, W. (2003) Spectral similarity versus structural similarity: infrared spectroscopy, *Analytica Chimica Acta* 490, 313-324.
- [186] Heinrich, J., and Ulrich, J. (2012) Application of Laser-Backscattering Instruments for In Situ Monitoring of Crystallization Processes - A Review, *Chem. Eng. Technol.* 35, 967-979.
- [187] Dave, K., Luner, P. E., Forness, C., Baker, D., Jankovsky, C., and Chen, S. (2018) Feasibility of Focused Beam Reflectance Measurement (FBRM) for Analysis of Pharmaceutical Suspensions in Preclinical Development, *AAPS PharmSciTech* 19, 155-165.
- [188] Ruf, A., Worlitschek, J., and Mazzotti, M. (2000) Modeling and Experimental Analysis of PSD Measurements Through FBRM, *Particle & Particle Systems Characterization* 17, 167-179.
- [189] Barthe, S., and Rousseau, R. W. (2006) Utilization of focused beam reflectance measurement in the control of crystal size distribution in a batch cooled crystallizer, *Chem. Eng. Technol.* 29, 206-211.
- [190] Grover, M. A., Barthe, S. C., and Rousseau, R. W. (2009) Principal Component Analysis for Estimating Population Density from Chord-Length Density, *AIChE Journal* 55, 2260-2270.
- [191] De Anda, J. C., Wang, X., and Roberts, K. (2005) Multi-scale segmentation image analysis for the in-process monitoring of particle shape with batch crystallisers, *Chemical Engineering Science* 60, 1053-1065.
- [192] Sarkar, D., Doan, X.-T., Ying, Z., and Srinivasan, R. (2009) In situ particle size estimation for crystallization processes by multivariate image analysis, *Chemical Engineering Science* 64, 9-19.
- [193] Schorsch, S., Vetter, T., and Mazzotti, M. (2012) Measuring multidimensional particle size distributions during crystallization, *Chemical Engineering Science* 77, 130-142.
- [194] Liu, S., and Deng, W. (2015) Very deep convolutional neural network based image classification using small training sample size, In *2015 3rd IAPR Asian Conference on Pattern Recognition (ACPR)*, pp 730-734.
- [195] Shewale, J. G., Kumar, K. K., and Ambekar, G. R. (1987) Evaluation of determination of 6-aminopenicillanic acid by p-dimethyl aminobenzaldedyde, *Biotechnology Techniques* 1, 69-72.

- [196] Zhang, H., Lakerveld, R., Heider, P. L., Tao, M., Su, M., Testa, C. J., D'Antonio, A. N., Barton, P. I., Braatz, R. D., Trout, B. L., Myerson, A. S., Jensen, K. F., and Evans, J. M. B. (2014) Application of Continuous Crystallization in an Integrated Continuous Pharmaceutical Pilot Plant, *Crystal Growth & Design* 14, 2148-2157.
- [197] Mesbah, A., Paulson, J. A., Lakerveld, R., and Braatz, R. D. (2017) Model Predictive Control of an Integrated Continuous Pharmaceutical Manufacturing Pilot Plant, *Organic Process Research & Development* 21, 844-854.
- [198] Seki, H., and Su, Y. (2015) Robust optimal temperature swing operations for size control of seeded batch cooling crystallization, *Chemical Engineering Science* 133, 16-23.
- [199] Gundlapalli, A. V., Beekmann, S. E., Graham, D. R., Polgreen, P. M., and Members of the Emerging Infections, N. (2018) Antimicrobial Agent Shortages: The New Norm for Infectious Diseases Physicians, *Open Forum Infectious Diseases* 5, ofy068-ofy068.
- [200] Patel, J. M., Fox, E. R., Zocchi, M., Lee, Z.-E., and Mazer-Amirshahi, M. (2017) Trends in United States Drug Shortages for Medications Used in Gastroenterology, *Medicine Access @ Point of Care* 1.
- [201] Quadri, F., Mazer-Amirshahi, M., Fox, E. R., Hawley, K. L., Pines, J. M., Zocchi, M. S., and May, L. (2015) Antibacterial Drug Shortages From 2001 to 2013: Implications for Clinical Practice, *Clinical Infectious Diseases* 60, 1737-1742.
- [202] Capellades, G., Joshi, P. U., Dam-Johansen, K., Mealy, M. J., Christensen, T. V., and Kiil, S. (2018) Characterization of a Multistage Continuous MSMPR Crystallization Process Assisted by Image Analysis of Elongated Crystals, *Crystal Growth & Design* 18, 6455-6469.
- [203] Jiang, M., and Xiong-Wei, N. (2019) Reactive crystallization of paracetamol in a continuous oscillatory baffled reactor, *Organic Process Research & Development* 23, 882-890.
- [204] Youngquist, G. R., and Randolph, A. D. (1972) Secondary nucleation in a class II system: Ammonium sulfate-water, *AIChE Journal* 18, 421-429.
- [205] Garside, J., and Shah, M. B. (1980) Crystallization kinetics from MSMPR crystallizers, *Industrial & Engineering Chemistry Process Design and Development* 19, 509-514.
- [206] Agnew, L. R., McGlone, T., Wheatcroft, H. P., Robertson, A., Parsons, A. R., and Wilson, C. C. (2017) Continuous Crystallization of Paracetamol (Acetaminophen) Form II: Selective Access to a Metastable Solid Form, *Crystal Growth & Design* 17, 2418-2427.

- [207] Li, J., Lai, T.-t. C., Trout, B. L., and Myerson, A. S. (2017) Continuous Crystallization of Cyclosporine: Effect of Operating Conditions on Yield and Purity, *Crystal Growth & Design* 17, 1000-1007.
- [208] Tahara, K., Kono, Y., Myerson, A. S., and Takeuchi, H. (2018) Development of Continuous Spherical Crystallization to Prepare Fenofibrate Agglomerates with Impurity Complexation Using Mixed-Suspension, Mixed-Product Removal Crystallizer, *Crystal Growth & Design* 18, 6448-6454.
- [209] Acevedo, D., Yang, X., Liu, Y., O'Connor, T. F., Koswara, A., Nagy, Z. K., Madurawe, R., and Cruz, C. N. (2019) Encrustation in Continuous Pharmaceutical Crystallization Process-A Review, *Organic Process Research & Development* 23, 1134-1142.
- [210] Capellades, G., Wiemeyer, H., and Myerson, A. S. (2019) Mixed-Suspension, Mixed-Product Removal Studies of Ciprofloxacin from Pure and Crude Active Pharmaceutical Ingredients: The Role of Impurities on Solubility and Kinetics, *Crystal Growth & Design* 19, 4008-4018.
- [211] Randolph, A. D., and Sikdar, S. K. (1976) Creation and Survival of Secondary Crystal Nuclei. The Potassium Sulfate-Water System, *Industrial & Engineering Chemistry Fundamentals* 15, 64-71.
- [212] Jerauld, G. R., Vasatis, Y., and Doherty, M. F. (1983) Simple conditions for the appearance of sustained oscillations in continuous crystallizers, *Chemical Engineering Science* 38, 1675-1681.
- [213] Song, Y. H., and Douglas, J. M. (1975) Self-generated oscillations in continuous crystallizers: Part II. An experimental study of an isothermal system, *AIChE Journal* 21, 924-930.
- [214] Larson, M. A., White, E., Ramanarayanan, K. A., and Berglund, K. A. (1985) Growth rate dispersion in MSMPR crystallizers, *AIChE Journal* 31, 90-94.
- [215] Tavares, N. S., Garside, J., and Akoglu, K. (1985) Multiplicity in continuous MSMPR crystallizers. Part II: Temperature multiplicity in a cooling crystallizer, *AIChE Journal* 31, 1128-1135.
- [216] Yin, Q., Wang, J., Xu, Z., and Li, G. (2000) Analysis of Concentration Multiplicity Patterns of Continuous Isothermal Mixed Suspension-Mixed Product Removal Reactive Precipitators, *Industrial & Engineering Chemistry Research* 39, 1437-1442.
- [217] Alvarez, A. J., Singh, A., and Myerson, A. S. (2011) Crystallization of cyclosporine in a multistage continuous MSMPR crystallizer, *Crystal Growth & Design* 11, 4392-4400.

- [218] Wang, J., and Lakerveld, R. (2017) Continuous Membrane-Assisted Crystallization To Increase the Attainable Product Quality of Pharmaceuticals and Design Space for Operation, *Industrial & Engineering Chemistry Research* 56, 5705-5714.
- [219] Vartak, S., and Myerson, A. S. (2017) Continuous Crystallization with Impurity Complexation and Nanofiltration Recycle, *Organic Process Research & Development* 21, 253-261.
- [220] Ferguson, S., Ortner, F., Quon, J., Peeva, L., Livingston, A., Trout, B. L., and Myerson, A. S. (2013) Use of continuous MSMPR crystallization with integrated nanofiltration membrane recycle for enhanced yield and purity in API crystallization, *Crystal Growth & Design* 14, 617-627.
- [221] Schall, J. M., Mandur, J. S., Braatz, R. D., and Myerson, A. S. (2018) Nucleation and Growth Kinetics for Combined Cooling and Antisolvent Crystallization in a Mixed-Suspension, Mixed-Product Removal System: Estimating Solvent Dependency, *Crystal Growth & Design* 18, 1560-1570.
- [222] Köllges, T., and Vetter, T. (2019) Polymorph Selection and Process Intensification in a Continuous Crystallization–Milling Process: A Case Study on l-Glutamic Acid Crystallized from Water, *Organic Process Research & Development* 23, 361-374.
- [223] Farmer, T. C., Carpenter, C. L., and Doherty, M. F. (2016) Polymorph selection by continuous crystallization, *AIChE Journal* 62, 3505-3514.
- [224] Farmer, T. C., Schiebel, S. K., Chmelka, B. F., and Doherty, M. F. (2018) Polymorph Selection by Continuous Precipitation, *Crystal Growth & Design* 18, 4306-4319.
- [225] Köllges, T., and Vetter, T. (2017) Model-Based Analysis of Continuous Crystallization/Reaction Processes Separating Conglomerate Forming Enantiomers, *Crystal Growth & Design* 17, 233-247.
- [226] Köllges, T., and Vetter, T. (2018) Design and Performance Assessment of Continuous Crystallization Processes Resolving Racemic Conglomerates, *Crystal Growth & Design* 18, 1686-1696.
- [227] Xiouras, C., Belletti, G., Venkatramanan, R., Nordon, A., Meekes, H., Vlieg, E., Stefanidis, G. D., and Ter Horst, J. H. (2019) Toward Continuous Deracemization via Racemic Crystal Transformation Monitored by in Situ Raman Spectroscopy, *Crystal Growth & Design* 19, 5858-5868.
- [228] Li, M., Shang, Z., and Hou, B. (2019) Optimizing the Aspect Ratio of Cephalexin in Reactive Crystallization by Controlling Supersaturation and Seeding Policy, *Transactions of Tianjin University* 25, 348-356.
- [229] Eder, R. J. P., Radl, S., Schmitt, E., Innerhofer, S., Maier, M., Gruber-Woelfler, H., and Khinast, J. G. (2010) Continuously seeded, continuously operated tubular

crystallizer for the production of active pharmaceutical ingredients, *Crystal Growth & Design* 10, 2247-2257.

- [230] Su, M., and Gao, Y. (2018) Air–Liquid Segmented Continuous Crystallization Process Optimization of the Flow Field, Growth Rate, and Size Distribution of Crystals, *Industrial & Engineering Chemistry Research* 57, 3781-3791.
- [231] Ferguson, S., Morris, G., Hao, H., Barrett, M., and Glennon, B. (2012) In-situ monitoring and characterization of plug flow crystallizers, *Chemical Engineering Science* 77, 105-111.
- [232] Sang-II Kwon, J., Nayhouse, M., Orkoulas, G., and Christofides, P. D. (2014) Crystal shape and size control using a plug flow crystallization configuration, *Chemical Engineering Science* 119, 30-39.
- [233] Lawton, S., Steele, G., Shering, P., Zhao, L., Laird, I., and Ni, X.-W. (2009) Continuous crystallization of pharmaceuticals using a continuous oscillatory baffled crystallizer, *Organic Process Research & Development* 13, 1357-1363.
- [234] McGlone, T., Briggs, N. E. B., Clark, C. A., Brown, C. J., Sefcik, J., and Florence, A. J. (2015) Oscillatory Flow Reactors (OFRs) for Continuous Manufacturing and Crystallization, *Organic Process Research & Development* 19, 1186-1202.
- [235] Dafnomilis, A., Diab, S., Rodman, A. D., Boudouvis, A. G., and Gerogiorgis, D. I. (2019) Multiobjective Dynamic Optimization of Ampicillin Batch Crystallization: Sensitivity Analysis of Attainable Performance vs Product Quality Constraints, *Industrial & Engineering Chemistry Research* 58, 18756-18771.
- [236] Jiang, M., and Xiong-Wei, N. (2019) Reactive crystallization of paracetamol in a continuous oscillatory baffled reactor, *Organic Process Research & Development* 23, 882-890.
- [237] Oroskar, A. R., and Turian, R. M. (1980) The critical velocity in pipeline flow of slurries, *AIChE Journal* 26, 550-558.
- [238] Luo, X., and Zhang, L. (2010) Immobilization of penicillin G acylase in epoxy-activated magnetic cellulose microspheres for improvement of biocatalytic stability and activities, *Biomacromolecules* 11, 2896-2903.
- [239] Zdarta, J., Meyer, A., Jesionowski, T., and Pinelo, M. (2018) A general overview of support materials for enzyme immobilization: characteristics, properties, practical utility, *Catalysts* 8, 92.
- [240] Netto, C. G., Toma, H. E., and Andrade, L. H. (2013) Superparamagnetic nanoparticles as versatile carriers and supporting materials for enzymes, *Journal of Molecular Catalysis B: Enzymatic* 85, 71-92.

- [241] Pamme, N., and Wilhelm, C. (2006) Continuous sorting of magnetic cells via on-chip free-flow magnetophoresis, *Lab on a Chip* 6, 974-980.
- [242] Wibowo, C., Chang, W. C., and Ng, K. M. (2001) Design of Integrated Crystallization Systems, *AIChE Journal* 47, 2474-2492.
- [243] Yazdanpanah, N., Ferguson, S. T., Myerson, A. S., and Trout, B. L. (2015) Novel Technique for Filtration Avoidance in Continuous Crystallization, *Crystal Growth & Design*.
- [244] Bourcier, D., Féraud, J. P., Colson, D., Mandrick, K., Ode, D., Brackx, E., and Puel, F. (2016) Influence of particle size and shape properties on cake resistance and compressibility during pressure filtration, *Chemical Engineering Science* 144, 176-187.
- [245] Perini, G., Salvatori, F., Ochsenbein, D. R., Mazzotti, M., and Vetter, T. (2019) Filterability prediction of needle-like crystals based on particle size and shape distribution data, *Separation and Purification Technology* 211, 768-781.
- [246] Yang, Y., Song, L., Zhang, Y., and Nagy, Z. K. (2016) Application of Wet Milling-Based Automated Direct Nucleation Control in Continuous Cooling Crystallization Processes, *Industrial & Engineering Chemistry Research* 55, 4987-4996.
- [247] Acevedo, D., Kamaraju, V. K., Glennon, B., and Nagy, Z. K. (2017) Modeling and Characterization of an in Situ Wet Mill Operation, *Organic Process Research & Development* 21, 1069-1079.
- [248] Yang, Y., Pal, K., Koswara, A., Sun, Q., Zhang, Y., Quon, J., McKeown, R., Goss, C., and Nagy, Z. K. (2017) Application of feedback control and in situ milling to improve particle size and shape in the crystallization of a slow growing needle-like active pharmaceutical ingredient, *International Journal of Pharmaceutics* 533, 49-61.
- [249] Salvatori, F., and Mazzotti, M. (2018) Experimental Characterization and Mathematical Modeling of Breakage of Needle-like Crystals in a Continuous Rotor-Stator Wet Mill, *Crystal Growth & Design* 18, 5957-5972.
- [250] Gelband, H., Miller-Petrie, M., Pant, S., Gandra, S., Levinson, J., Barter, D., White, A., Laxminarayan, R., Ganguly, N. K., and Kariuki, S. (2015) The State of the World's Antibiotics 2015, *Wound Healing Southern Africa* 8, 30-34.
- [251] Cacace, D., Fatta-Kassinos, D., Manaia, C. M., Cytryn, E., Kreuzinger, N., Rizzo, L., Karaolia, P., Schwartz, T., Alexander, J., Merlin, C., Garelick, H., Schmitt, H., de Vries, D., Schwermer, C. U., Meric, S., Ozkal, C. B., Pons, M.-N., Kneis, D., and Berendonk, T. U. (2019) Antibiotic resistance genes in treated wastewater and in the receiving water bodies: A pan-European survey of urban settings, *Water Research* 162, 320-330.

- [252] Li, D., Yang, M., Hu, J., Zhang, J., Liu, R., Gu, X., Zhang, Y., and Wang, Z. (2009) Antibiotic-resistance profile in environmental bacteria isolated from penicillin production wastewater treatment plant and the receiving river, *Environmental Microbiology* 11, 1506-1517.
- [253] Hoeben, M. A., van Hee, P., van der Lans, R. G. J. M., Kwant, G., and van der Wielen, L. A. M. (2009) Design of a Counter-Current Interfacial Partitioning Process for the Separation of Ampicillin and Phenylglycine, *Industrial & Engineering Chemistry Research* 48, 7753-7766.
- [254] Deschamps, E., Vasconcelos, O., Lange, L., Donnici, C. L., Silva, M. C. d., and Sales, J. A. (2012) Management of effluents and waste from pharmaceutical industry in Minas Gerais, Brazil, *Brazilian Journal of Pharmaceutical Sciences* 48, 727-736.
- [255] Schellenberger, V., and Jakubke, H. D. (1991) Protease-catalyzed kinetically controlled peptide synthesis, *Angewandte Chemie International Edition in English* 30, 1437-1449.
- [256] Tilbury, C. J., and Doherty, M. F. (2017) Modeling layered crystal growth at increasing supersaturation by connecting growth regimes, *AIChE Journal* 63, 1338-1352.
- [257] Jiang, M., Zhu, X. X., Molaro, M. C., Rasche, M. L., Zhang, H. T., Chadwick, K., Raimondo, D. M., Kim, K. K. K., Zhou, L. F., Zhu, Z. L., Wong, M. H., O'Grady, D., Hebrault, D., Tedesco, J., and Braatz, R. D. (2014) Modification of Crystal Shape through Deep Temperature Cycling, *Industrial & Engineering Chemistry Research* 53, 5325-5336.
- [258] Salvalaglio, M., Vetter, T., Mazzotti, M., and Parrinello, M. (2013) Controlling and predicting crystal shapes: The case of urea, *Angewandte Chemie International Edition* 52, 13369-13372.
- [259] Majumder, A., and Nagy, Z. K. (2013) Prediction and control of crystal shape distribution in the presence of crystal growth modifiers, *Chemical Engineering Science* 101, 593-602.
- [260] Schroen, C., Nierstrasz, V., Bosma, R., Kroon, P., Tjeerdsma, P., DeVroom, E., VanderLaan, J., Moody, H., Beeftink, H., and Janssen, A. (2002) Integrated reactor concepts for the enzymatic kinetic synthesis of cephalixin, *Biotechnology and Bioengineering* 80, 144-155.
- [261] Lacmann, R., and Tanneberger, U. (1995) Growth rate dispersion of single potassium alum crystals, *Journal of Crystal Growth* 147, 194-199.
- [262] Tanneberger, U., Lacmann, R., Herden, A., Klapper, H., Schmiemann, D., Becker, R. A., Mersmann, A., and Zacher, U. (1996) The dispersion of growth rate as a result of different crystal perfection, *Journal of Crystal Growth* 166, 1074-1077.

- [263] Borchert, C., Temmel, E., Eisenschmidt, H., Lorenz, H., Seidel-Morgenstern, A., and Sundmacher, K. (2014) Image-Based in Situ Identification of Face Specific Crystal Growth Rates from Crystal Populations, *Crystal Growth & Design* 14, 952-971.
- [264] Godinho, J. R. A., and Stack, A. G. (2015) Growth Kinetics and Morphology of Barite Crystals Derived from Face-Specific Growth Rates, *Crystal Growth & Design* 15, 2064-2071.
- [265] Toyokura, K., Tawa, K., and Ueno, J. (1979) Reaction Crystallization of Sulfamic Acid from Urea and Fuming Sulfuric Acid, *Journal of Chemical Engineering of Japan* 12, 24-28.
- [266] Kelkar, V. V., and Ng, K. M. (1999) Design of reactive crystallization systems incorporating kinetics and mass-transfer effects, *AIChE Journal* 45, 69-81.
- [267] Salami, H., Lagerman, C. E., Harris, P. R., McDonald, M. A., Bommarius, A. S., Rousseau, R. W., and Grover, M. A. (2020) Model development for enzymatic reactive crystallization of β -lactam antibiotics: a reaction–diffusion–crystallization approach, *Reaction Chemistry & Engineering*.
- [268] Yu, K. M., and Douglas, J. M. (1975) Self-generated oscillations in continuous crystallizers: Part I. Analytical prediction of the oscillating output, *AIChE Journal* 21, 917-924.

VITA

Matthew McDonald was born and raised in Annandale, New Jersey. In 2011 Matt began attending Princeton University, where he received a Bachelor of Science degree in Chemical and Biological Engineering with a certificate in Applications of Computing in 2015. At Princeton, his undergraduate thesis explored creating aerogels from graphene for use as stretchable electrical conductors, winning the department award for innovative undergraduate research. Matt was also the captain of the Men's Cross Country and Track teams. In 2015 he moved to Georgia Institute of Technology to pursue a PhD, joining the lab groups of Prof. Andreas S. Bommarius and Prof. Ronald W. Rousseau, studying biocatalysis and crystallization. He would additionally join the advisees of Martha A. Grover in 2016 as his research began incorporating more modeling and optimization. Matt's passion for long distance running followed him to Atlanta; he now competes as a professional marathon runner, representing Atlanta Track Club. He narrowly missed representing Team USA at the Tokyo Olympics, placing tenth at the Olympic Trials after climbing to third place by mile 21 of the race.